The University of Texas at Dallas
Center for Quantum Electronics
The Gamma-Ray Laser Project
Annual Report FY-1988

DTIC
SELECTE
SEP 0 1 1989
D

Best Available Copy

89   9   01 045

Report GRL/8805

PROOF OF THE FEASIBILITY
OF COHERENT AND INCOHERENT SCHEMES
FOR PUMPING A GAMMA-RAY LASER

Principal Investigator: Carl B. Collins
The University of Texas at Dallas
Center for Quantum Electronics
P.O. Box 830688
Richardson, Texas   75083-0688

June 1989

Annual Technical Progress Report
1 April 1988 through 31 March 1989
Contract Number N00014-86-C-2488

This document has been approved
for public release and sale;
its distribution is unlimited.

Prepared for
INNOVATIVE SCIENCE AND TECHNOLOGY DIRECTORATE
OF STRATEGIC DEFENSE INITIATIVE ORGANIZATION

Contracting Officer's Technical Representative
Dr. Paul Kepple, Code 4720
Naval Research Laboratory
4555 Overlook Avenue, SW
Washington, DC   20375-5000

A-1

REPORT DOCUMENTATION PAGE		READ INSTRUCTIONS BEFORE COMPLETING FORM
1. REPORT NUMBER GRL/8805	2. GOVT ACCESSION NO.	3. RECIPIENT'S CATALOG NUMBER
4. TITLE (and Subtitle) PROOF OF THE FEASIBILITY OF COHERENT AND INCOHERENT SCHEMES FOR PUMPING A GAMMA-RAY LASER		5. TYPE OF REPORT & PERIOD COVERED Annual Technical Progress 4/1/88 - 3/31/89
		6. PERFORMING ORG. REPORT NUMBER
7. AUTHOR(s) Carl B. Collins		8. CONTRACT OR GRANT NUMBER(s) N00014-86-C-2488
9. PERFORMING ORGANIZATION NAME AND ADDRESS University of Texas at Dallas Center for Quantum Electronics P.O. Box 830688 Richardson, TX 75083-0688		10. PROGRAM ELEMENT, PROJECT, TASK AREA & WORK UNIT NUMBERS
11. CONTROLLING OFFICE NAME AND ADDRESS INNOVATIVE SCIENCE AND TECHNOLOGY DIRECTORATE OF STRATEGIC DEFENSE INITIATIVE ORGANIZATION		12. REPORT DATE June 1989
		13. NUMBER OF PAGES 230
14. MONITORING AGENCY NAME & ADDRESS(If different from Controlling Office) Dr. Paul Kepple, Code 4720 Naval Research Laboratory 4555 Overlook Avenue, SW Washington, DC 20375-5000		15. SECURITY CLASS. (of this report) Unclassified
		15a. DECLASSIFICATION, DOWNGRADING SCHEDULE

16. DISTRIBUTION STATEMENT (of this Report)

This document has been approved for public release and sale;
its distribution is unlimited.

17. DISTRIBUTION STATEMENT (of the abstract entered in Block 20, if different from Report)

18. SUPPLEMENTARY NOTES

19. KEY WORDS (Continue on reverse side if necessary and identify by block number)

Gamma-ray laser, Ultrashort wavelength laser

20. ABSTRACT (Continue on reverse side if necessary and identify by block number)

Recent approaches to the problem of the gamma-ray laser have
focused upon upconversion techniques in which metastable nuclei
are pumped with long wavelength radiation. At the nuclear level
the storage of energy can approach tera-Joules (10^{12}J) per liter
for thousands of years. However, any plan to use such a resource
for a gamma-ray laser poses problems of a broad interdisciplinary
(continued on next page)

20. Abstract (continued)

nature requiring the fusion of concepts taken from relatively unrelated fields of physics. Our research group has described several means through which this energy might be coupled to the radiation fields with cross sections for stimulated emission that could reach 10^{-17} cm^2. Such a stimulated release could lead to output powers as great as 3×10^{21} Watts/liter. Since 1978 we have pursued an approach for the upconversion of longer wavelength radiation incident upon isomeric nuclear populations that can avoid many of the difficulties encountered with traditional concepts of single photon pumping. Recent experiments have confirmed the general theory and have indicated that a gamma-ray laser is feasible if the right combination of energy levels and branching ratios exists in some real material. Of the 1,886 distinguishable nuclear materials, the present state-of-the-art has been adequate to identify 29 first-class candidates, but further evaluation cannot proceed without remeasurements of nuclear properties with higher precision. A laser-grade database of nuclear properties does not yet exist, but the techniques for constructing one have been developed under this contract and are now being utilized. Resolution of the question of the feasibility of a gamma-ray laser now rests upon the determination of: 1) the identity of the best candidate, 2) the threshold level of laser output, and 3) the upconversion driver for that material.

This third year's report continues to focus upon our approach that is the nuclear analog to the ruby laser. It embodies the simplest concepts for a gamma-ray laser and not surprisingly, the greatest rate of achievement in the quest for a subAngstrom laser continues in that direction. For ruby the identification and exploitation of a bandwidth funnel were the critical keys in the development of the first laser. There was a broad absorption band linked through efficient cascading to the narrow laser level.

In 1987 we had reported a major milestone which showed that comparable structure existed at the nuclear scale in the first of the 29 candidate isomers available for testing, ^{180}Ta^m. Populations of the isomer were successfully pumped down with flashes of x-rays absorbed through an astonishingly large cross section of 40,000 on the usual scale ($\times 10^{-29}$ cm^2 keV) where 10 describes a fully allowed process. This corresponded to a partial width for useful absorption of 0.5 eV, even better than what had been assumed for idealized nuclei. In this past year we discovered that the giant pumping resonances occur with a gratifying frequency throughout the table of nuclides, reaching optimal size and strength in the mass region where the better candidates lie. Nineteen isomers were successfully pumped with the bremsstrahlung from both a 4 MeV linac and a 6 MeV linac. The giant resonances for pumping the candidate isomers ^{180}Ta^m and ^{123}Te^m were found to open at gateway energies well below 4 MeV. These candidates have the largest integrated cross sections for pumping with x-rays ever found below 4 MeV in any nuclei. These two poorest of the 29 candidates are the only ones available for testing and they continue to outperform even the most optimistic expectations. The likelihood for the full feasibility of one of the better candidates continues to be raised by the successes enjoyed with the least attractive of the 29 candidates.

TABLE OF CONTENTS

        "Depopulation of the Isomeric State ^{180}Ta^m by the Reaction
            ^{180}Ta$^m(\gamma,\gamma')^{180}$Ta," by C. B. Collins, C. D. Eberhard,
            J. W. Glesener, and J. A. Anderson, Phys. Rev. C 37,
            2267-2269 (1988).

        "Diamond-like Carbon Films Prepared with a Laser Ion Source,"
            by S. S. Wagal, E. M. Juengerman, and C. B. Collins, Appl.
            Phys. Lett. 53, 187-188 (1988).

        "Activation of ^{115}In^m by Single Pulses of Intense Bremsstrah-
            lung," by C. B. Collins, J. A. Anderson, Y. Paiss,
            C. D. Eberhard, R. J. Peterson, and W. L. Hodge, Phys.
            Rev. C 38, 1852-1856 (1988).

        "A Flash X-Ray Source Excited by Stacked Blumlein Generators,"
            by F. Davanloo, J. J. Coogan, T. S. Bowen, R. K. Krause,
            and C. B. Collins, Rev. Sci. Instrum. 59, 2260-2264
            (1988).

        "Activation of ^{111}Cd^m by Single Pulses of Intense Bremsstrah-
            lung," by J. A. Anderson, M. J. Byrd, and C. B. Collins,
            Phys. Rev. C 38, 2838-2842 (1988).

        "Comment on 'Mössbauer Sidebands from a Single Parent Line',"
            by C. B. Collins, P. W. Reittinger, and T. W. Sinor, Phys.
            Rev. B 39, 9655-9659 (1989).

        "Large Scale Effects of the Magnetic Phase Modulation of Re-
            coilless Gamma Transitions," T. W. Sinor, P. W. Reittinger,
            and C. B. Collins, Phys. Rev. Lett. 62, 2547-2551 (1989).

        "A Laser Plasma Source of Amorphic Diamond," C. B. Collins,
            F. Davanloo, E. M. Juengerman, W. R. Osborn, and
            D. R. Jander, Appl. Phys. Lett. 54, 216-218 (1989).

PREFACE

Emphasis this year has continued to focus upon the successes enjoyed along the approach to the gamma-ray laser that depends upon incoherent pumping. Last year we had first reported the giant resonance for the dumping of the $^{180}Ta^m$ isomer by pumping samples with flash x-rays of relatively modest intensities from a 6 MeV linac in a scheme which is the nuclear analog of the ruby laser. This particular material, the worst of the 29 actual candidates, showed what was at that time the largest integrated cross section ever reported for interband transfer in any nuclear material, 4×10^{-22} cm^2 eV. This was an enormous value for bandwidth funneling to a fluorescent level, corresponding to about 0.5 eV of useful width for the absorption of the pump x-rays.

Studies conducted this year have shown that the giant pumping resonances occur with a gratifying frequency throughout the table of nuclides. Concern had first arisen that these seemingly favorable structures might lie at high energies of excitation near the threshold for neutron evaporation, and so be associated in some way with the high density of nuclear states expected there. This has not proven to be the case. This particular experimental series culminated in a major milestone achievement in which *nineteen isomers were successfully pumped with the bremsstrahlung from a 4 MeV linac*. The density of nuclear states near 4 MeV should be exponentially reduced from values expected near 6 MeV, and yet most isomers were excited with comparable efficiencies by linacs operated at the two energies. The two poorest of the 29 candidates for a gamma-ray laser, $^{180}Ta^m$ and $^{123}Te^m$, showed the least variation in excitation when the end point of the bremsstrahlung was lowered from 6 to 4 MeV. Still, no other candidates are available, but results for these two would encourage expectations that the great width associated with pumping candidate isomers is concentrated at relatively few discrete transition energies.

As usual with these experiments, no significant contributions were made by spurious neutrons evaporated from environmental materials. Although this point has been made in the past, contemporary discussions of the giant resonances for pumping (γ,γ') reactions often still become concerned with potential neutron contaminations. Summarized in this annual report are all of the results of the exhaustive attention that had been paid to the elimination of this problem in the irradiation

i

environment produced with the 6 MeV linac. At 4 MeV the possibilities for neutrons to contribute activation are even more reduced: shrinking from the few tenths of a percent that characterized the 6 MeV work to completely negligible values.

So much attention has been paid to the direct approach to the pumping of a gamma-ray laser that it has tended to eclipse the sustained progress enjoyed in our other approaches. One of the most difficult breakthroughs was realized this past year along the more complex direction of coherent pumping. In this process the intent is to mix the quantum properties of long-lived nuclear states with those able to radiate freely. In this way the metastability of an isomeric state could be "switched off." The critical experiment is to show that some laboratory level <u>coherent</u> input power can affect the properties of a nuclear level. Reported recently in Phys. Rev. Lett. was the demonstration that large levels of modulation of the phases of nuclear states can be obtained with relatively modest input powers.

As has been the case since 1982, there are still no known factors which inhibit the realization of a gamma-ray laser. Neither the level of pump fluence required for laser threshold nor the waste heat to reject presents any particular problem in idealized materials. *A gamma-ray laser is feasible if the right combination of energy levels occurs in some real material.* When actually tested, the two poorest of the 29 candidate nuclei did surprisingly well, performing 1,000 to 10,000 times better than expected. The overriding question in resolving the feasibility of the nuclear analog to the ruby laser is whether or not one of the better of the 29 has its isomeric level in a position sufficiently near the ideal.

This annual report has been prepared from three components. First are the reports of major milestone achievements realized during this reporting period, followed by the individual articles elaborating upon results that have not yet been published in technical journals. Finally, in the Appendix are found reprints of those results appearing in the reviewed journals during this past year. In this regard, I wish to thank again all our staff for their splendid efforts in supporting the preparation of these manuscripts to a rather demanding timetable.

- C. B. Collins
- Director
- Center for Quantum Electronics

MAJOR MILESTONE REPORT

Strengthening the Feasibility of the Tuning
and Stimulation of Nuclear Radiation

June 1, 1988

C. B. Collins, Center for Quantum Electronics, University of Texas at Dallas

Achievement

Tunable sidebands have been produced on gamma-ray transitions by directly modulating the phases of nuclear states at levels far exceeding any noise contributed by magnetoacoustic effects.

Technical Background

The approach to the gamma-ray laser with the greatest potential efficiency depends upon the mixing of nearly resonant nuclear states with interaction energies developed by the external modulation of the hyperfine fields. In this way stored isomeric populations could be dumped into freely radiating states.

The first milestone would be a demonstration that significant interaction energies can be developed at the nuclear level by externally applied fields. Overseas efforts have shown that a magnetic field oscillating at radiofrequencies can directly modulate the phase of a nuclear state by coupling to its magnetic moment. In the frequency domain such modulation is observed as sidebands on gamma-ray transitions originating on the state, but the effect is very small at all reasonable levels of applied power.

The conceptual key to thousandfold enhancements lies in the use of small fields to manipulate the greater magnetic fields arising from the natural correlations of individual magnons in ferromagnetic materials. For several years we have observed the production of sidebands to Mössbauer transitions on such a large scale in ferromagnetic materials, but the concern has lingered that the dominant effect might have actually arisen from periodic Doppler shifts produced by vibrations in the host lattice driven by magnetostriction.

Report

As a basis for comparison, sidebands were excited on the unsplit absorption transition of ^{57}Fe nuclei at 14.4 keV in a stainless steel foil by sinusoidal vibrations injected with a piezoelectric source as shown in Fig. 1a. In the usual longitudinal geometry for a transmission experiment a convenient level of input power produced a reference level of sideband development in which the 4th order contained 20% of the intensity remaining in the parent line. In the transverse geometry the effect of phonons transported in the foil about 1 cm around a bend of 90 degrees could not be detected, even with a tenfold increase in power above the reference level
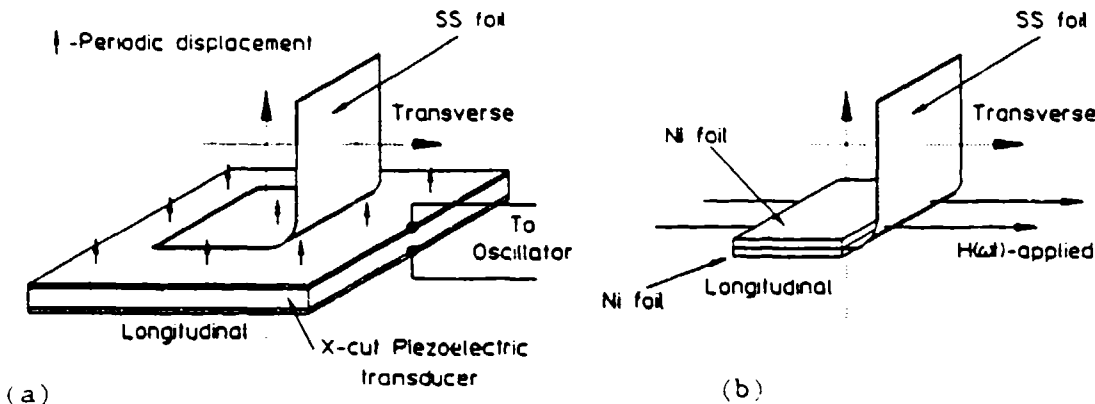
Figure 1: Schematic representation of the mounting of the enriched stainless steel foil 2.5 μm thick used in these transmission experiments. The vectors of the propagation of the gammas from sources to detectors are shown by the dotted arrows for the longitudinal and transverse arrangements shown.
a) (left) Sidebands driven by phonons from an X-cut quartz crystal.
b) (right) Sidebands driven by the oscillating magnetization of the two Ni foils immersed in the applied H field shown.

Replacing the piezoelectric source with a pair of 2.5 μm foils of ferromagnetic Ni sinusoidally magnetized as shown in Fig. 1b, gave the opportunity to launch what we believe are large amplitude spin waves into the magnon fluid in the paramagnetic stainless foil. Boundary effects known as flux refractions favor the transfer of ferromagnetic magnetization of the Ni across the interface where it can serve as a source term for local alignment of the magnons in the stainless foil. The longitudinal geometry was used to set the same reference level of sideband development at the source. In the transverse geometry at this same level of input power, the first order sidebands were found to have 20% of the intensity of the parent line, a level 10 times the threshold for detection and hence, 100 times any component contributed by acoustic phonons.

Significance

There is a twofold significance to this major milestone experiment.

1) In stainless steel spin waves can be transported more efficiently than phonons, thus providing a means for studying the direct modulation of nuclear states in an environment free from acoustic noise.

2) Even with transport the intensities of magnetic sidebands are greatly enhanced by ferromagnetic sources meaning that relatively large interaction energies can be developed at the nuclear level with modest applied powers.

MAJOR MILESTONE REPORT

Strengthening the Feasibility of a Gamma-Ray Laser

June 30, 1988

C. B. Collins, Center for Quantum Electronics, University of Texas at Dallas

Achievements

Giant resonances for pumping isomeric nuclei with flash x-rays have been found in many isotopes, but the best x-ray energies for exciting them have been impossible to determine. Now, one has been located in a demonstration nucleus with an enormous cross section at a practical value of x-ray energy.

Technical Background

The nuclear analog of the ruby laser embodies the simplest concepts for a gamma-ray laser. Not surprisingly, the greatest rate of achievement in the quest for a subAngstrom laser continues in that direction. For ruby the identification and exploitation of a bandwidth funnel were the critical keys in the development of the first laser. There was a broad absorption band linked through efficient cascading to the narrow laser level.

Recently we reported a major milestone which showed that comparable structure existed at the nuclear scale in the first of the 29 candidate isomers available for tests, $^{180}Ta^m$. Populations of the isomer were successfully pumped down with flashes of x-rays absorbed through an astonishingly large cross section of 40,000 on the usual scale ($\times$ 10^{-29} cm^2 keV) where 10 describes a fully allowed process. Then we discovered that these giant funnels for pumping isomers occurred rather frequently. We found them in the second of the 29 candidates, $^{123}Te^m$, as well as in other demonstration nuclei such as ^{197}Au and ^{195}Pt. However, until now, no experiment could pinpoint the location of such giant resonances in the scheme of energy levels for any nucleus.

Reported here is success in locating at 2600 keV the giant resonance for pumping $^{197}Au^m$ with flash x-rays through an integrated cross section of 3700 units. Another discrete resonance was found at a more difficult energy of 4800 keV, but it had an even larger cross section of 100,000 units.

Report

The inability to vary the spectrum of the x-rays pumping the isomers had previously prevented us from locating the precise energy necessary to reach the giant resonances. The spectrum of intensities normally used is the bremsstrahlung from a 6 MeV linac shown in Fig. 1 by the solid curve. In this major milestone experiment we obtained other spectral distributions from the Compton scattering of those primary x-rays through different angles. One example is shown in Fig. 1 by the dotted curve.

Samples of gold foils were run in pneumatic shuttles through the scattered x-rays and into the well of a NaI(Tl) crystal where the $^{197}Au^m$ nuclei were detected by the emission of fluorescent photons. The unique combination of a short lifetime for the isomer and a giant resonance for pumping it enabled us to obtain statistically significant numbers of fluorescent photons from such a weakened pump source as resulted from the Compton scattering.

Previously we had reported a simple procedure for obtaining possible values of integrated cross sections for pumping isomers as functions of the energy at which the gateway state might be assumed to lie. Used upon the yields of $^{197}Au^m$, we got a different curve of cross section as a function of energy for each of the five angles at which scattered radiation could be accessed. Such curves should pass through points corresponding to real gateway states and the intersection of two is shown in Fig. 2. The other three curves crossed at the higher energy gateway.

Significance

There is a threefold significance to this milestone result.

1) The giant resonance in ^{197}Au for bandwidth funneling to the isomer is the largest ever demonstrated below 3 MeV. The previous record had been the 430 unit cross section found in ^{87}Sr in 1967 at 2.7 MeV. It had been considered anomalous, being 10 X larger than all others.

2) This first giant funnel to be located in energy was found at a value comparable to the excitation energies of some of the higher lying isomers. This shows that the accidental resonance of such an ideal pumping level and an isomer is possible.

3) The strength of this giant resonance for pumping was concentrated at a discrete energy rather than being distributed at a low level over the whole continuum. This makes it much easier to pump the nuclear levels in one layer while passing the waste heat into another for disposal.
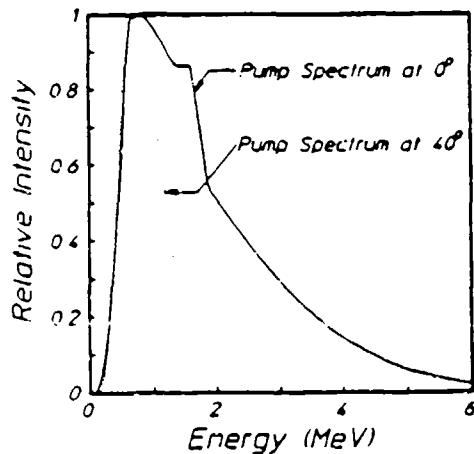
Figure 1: Two of the five spectra available for pumping ^{197}Au^m in this experiment. The solid curve describes the unscattered bremsstrahlung from the 6 MeV linac and the dotted curve plots the intensities computed to be present after scattering through 40° by an iron cylinder 25 mm in diameter and 25 mm long.
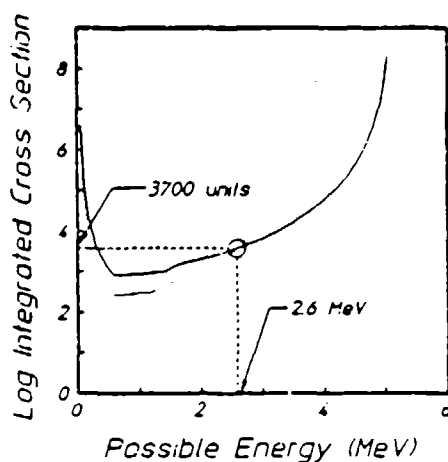
Figure 2: Integrated cross sections for the (γ, γ') reactions pumping ^{197}Au^m through an unknown gateway state as functions of the energies at which they could be assumed to lie. Units are 10^{-29} cm^2 keV. Dotted and solid curves plot results obtained with radiation scattered through 24 and 16°, respectively. The intersection locates the new gateway.
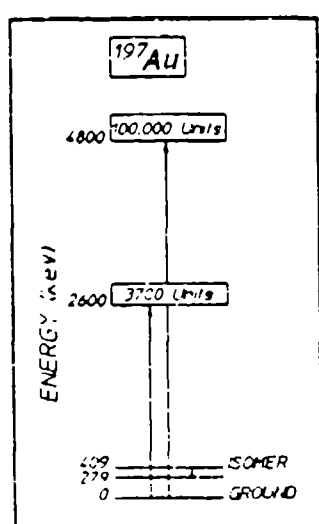
Figure 3: Energy level diagram of the newly discovered states dominating the production of the isomer, ^{197}Au^m. The great widths of these resonances are indicated schematically by the widths of the rectangles and the actual cross sections are given for excitation by the transitions represented by the upward arrows. The downward arrow locates a transition useful in the detection of the isomer.

MAJOR MILESTONE REPORT

Strengthening the Feasibility of a Gamma-Ray Laser

March 21, 1989

C. B. Collins, Center for Quantum Electronics, University of Texas at Dallas

Achievement

Discovered in the first two of the 29 candidate isomers to be tested for a gamma-ray laser were giant pumping resonances which enabled performances to approach the ideal when used with hard x-ray pump sources. Now, these same resonances have been excited with much softer x-rays emitted by a 4 MeV linac.

Technical Background

The nuclear analog of the ruby laser embodies the simplest concepts for a gamma-ray laser. Not surprisingly, the greatest rate of achievement in the quest for a subAngstrom laser continues in that direction. For ruby the identification and exploitation of a bandwidth funnel were the critical keys in the development of the first laser. There was a broad absorption band linked through efficient cascading to the narrow laser level.

Last year we reported a major milestone which showed that comparable structure existed at the nuclear scale in the first of the 29 candidate isomers available for testing, $^{180}Ta^m$. Populations of the isomer were successfully pumped down with flashes of x-rays absorbed through an astonishingly large cross section of 40,000 on the usual scale ($\times 10^{-29}$ cm^2 keV) where 10 describes a fully allowed process. This corresponded to a partial width for useful absorption of 0.5 eV, even better than what had been assumed for idealized nuclei. Then we discovered that these giant funnels for pumping isomers occurred rather frequently. We found them in the second of the 29 candidates, $^{123}Te^m$, as well as in other demonstration nuclei such as ^{197}Au and ^{195}Pt. However, until now, no experiment could pinpoint the location of such giant resonances in the scheme of energy levels for any of the candidate isomers nor determine whether they lay at small enough energies to be practical.

Reported here is success in pumping the two candidate isomers, $^{180}Ta^m$ and $^{123}Te^m$ with a 4 MeV linac through the same giant gateways that had been previously accessed with a 6 MeV device.

Report

The inability to vary the spectrum of the x-rays pumping the isomers generally prevent us from locating the precise energies necessary to reach the giant resonances. The spectrum of intensities previously used was the bremsstrahlung from a 6 MeV linac shown in Fig. 1. In this major milestone experiment we obtained another spectral distribution as seen in Fig. 1 from a 4 MeV linac.

Samples with relatively short-lived signatures were run in pneumatic shuttles through the linac x-rays and into the well of a NaI(Tl) crystal where the pumped nuclei were detected. Materials with longer-lived signatures were simply carried to the counting chamber after the pumping terminated. Some non-candidate control nuclei, such as ^{77}Se and ^{89}Y, could only be activated through giant resonances by the 6 MeV linac. However, to within uncertainties in the spectral intensities from the two sources the same levels of activation per unit dose were found in changing from one linac to the other for both the candidates, ^{180}Ta and ^{123}Te. This means that the giant resonances for pumping those two candidates lie at the lower energies common to both pump sources.

<u>Significance</u>

There is a threefold significance to this milestone result.

1)   The giant resonances for pumping the candidate isomers $^{180}Ta^m$ and $^{123}Te^m$ can be reached at gateway energies well below 4 MeV. These candidates have the largest integrated cross sections for pumping with x-rays ever found below 4 MeV in any nuclei.

2)   Concern had lingered that the giant pumping resonances previously found with the 6 MeV linac might need the full 6 MeV of energy for excitation. At such values the density of states is high and the onset of evaporation of particles from nuclei is near. Either would make the resonances useless to laser development but neither detrimental effect can occur at energies as low as 4 MeV.

3)   The two poorest of the 29 candidates are the only ones available for testing and they continue to outperform even the most optimistic expectations. The likelihood for the full feasibility of one of the better candidates continues to be raised by the successes enjoyed with the least attractive of the 29 candidates.
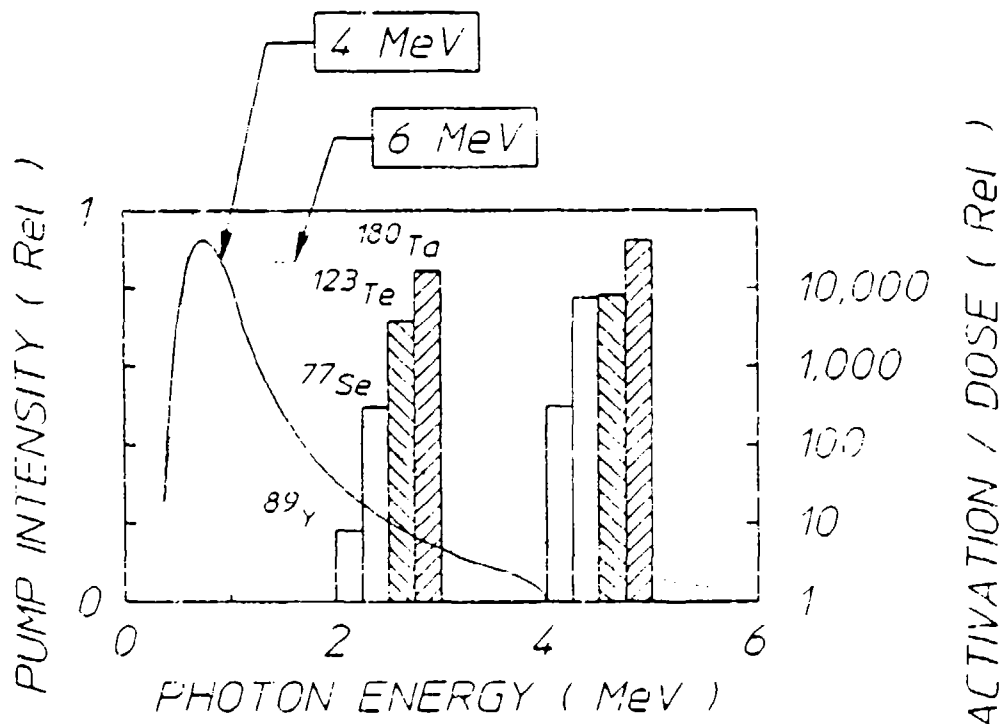
Figure 1.   Solid and dotted curves plot the relative spectral intensities in photons/cm²/keV/sec as functions of photon energies that are expected from the two linac sources identified by the endpoint energies used in these experiments. Bars plot the isomeric activation, or deactivation in the case of $^{180}Ta^m$, on the rightmost scale as determined from the nuclear fluorescence observed after pumping with x-rays from the linacs. The leftmost set of bars give results from the 4 MeV linac and the rightmost were obtained with the 6 MeV source. Precise values of the gateway energies remain unknown and the placement of the bars is only to indicate that they lie below 4 or 6 MeV, respectively. Hatched bars identify actual candidate isomers and open bars pertain to non-candidate comparison nuclides.

THERMAL ECONOMY OF A GAMMA-RAY LASER

by C. B. Collins

One of the most inhibiting factors in the development of a gamma-ray laser has been the heavy load of theoretical dogma[1] which confounds the start of each experiment. Too obvious to warrant proof, these tenents of faith are often believed to frustrate even the more positive modeling we reported[2] in 1982. While sometimes combined in various packagings, the barriers to the realization of a gamma-ray laser are usually purported to be fourfold:

1)   The electrons will screen the nuclei so analogs of optical pumping will not work for nuclear states.

2)   The absorption widths which nuclei display toward pump photons cannot exceed 1 μeV in any useful cases.

3)   The isomeric states which would be the most attractive to pump cannot be dumped by photons because they have angular momenta which are too different from the freely radiating levels.

4)   The waste heat associated with any pumping process will lodge in the host lattice and destroy the Mössbauer effect needed for a sharpened cross section for stimulated emission.

The sequence of experimental results we reported in 1987 completely destroyed the first three of these tenents of faith. Achieving a first major milestone, we reported[3] the experimental observation of eleven orders of magnitude of increase in the amount of fluorescence which could be obtained when narrow nuclear levels of ^{79}Br and ^{77}Se were pumped with flash x-rays through broad states able to funnel their populations down to the radiating level. Those results confirmed the existence at the nuclear level of the analogs of the processes of bandwidth funneling which made the first ruby laser possible. Clearly the first barrier had been only an illusion.

The second and third articles of faith were destroyed by our more recent major milestone report of the successful dumping of some of the population of a nuclear isomer, ^{180}Ta^m. Offset by eight quanta of angular momenta from the normal rotational bands, populations of this

1

state were dumped into the freely radiating system of levels through an enormous integrated cross section approaching 10^{-21} cm^2 eV by pumping them with flash x-rays.[4] *This result implies a useful absorption width of about 0.5 eV for the interband transfer of population from isomeric to radiating level systems.* Experimentally, the occurrence of these giant resonances for mixing levels across such great spans of angular momenta was subsequently shown to be a rather common occurrence among nuclides.[5, 6, 7]

At this point we have realized nearly seventeen orders-of-magnitude of increase in feasibility over the pessimistic evaluation[1] from which the current renaissance in this field departed. Present capabilities exceed even the more optimistic projection[2] upon which our project is based. However, the concern for the thermal economy has persisted.

In 1986 we reported a study[8] which showed that the waste heat associated with the pumping of nuclei with flash x-rays presented a manageable problem to the design of a device. However, that work received little attention and even the most recent studies[9] pursued elsewhere admit no domain in parameter space in which a threshold level of inversion could be pumped without the concomitant loss of the recoilless fraction of the output transitions. Of course, without the recoilless fraction the cross section for stimulated emission would be so reduced by broadening as to be impossible to excite.

Perhaps, unrecognized, is the fact that the critical parameter in the thermal economy is the average excess energy, E by which the energies of the dominant nuclear transitions exceeds the K-edge energy of the electrons of the material. In the early stages the waste heat is almost entirely contained in the primary photoelectron population produced either by the pump radiation or by the internal conversion of the various nuclear transitions. To have a hopeless situation one need only to limit studies to the rather few instances in which the kinetic energy, E of the primary photoelectrons is so small that the range of such particles is less than the dimensions of the layer being pumped. Then, they cannot escape and the waste energy will be degraded to heat precisely in the sensitive area in which the population inversion is developed. Just such a failure mode was built into the unfortunate

example of the excitation of the 14.4 keV transition of ^{57}Fe in an iron matrix.[9]

It is the purpose of this manuscript to explore the problem of the thermal economy of the ruby-laser analog in systems benefitting from the new discoveries which remove the first three traditional inhibitions to the design of a gamma-ray laser. It will be seen that for a wide margin of material parameters, the problem of the waste heat is readily manageable. As a consequence, the fourth and last of the traditional tenents of dogma is destroyed as a paramount concern. Reduced to the level of an engineering challenge, the solution to the problem of waste heat remains to be tailored to the particular characteristics of the nuclear system finally employed.

Whether or not the initial state to be pumped is isomeric, the principal figure of merit for bandwidth funneling is the partial width for the transfer, $b_a b_o \Gamma$. Constituent parameters are identified in Fig. 1 where it can be seen that the branching ratios b_a and b_o specify the probabilities that a population pumped by absorption into the i-th broad level will decay back into the initial or fluorescent levels, respectively. It is not often that the sum of branching ratios is unity, as channels of decay to other levels are likely. However, the maximum value of partial width for a particular level i occurs when $b_a = b_o = 0.5$.

The actual measurement of partial widths has involved the correlation of fluorescence yields excited by a pulse of x-rays in the scheme of Fig. 1 with those expected from the expression,[4-9]

$$N_f = N_o \sum_i \xi_i \frac{\varphi_i}{A} \quad , \tag{1a}$$

where N_o and N_f are the numbers of initial and fluorescent nuclei respectively, (φ_i/A) is the spectral intensity of the pump radiation in $keV/keV/cm^2$ at the energy E_i of the i-th pump band, and the summation is taken over all of the possible pump bands capable of cascading to the same fluorescence level of interest. The ξ_i is a combination of nuclear parameters including the partial width $b_a b_o \Gamma$ in keV,

$$\xi_i = \frac{(\pi b_a b_0 \Gamma \sigma_0/2)_i}{E_i} \quad , \tag{1b}$$

where σ_0 is the peak of the Breit-Wigner cross section for the absorption step. The combination of parameters in the numerator of Eq. (1b) is termed the integrated cross section for the transfer of population according to the scheme of Fig. 1.
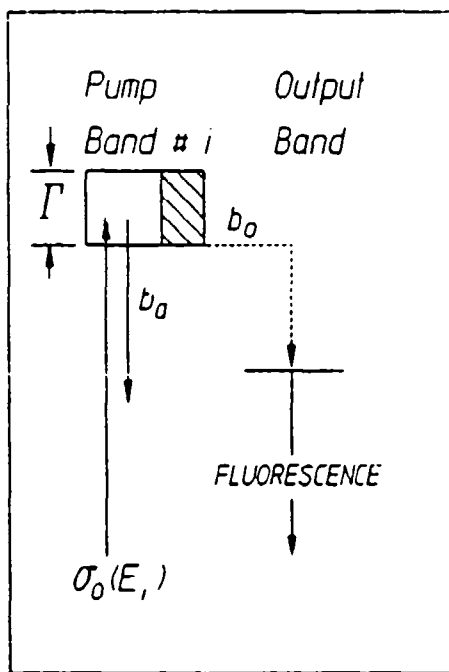
Figure 1: Schematic representation of the decay modes of a gateway state of width Γ sufficiently large to promote bandwidth funneling. The initial state from which population is excited with an absorption cross section σ_0 can be either ground or isomeric, in principle.

The Breit-Wigner cross section peaks at

$$\sigma_0 = \frac{\lambda^2}{2\pi} \frac{2I_e+1}{2I_g+1} \frac{1}{\alpha_p+1} \quad , \tag{2}$$

where λ is the wavelength in cm of the gamma ray at the resonant energy. E_i; I_e and I_g are the nuclear spins of the excited and initial states,

respectively; and α_p is the total internal conversion coefficient for the two-level system comprised by the initial and pump levels. The value of α_p is essentially zero for a transition which is highly allowed; and even were it not, σ_0 would be reduced further and the partial width would become correspondingly larger so that the quantity ξ_i would remain unaffected.

In this development it has been assumed that the width of the pump spectrum is sufficiently greater than Γ that the pump can be considered to be continuous and without structure over the width of the absorption line. Other than this assumption the development, so far, is general. Restrictive assumptions necessary for the management of the thermal economy can be explicitly stated as follows:

1) The pump band i in Fig. 1 is one of the newly discovered giant pumping resonances with a partial width of $b_a b_o \Gamma \sim 1$ eV.

2) The pump transition is centered on an energy $E_i \sim 30$ keV.

3) The initial state is assumed to be isomeric with an excitation energy so high that 2) is possible.

4) The output transition is around 100 keV.

5) The nuclei are diluted in a thin film of diamond.

6) The Borrmann effect contributes a factor of 10 to the enhancement of the ratio of cross sections for resonant to non-resonant transitions.

An immediate issue is the plausibility of these assumptions. While the widths for pumping interband transfer of population to and from isomers have been shown to approach 1 eV in many cases,[4-7] it had not been previously demonstrated that such a width corresponded to a discrete level. Described in the Major Milestone Report for this quarter is the use of a Compton spectrometer to search for a gateway energy, E_i through which the photon pumping reaction, $^{197}Au(\gamma,\gamma')^{197}Au^m$ proceeds. As described elsewhere in this quarterly report the enormous integrated cross section of 3700 in the usual units ($\times 10^{-29}$ cm^2 keV) was found to be localized at an energy 2.6 MeV above the ground state. At

least in this case, the experiment supported the identification of such
favorable pumping resonances with a discrete, well-defined pump energy
so that Assumption 1) is plausably supported.

Plausibility of the second and third assumptions must be considered
together. The range of excitation energies over which isomers can be
found is very large, reaching 6 MeV if one considers the shape isomers
proposed by Weiss et al.[10] We have 'ready shown that isomers can be
dumped into the freely radiating s. .tem, even through $\Delta J = 8$, so the
only doubt here is a statistical one; whether or not a giant pump
resonance can be found within 30 keV of an isomer.

Assumption 4) is quite likely and the feasibility of 5) has been
greatly increased by a recent "breakthrough" in the deposition of thin
film diamond from laser plasmas. As described in one of the following
manuscripts, we have been able to grow very uniform thin films of
amorphic diamond from the plasma ablated from a carbon target in an
environment especially suited to doping with nuclei of interest to the
gamma-ray laser. While proper single crystal substrates have not yet
been used to try to organize the growth of single cyrstal diamond, the
largest step of fabricating a diamond film has been accomplished.
However, until a single lattice is demonstrated the combination of
assumptions 5) and 6) remains uncertain. By itself, the anticipation of
a factor of ten reduction in the ratio of probabilities for non-resonant
to resonant absorption is modest but still questionable for diamond at
this time. As a consequence, single crystal Be is also modeled as a
second preference. Thus, it can be reasonably asserted that the six
assumptions upon which rest the model reported here are plausible and
consistent.

Following our development[2] of 1982 under small signal conditions
the overall logarithmic amplification, α for a single pass down the
length, z of the strip of pumped material shown in Fig. 2, is,

$$\alpha = N_f \sigma_R z - N_o \sigma_{NR}^{(m)} z - N_d \sigma_{NR}^{(d)} z \qquad , \qquad (3)$$

where N_f is the number of nuclei in the fluorescent level which it is
desired to pump to threshold, and where σ_R and σ_{NR} denote the cross
sections for the resonant emission given by Eq. (2) evaluated at the
output wavelength (100 keV) and for the non-resonant absorption in the
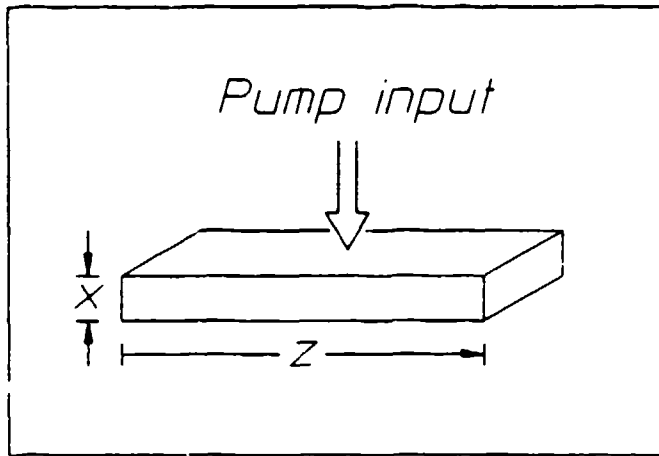
Figure 2: Geometry of the thin strip of diamond
doped with the nuclei to be pumped with flash x-rays.

medium, (m) and diluent, (d), respectively. To reach the threshold for
laser output, α must become positive so that the minimal condition is

$$0 \leq N_f \sigma_R z - N_o \sigma_{NR}^{(m)} z - N_d \sigma_{NR}^{(d)} z \qquad , \qquad (4)$$

which necessitates,

$$\frac{N_f}{N_o} \geq \frac{\sigma_{NR}^{(m)}}{\sigma_R} \left(1 + \frac{N_d}{N_o} \frac{\sigma_{NR}^{(d)}}{\sigma_{NR}^{(m)}} \right) \qquad . \qquad (5)$$

For estimations to within a factor of two the latter term in the
parentheses can be neglected for concentrations greater than 3%. At the
100 keV output transition,

$$\sigma_{NR}^{(d)} \ (Be) \ \approx \ 0.13 \ cm^2/gr \qquad , \qquad (6a)$$

$$\sigma_{NR}^{(d)} \ (C) \ \approx \ 0.15 \ cm^2/gr \qquad , \qquad (6b)$$

$$\sigma_{NR}^{(m)} \ (Ta) \ \approx \ 4.3 \ cm^2/gr \qquad , \qquad (6c)$$

where Ta has been arbitrarily selected as representative of the region
of nuclides where the better candidates for a gamma-ray laser medium may
be found. So it can be seen that at 3% concentration by mass, losses in
the diluent increase the right hand side by a factor of 2×.

Simplifying Eq. (5) gives,

$$\frac{N_f}{N_o} \geq \frac{\sigma_{NR}^{(m)}}{\sigma_R} \quad , \tag{7}$$

so that the fraction pumped must exceed the ratio of the cross sections for non-resonant loss to resonant stimulated emission. Unfortunately the dependence of the right hand side of Eq. (7) upon nuclear parameters is tedious and structured. Baldwin[1] has presented a convenient review which shows Eq. (7) is optimized for an output energy of 100 keV as assumed here. Values range from 10^{-2} to 10^{-4} and can be assumed to be improved (lowered) by the Borrmann effect. To be consistent with the earlier assumptions, the Borrmann effect is supposed to enhance the mid-range value of 10^{-3} yielding a requirement of 10^{-4} for the pumped fraction,

$$\frac{N_f}{N_o} \geq 10^{-4} \quad , \tag{8}$$

This sets the pump intensity needed for threshold, and with it the amount of waste heat to dissipate.

Substituting into Eq. (8) from Eq. (1a) and assuming the single giant resonance dominates so that the sum is unnecessary, gives,

$$\frac{\pi b_a b_o \Gamma \sigma_o F_i}{2} \geq 10^{-4} \quad , \tag{9a}$$

where

$$F_i = \frac{\varphi_i}{E_i A} \quad , \tag{9b}$$

that is, F_i is the pump flux integrated over the lifetime of the fluorescent level in units of photons/cm^2/eV, if Γ is now in eV. Assuming $I_e = I_g$ in Eq. (2) and $\alpha = 0$, then at 30 keV, $\sigma_o = 2.72 \times 10^{-18}$ cm^2 and letting $\pi b_a b_o \Gamma / 2 = 1$ eV gives

$$F_i \geq 3.7 \times 10^{13} \text{ photons/cm}^2/\text{eV} \quad , \tag{10a}$$

or since each photon is 30 keV,

$$\Phi_i \geq 177 \ \text{mJ/cm}^2/\text{eV} \qquad . \tag{10b}$$

In the geometry of Fig. 2, it is next important to determine the thickness, x of the pumped layer. At the level of 10% concentration, N_o = 5.5 × 10^{21} cm^{-3} so the extinction coefficient for pumping is,

$$\sigma_o N_o = 1.5 \times 10^4 \ \text{cm}^{-1} \qquad , \tag{11a}$$

and so,

$$x \simeq (\sigma_o N_o)^{-1} = 0.67 \ \mu\text{m} \qquad . \tag{11b}$$

At the 30 keV pump energy

$$k_{NR} \ (\text{Be}) = 0.332 \ \text{cm}^{-1} \qquad , \tag{12a}$$

$$k_{NR} \ (\text{diamond}) = 0.900 \ \text{cm}^{-1} \qquad , \tag{12b}$$

$$k_{NR} \ (10\% \ \text{Ta}) = 35.4 \ \text{cm}^{-1} \qquad , \tag{12c}$$

where the k_{NR} are the extinction coefficients for the non-resonant absorption of the pump x-rays. It is important to notice that this is a typical case in which the pump radiation is not particularly close to an absorption edge. In this case the emerging photoelectrons will have some kinetic energy, and may escape from the region being pumped. Had the example been arranged to be more pathological as in the recently reported case[9] of the ^{57}Fe, Eq. (12c) would have given a much larger absorption coefficient. As it is, the non-resonant absorption by the working medium in the 0.67μm layer is only,

$$f_1 = k_{NR} \ (10\% \ \text{Ta}) \ x = 2.4 \times 10^{-3} \qquad , \tag{13}$$

where f_1 is the fraction of the incident fluence stopped in the laser medium by non-resonant absorption. However, this fraction is reduced further by the escape of the primary photoelections from the pumped layer.

Figure 3 shows the mean extrapolated ranges, E/(dE/dx) computed by standard techniques[12] for the escape of photoelectrons having the energies shown in the materials indicated. In this case the Ta is considered to be in the normal (100%) concentration. In the 10% concentration being assumed the ranges would be 10x greater and so the

contribution of the working medium to the absorption of the primary photoelectrons would be dominated by the effects of the diluent.
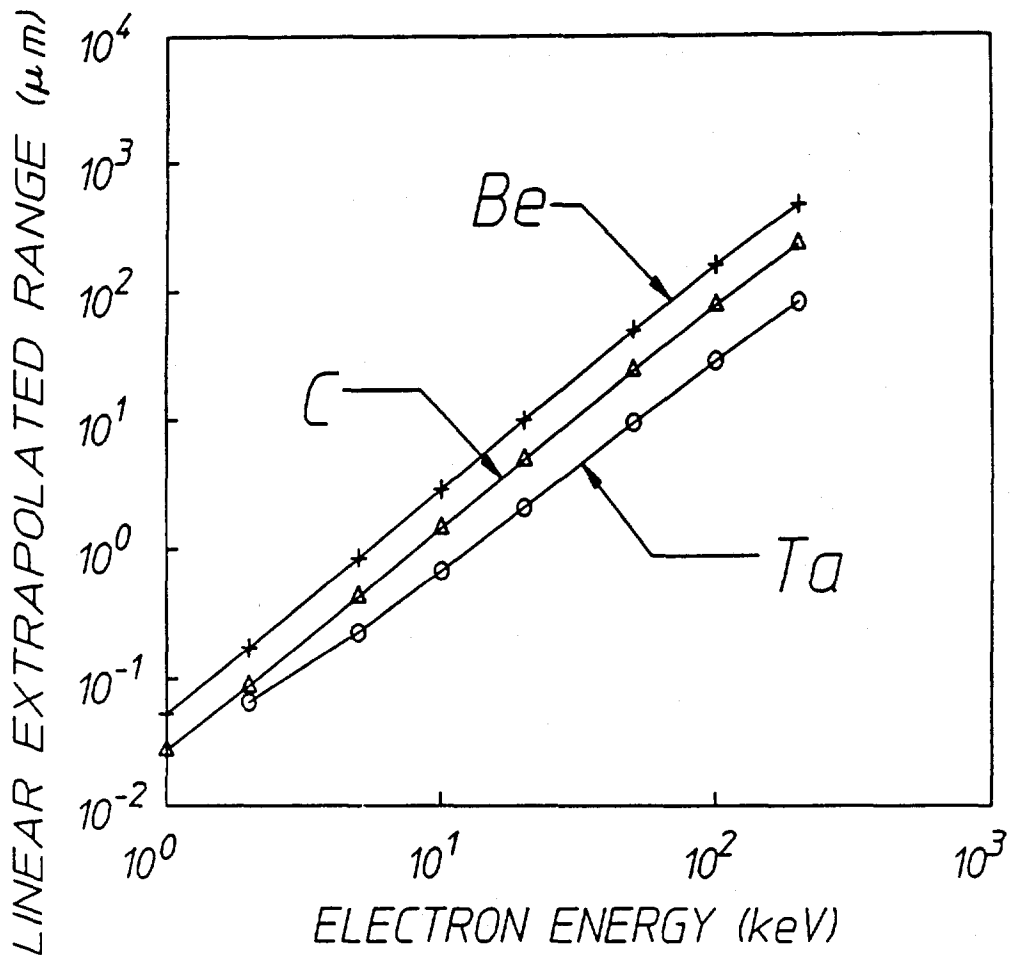
Figure 3: Plot of the linear extrapolated range of electrons in foils of the materials shown.

For the likely cases of rare earth or platinide elements the pump energy we assume lies below the K-edge and about 15 keV above the L-edge. As a result, the primary photoelectrons resulting from the non-resonant absorption in the active medium should have energies of the order of 15 keV and ranges of 6.0 and $3.0\mu m$ in Be and C, respectively. Thus, only about 10% and 20% respectively, of the primaries, should be stopped in the $0.67\mu m$ thick host films of Be or diamond. Multiplying the fraction of Eq. (13) by these probabilities for collision of the primary in the foil gives the fractions,

$$f_2 \text{ (Be)} = 2.4 \times 10^{-4} \qquad , \qquad\qquad\qquad (14a)$$

$$f_2 \text{ (C)} = 4.8 \times 10^{-4} \qquad , \qquad\qquad\qquad (14b)$$

for the fraction of the energy from the incident pump degraded into heat in the laser film because of non-resonant absorption.

Considering that edge filters or ablation layers could reduce the bandwidth of the pump radiation to 3 keV, before reaching the doped layer of Fig. 2, the incident fluence lying outside the bandwidth for resonant absorption would be 3000x greater than the value of Eq. (10b). However, only the fractions of Eqs. (14a) and (14b) are capable of being degraded into heat in the sensitive layer. The resulting energy balance can then be summarized at threshold:

Lattice	Be	C(diamond)
Resonant input fluence	177mJ/cm^2	177mJ/cm^2
Fluence degraded to heat	127mJ/cm^2	255mJ/cm^2

There is an additional potential for heating in the resonant term as well. Reference to Fig. 1 will show that for each absorption to the giant funneling state, a cascade is started that reaches finally to the level being inverted. Since the isomer may start at several MeV, while the output transition accounts for only 100 keV, there is the possibility of exciting a sequence of radiative transitions emitting a total of several MeV for each nuclei inverted. Were this to occur in a sequence of many soft transitions of a few keV these could be internally converted to give low energy electrons which would then be unable to escape the 0.67μm layer being pumped. They would deposit their energies in the layer as heat.

For a number of reasons a significant contribution to the heating from cascades following resonant absorption is unlikely. The most probable spontaneous transitions are those spanning larger gaps of energy and those are seldom converted internally. The ones that are converted will give electrons of higher energies which Fig. 3 shows to have higher probabilities of escape from the layer. It is most reasonable to expect the dominant source of heat to be the energy lying in the broader bandwidth of the pump continuum as discussed above.

11

The elements of the energy economy tabulated above are the fluences stopped in the thin working layer in which the nuclear populations are being inverted. Dividing those fluences by the $0.67\mu m$ thickness gives the energy loading of the laser film,

Lattice	Be	C(diamond)
Resonant energy density	$2.6KJ/cm^3$	$2.6KJ/cm^3$
Thermal lo ding	$1.9KJ/cm^3$	$3.8KJ/cm^3$

These values are quite significantly below the levels of heating required to degrade the recoil free fractions in the case of the diamond lattice. Baldwin has summarized[13] the involved dependence of the recoil free fraction of gamma transitions upon recoil energy, lattice parameters and temperature. He shows that even at a temperature, T equal to the Debeye temperature, Θ_D the recoil free fraction is not significantly degraded (by more than a factor of 2) for a transition even as energetic as to give a classical recoil energy of 0.14 Θ_D. In diamond with Θ_D - $2230°$ K this means a transition of 100 keV is little affected by a temperature increase up to T - Θ_D.

It is a textbook computation[14] to estimate that the energy content of the phonons of a material with Θ_D - $2230°$ K at a temperature of T - Θ_D is about $11KJ/cm^3$. Comparing this with the estimated loading of $3.8KJ/cm^3$ gives a "safety factor" of almost 3x. A comparable margin is obtained for the Be.

To summarize, it is convenient to recast the threshold fluence of Eq. (10b) into more tangible terms. The spectral fluence of $1.77mJ/cm^2/eV$ corresponds to 530 J/cm^2 if the bandwidth of the pump x-rays is arranged to be 3 keV, a practical separation which might be filtered between K-edges. Even if pumped instantaneously, so that no waste heat were transported away, the thermal loading would reach only 1/3 of the way to the limit for retaining the Mössbauer effect. If derived from an x-ray line of 30 eV width, the threshold fluence would be only 5.3 J/cm^2. In that case the thermal loading would reach only 1/300 of the critical limit for a diamond lattice.

Even beyond this point much can be done to reduce heating further. All calculations so far were done for the instantaneous generation of the waste heat. The time for the transport of a phonon across the $0.67\mu m$ thickness of the working layer is of the order of only 100 psec so that the transport of significant amounts of heat from that layer into a diamond heat sink is possible on a nanosecond time scale. Yet the lifetimes of most of the fluorescent levels of interest for inversion[2] have lifetimes of tens of nsec to tens of μsec. This is many times the period for the transport of phonons out of the inverting layer so that more orders of magnitude can be realized in reducing the thermal loading further below the limits specified so far. However, all these techniques require precise knowledge about the energy levels and absorption edges of the materials involved. Until the identity of the best candidate for a gamma-ray laser is known, the exact specifications of the solution to the disposal of the waste heat cannot be generally articulated. The examples considered here show that there are many orders of magnitude in the safety margin between likely amounts of heating and the much larger amounts which can be tolerated in stiff lattices such as Be and diamond.

The greatest significance is that the fourth and last of the tenents of theoretical dogma inhibiting the development of a gamma-ray laser is eliminated by these arguments. There is no need to melt the host lattice in order to pump a nuclear system to the laser threshold. There are no a _priori_ obstacles to the realization of a gamma-ray laser. A gamma-ray laser is feasible if the right combination of energy levels occurs in some real material. The overriding question to resolve is whether or not one of the better of the 29 candidates has its isomeric level within a few tens or even hundreds of keV of one of the giant resonances for dumping angular momenta, such as found in $^{180}Ta^m$ and $^{123}Te^m$.

13

REFERENCES

1. G. C. Baldwin, J. C. Solem, and V. I. Goldanskii, Rev. Mod. Phys. 53, 687 (1981).

2. C. B. Collins, F. W. Lee, D. M. Shemwell, and B. D. DePaola, J. Appl. Phys. 53, 4645 (1982).

3. J. A. Anderson and C. B. Collins, Rev. Sci. Instrum. 58, 2157 (1987).

4. C. B. Collins, C. D. Eberhard, J. W. Glesener, and J. A. Anderson, Phys. Rev. C 37, 2267 (1988).

5. C. D. Eberhard, J. W. Glesener, Y. Paiss, J. A. Anderson, C. B. Collins, W. L. Hodge, E. C. Scarbrough, and P. O. Antich, Phys. Rev. C (pending).

6. C. B. Collins, J. A. Anderson, C. D. Eberhard, J. F. McCoy, J. J. Carroll, E. C. Scarbrough, and P. P. Antich, in Center for Quantum Electronics Report #GRL 8703, University of Texas at Dallas, 1987 (unpublished) pp 35-53.

7. J. A. Anderson, C. D. Eberhard, J. F. McCoy, K. N. Taylor, J. J. Carroll, M. J. Byrd, C. B. Collins, E. C. Scarbrough and P. P. Antich, in Center for Quantum Electronics Report #GRL 8704, University of Texas at Dallas, 1988 (unpublished) pp 11-35.

8. C. B. Collins in Center for Quantum Electronics Report #GRL 8601, University of Texas at Dallas, 1986 (unpublished) pp 1-14.

9. D. A. Swallow, Bull. Am. Phys. Soc. 33, 1017 (1988), Presentation GC3.

10. M. S. Weiss, Bull. Am. Phys. Soc. 33, 1017 (1988), Presentation GC4.

11. S. S. Wagal, E. M. Juengerman and C. B. Collins, Appl. Phys. Lett. 53, 187 (1988).

12. G. Knop and W. Paul, in: Alpha, Beta and Gamma-Ray Spectroscopy (ed. Kai Siegbahn, North-Holland Co., Amsterdam, 1965), p 1-25.

13. See Ref 1, Fig. 14.

14. C. Kittel, Introduction to Solid State Physics, 6th ed. (Wiley, New York, 1986), p. 106.

DETERMINATION OF GATEWAY STATES IN ^{197}Au WITH A COMPTON γ-RAY SPECTROMETER

by C. D. Eberhard, J. A. Anderson, M. J. Byrd, J. J. Carroll
and C. B. Collins
Center for Quantum Electronics, University of Texas at Dallas
and E. Scarbrough and P. P. Antich
University of Texas Southwestern Medical Center

Introduction

Recent experiments[1,2,3,4] have shown that cross sections for (γ,γ') reactions that populate nuclear isomers can be orders of magnitude larger than previously expected at excitation energies above about 2 MeV. These results were obtained by pumping nuclear populations with the bremsstrahlung radiation from a Varian CLINAC 1800 linear accelerator normally employed for radiation therapy treatments. Unfortunately, such bremsstrahlung sources are inherently continuous and cannot be used to selectively probe for the intermediate gateway states through which the isomeric excitation occurs. Moreover, not even the endpoint energy of this particular device can be varied around its operating point of 6 MeV. Thus, in this previous work there was no direct way of identifying the gateway levels which mediated the population of the observed isomeric states. To facilitate this identification process, a technique has been developed in which Compton scattering is used to progressively modify the energy endpoint and spectral distribution of the incident radiation. The current work describes this method and discusses its application to the study of the gateway states through which the reaction ^{197}Au$(\gamma,\gamma')^{197}$Au^m is excited.

The Compton Effect

The Compton effect[5] describes the collision of a primary photon of energy E_0 with an essentially unbound atomic electron assumed to be initially at rest. The process is named for A. H. Compton, who established it quantitatively in 1923 after careful spectroscopic measurements of x-rays scattered through various angles by light elements. In the collision, the incident momentum and energy must be conserved between the scattered photon and the struck electron, which recoils. The scattered photon has less momentum and energy than the primary photon, with the remaining momentum and energy being imparted to the electron. The consequences of this phenomena can be quantitatively described by a rather straightforward approach.
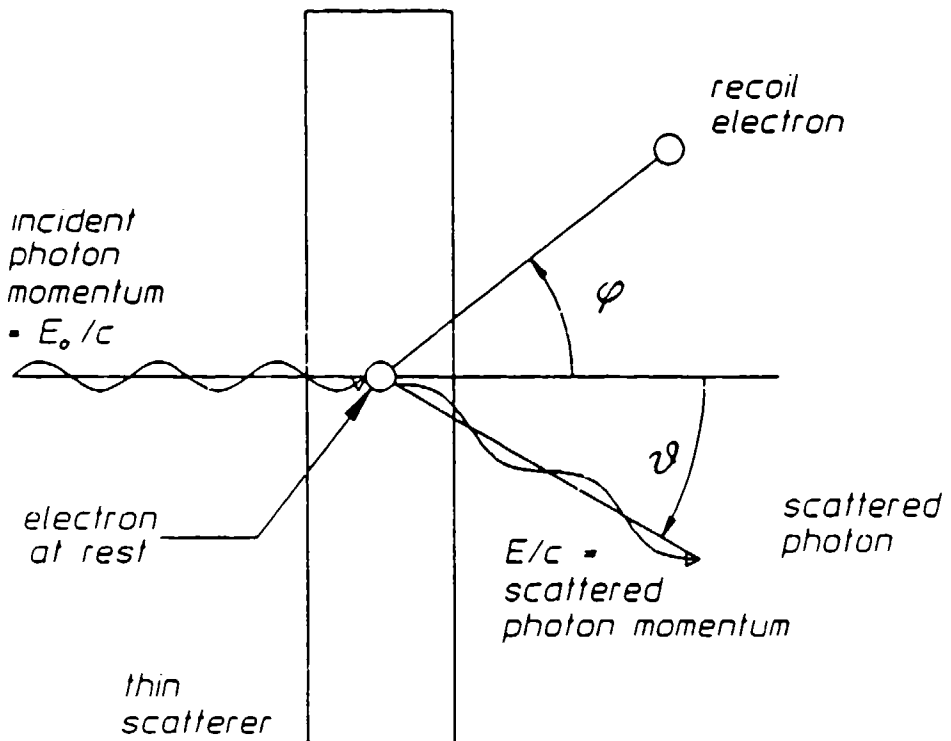

Figure 1: Diagram of the initial and final momenta for Compton scattering.

Let the angle between the propagation vectors of the primary and scattered photons be denoted by θ as shown in Fig. 1. From the relativistic energy-momentum relation and the conservation of energy and momentum, the energy of the scattered photon is found to be given by

$$E = \frac{E_o}{[1 + (E_o/mc^2)(1 - \cos \theta)]} \qquad , \qquad (1)$$

where mc^2 is the rest mass of the electron. There is a one-to-one correlation between the energy of the scattered photon and the angle θ for a given primary photon energy E_o. Therefore, photons from a monochromatic source which are scattered into a given angle from a point scatterer will be monochromatic. This leads to the possibility of performing nuclear spectroscopy with Compton scattered radiation having a known spectral distribution. A configuration for a Compton spectrometer to be used in the study of the activation of short lived isomers is shown in Fig. 2.
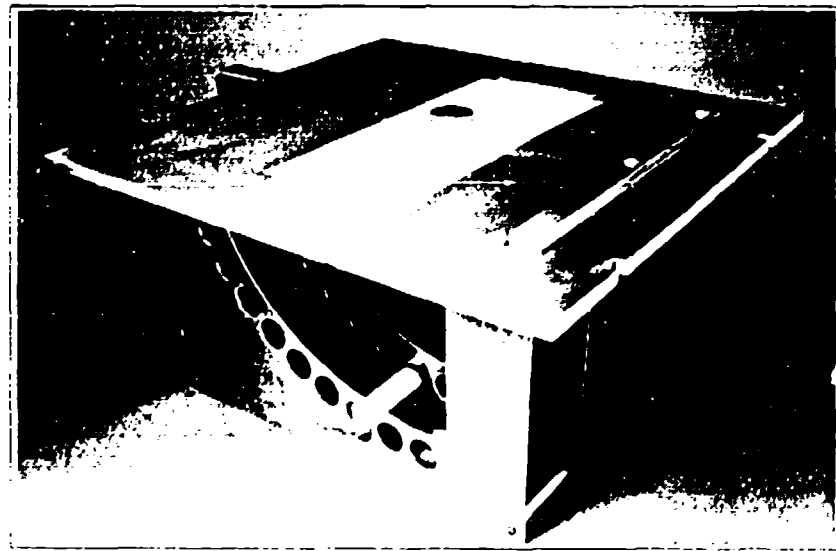

Figure 2: Irradiation fixture of the Compton spectrometer showing a sample in the $\theta = 8°$ position. The pneumatic tubing of the transport system passed through the holes in the sample holder so that the sample was positioned as shown. The tubing was moved from site to site manually.

17

In the theory of the Compton effect, the struck electron is considered to be free or unbound. This limits the theory to cases for which the atomic binding energy of the electron is small compared with E_0, which is the case for the primary photon spectrum considered here. Also, the electron is assumed to be at rest. Although the general case of non-zero electron momentum can be obtained from this special case by a Lorentz transformation, this refinement is generally not considered necessary. In 1928 the complete theory for the effect was worked out by Klein and Nishina using Dirac's relativistic theory of the electron. The differential cross section obtained for the scattering of unpolarized incident photons of energy E_0 into the solid angle $d\Omega$ at the polar angle θ is given by

$$\frac{d\sigma}{d\Omega} = r_0^2 \left(\frac{1}{1 + \alpha_i (1 - \cos \theta)} \right)^2 \left(\frac{1 + \cos^2 \theta}{2} \right) \times \qquad (2)$$

$$\left(1 + \frac{\alpha_i^2 (1 - \cos \theta)^2}{(1 + \cos^2 \theta)[1 + \alpha_i (1 - \cos \theta)]} \right) \quad .$$

where $\alpha_i = E_0/mc^2$ is the incident photon energy in units of mc^2 and $r_0 = e^2/mc^2$ is the classical radius of the electron. The differential scattering cross section is defined through the relationship

$$dR(\theta, E_0) = dI_i(E_0) N_{sc} \frac{d\sigma}{d\Omega} (E_0, \theta) \; d\Omega(\theta) \qquad , \qquad (3)$$

where

      dR = number of photons per second scattered into solid angle $d\Omega$ at θ,

      N_{sc} = number of electrons per cm^3 in the scatterer, and

      $dI_i(E_0)$ = incident photon flux with energy E_0 in photons per cm^2 per s.

After substitutions for the solid angle,

$$d\Omega = 2\pi \sin\theta \, d\theta \quad , \tag{4}$$

and the area at the target location at radius r intersected by the conical fan described by $d\Omega$,

$$dA = 2\pi r^2 \sin\theta \, d\theta \quad , \tag{5}$$

Eq. (3) may be rewritten for the scattered flux as

$$dI_f = \frac{dR}{dA} = dI_i \frac{d\sigma}{d\Omega} \frac{1}{r^2} \quad . \tag{6}$$

A real experimental source is not monochromatic, but a small portion of the spectrum can be represented by

$$dI_i = \frac{dI_i}{dE} dE_i \quad , \tag{7}$$

where dI_i/dE is the spectral density of the incident flux. Written in terms of the spectral density, Eq. (6) becomes

$$dI_f = \frac{dI_i}{dE_i} \frac{d\sigma}{d\Omega} \frac{1}{r^2} dE_i \quad , \tag{8}$$

The energy spread of the scattered photons relative to the energy spread of the incident photons is found by differentiating equation (1),

$$dE = dE_i \left[1 + \alpha_i (1 - \cos\theta) \right]^{-2} \quad . \tag{9}$$

Equation (8) becomes

19

$$\frac{dI_f}{dE} = \frac{dI_i}{dE_i} \frac{d\sigma}{d\Omega} (\theta, E_o) \frac{[1 + \alpha_i (1 - \cos\theta)]^2}{r^2} \qquad (10)$$

The quantity dI_f/dE is the output spectral density, a function of θ and E, the scattered photon energy. Thus for a non-monochromatic incident spectrum, the output spectral density can be calculated on a point-by point basis.

The preceding discussion assumed a point scatterer and a point absorber at which one could calculate the spectral density of the scattered radiation. As shown in Fig. 2, both scatterer and absorber have finite volumes which must be accommodated in the calculation of the output spectral density. Since the scattering target must in practice be chosen large enough to produce a significant scattered photon flux, it cannot be considered to be thin in comparison to the mean free path of a photon. Therefore there will be significant multiple scattering in a real target. Although the correct solution of this problem requires a full radiation transport calculation, a first approximation has been made in this work by treating the scattering target as a collection of individual point scatterers and using a simple attenuation calculation to adjust the incident and scattered intensities from each point. This in effect assumes that all secondary scattering events result in absorption. The output spectral density at a given point in the absorber is then the summation of the contributions from all the volume elements in the scatterer. Since the output spectrum is sensitive to position within the absorber, it is necessary to average this output spectral density over the volume of the absorbing sample. A more complete, Monte Carlo based calculation is in progress.

The source of primary photons used in this work was a Varian Clinac 1800 linear accelerator designed for medical applications. Electrons accelerated to an energy of 6 MeV impact a copper target to produce a photon beam with a well characterized bremsstrahlung spectrum[6]. The spatial variation of this bremsstrahlung spectrum over the area of the scatterer has been measured and is negligible[7].

The output spectral density for the Compton spectrometer was calculated using Eq. (10). For every pair of volume elements in the scatterer and absorber, the geometrical factors r and $\cos\theta$ were determined. Then, for each value of the output energy to be considered,

20

the corresponding E_0 was found, and the input spectral density was obtained from a piecewise-continuous fit generated from the results of Mohan et al. This spectrum was adjusted for exponential attenuation of the incident radiation by applying the factor $\exp(-\mu(E_0)z)$, where z is the vertical distance of the scattering point from the top of the scattering target and $\mu(E_0)$ is the mass attenuation coefficient at incident photon energy E_0. After the application of Eq. (10) to obtain the spectrum dI_f/dE of the Compton scattered radiation, a second attenuation correction of $\exp(-\mu(E)d)$ was made. Here, d is the path-length the scattered photon of energy E travels as it exits the scattering target. These results were summed over the scatterer volume and averaged over the absorber volume to produce the spectral density seen by the absorber. In order to test the sensitivity of the model to the geometrical assumptions, the output spectral density at $\theta = 16°$ was calculated for the following four possible geometrical cases:

1. Point scatterer/point absorber: the masses of the scatterer and absorber were considered to be concentrated at the respective geometrical centers. Attenuation in the scatterer was calculated using the appropriate path lengths from the boundary of the scatterer to its center.

2. Extended scatterer/point absorber: the scatterer was divided into volume elements but only the central point of the absorber was considered.

3. Point scatterer/extended absorber: the scatterer was concentrated at its center but the absorber was considered to have an extended volume. Attenuation in the scatterer was calculated using the appropriate path lengths from the boundary of the scatterer to its center.

4. Extended scatterer/extended absorber: the finite dimensions of both scatterer and absorber were considered in this model.

21
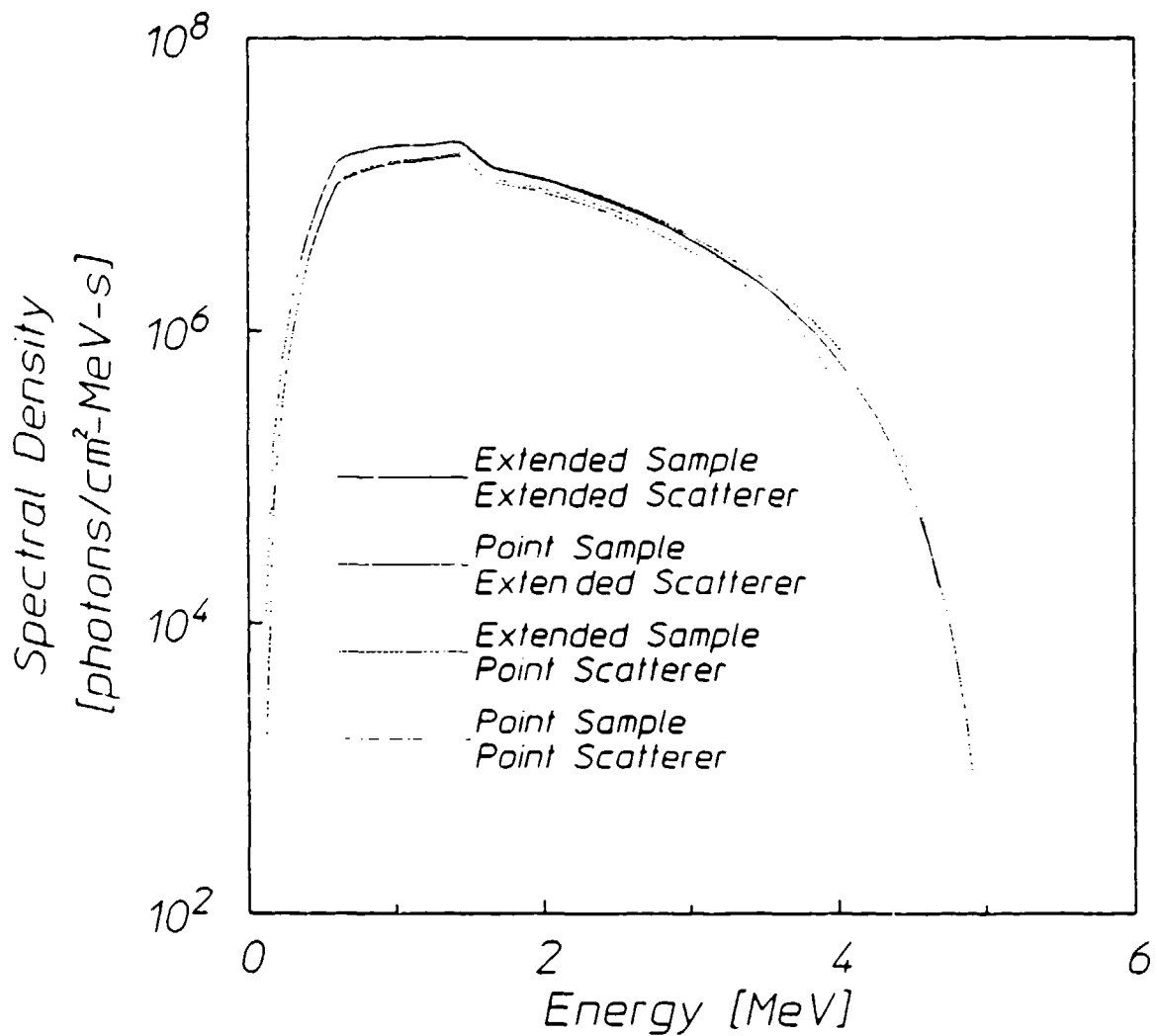
Figure 3: Modelled output spectral densities at the position of the absorber at the 16° spectrometer position for the four geometrical assumptions.

The results of these calculations are shown in Fig. 3. It should be noted that the single-point scatterer models underestimate the low energy portion of the spectrum because of the relatively long absorption path from the center of the scattering target to its boundary. Inclusion of the finite extent of the absorber sample increased the maximum photon energy incident on the absorber because it allowed contributions from lower scattering angles in the Compton process to be made for a given central angle θ. The extended source/extended scatterer model was used throughout the remainder of the work. These extended geometry calculations were performed for scattering angles of 0°, 16°, 24°, 32°

and 40°.   The Compton scattered spectral densities are shown plotted in Fig. 4.
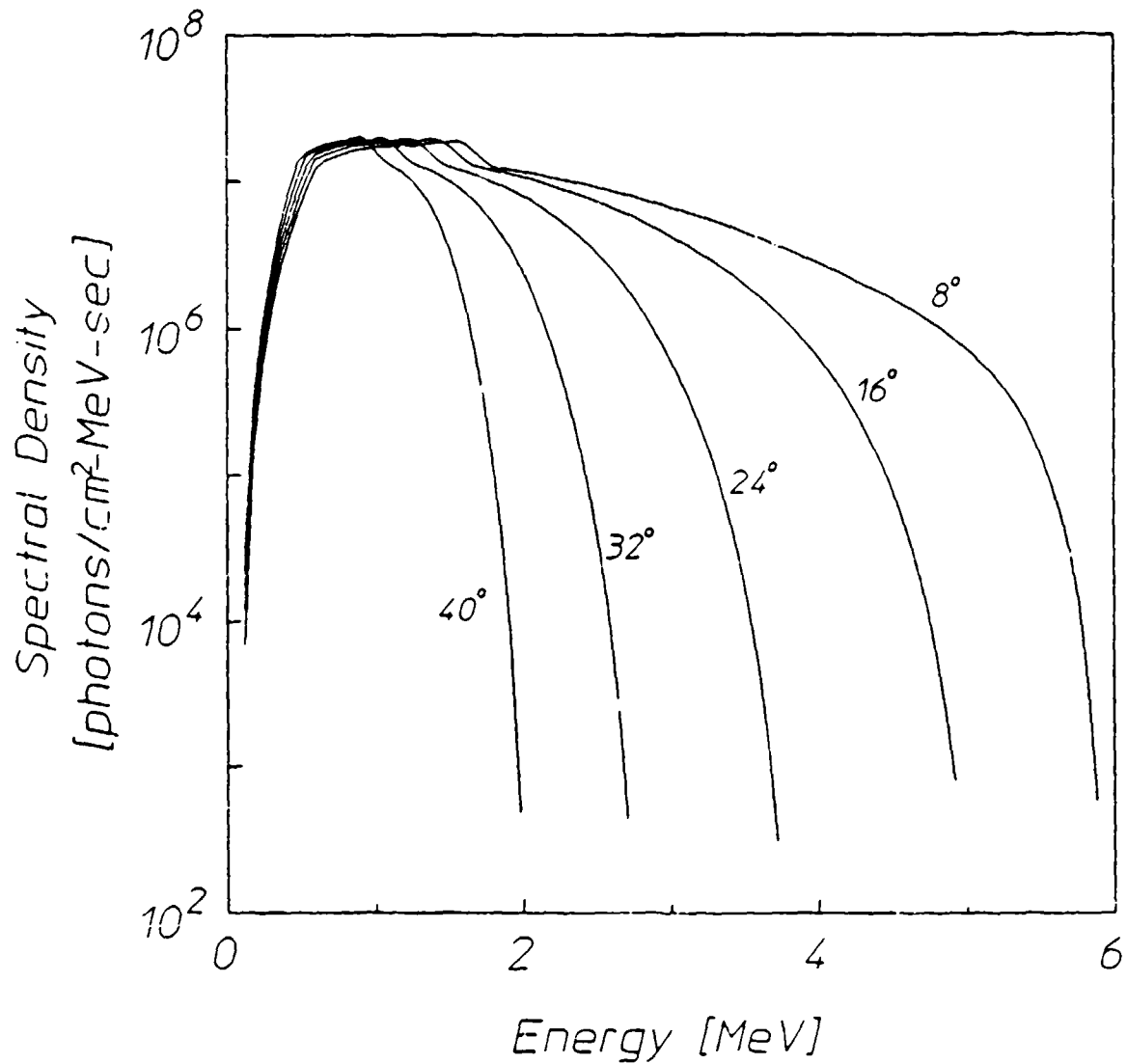
Figure 4.   Modelled output spectral densities of the extended scatterer/extended absorber geometry for the scattering angles of 0°, 8°, 16°, 24°, and 32°.

A point of interest concerning the output spectrum is the end-point energy, or that point above which there is no spectral density. By the point-to-point model, the end-point energy, E_{max}, is given by Eq. (1).   However, due to the extended geometry of the scatterer and target, lower angles are encountered which contribute energies higher than the

point-to-point value, increasing the maximum energy of the radiation illuminating the sample. A comparison of the calculated E_{max} for the point-to-point case and the extended geometry model is shown in Table I.

Table I

End-point energies for extended and point-to-point and geometry calculations.

Angle	E_{max} Extended Geometry	E_{max} Point-to-Point Geometry
0°	6.00	6.00
8°	5.88	5.38
16°	4.92	4.12
24°	3.72	2.98
32°	2.70	2.16
40°	1.98	1.60

Long lived isomeric states can be activated either directly or through one or more gateway[8] states as shown in Fig. 5. The long halflife of the isomeric state leads to a very narrow linewidth. Since the excitation of a particular state is proportional to the linewidth, direct activation of the isomer is considered to be negligible. A gateway state must be excited from the ground state by the absorption of a single photon. Some fraction of the decays from the gateway state then leads to the isomeric state either directly or through a multi-step cascade.

If the activation of the metastable state is assumed to proceed through one gateway state, then the total number of activations is given by

24

$$N_m - b_o N_t T \int_0^\infty \sigma(E) dI(E) - b_o N_t T \int_0^\infty \sigma(E) \frac{dI(E)}{dE} dE \qquad , \quad (11)$$
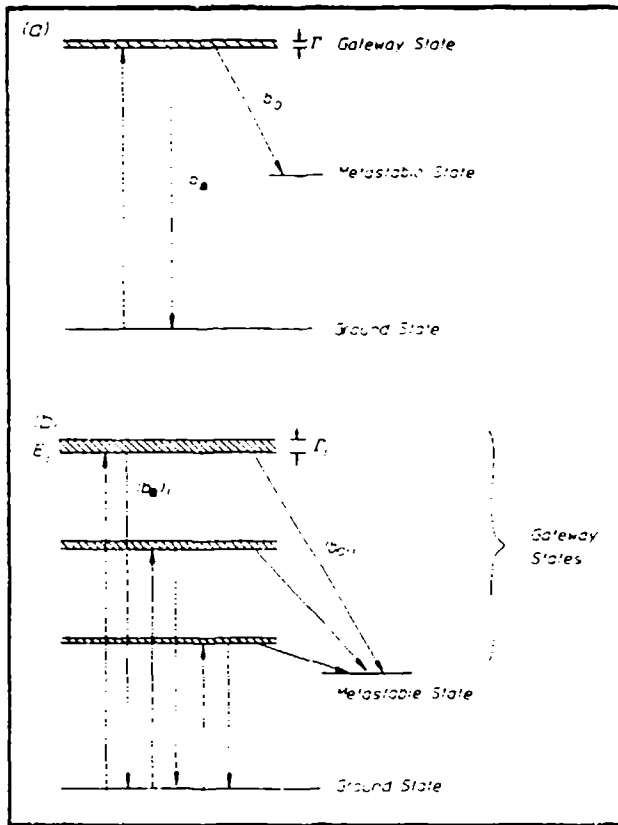
Figure 5(a): Energy level diagram of a single gateway isotope. (b): Energy level diagram of a multiple gateway isotope.

where b_o is the branching ratio of the decay of the gateway state into the metastable state, T is the irradiation time, and $dI(E)$ is the differential increment of flux with energy between E and $E + dE$. The Breit-Wigner cross section $\sigma(E)$ for the absorption of a photon when the resonant transition energy is E_r is given by

$$\sigma(E) = \frac{\lambda^2}{8\pi} \cdot \frac{2I_f + 1}{2I_i + 1} \frac{\Gamma_a \Gamma}{[(E - E_r)^2 + (\Gamma/2)^2]} \qquad \cdot \qquad (12A)$$

25

$$- \frac{\sigma_0}{4} \frac{b_a \Gamma^2}{[(E - E_r)^2 + (\Gamma/2)^2]} \qquad , \qquad (12B)$$

where the symbols are defined as follows:

λ — photon wavelength,

I_i, I_f — initial and final angular momenta of the nucleus,

Γ — total level width of the gateway state,

$\Gamma_a = b_a \Gamma/(1+ \alpha_p)$ — partial width of the gateway state for electromagnetic transitions to the ground state,

α_p — total internal conversion coefficient for the absorption transition, and

$$\sigma_0 = \frac{\lambda^2}{2\pi} \frac{2I_f + 1}{2I_i + 1} \frac{1}{(\alpha_p + 1)} \qquad ,$$

This nomenclature is consistent with that used in the Mossbauer spectroscopy community.

If the spectral density (dI/dE) can be considered to be constant in the vicinity of the absorption line, the integral in Eq. (11) becomes

$$N_m = N_t b_0 \left. \frac{dI}{dE} \right|_{E_r} T \int_0^\infty \sigma(E) dE \qquad (13)$$

$$= N_t (\pi \sigma_0 b_a b_0 \Gamma/2) \left. \frac{dI}{dE} \right|_{E_r} T \qquad ,$$

where $(dI/dE)|_{E_r}$ is the spectral density evaluated at the resonance energy, E_r. Thus the effective cross section for this activation is given by

26

$$\sigma_{eff} = \pi b_a b_0 \sigma_3 \Gamma / 2 \quad cm^2-keV \quad , \quad (14)$$

and the activation A may be written

$$A = (N_m/N_t) = \sigma_{eff} \left. \frac{dI}{dE} \right|_{Er} T \quad . \quad (15)$$

When there are two or more gateway states which may decay into the metastable level, the integral in Eq. (11) is replaced by a summation of integrals, one for each of the i gateway states, and it must be rewritten as

$$N_m = N_t T \sum_i \left[\sigma_{eff}(E_i) \left. \frac{dI}{dE} \right|_{Ei} \right] \quad . \quad (16)$$

While some gateway energies have been found through the use of variable end-point devices[9,10], in many cases the gateways have not been identified. The spectra shown in Fig. 4 indicate that by using a Compton spectrometer one may achieve results similar to those obtained with a variable end-point device, provided that the scattered radiation has adequate intensity. That is, although the scattered intensity will be substantially reduced from that in the primary beam, it must still be sufficient to produce statistically significant activation within the lifetime of the fluorescent level. As an example of this potential application, the spectra of Fig. 4 were used to generate sample activation results for several configurations of gateway states. These numbers correspond to the time corrected activations which would be observed in the samples after irradiation at the appropriate Compton angle. Based on the output spectral density dI/dE of the spectrometer as a function of angle, the effective cross section is obtained from Eq. (15) as

$$\sigma_{eff} = \frac{N_m}{N_t \dfrac{dI}{dE} T} = \frac{A}{\dfrac{dI}{dE} T} \quad . \quad (17)$$

A family of these curves based on the assumption that there is only one gateway state producing the isomer is shown in Fig. 6. These

27

curves are seen to intersect at the one energy corresponding to that of the gateway state. When there are two possible gateways, the family of curves similar to those seen in Fig. 7 is generated. This hypothetical case has one gateway at 2 MeV having a cross section of 10^{-26} cm^2-keV and a second gateway at 4 MeV with a corresponding cross section of 10^{-25} cm^2-keV. The family of curves obtained demonstrates considerably more complexity and the contributing gateways cannot be visually identified as they were in Fig. 6.
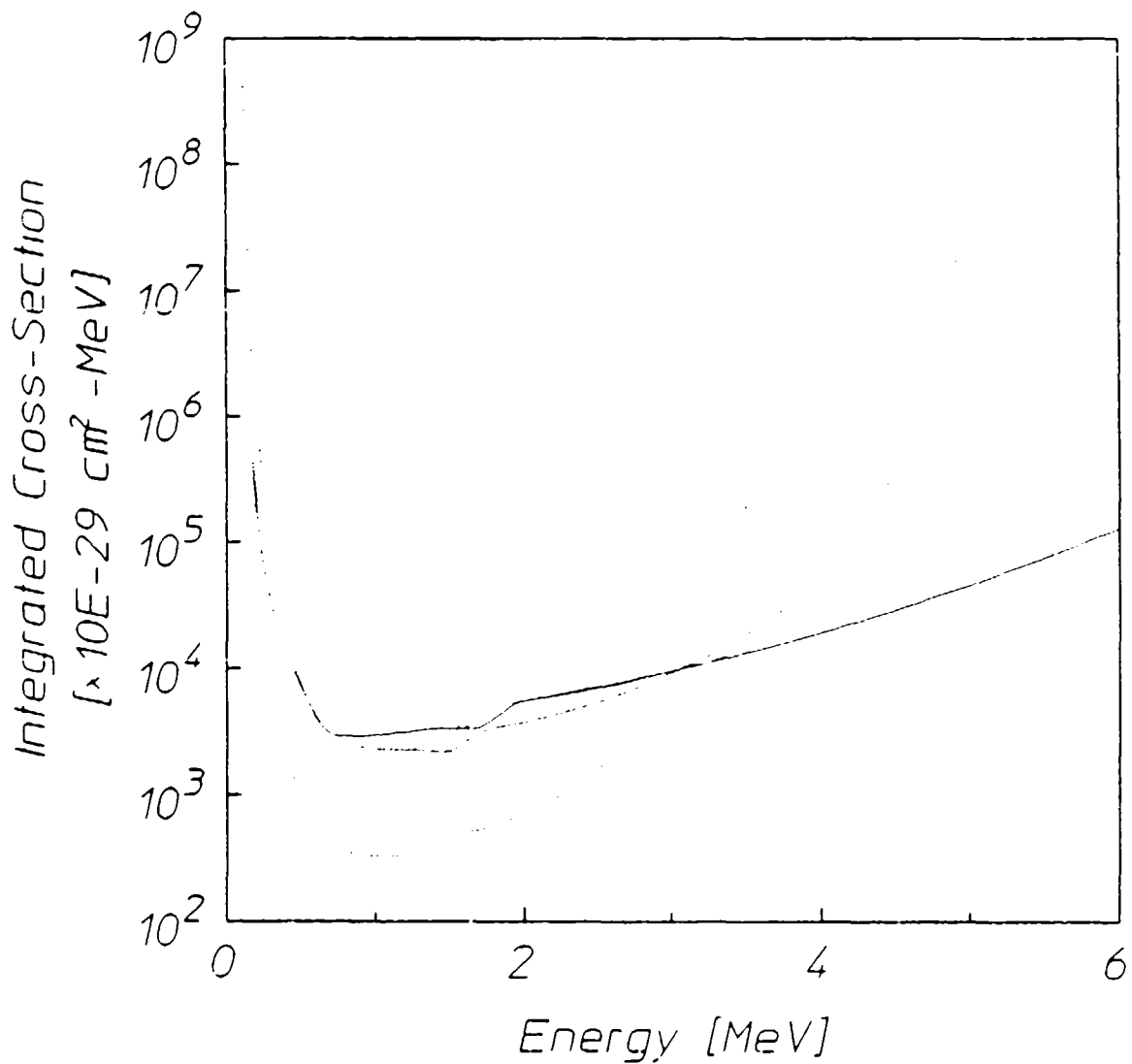
Figure 6: Synthetic curves of the cross section in units of 10^{-29} cm^2-keV as a function of gateway energy for the case of a single gateway state. The assumed spectral densities were those shown in Figure 4.
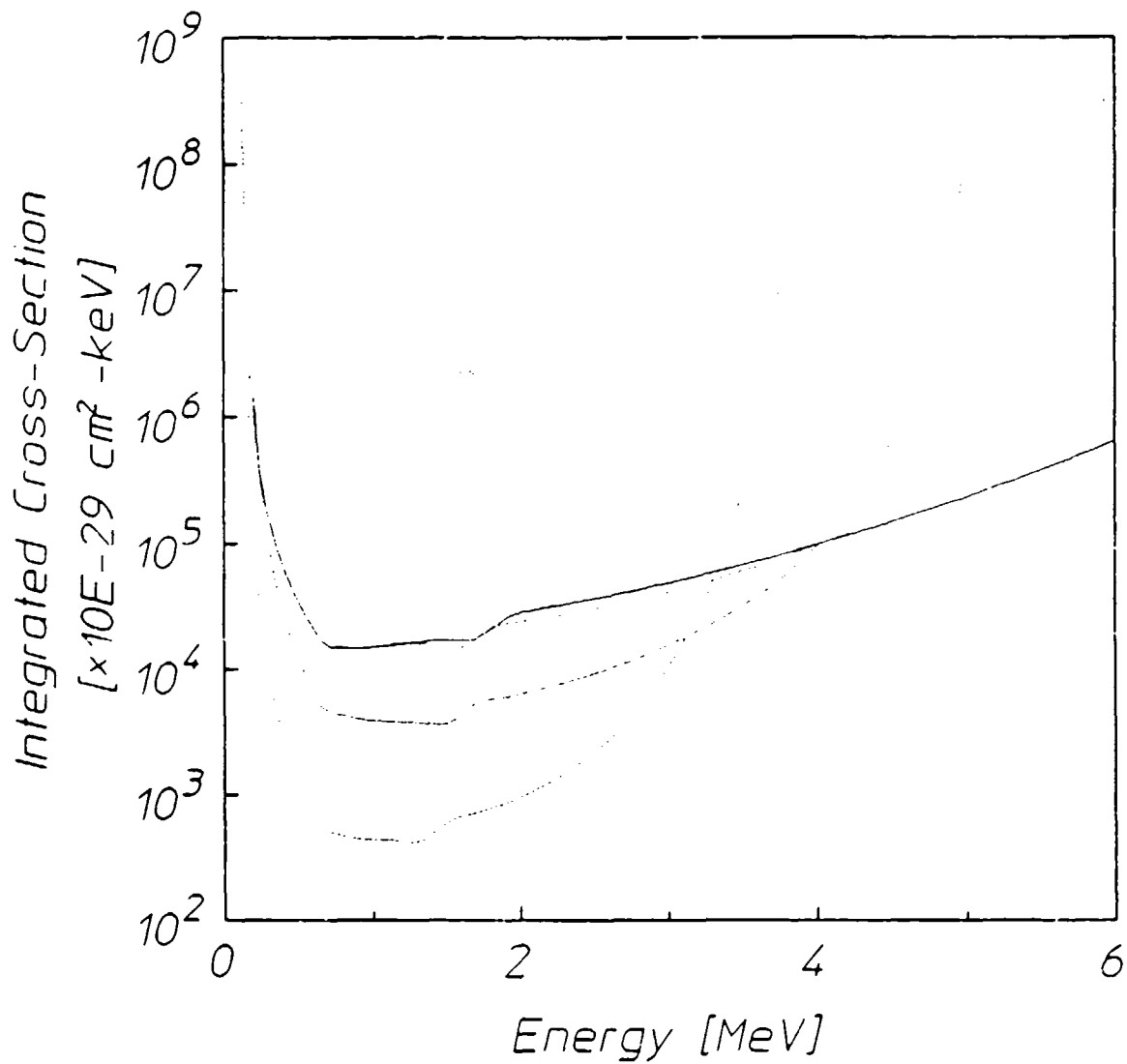
Figure 7: *Synthetic curves of the cross section in units of 10^{-29} cm^2-keV as a function of gateway energy for the case of two gateway states.*

Experimental Details

The irradiation fixture pictured in Fig. 2 was constructed to hold the samples during exposure. This jig was mounted at the filter tray position of the Varian Clinac 1800 linac employed for this work, thus holding the scattering center 65 cm from the x-ray converter target. The total incident photon flux at this position is $2.2 \cdot 10^{10}$ pho-

tons/cm^2-sec. A layer of 5 cm of lead shielding was placed in the plane of the Compton target to prevent radiation scattered off the Clinac collimator: 'om reaching the sample positions and contaminating the experiment. .he 2.54 cm diameter by 2.54 cm long stainless steel cylinder used as the scattering element nested in an aperture through this secondary shield. Bremsstrahlung radiation from the linac was restricted by the machine collimators until it illuminated only the scattering center.

The fixture had provisions for placing samples at angles corresponding to integral multiples of 8°. Samples were held inside a pneumatic transfer tube at a radial distance of 20.3 cm from the center of the scattering target. The wall thickness of the aluminum transfer tube was only 0.025 cm, presenting a negligible attenuation in the energy range of interest (>1 MeV) in this experiment. A valve on the pneumatic system also allowed the sample to be transferred back to the irradiation site. This was a great convenience, since entry into the CLINAC cell to relocate the sample for exposure would have otherwise required an additional 2 minutes per irradiation.
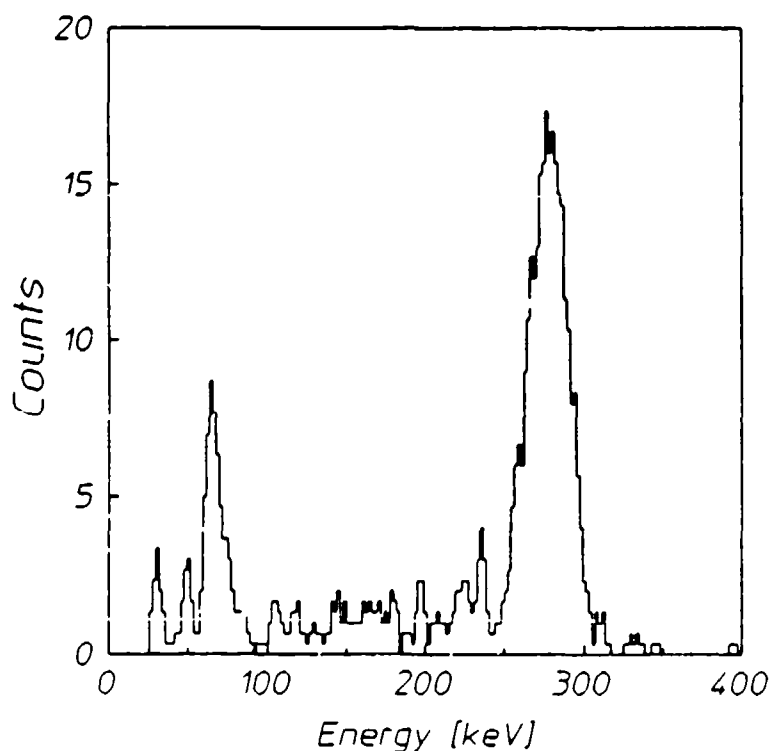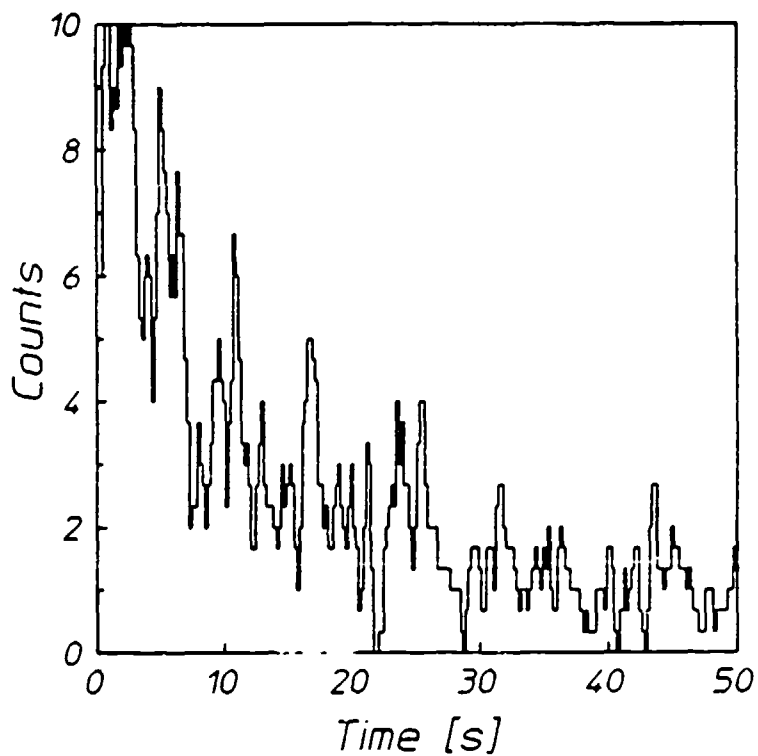
Figure 9: Time decay spectrum of the decay of the $^{197}Au^m$ produced by the exposure to the Compton scattered spectrum of the LINAC.

In each trial, the sample was exposed for 60 s. Immediately after the irradiation, the sample was automatically transferred from the exposure position to the detector, where it was counted for 20 s. A timer was started at the end of the exposure and stopped by the arrival of the sample at the detector. This timing information was used to correct the observed number of counts for losses during the transit interval.

The detector used in this work was a 7.62 cm x 7.62 cm NaI(Tl) detector with a 2.54 diameter well 5.08 cm deep. Data acquisition began automatically upon arrival of the sample at the detector. A pulse

*Figure 8 (Opposite): Pulse height spectrum of the decay of the $^{197}Au^m$ produced by the exposure of the Compton scattered spectrum of the LINAC.*

automatically upon arrival of the sample at the d.:tector. A pulse height spectrum and a time decay spectrum were simultaneously obtained for each case. Examples of these spectra are shown in Figs. 8 and 9. The pulse height spectra were used to obtain the results discussed here. Absolute counting efficiencies for this system were obtained by calibration against standardized sources. The observed counts in the 279 keV peak of $^{197}Au^m$ were corrected for absolute efficiency, self-absorption of the emitted gamma-rays, counting losses during irradiation and transit, and for the gamma-ray intensity to obtain the total number of excitations occurring during the exposure. Table II contains the number of trials made at each angle, the transit time for each trial, the number of photopeak counts observed, and the number of excitations produced. Table III lists the characteristic parameters for the gold sample used in this work. From the measured values, the product

$$\sigma_{eff} \times \frac{dI}{dE} = \frac{N_m}{N_t\,T} \tag{18}$$

was calculated for each observed angle for use in the analysis that has been previously described.

Table II

Summary of data from the Compton spectrometer experiments. Corrections to the observed photopeaks were made as described in the text. Photopeak areas were obtained using the commercial peak analysis program GDR Version 4.0

Angle (deg)	Number of Trials	Transit Time(s)	Total Photopeak	Average Isomeric
0*	1	1.87	19374	$1.08 \times 10^6 \pm 7.3 \times 10^3$
8	1	1.90	244	$3.51 \times 10^3 \pm 2.2 \times 10^2$
16	2	1.82	84	$6.00 \times 10^2 \pm 6.6 \times 10^1$
24	4	1.82	78	$2.86 \times 10^2 \pm 3.2 \times 10^1$
32	4	1.87	40	$1.44 \times 10^2 \pm 2.3 \times 10^1$
40	4	1.80	45	$1.57 \times 10^2 \pm 2.4 \times 10^1$

* No scatterer, exposed to primary beam. [4]

Table III

Sample parameters for this work.

Sample Composition	99+	% Au
Sample Mass	31.6	g
Isotopic Abundance	100	%
Number of Target Nuclei	9.52×10^{22}	
Gamma-ray energy	279	keV
Gamma-ray intensity @ 279 keV	73.11	%
Self-absorption factor	0.305	

Data Analysis

The spectral intensity was calculated using the techniques described above for each of the sample positions used in the experiment. As previously discussed, the input spectrum used in this work was a piecewise-continuous curve fitted to the results of Mohan et al.[6] Expected uncertainties associated with the spectral intensity calculation were obtained by fitting a second piece-wise continuous curve to the reported uncertainties in Mohan's work. The two curves representing the envelope of the input model spectrum plus and minus these fitted uncertainties are plotted in Fig. 10 with the original results from Mohan. The envelope curves bound the Monte Carlo results and are consistent with their error bars. Uncertainties in the Compton scattered intensities were obtained by repeating the extended geometry calculations with the envelope curves of Fig. 10 as input data. The results for the case $\theta = 16°$ are shown in Fig. 11.
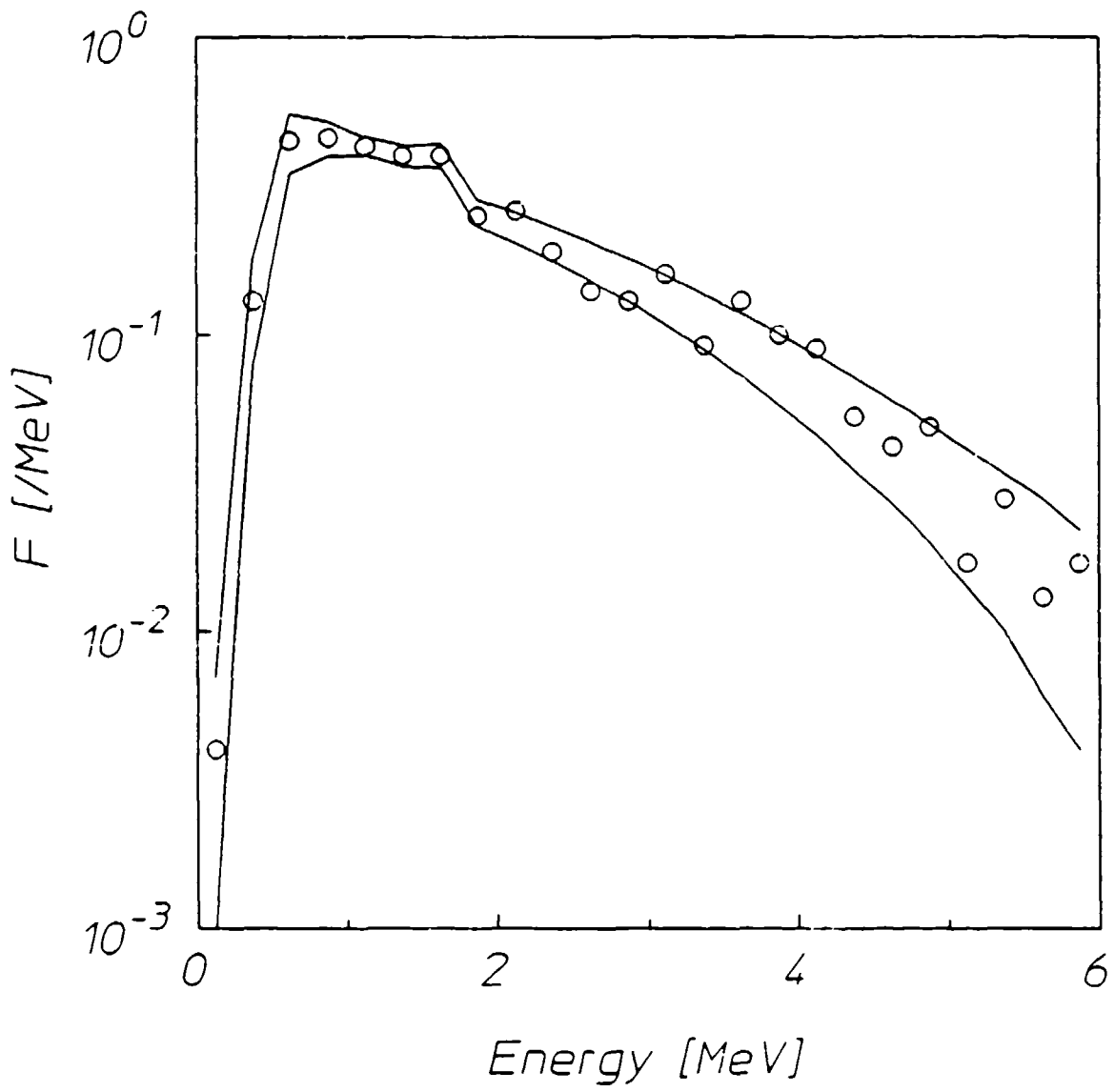
Figure 10: Curves representing the envelope of uncertainty of the input spectral density. This was obtained by fiting piece-wise continuous curves to the uncertainties of the spectrum generated by Mohan. The open circles represent the most porbable values of the spectral density as generated by Mohan.
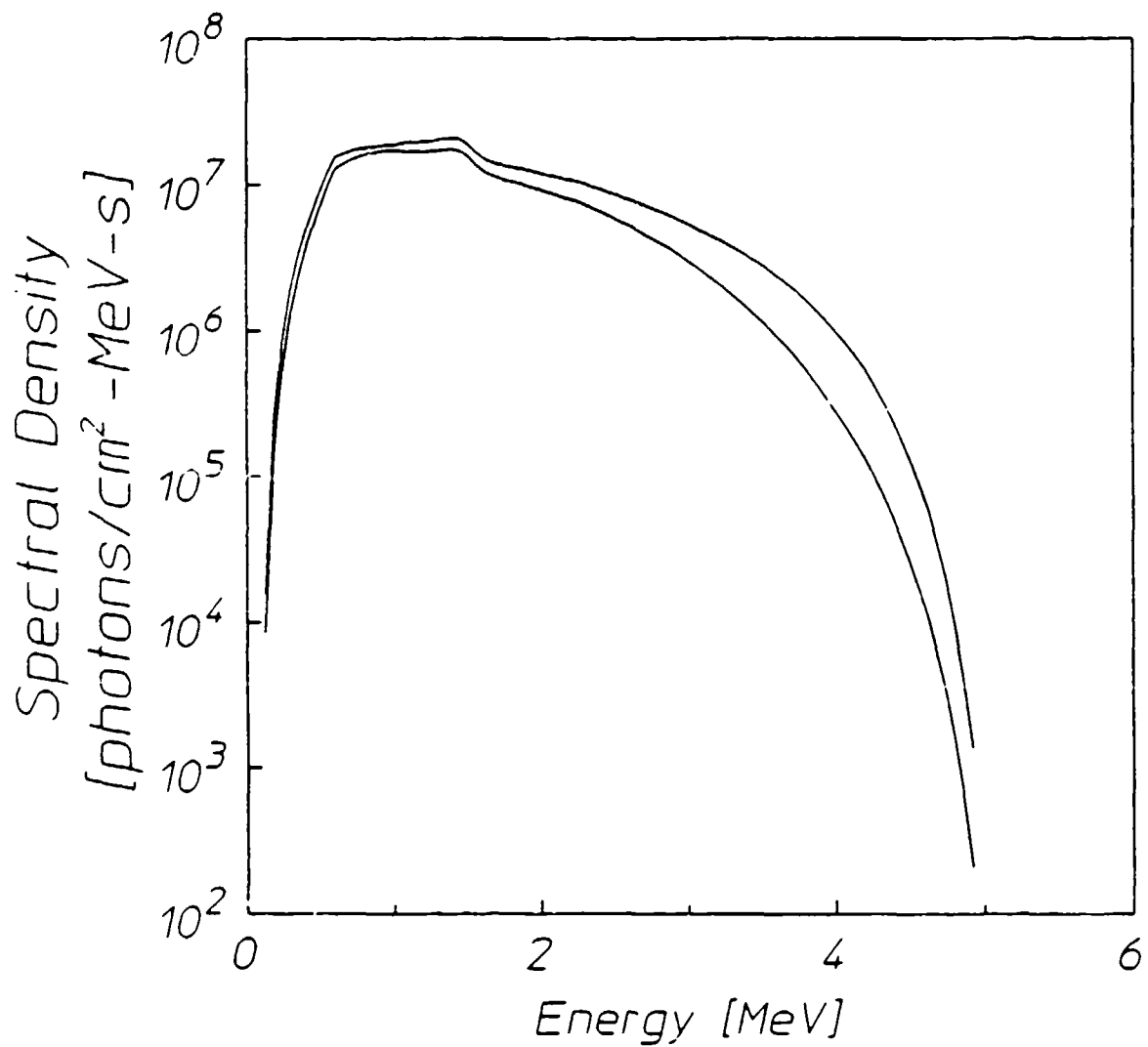
Figure 11: *The uncertainty envelope of the compton scattered spectral density at 16° calculated with the extended scatterer/extened absorber geometry.*

From the activation data of Table II, the product of cross section and spectral intensity was calculated using Eq. 18. Based on the assumption of a single gateway, a plot of σ_{eff} versus the gateway energy was made for each value of θ by utilizing the modeled spectral intensities and Eq. 17. The family of curves obtained by the employing this procedure for Compton spectrometer angles of 8°, 16°, and 24° is shown in Fig. 12. Also included in this figure is the curve obtained by a similar analysis of the activation due to the direct exposure of the gold sample to the primary beam of the linac.
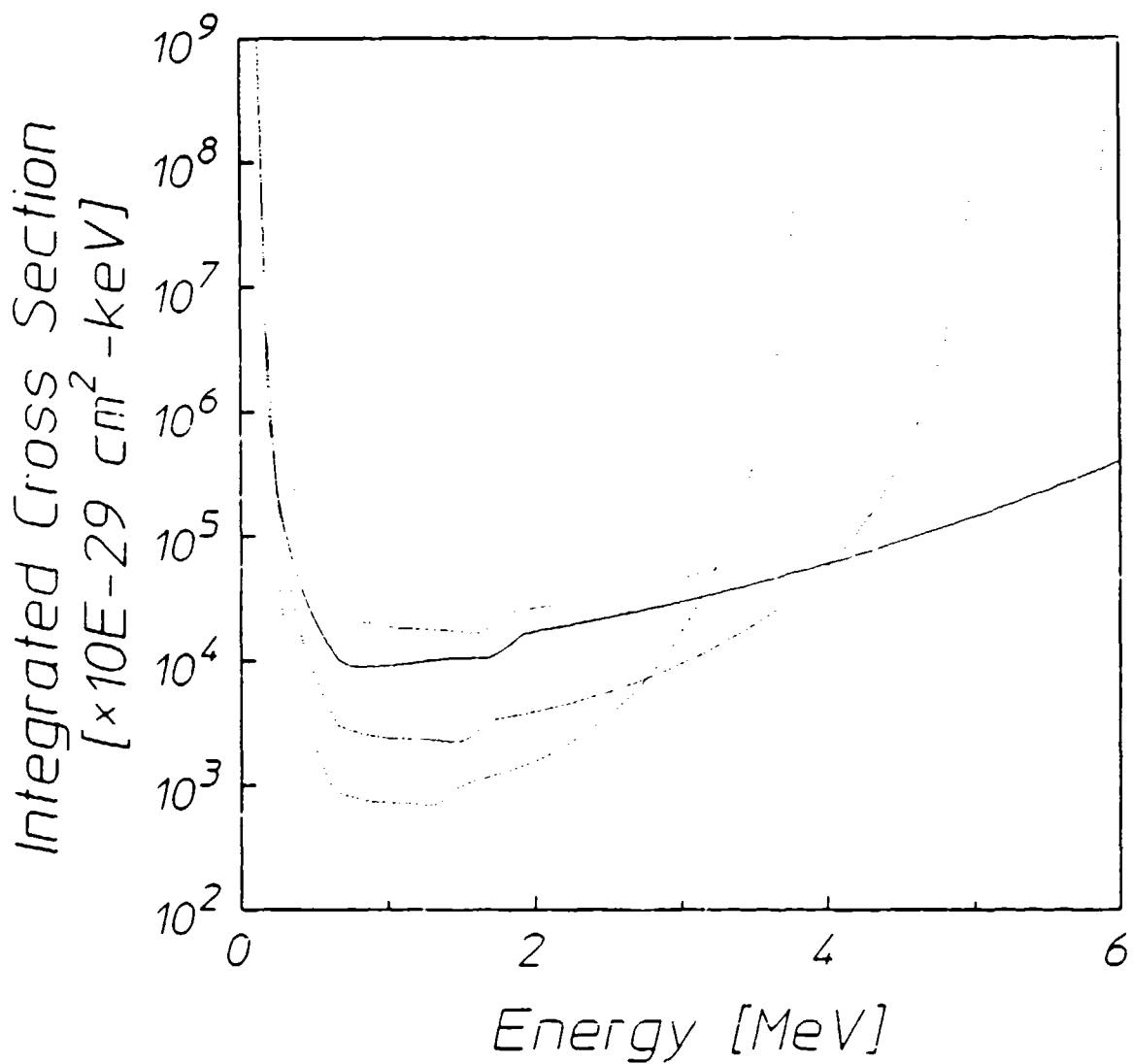
Figure 12: Cross section curves generated from the data taken with the Compton spectrometer and the modelled output spectral densities as shown in Figure 4.

The marked difference between these results and the synthetic curves of Fig. 6 suggests the presence of more than one gateway state, but may be due to experimental uncertainties. The data were analyzed using models incorporating both one and two gateways. In the case of one gateway, there are two unknowns -- the energy E_g and cross section σ for the single gateway -- and four simultaneous non-linear equations of the form

37

$$A_i' - \phi_i(E_g)\sigma \qquad , \qquad\qquad (19)$$

where the A_i' are the activation values of Eq. 15 normalized to the exposure time and the $\phi_i(E_g)$ are the spectral intensities (dI/dE) at the gateway energy E_g. This set of equations was solved using an iterated Marquardt procedure[11], yielding the values $E_g - 3.57 \pm 0.14$ MeV and $\sigma - 42000 \pm 4000 \cdot 10^{-29}$ cm^2-keV.

If two gateway states are assumed to exist, then there are four unknown parameters to be found. These are the energies E_1 and E_2 and cross sections σ_1 and σ_2 associated with the lower and upper gateways. Again, a series of four simultaneous non-linear equations can be written relating these parameters to the observed levels of activation. A set of N simultaneous nonlinear equations in N unknowns may have no real solutions, a single solution, or a degenerate set of solutions. Unfortunately, when a solution was sought using the same Marquardt technique described above, successive iterations did not converge to a set of unique values, but instead produced results that were strong functions of the input estimates for the parameter values. Thus, experimental data at additional values of angle θ would be required to obtain an unique solution for the multi-gateway model.

Conclusions

The Compton spectrometer can be used to determine gateway energies and nuclear photo-activation cross sections when used with a linear accelerator producing a well-characterized continuous spectrum. The complexity of the model which can be used to analyze a given system is limited by the number of angles in the Compton spectrometer for which data are available. Models incorporating more gateway states require data at additional angles.

In the present work, a rudimentary analysis was made of the spectrum produced by the Compton spectrometer. This analysis would tend to underestimate the spectral intensity at lower energies, since it does not properly account for multiple Compton scattering in the spectrometer. Thus, the curves of Fig. 12 should lie lower than shown at the

lower photon energies. A comprehensive Monte Carlo transport calculation is planned to realistically estimate the total scattered spectral intensity at each of the sample positions.

Preliminary results from this work indicated that if a single gateway were responsible for the observed activation, the gateway would lie near 3.6 MeV and have a cross section of $4.2 \cdot 10^{-25}$ cm^2-keV. Although this is not inconsistent with the results of several other investigators[12,13], previous work in this Center[14] and by Lukens[15] also indicates the presence of at least one more gateway in the range between 1 and 3 MeV. Additional experiments with better angular resolution, statistical accuracy, and spectral characterization should further improve the understanding of the photoactivation mechanism in ^{197}Au.

While mathematical rigor cannot be maintained at any higher level of analysis, some further arguments can be presented based on physical insight. In the first place it must be recalled that the model error is not estimated by the Marquardt procedure. It was shown above that if there were only a single gateway within the interval between 1 and 6 MeV, then it would lie near 3.6 MeV. However, if there are two gateways, then neither is constrained to be near that energy.

Since the observation of any large gateways at all below the onset of the continuum of states was initially surprising, it is reasonable to propose a model with only a minimal number of them at lower energies. Lukens[16] reported the excitation of ^{197}Au with bremsstrahlung having an endpoint energy of 3 MeV. If this activation observed by Lukens is assumed to be due to a single gateway below 3 MeV, several interesting conclusions may be drawn.

The intensities for energies above 3 MeV are relatively small for scattering at $\theta = 24°$, and therefore the corresponding curve for σ in Fig. 12 approaches the vertical near this energy. Under the assumption made above, this curve represents the cross section of the single gateway observed by Lukens as a function of the energy at which it might lie. The correct choice of the energy can be approximated by considering the intersection of this curve with those obtained at other angles, in analogy to the situation shown in Fig. 6.

Wherever the higher energy gateways may lie, the data obtained at $\theta = 16°$ will be that which is least affected by their presence. Therefore, the intersection near 2.6 MeV of the $\theta = 16°$ and $\theta = 24°$ curves[16]

in Fig. 17 should give the best approximation to the location of the gateway observed by Lukens. Consistent with this conclusion is the observation that the $\theta = 8°$ curve, which shows elevated cross section values due to activation at higher energies, intersects the $\theta = 24°$ curve near 3 MeV. If the $\theta = 8°$ curve were corrected by removing the contributions of the higher gateways, the shape of the curve would be preserved, but its location would be translated downward on the plot of Fig. 12. This would shift the intersection down from 3 MeV toward the 2.6 MeV value noted above.

Of course, the $\theta = 16°$ curve may also carry some contamination from higher gateways and thus require a similar downward correction if the effects of the upper gateways were to be removed. The extent of this correction cannot be determined, but its presence insures that 2.6 MeV is an upper limit for the energy of the assumed single gateway. Moreover, reference to Fig. 12 shows that below 1.5 MeV the cross section required by the $\theta = 24°$ curve is $1000 \cdot 10^{-29}$ cm^2-keV or more, which is much greater than the values[15] obtained using the PITHON bremsstrahlung source operated with a 1.5 MeV endpoint energy. Thus, the gateway must be bracketed by these two points.

While the rigorous resolution of the merits of this interpretation must await additional data, there seems to be a strong argument that the gateway originally observed by Lukens lies near 2.6 MeV. This result has an interesting precedent in the literature[17] that has largely been ignored as an anomaly. This is the discrete gateway for the reaction $^{87}Sr(\gamma,\gamma')^{87}Sr^m$, having an integrated cross section of $430 \cdot 10^{-29}$ cm^2-keV at 2.66 MeV. This cross section was about one and a half orders of magnitude greater than any other reported for a discrete gateway and has remained unexplained for 20 years. Now it appears that there is a second such example in $^{197}Au(\gamma,\gamma')^{197}Au^m$.

Acknowledgements

References

1. C. B. Collins, C. D. Eberhard, J. W. Glesner, and J. A. Anderson, Phys Rev C 37, 2267 (1988).

2. C. D. Eberhard, J. W. Glesener, Y. Paiss, J. A. Anderson, C. B. Collins, W. L. Hodge, E. C. Scarbrough, and P. P. Antich, Report GRL/8702, 89 (1987).

3. C. B. Collins, J. A. Anderson, C. D. Eberhard, J. F. McCoy, J. J. Carroll, E. C. Scarbrough, and P. P. Antich, Report GRL/8703, 37 (1988).

4. J. A. Anderson, C. D. Eberhard, J. F. McCoy, K. N. Taylor, J. J. Carroll, M. J. Byrd, C. B. Collins, E. C. Scarbrough, and P. P. Antich, Report GRL/8704, 11 (1988).

5. R. D. Evans, "Gamma Rays" in American Institute of Physics Handbook, ed. D. E. Gray (McGraw-Hill, New York, 1963).

6. R. Mohan, C. Chui, and L. Lidofsky, Med. Phys. 12, 592 (1985).

7. N. C. Ikoro, D. A. Johnson, and P. P. Antich, Med. Phys. 14, 93 (1987).

8. Y. Paiss, C. D. Eberhard, and C. B. Collins, Report GRL/8702, 71 (1987).

9. C. B. Collins, J. A. Anderson, Y. Paiss, C. D. Eberhard, R. J. Peterson, W. L. Hodge, Phys. Rev. C (accepted for publication).

10. J. A. Anderson, M. J. Byrd, and C. B. Collins, Phys. Rev. C (accepted for publication).

11. W. H. Press, B. P. Flannery, S. A. Teukolsky, and W. T. Vettering, Numerical Recipes, (Cambridge University Press, Cambridge, 1986).

12. W. T. K. Johnson and C. E. Dick, Nucl. Instr. and Meth. 99, 221 (1972).

13. Zs. Nemeth, L. Lakosi, I. Pavlicsek, and A. Veres, Appl. Radiat. Isot. 37, 1155 (1986).

14. C. B. Collins and J. A. Anderson, Report GRL/8701, 35 (1987).

15. H. R. Lukens, Jr., J. W. Otvos and C. D. Wagner, Int. J. Appl. Radiat. and Isot. 11, 30 (1961).

16. The results shown in Fig. 12 and discussed in this chapter are the current values at press time, and are somewhat larger than preliminary values used elsewhere in this report.

17. E. C. Booth and J. Brownson, Nucl. Phys. A 98, 529 (1967).

DETERMINATION OF PHOTOEXCITATION CROSS SECTIONS FOR ^{176}Lu(γ,γ') ^{176}Lu^m USING A 6 MeV BREMSSTRAHLUNG SOURCE

by J. A. Anderson, K. N. Taylor, J. J. Carroll, M. J. Byrd, and
C. B. Collins
Center for Quantum Electronics, University of Texas at Dallas
E. C. Scarbrough and P. P. Antich
University of Texas Southwestern Medical Center

Introduction

The isomer ^{176}Lu^m is of intrinsic interest in nuclear photoactivation studies because of its proximity in the chart of nuclides to other isomeric nuclei, such as ^{167}Er, ^{179}Hf, ^{180}Ta, and ^{191}Ir, which have been found[1,2,3,4] to manifest very large (γ,γ') cross sections in the range below 6 MeV. The mechanisms for populating the isomeric state in this nuclide are also of interest for astrophysical applications, since the long half-life of the ground state ^{176}Lu $(3.6 \times 10^{10}$ y) makes it a candidate for use as an astrophysical chronometer. Several investigators[5,6,7] have recently studied it for this purpose. However, the existence of the relatively short-lived isomeric state ^{176}Lu^m (E - 126 keV, $T_{1/2}$ - 3.68 h), which beta decays to form ^{176}Hf, complicates this scheme. Because of this state, photoexcitation of the isomer could prematurely bleed away the ground state population and invalidate the operation of the chronometer. The work described here is concerned with determining the size of the transfer cross section for the reaction ^{176}Lu$(\gamma,\gamma')^{176}$Lu^m by using a bremsstrahlung source with a fixed endpoint near 6 MeV. A separate paper[8] considers the astrophysical implications of these experiments.

Because of the very narrow linewidths associated with long-lived, isomeric nuclear states, the cross sections for directly exciting these states by photoabsorption are quite small. However, the cross sections for isomeric excitation via a cascade from higher-lying intermediate states can be many orders of magnitude greater than those for the direct process. This mechanism has previously been discussed in Refs. 1-4.

The resulting total activation, N_e, of an irradiated sample can be described by

$$N_e - N_T \sum_i [\pi b_a b_o \sigma_o \Gamma / 2]_i \; \Phi(E_i) \qquad . \qquad (1)$$

where N_T is the number of target nuclei in the sample, the quantity in square brackets is the effective integrated cross section for transfer through the ith gateway state, Φ_i is the time-integrated, incident photon flux at the energy E_i of the ith gateway, and the summation is taken over all accessible gateways. The terms appearing in the integrated cross section are the Breit-Wigner cross section, σ_o, the width of the resonance, Γ, and the branching ratios from the gateway state to the ground and excited states, b_a and b_o. The units of the integrated transfer cross section are cm^2-keV; the units for the time-integrated photon flux are photons/(cm^2-keV).

For the case of $^{176}Lu^m$, at least one intermediate gateway state has been observed by Norman et. al.[5] in the energy range between 661 keV and 1332 keV. In that work, lutetium samples were exposed to radiation from medical irradiation machines using both ^{137}Cs and ^{60}Co sources. They found that the isomeric level was photoactivated slightly by the ^{60}Co source (E_{max} - 1332 keV), but not by the ^{137}Cs source (E_{max} - 662 keV). Because of the extended nature of the source and shielding configurations in these devices, the gamma-ray spectra in such cases are not simple line spectra, but show broad continua on the low energy side of the line(s) due to the radiation transport process.[9] Unfortunately, Norman et al. did not use the real spectral distribution from the irradiation source. Moreover, they analyzed their results as if the photoabsorption process were a bound-free transition with a threshold rather than treating the case of bound-bound transitions that would actually hold in this energy range. Without an accurate knowledge of the spectral intensity function for the irradiation source and of the energy of the gateway state, it is not possible to determine the integrated cross section for transfer into the isomeric state.

The study described here has approached the source definition problem by using a relatively well characterized bremsstrahlung source,[10] the Varian CLINAC 1800 operated in the 6 MeV mode. The spectrum from this device is shown in Fig. 1. By measuring the total activation obtained during an exposure and employing the relative

44

intensity information contained in Fig. 1, it is possible to generate a plot of integrated cross section as a funtion of the energy assumed for a single gateway. The results of the current study are presented in this form.
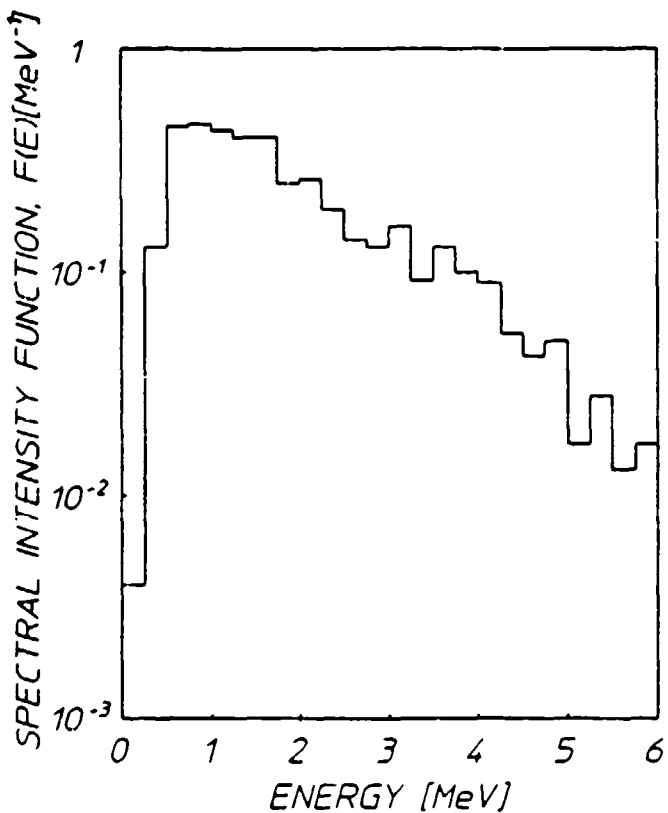
Figure 1: Spectral intensity for the Varian CLINAC 1800 operated in the 6 MeV mode. The curve has been normalized to represent a single incident photon. Actual photon fluxes were obtained from this information by dividing the measured dose by the dose-per-photon calculated on the basis of this intensity distribution.

Detection of the isomeric state $^{176}Lu^m$ once it has been created presents some difficulties. A partial energy level diagram[11] showing $^{176}Lu^m$ and its beta-decay daughter product, ^{176}Hf, is shown in Fig. 2. The long-lived ground state decays principally (99.1%) to the state lying at 597 keV in ^{176}Hf. The characteristic signature of this decay is

a beta-particle with an endpoint of 565 keV and major gamma rays at 88.4 keV (13.1% intensity), 201.9 keV (84%), and 306.9 keV (93%). Photoexcitation of the isomer is indicated as proceeding through an as yet uncharacterized intermediate state. The isomer decays wholly by beta decay, with 39.6% of the decays terminating on the ground state in ^{176}Hf and having a beta decay endpoint energy of 1313 keV. The other 60.4% of the decays terminate on the ^{176}Hf state at 88.4 keV, have an endpoint energy of 1225 keV, and are accompanied by several low intensity gamma rays. The most prominent of these gamma rays is the 88.4 keV line, which has an intensity of 8.9%. Thus, detection schemes for the isomer which are based on gamma-ray counting must utilize the 88.4 keV line, which suffers strong interference from the ground state ^{176}Lu decay.
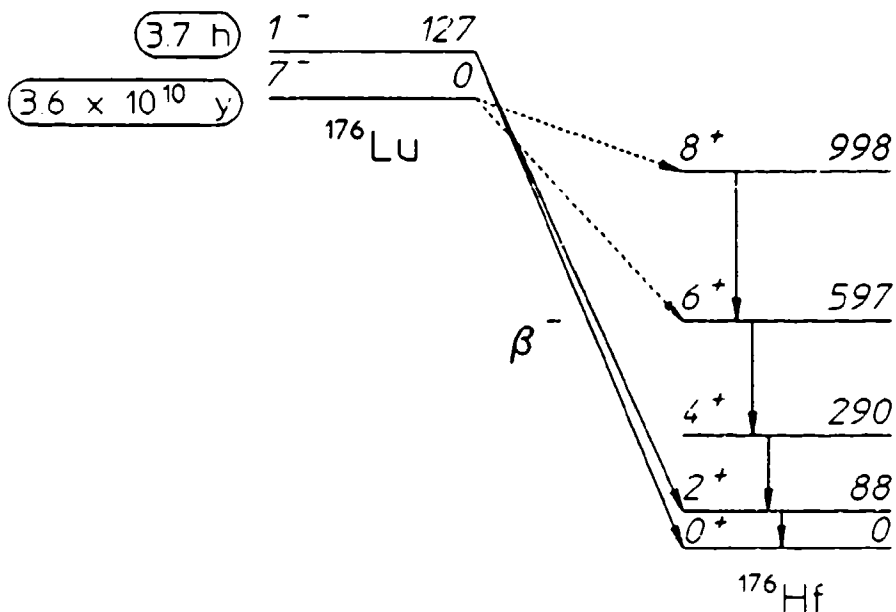
Figure 2: Energy level diagram for ^{176}Lu, showing the beta decay of the isomeric state to ^{176}Hf. The advantage of the Cerenkov detection scheme used in this work is that the beta particles from decay of the isomeric state can be cleanly separated from those resulting from decay of the ground state.

An alternative approach to gamma-ray counting is to directly detect the beta particles emitted during the decay process. This can be done either by standard liquid scintillation counting, or, because of the high end-point energy of the decay, by counting Cerenkov photons generated by the passage of the beta particles through the sample

46

solvent. Both processes offer high net efficiencies compared to the gamma-ray counting technique, but the Cerenkov method has the additional advantage of being relatively insensitive to interference from the lower energy beta particles emitted by the decay of the ground state. The threshold for production of Cerenkov radiation by beta particles passing through a medium is given by[12]

$$E_{th} = m_0c^2\{-1 + [n^2/(n^2-1)]^{1/2}\} \quad , \quad (2)$$

where n is the index of refraction of the medium and m_0c^2 is the 511 keV rest mass energy of the electron. Thus, for water (n = 1.33) no Cerenkov radiation will be emitted for electrons with energies less than about 260 keV. Above threshold, the efficiency for the production of Cerenkov photons in water rises steeply, being about eight times greater at 1000 keV than it is at 500 keV.[13] The net result of these two effects is to make the Cerenkov detector almost blind to the steady background generated by the decay of the [176]Lu ground state. Since the Cerenkov process causes many photons to be emitted as the electron is slowed down, background contributions due to photomultiplier noise can also be suppressed by using a coincidence counting technique.

Experimental Detail

The samples used for this work consisted of a nominal 5 grams of lutetium chloride ($LuCl_3 \cdot 6H_2O$) dissolved in water to produce approximately 20 ml of solution. Table I lists sample weights and other pertinent parameters. Samples were held in standard 20 ml polyethylene scintillation vials obtained from Research Products Incorporated.

Table I: Sample parameters for the Cerenkov counter experiments. N_T is the number of target ^{176}Lu nuclei in the sample. The natural abundance of ^{176}Lu was taken to be 2.59%[14].

Sample ID	Mass, $LuCl_3 \cdot (6H_2O)$ [g]	N_T
I	4.993	2.00×10^{20}
III	4.971	1.99×10^{20}

A simple coincidence counter was constructed using two RCA 8850 photomultipliers mounted on a common axis in E. G. & G. 9201 tube bases. A special lightproof fixture held the scintillation vials centered between the two photomultipliers. The fast (approximately 6 ns) outputs from these tubes were amplified, time synchronized, and input to a discriminator in order to produce logic pulses which could drive a 150 MHz logic unit (Phillips Model 755). The output from the logic unit could be accumulated on either a simple counter or a multichannel scaler (MCS). A schematic diagram of the data acquisition system is shown in Fig. 3.
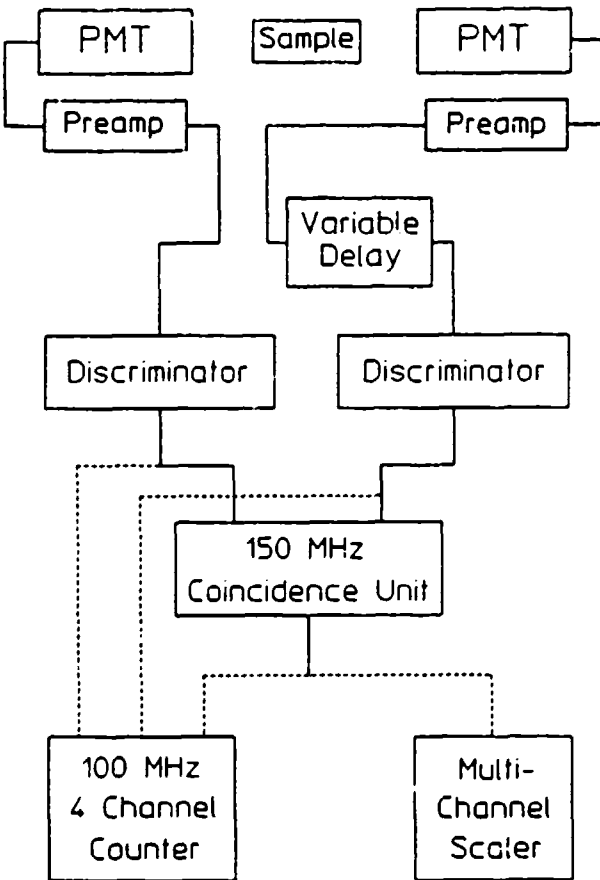
Figure 3: Data acquisition system for the Cerenkov counter used in this work. Coincidence circuitry was used to suppress dark noise in the photomultipliers since counting rates in the experiment were less than 10 counts/s.

Because the efficiency of a Cerenkov counter varies strongly with the endpoint energy of the beta decay being monitored, it is necessary to use a calibration standard having essentially the same endpoint as the nuclide to be counted. As noted above, the endpoints of the beta decay channels from the isomer are 1225 keV and 1313 keV, with a weighted average of 1260 keV. Naturally occurring radioactive ^{40}K has a beta endpoint energy of 1330 keV, and for reasons of convenience was chosen as the calibration standard for this work. Calibration standards with nominal amounts of 1, 2, 3, 4, and 5 grams of KCl dissolved in

water to make 20 ml of sample were prepared and were placed in counting vials. These vials were counted before each run to determine the detector efficiency for the particular choice of discriminator settings, PMT voltages, etc. used in a given experiment. The net counting efficiency was found to lie in the range 10.3-13.6%.

Three different sample exposures, each of about 40 minutes, were made. The samples were oriented with the cylindrical axis of the sample vial perpendicular to the x-ray beam axis. The vials were located 63.7 cm from the x-ray converter. At this position, the total dose delivered to the sample was about 44.2 kRad during a 40 minute exposure. Table II lists the exposure times, sample identifications, and counting times for the different exposures.

Table II: Exposure and counting conditions for $^{176}Lu^m$ excitation. Transit time is the time elapsed between the end of the irradiation and the start of the counting measurement. Effective dwell time is the dwell time obtained after collapsing the number of channels in the MCS spectrum; the actual MCS dwell time was typically 40 s.

Exposure	Sample ID	Exposure Time [s]	Transit Time [s]	Effective Dwell Time [s]
1	I	2805	2955	320
2	I	2400	3165	320
3	III	1799	3315	320

Analysis

In the first experiment, a significant amount of activation was observed following the irradiation, as shown in the multichannel spectrum of Fig. 4. As can be seen from the figure, the principal decay component observed has a half-life of 3.83 ± 0.05 h, in reasonable

agreement with the accepted value of 3.68 h for [176]Lu[m]. This value was
obtained by fitting a line to the log of the number of counts per
channel, after correction for background, for data between t − 20070 s
and t − 60070 s. Here, t is the time elapsed after the end of the
irradiation.
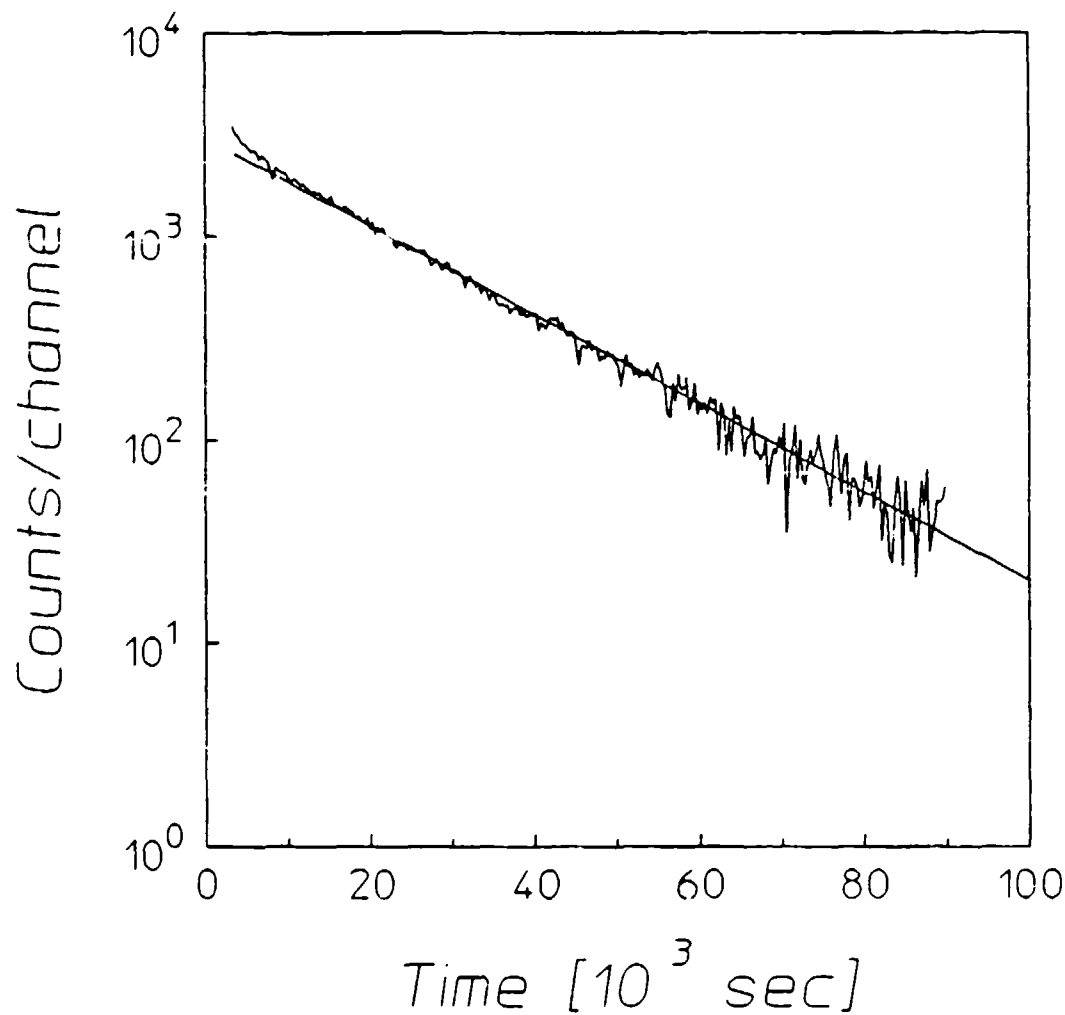


Figure 4: Decay spectrum for trial 1. Here, and in Figs. 5
and 6, the number of backgrcund-corrected counts per channel
of the multichannel scaler are plotted vs. the time since the
end of the irradiation. The spectrum shows the superposition
of the [176]Lu[m] decay and the the:noluminescence decay from the
polyethylene bottle. The line fitted to the data corresponds
to a half-life of 3.83 h.

A second component with a faster decay is also clearly present at early times in the MCS spectrum of Fig. 4. Subsequent experiments in which the bottle, the fluid, and the bottle cap were separately counted identified the source of this fast component as count-rate generated coincidences from single-photon thermoluminescence phenomena arising in the polyethylene bottle. In these secondary experiments, a sample was irradiated and then broken apart into its components (cap, bottle, fluid). From these components and from pristine, non-irradiated parts, three samples, which were identical except for the choice of the irradiated component, were created. These samples were then counted to unambiguously identify the source of the fast decay component. It was found that the phenomena was present regardless of whether the fluid was the $LuCl_3$ solution or pure water. Examination of the count-rates from the individual photomultipliers indicated that the fast component was due to accidental coincidences between independent, random events occurring on the two detector channels when the irradiated polyethylene bottle was counted. Further experiments demonstrated that the fast decay component could be either "stored" by cooling the bottle with liquid nitrogen or quenched by heating the bottle, thus identifying the process as some type of radiation-induced thermoluminescence.

A second run, made after the fast decay component had been identified and steps were taken to remove it, yielded a half-life value of 3.58 ± 0.05 h for the lutetium activation. The data between t = 3325 s and t = 32125 s were fit to obtain this result. These data are shown in Fig. 5. However, the intensity of the observed Cerenkov radiation was much less in this second case. This decrease in intensity was traced to the deterioration of the cap on the scintillation vial and an attendant buildup of readily visible debris suspended in the lutetium solution. A third and final run made with a freshly prepared sample is shown in Fig. 6. It yielded a value of 3.57 ± 0.04 h for the half-life when a fit was made to the data between t = 3795 s and t = 60115 s. The average value for the half-life obtained from these experiments is therefore 3.66 ± 0.08 h, in good agreement with the literature value.
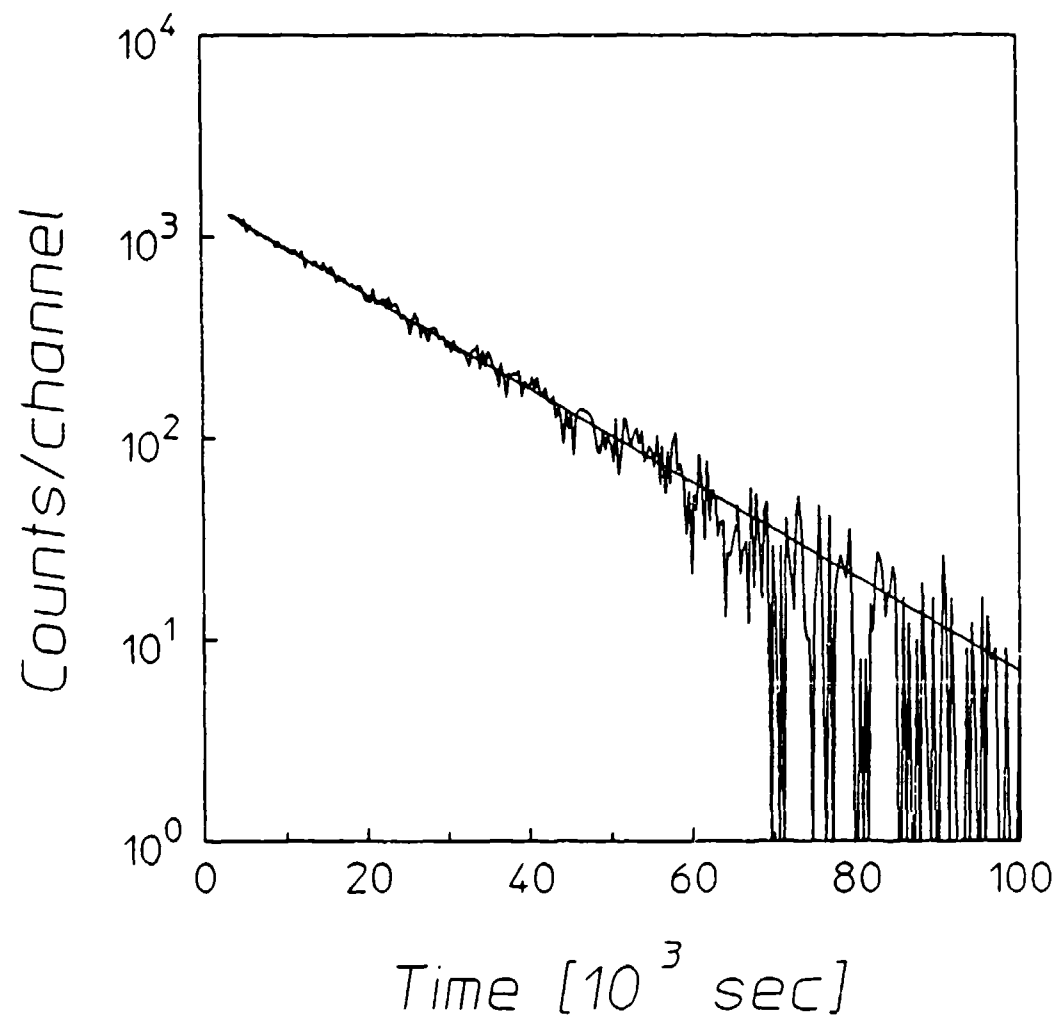
Figure 5: Decay spectrum for trial 2. The thermoluminescence contribution was removed by quenching the bottle in hot water before counting. The reduced intensity of this data set compared to Trials 1 and 3 was traced to suspended debris in the counting solution. The line fitted to the curve corresponds to a half-life of 3.58 h.
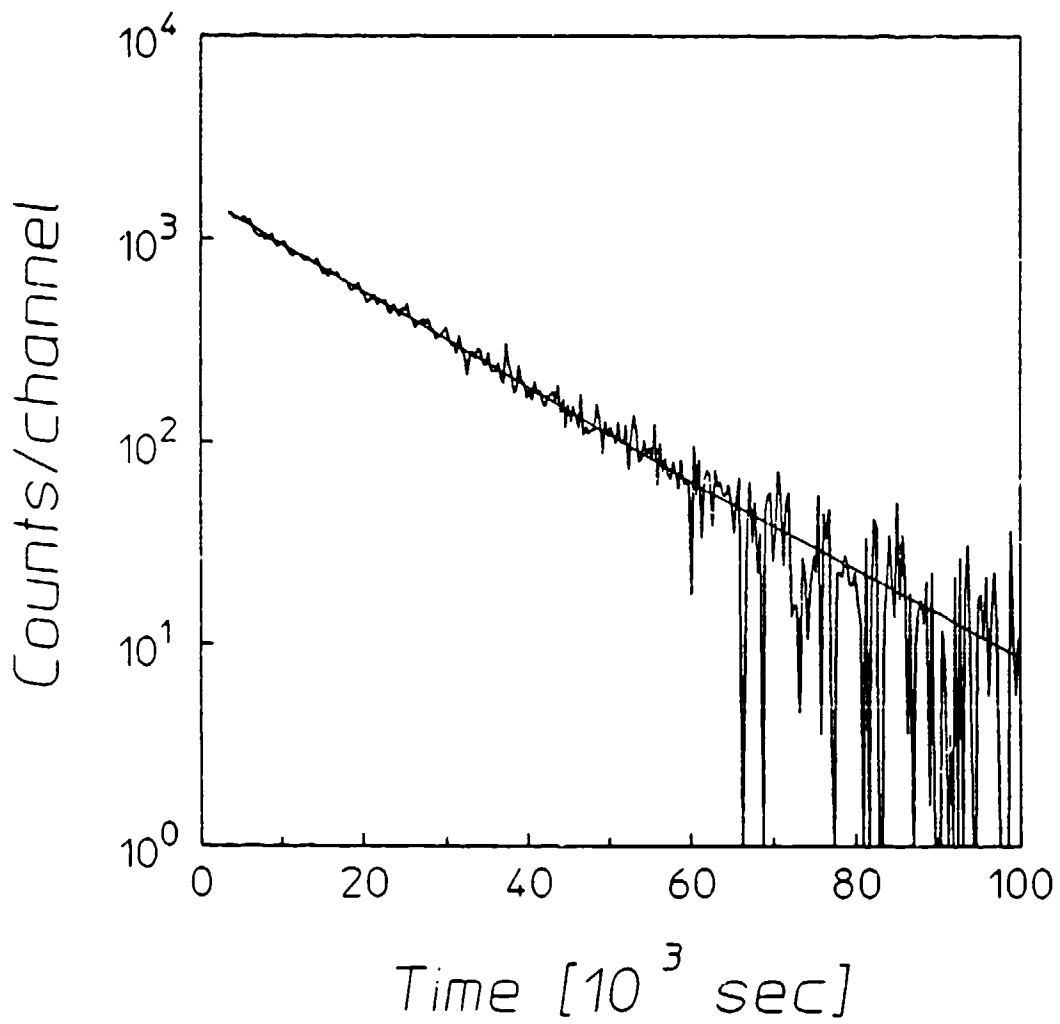
Figure 6: Decay spectrum for trial 3. The thermoluminescence contribution was removed by transferring the counting solution to an unirradiated bottle. The half-life of the fitted curve is 3.57 h.

The fits to the experimental data for the number of net counts in a channel, C, were of the form

$$C = (C_{obs} - C_{bkg}) = C_o e^{-\lambda t} \qquad , \qquad (3)$$

where C_{obs} is the number of counts observed in a channel of the multi-channel scaler spectrum and C_{bkg} is the number of counts in the channel due to background. In Eq. (3), the number of counts per channel immediately after the irradiation, C_o, and the decay constant, λ, are

the fitted parameters. The decay constant is related to the half-life, $T_{1/2}$, by $\lambda = \ln(2)/T_{1/2}$. The net activity, A_o, for the sample at the end of the irradiation can then be obtained from

$$A_o = \frac{C_o}{\eta f t_d} \quad . \tag{4}$$

where η is the efficiency of the counter, f is the branching ratio for the beta decay (100% in this case), and t_d is the dwell time for the MCS spectrum. By using the general relationship between the activity of a sample and the number of radioactive nuclei in it, one can calculate the number of excited nuclei in the sample at the end of the irradiation, $N_{e,o}$, from

$$N_{e,o} = \frac{A_o}{\lambda} \quad . \tag{5}$$

Finally, the total number of excitations induced by the exposure, N_e, will be somewhat larger than this because of decays which occurred during the irradiation. The correction takes the form

$$N_e = N_{e,o} \times \frac{\lambda t_e}{(1 - e^{-(\lambda t_e)})} \quad , \tag{6}$$

where t_e is the exposure period.

The integrated cross section, $\sigma\Gamma$, is related to the number of excited nuclei by

$$\sigma\Gamma = \frac{N_e}{N_T \phi(E) t_e} \quad , \tag{7}$$

where N_T is the number of target nuclei in the sample and $\phi(E)$ is the photon flux, expressed in photons/(cm^2-keV-s) at the energy of the gateway state. In this expression, $\phi(E) t_e$ has replaced the integrated photon flux Φ appearing in Eq. (1). As noted above, the energy of the gateway state (or states) is unknown in this case. Therefore, a single gateway will be assumed and the results will be presented in the form of a plot of cross section as a function of the possible values of this

gateway state. For the purpose of initially calculating the cross sections, the flux at an assumed gateway of 2.125 MeV will be used; the cross sections at other energies are obtained by multiplying this by a factor expressing the relative intensities shown in Fig. 1.

The fits to the experimental data of Figs. 4 and 6 yielded values for C_o of 3022 and 1619 counts. Use of the fitted values for λ and the appropriate efficiencies and exposure times indicated that 1.48×10^6 and 8.96×10^5 excited nuclei were produced in trials 1 and 3. trial 2 was not considered in this analysis because of the sample contamination problem discussed above. One further correction, not discussed above, is required to account for interferences from neutron capture processes that populate the isomeric state through the reaction $^{175}Lu(n,\gamma)^{176}Lu^m$. The natural abundance of the parent species in this reaction is 97.41%. In a previous study[1], the thermal and epithermal neutron fluxes at the sample position were found to be $\phi_{therm} = 12$ n/(cm^2-s) and $\phi_{epi} = 6$ n/(cm^2-s). Using these fluxes and the cross sections for populating the isomer through the capture process ($\sigma_{therm} = 16$ barns and $\sigma_{epi} = 550$ barns)[15], the number of excited nuclei produced by neutron capture, $N_{e,n}$, can be calculated from

$$N_{e,n} = N_{T'}[\phi_{therm}\sigma_{therm} + \phi_{epi}\sigma_{epi}]t_e \qquad , \qquad (8)$$

where $N_{T'}$ is the number of ^{175}Lu nuclei in the sample. Before the photoactivation cross sections were calculated, the neutron contamination from this source was subtracted from the values of N_e cited above . Because of the large epithermal cross section and the high natural abundance of the parent nuclide, the neutron capture contribution is considerably larger than those seen in the previous study. It amounts to approximately 5% of the total number of excited nuclei observed in these experiments.

At a distance of 63.7 cm from the x ray source, the photon intensity at 2.125 MeV was 5.94×10^6 photons/(cm^2-keV-s). From this intensity, integrated cross sections of 39.9×10^{-26} and 42.2×10^{-26} cm^2-keV were calculated using the corrected values for the number of excited nuclei produced in trials 1 and 3. The average of these two measurements,

$$[\sigma\Gamma](E = 2.125 \text{ MeV}) = 41.0 \times 10^{-26} \text{ cm}^2\text{-keV} \qquad , \qquad (9)$$

is taken to be the experimental result for the cross section for an assumed gateway at 2.125 MeV. A plot of integrated cross section vs. the energy of the hypothetical single gateway state is shown in Fig. 7.
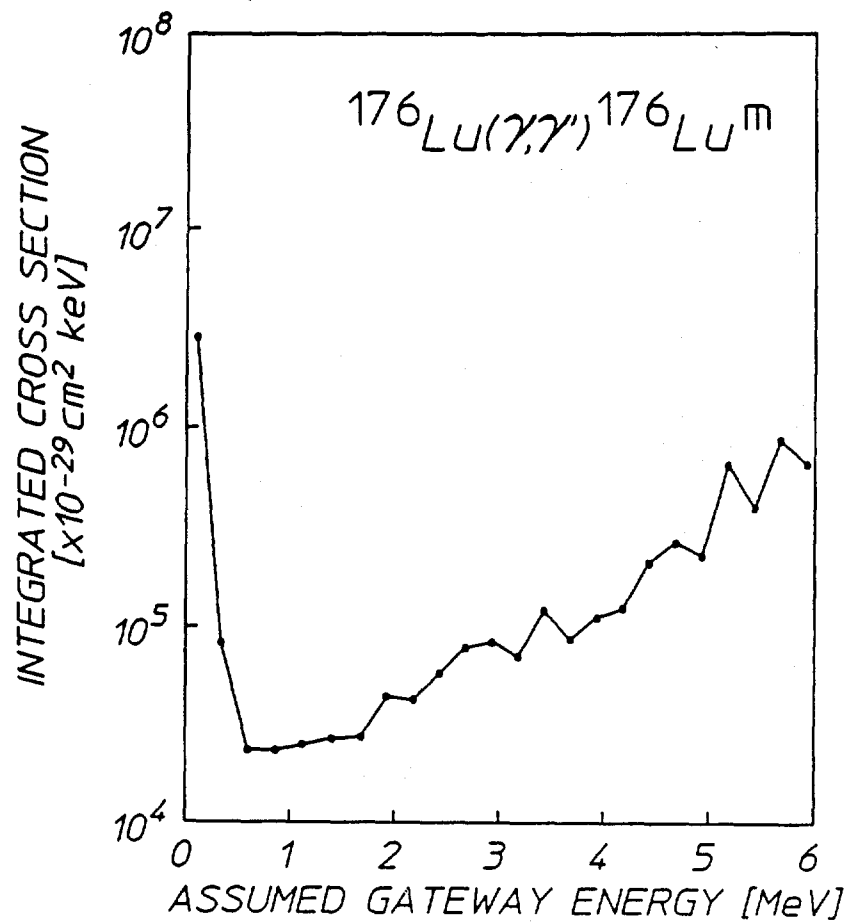
Figure 7. Integrated cross section for the reaction $^{176}Lu(\gamma,\gamma')^{176}Lu^m$ as a function of the assumed gateway energy.

Discussion

The cross section we have obtained for the process $^{176}Lu(\gamma,\gamma')^{176}Lu^m$ is comparable to those obtained for other materials[1] in this region of the nuclide chart. Assuming for the sake of comparison that the gateway energies are all about 2.125 MeV, the value given above is commensurate with those obtained for ^{167}Er ($\sigma\Gamma$ = 43 × 10^{-26} cm²-keV), ^{179}Hf ($\sigma\Gamma$ = 31 × 10^{-26} cm²-keV), $^{180}Ta^m$ ($\sigma\Gamma$ = 49 × 10^{-26} cm²-keV), ^{191}Ir ($\sigma\Gamma$ = 41 × 10^{-26} cm²-keV), ^{195}Pt ($\sigma\Gamma$ = 21 × 10^{-26} cm²-keV), and ^{197}Au ($\sigma\Gamma$ = 15 × 10^{-26}

cm^2-keV). Only two of the materials tested in this mass region have exhibited substantially lower cross sections under the assumption of a 2.125 MeV gateway, these being ^{183}W ($\sigma\Gamma = 2 \times 10^{-26}$ cm^2-keV) and ^{199}Hg ($\sigma\Gamma = 2 \times 10^{-26}$ cm^2-keV).

Although the contributions of neutron capture processes were included in the analysis above, interferences due to inelastic neutron scattering have not been considered. The cross section σ_{fast} for the ^{176}Lu(n,n')^{176}Lu^m reaction was not available in the barn book (BNL 325),[16] probably because of the low natural abundance of ^{176}Lu. However, if the assumption is made that the observed activation was entirely due to inelastic neutron scattering, the cross section required for the scattering process can be calculated from the relation

$$N_{e,fast} = N_T \phi_{fast} \sigma_{fast} c_e \qquad , \qquad (10)$$

where ϕ_{fast} is the fast neutron flux. In the previous study of neutron effects,[1] it was estimated that the total fast neutron flux at the sample location was about 900 n/(cm^2-s). Using this estimate, one obtains a value of approximately 2800 barns for σ_{fast}. This is three to four orders of magnitude greater than typical values of cross sections for inelastic neutron scattering, which are normally in the range of several hundred millibarns. On the basis of this result, it appears unlikely that inelastic neutron scattering plays a role in the phenomena examined here.

Conclusions

The large photoactivation cross section obtained for ^{176}Lu in the 1-6 MeV range is consistent with the empirical trend noted for other nuclides in the island of high-mass isomers lying near A = 180. Determination of the nature and location of the gateways responsible for this phenomena will require some form of energy selective x-ray source. As in previous experiments, interferences due to neutron reactions appear to play a minor role in activating the sample.

References

1. J. A. Anderson, C. D. Eberhard, J. J. Carroll, M. J. Byrd, C. B. Collins, E. Scarbrough, and P. P. Antich, "Limits on Neutron Activation Interferences in Photoactivation Cross Section Measurements in the 1.5-6 MeV Range," in Center for Quantum Electronics Report #GRL/8801, University of Texas at Dallas, 1988 (unpublished), pp. 43-72.

2. C. B. Collins, C. D. Eberhard, J. W. Glesener, and J. A. Anderson, Rapid Communications, Phys. Rev. C 37, 2267 (1988).

3. C. B. Collins, J. A. Anderson, C. D. Eberhard, J. F. McCoy, J. J. Carroll, E. C. Scarbrough, and P. P. Antich, "Large Changes of Angular Momenta Pumped by Bremsstrahlung in Selected Nuclei," in Center for Quantum Electronics Report #GRL/8703, University of Texas at Dallas, 1987 (unpublished), pp. 37-56.

4. J. A. Anderson, C. D. Eberhard, J. F. McCoy, K. N. Taylor, J. J. Carroll, M. J. Byrd, C. B. Collins, E. C. Scarbrough, and P. P. Antich, "Photoactivation of Short-Lived Isomers with Bremsstrahlung Radiation from a Medical Linear Accelerator," in Center for Quantum Electronics Report #GRL/8704, University of Texas at Dallas, 1988 (unpublished), pp. 11-35.

5. E. B. Norman, T. Bertram, S. E. Kellogg, S. Gil, and P. Wong, Astrophys. J. 291, 834 (1985).

6. M. A. Gardner, D. G. Gardner, and R. W. Hoff, in Capture Gamma-ray Spectroscopy 1987, Inst. Phys. Conf. Ser. No. 88/J. Phys. G: Nucl. Phys. 14 Suppl., S315 (1987).

7. H. Beer and F. Keppeler, Phys. Rev C 21, 534 (1980).

8. J. J. Carroll, J. A. Anderson, J. W. Glesener, C. D. Eberhard, and C. B. Collins, "Accelerated Decay of $^{180}Ta^m$ and ^{176}Lu in Stellar Interiors Through (γ, γ') Reactions," in Center for Quantum Electronics Report #GRL/8803, University of Texas at Dallas, 1989 (unpublished).

9. K. Han, D. Ballon, C. Chui, and R. Mohan, Med. Phys. 14, 414 (1987).

10. R. Mohan, C. Chui, and L. Lidofsky, Med. Phys. 12, 93 (1987).

11. Table of Isotopes, Seventh Edition, Eds. C. M. Lederer and V. S Shirley (Wiley-Interscience, New York, 1978).

12. G. F. Knoll, Radiation Detection and Measurement (John Wiley & Sons, New York, 1979) pg. 746.

13. B. D. Sowerby, Nucl. Instrum. and Meth. 97, 145 (1971).

14. J. K. Tuli, Nuclear Wallet Cards (National Nuclear Data Center, Brookhaven National Laboratory, 1985).

15. F. W. Walker, K. G. Miller, and F. Feiner, Eds., Chart of the Nuclides, Thirteenth Edition (General Electric Company, San Jose, California, 1983).

16. D. I. Garber and R. R. Kinsey, Eds., Neutron Cross Sections, Volume II: Curves, National Neutron Cross Section Center, Brookhaven National Laboratory, Publication BNL 325.

ACCELERATED DECAY OF ^{180}Ta^{m} AND ^{176}Lu IN STELLAR INTERIORS THROUGH (γ,γ') REACTIONS

by J. J. Carroll, J. A. Anderson, J. W. Glesener, C. D. Eberhard, and C. B. Collins
Center for Quantum Electronics, University of Texas at Dallas

Introduction

The study of naturally occurring radioactive isotopes such as ^{176}Lu and ^{180}Ta has become increasingly important to the astrophysical community since these species have been envisioned as stellar chronometers. Provided the mechanisms of nucleosynthesis are sufficiently understood, the creation of these types of nuclei can be dated from their predicted initial abundance, their presently observed abundance and their half-lives.

The analysis for ^{176}Lu and ^{180}Ta is complicated by the fact that each possesses an isomer. In these cases stellar nucleosynthesis may branch to both the ground state and the isomer, providing a different initial population in each state than would result were only a single level present. This branching is critical to the observation of ^{180}Ta^{m}, nature's rarest stable isotope,[1] because the isomer ($T_{1/2} \geq 1.2 \times 10^{15}$ years) is the surviving state rather than the shorter lived ground state ($T_{1/2} = 8.152$ hours).

The presence of an isomer produces an additional effect when the excited nucleus can undergo transmutation without first decaying radiatively to the ground state. If there is a sufficiently strong channel for the transfer of a population of nuclei between the ground state and the isomer, the effective half-lives of the states will be drastically different in the stellar environment than those measured in the laboratory. Processes which may provide such a channel include photoexcitation, positron annihilation excitation, inelastic neutron

scattering and Coulomb excitation. In particular, for ^{176}Lu and ^{180}Ta, photoexcitation through (γ,γ') reactions has been investigated.[2,3]

Critical early works[2,3] described experiments in which samples containing naturally abundant lutetium and tantalum were irradiated with medical ^{137}Cs and ^{60}Co sources. Following exposure, the x-ray spectra of the samples were examined for signatures of the decays of ^{176}Lu^m and ^{180}Ta. No activation of the tantalum sample was in evidence but some activation of the lutetium sample was observed. In order to calculate the reaction cross section for ^{176}Lu from the observed activation and to estimate an upper bound on the cross section for ^{180}Ta^m, it was assumed that the reactions were non-resonant, threshold processes in keeping with conclusions from previous experiments[4,5] on ^{115}In and ^{111}Cd. The irradiating spectrum was therefore integrated above the assumed threshold and the large number of available photons resulted in the report of small values for the cross sections. The absence of larger cross sections was then used to imply the usefulness of ^{176}Lu and ^{180}Ta^m nuclei as stellar chronometers.

In contrast to earlier work, the most recent studies of the reactions ^{115}In$(\gamma,\gamma')^{115}$In^m and ^{111}Cd$(\gamma,\gamma')^{111}$Cd^m have shown no evidence for the appearance of non-resonant effects.[6,7,8,9] Instead it was reported that previous evidence for threshold processes could be attributed to departures of the experimental photon sources from expectations. Evidently (γ,γ') reactions proceed through relatively narrow resonant "gateway" levels rather than through non-resonant excitation. In this context, the most recent measurements[10,11] of the cross sections for the reactions ^{176}Lu$(\gamma,\gamma')^{176}$Lu^m and ^{180}Ta$^m(\gamma,\gamma')^{180}$Ta make possible a reevaluation of the degree to which these nuclei are useful as stellar chronometers.

Experimental Detail and Analysis

A set of experiments was performed by exposing lutetium and tantalum samples to the bremsstrahlung from a Varian Clinac 1800 medical linear accelerator operating in a 6 MeV mode. An enriched tantalum sample containing 1.3 mg of ^{180}Ta^m in 24.7 mg of ^{181}Ta was used. The

tantalum was deposited as a dusting of oxide near the center of a 5 cm square plate of aluminum. This sample composition was chosen in order to minimize the self-absorption of fluorescent x-rays. Following irradiation, the sample was transported to an N-type HPGe spectrometer system for counting. As the ground and isomeric states of ^{180}Ta decay by β^- emission and electron capture, as shown by the partial decay level diagram of Fig. 1(a), the 4096-channel pulse-height spectra contained x-ray peaks emitted from the daughter nucleus ^{180}Hf. The identities of the observed photopeaks were verified by their energies and counting rate decays. A typical spectrum for the tantalum sample showing the ^{180}Hf K_α and K_β peaks is given in Fig. 2.
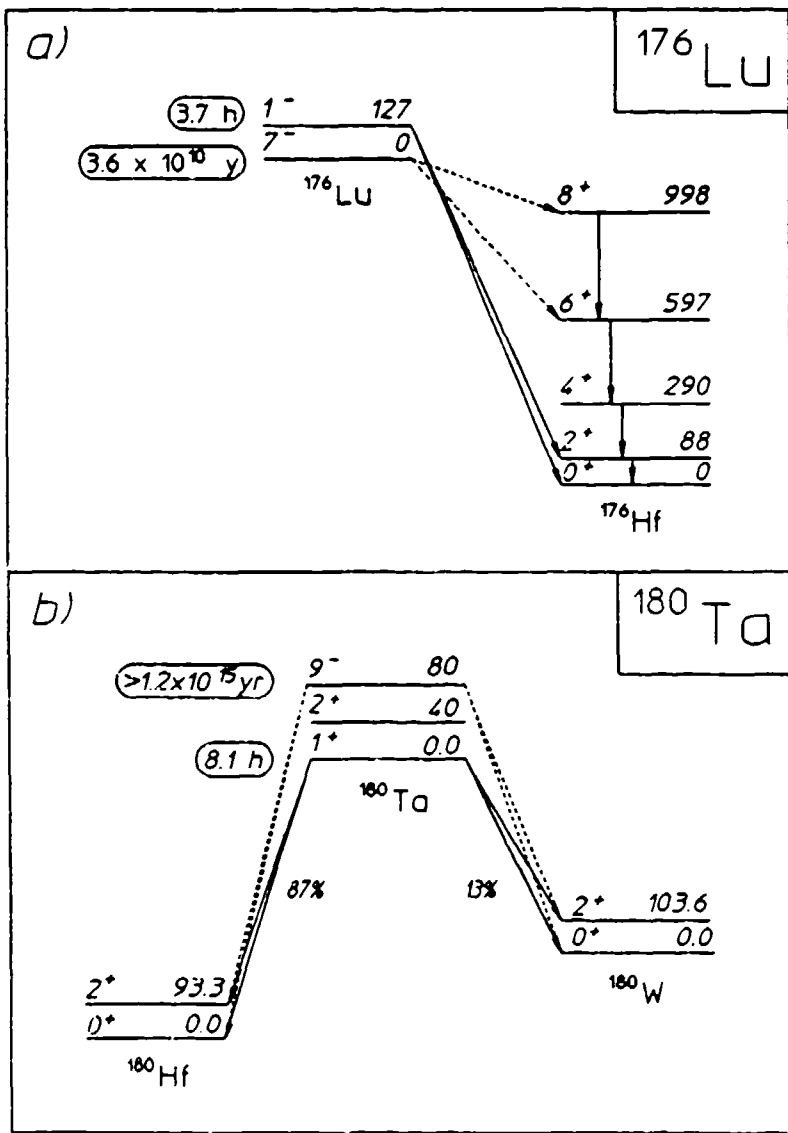
Figure 1: Partial decay level diagrams of a) [176]Lu and b) [180]Ta depicting parent and daughter nuclei. Half-lives are shown in ovals to the left of the ground and isomeric levels. The nuclear spins, parities, and energies in keV of each state is given. β^- decays are shown by diagonal arrows on the right of the parent levels and electron capture decays are shown by diagonal arrows on the left.
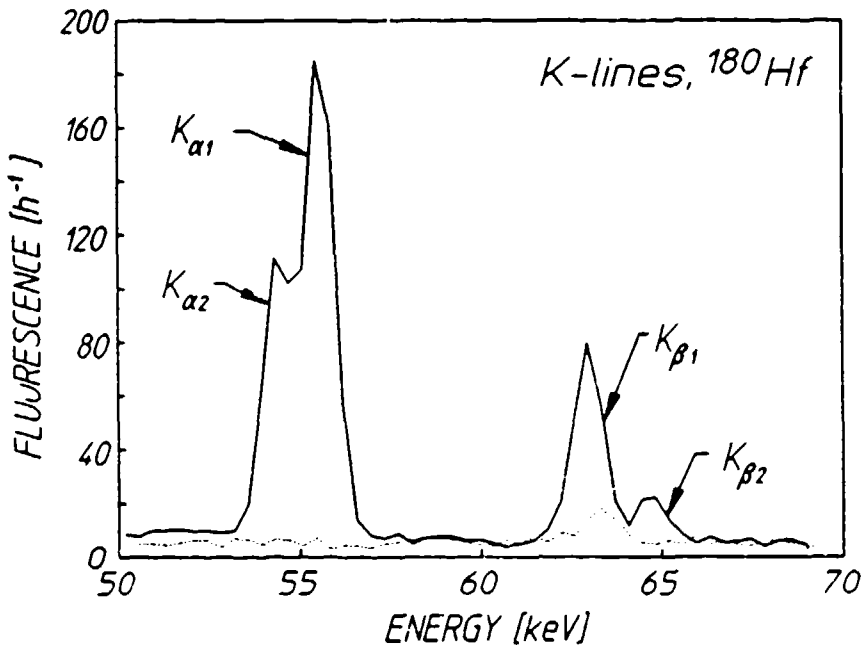
Figure 2: Dotted and solid curves show, respectively, the spectra obtained before and after irradiation of a tantalum sample containing ^{180}Ta enriched to 5%. An HPGe detector was used to obtain the spectra. The feature at 63 keV is due to traces of natural activity in the counting shield. The solid curve shows activity resulting from the transmutation of ^{180}Ta ground state nuclei measured in the sample following irradiation. The prominent additions are the ^{180}Hf K_α and K_β x-ray lines resulting from electron capture in the ^{180}Ta.

Each lutetium sample consisted of approximately 5 g of LuCl$_3$ dissolved in distilled water to make about 20 ml of solution contained within a polyethylene scintillation bottle. The samples were fashioned in this way in order to employ an alternate detection scheme which was better suited to the examination of ^{176}Lu. The ground state of ^{176}Lu β^- decays with an endpoint energy of 565 keV and the isomer with endpoint energies of 1313 keV (39.6%) and 1225 keV (60.4%), as depicted in the partial decay level diagram of Fig. 1(b). Since these nuclei were suspended in solution, the particles emitted in these decays produced Cerenkov radiation in the water with efficiencies dependent on the

differences in the particle energies and the Cerenkov threshold energy at about 250 keV.

In these experiments the efficiency for production of Cerenkov radiation from isomeric decays was over 10 times larger than that from ground state decays. This made possible an accurate measurement of the number of isomeric decays, and thus of isomeric production from the ground state, by counting the Cerenkov events with a detector consisting of two RCA 8850 photomultiplier tubes in EG & G 9201 bases. The tubes were operated in a coincidence mode by connecting the time synchronized outputs through a 150 MHz Phillips 755 logic unit. This insured that only events detected in coincidence by both tubes were counted, improving the signal to noise ratio. Then, the number of coincident counts as a function of time was stored as a 4096 channel MCS spectra with a 40 sec dwell time. A typical spectrum is shown in Fig. 3. The counter was calibrated with a $^{40}KCl_3$ solution of known activity which emitted β^- particles having roughly the same endpoint energy as $^{176}Lu^m$.
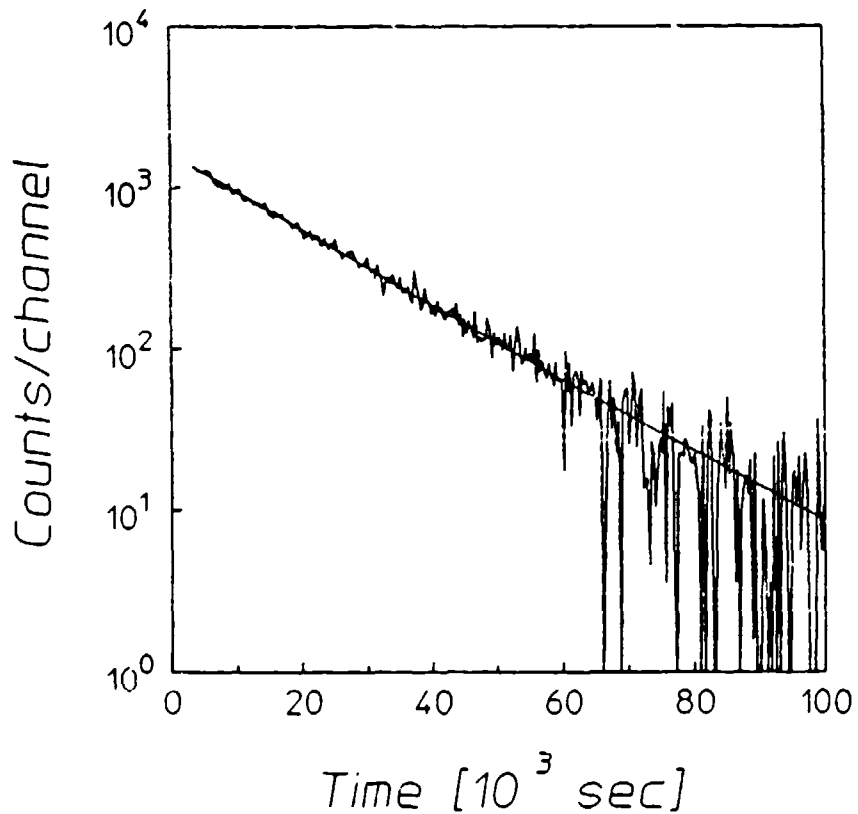
*Figure 3: A typical decay spectrum from a lute-
tium sample following a 40-minute irradiation.
Each channel represents an interval of 320 sec.
The solid line indicates a fit to the data which
gives a half-life for $^{176}Lu^m$ of 3.58 ± .05 h; the
literature value is 3.68 hours.*

The rate of excitation of nuclei, $dN_{excited}/dt$ was determined for
each sample from the observed photopeak counts for the pulse height
spectra and from the decay of the counting rate for the coincidence
spectra.   These were corrected for self-absorption of fluorescent
photons, detector efficiency, signature photon or β^- decay intensity and
finite times for counting, transport and irradiation.   From the view-
point of photoexcitation through resonant gateways, the excitation rate
is given by

$$\frac{dN_{excited}}{dt} = N_T \sum_i (\sigma\Gamma)_i \Phi(E_i) \quad , \tag{1}$$

where N_T is the number of target nuclei in the sample, $\Phi(E_i)$ is the incident photon flux in photons/cm^2-keV-sec at the gateway energy E_i, and $(\sigma\Gamma)_i$ is the integrated cross section in cm^2-keV,

$$(\sigma\Gamma)_i = \int \sigma_i(E)\ dE \qquad . \qquad\qquad (2)$$

The quantity Γ_i represents the natural width of the ith gateway state, given by $\Gamma_i \geq \hbar/\tau_i$ where τ_i is the lifetime of the state. Determinations of the integrated cross sections depend primarily on knowledge of the E_i since the output of the linac is well characterized.[12,13] The relative spectral intensity normalized to unit total flux for the linac operating in the 6 MeV mode is shown in Fig. 4.
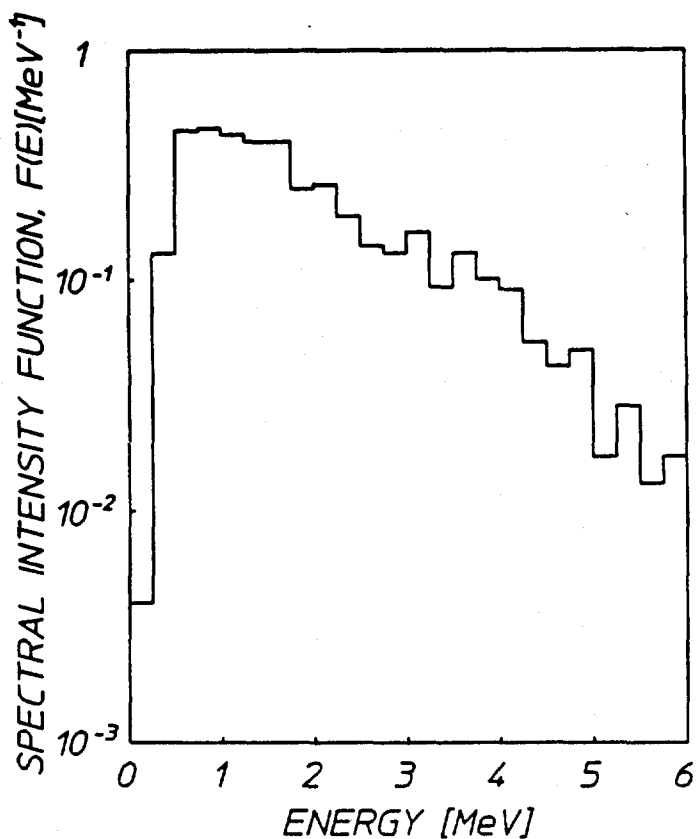
Figure 4: Relative spectral intensities of the bremsstrahlung from the Varian Clinac 1800 used in these experiments. The function $F[MeV^{-1}]$ is normalized to the total delivered flux, which for linac operation in the 6 MeV mode at 300 Hz is 2.28×10^7 photons/cm^2-keV-sec at a distance of 63.7 cm from the x-ray source.

The fixed endpoint of the linac did not allow the gateways to be located. However, by assuming the excitation proceeds through a single gateway state, cross sections were found as functions of the possible gateway energies. Previous examinations[14,15,16] of known nuclear states have indicated that the lowest likely gateway states lie at about 1 MeV for ^{176}Lu and about 750 keV for ^{180}Ta^m. Consistent with these suggestions, the cross sections for ^{176}Lu and ^{180}Ta^m are shown in Figure 5. The gateway energies indicated by the data points are located at the centers

of energy bins corresponding to mesh points at which intensities are available from published linac spectra.
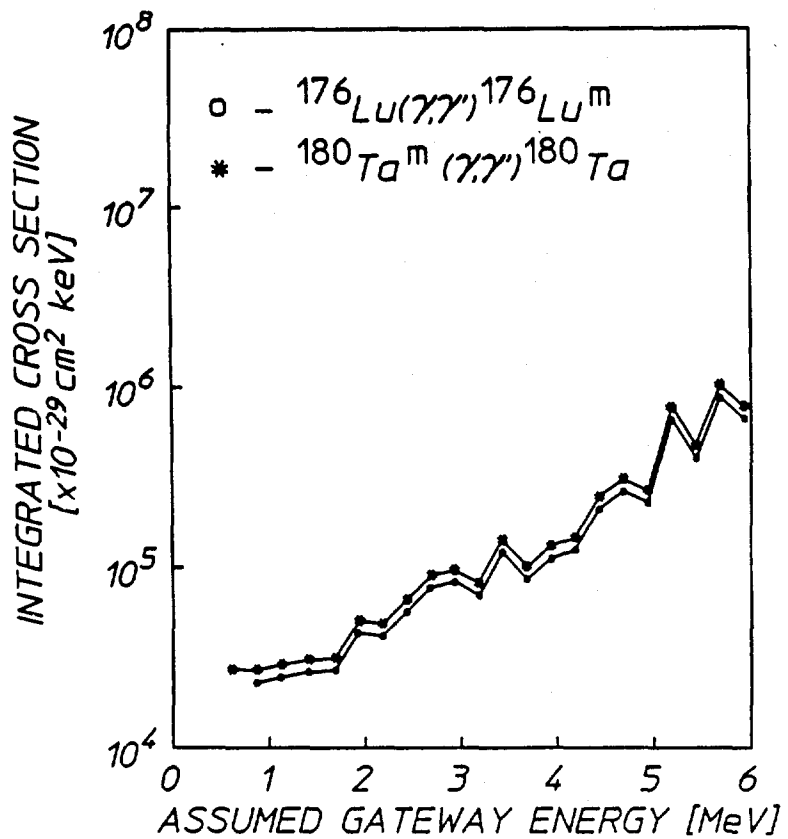
Figure 5: Integrated cross sections for the reactions $^{176}Lu(\gamma,\gamma')^{176}Lu^m$ and $^{180}Ta^m(\gamma,\gamma')^{180}Ta$, each plotted as a function of the energies at which a single gateway state could be assumed.

It is difficult to directly compare the results of Fig. 5 with the cross sections of Refs. 2 and 3 since the irradiating spectra used in those experiments are not known. However, as a point of contact between the two approaches, for $^{180}Ta^m$ a single resonant gateway at 750 keV would correspond to an integrated cross section of 27700×10^{-29} cm²-keV while a non-resonant process with a threshold at 750 keV would have a cross section of 148 μbarns. This is more than 3 orders of magnitude larger than the cross section reported in Ref. 3.

Effective Half-Life of ^{176}Lu

The ground and isomeric states of ^{176}Lu can be considered to comprise two components of a coupled system of populations governed by the standard rate equations for radioactive decay. For the ground and metastable populations N_0 and N_1, these are

$$\frac{dN_1}{dt} = -(R_1 + R_{10})N_1 + R_{01}N_0 \qquad , \qquad (3)$$

and

$$\frac{dN_0}{dt} = -(R_0 + R_{01})N_0 + R_{10}N_1 \qquad . \qquad (4)$$

The quantities R_0 and R_1 are the radioactive decay rates for these states, taken from laboratory values for the half-lives, $(T_{1/2})_0 \geq 3.59 \times 10^{10}$ years and $(T_{1/2})_1 = 3.635$ hours. The R_{01} and R_{10} are the total transfer probability rates from ground to isomer and from isomer to ground states through (γ, γ') reactions.

The rate for excitation to the isomer through a single gateway is found by recognizing that $R_{01} = N_T^{-1} \cdot dN_{excited}/dt$, where N_T is the number of target nuclei. Eq. (1) then gives

$$R_{01} = (\sigma_{01}\Gamma) \, \Phi(E_{01}) \qquad , \qquad (5)$$

where E_{01} is the gateway energy relative to the ground state and the width of the gateway has been assumed to be sufficiently narrow so that the flux may be considered as constant over the gateway. Employing the Plank distribution to represent the stellar interior at temperature T,

$$\Phi(E_{01}) = \frac{8\pi E_{01}^2}{h^3 c^2} \, [\exp(E_{01}/kT) + 1]^{-1} \qquad . \qquad (6)$$

Thus, in terms of the experimentally measured integrated cross section,

$$R_{01} = \frac{8\pi}{h^3 c^2} \, (\sigma_{01}\Gamma) \, E_{01}^2 \, [\exp(E_{01}/kT) + 1]^{-1} \qquad . \qquad (7)$$

The rate for the inverse reaction is found by considering the question of thermal equilibrium. If it were possible for both states to come into equilibrium with the photon bath, the net photoexcitation rate would vanish,

$$\left(\frac{dN_1}{dt} + R_1 N_1\right)_{eq.} = 0 \qquad .\qquad (8)$$

This indicates that as a function of the ground and isomeric state angular momenta J_0 and J_1 and the energy of the isomer relative to the ground state, E_1, the ratio of populations would become,

$$\left(\frac{N_1}{N_0}\right)_{eq.} = \frac{R_{01}}{R_{10}} = \frac{2J_1 + 1}{2J_0 + 1} \exp(-E_1/kT) \qquad .\qquad (9)$$

For the ^{176}Lu isotope, $J_0 = 7$, $J_1 = 1$ and the isomer energy is $E_1 = 126$ keV. Then, the solution to the rate Eqs. (2) and (3) is given by,

$$\frac{N_1}{N_0}(t) = \frac{a + b \coth(bt/2)}{2R_{10}} \qquad ,\qquad (10)$$

where

$$a = R_0 + R_{01} - R_1 - R_{10} \qquad ,$$

and

$$b = \sqrt{a^2 + 4R_{01}R_{10}} \qquad .$$

The effective half-life of ^{176}Lu nuclei in the stellar environment is finally evaluated for this two level system from the expression,

$$(T_{1/2})_{eff} = \left[1 + \frac{N_0}{N_1} ((T_{1/2})_1) \right] (T_{1/2})_1 \qquad .\qquad (11)$$

Figure 6 shows the effective half-life as a function of temperature for several assumed gateway energies.
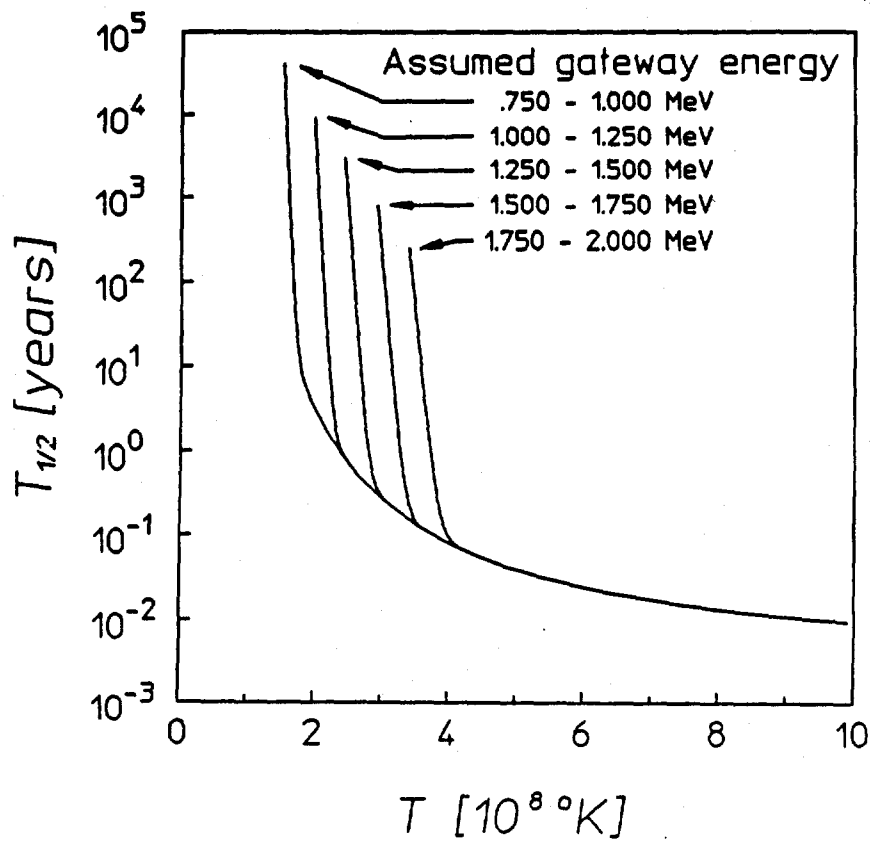
Figure 6: *Effective half-life of ^{176}Lu nuclei as a function of the temperature of the stellar environment in which it is immersed. The different curves are parametrized by assumed gateway energies lying in the indicated energy ranges.*

Effective Half-Life of ^{180}Ta

The possibility of decay of ^{180}Ta nuclei by electron capture introduces an additional temperature dependence. The half-life of the isomer is so long that an accurate result can be obtained by considering it to be temperature independent. However, the depletion of its electron shells at stellar temperatures will appreciably alter the half-life of the ground state. Detailed calculations of this effect have been made,[17] but the nuclear data that were used are now dated. Considering

the simpler problem of the depletion of the K shell only, the ground state half-life may be written as[18]

$$(T_{1/2})_0 = [(T_{1/2})_0]_{lab.} \ [b_{ec} \ r(T) + b_\beta]^{-1} \qquad , \qquad (12)$$

where $b_{ec} = .87$ and $b_\beta = .13$ are the branching ratios for the two decay modes. The ratio $r(T)$ of K shell occupancy at T to that as $T \rightarrow 0$ is given by

$$r(T) = [\exp(\mu - E_K/kT) + 1]^{-1} \qquad , \qquad (13)$$

where $E_K = 67.416$ keV is the K shell energy and μ is the fermion chemical potential,

$$e^\mu = \frac{2}{h^3 N_e} \ (2\pi m_e kT)^{3/2} \qquad , \qquad (14)$$

where N_e is the number density of electrons in pure He stellar matter, for which a typical value of 10^3 g/cm^3 is taken and m_e is the electron mass. The half-life of the ^{180}Ta ground state as a function of temperature is given in Figure 7
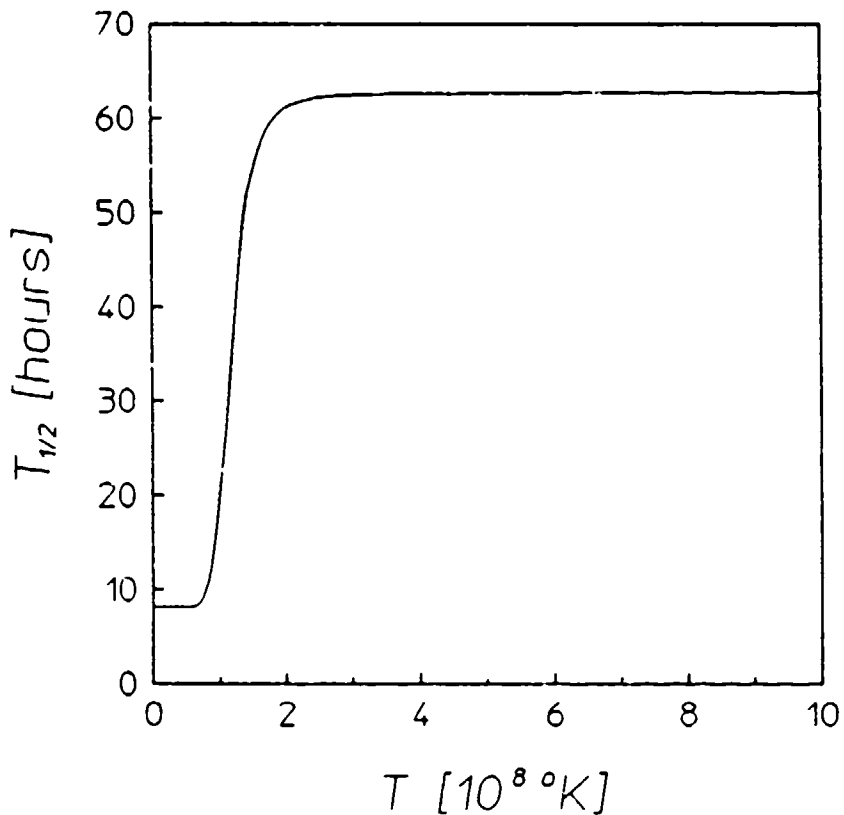
Figure 7: Half-life of ground state nuclei of ^{180}Ta as a function of temperature in the surrounding stellar environment. At temperatures above 2×10^8 °K, the K shell is completely depleted and the nuclei decay only through β^- emission.

With the inclusion of this mechanism, the previous analysis is used to determine the half-life of ^{180}Ta for which $J_0 = 7$, $J_1 \simeq 1$ and $E_1 = 127$ keV from

$$(T_{1/2})_{eff} = \left[1 + \frac{N_1}{N_0} \left((T_{1/2})_0 \right) \right] (T_{1/2})_0 \qquad . \qquad (15)$$

These results are displayed in Figure 8.

75
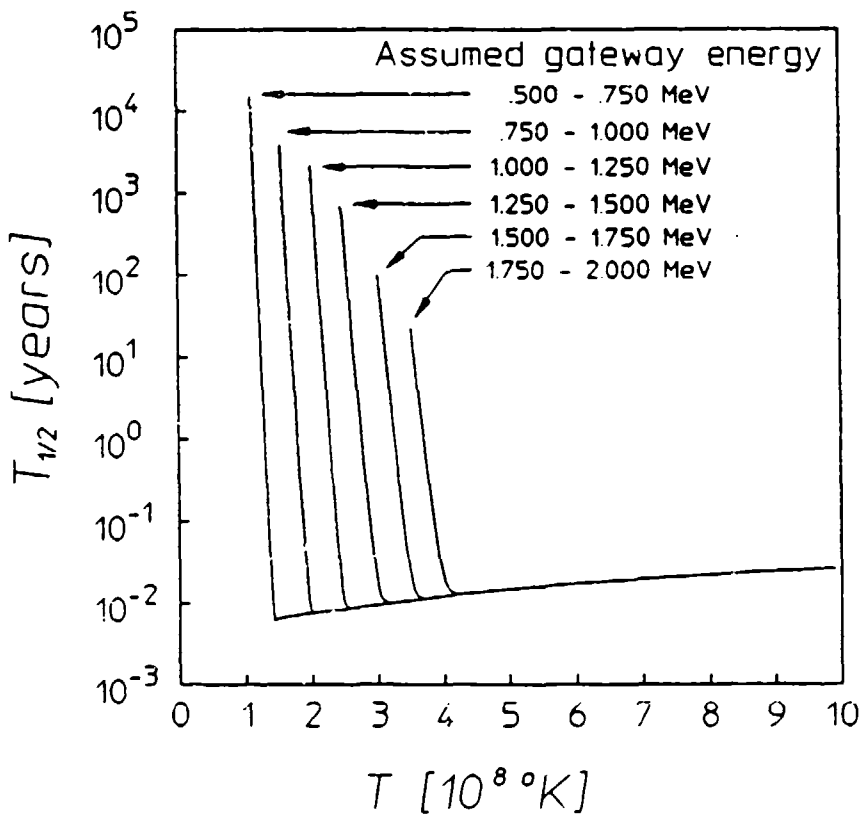
Figure 8:   Effective half-life of ^{180}Ta nuclei as a function of the temperature of the stellar environment in which it is immersed.   The different curves are parametrized by assumed gateway energies lying in the indicated energy ranges.

Discussion

An origin which is strictly s-process in character has been proposed[19,20] for ^{176}Lu and the appropriate neutron capture chain has been examined.[21,22]   This isotope is shielded from the r-process by ^{176}Yb, which is stable against β^- decay.   The s-process of stellar nucleosynthesis is thought to require temperatures of around 3.5×10^8 °K and to occur primarily in stable red giants,[23] possibly during thermal relaxation oscillations.[24]   Examination of Fig. 6 indicates that at this temperature at least partial equilibration of the ground state and isomer of ^{176}Lu will occur unless the gateway is located at an energy

above about 1.5 MeV. Should the gateway lie within the 1 - 1.25 MeV range as has been suggested, an s-process origin may still apply. However, the strong temperature dependence of the half-life would render ^{176}Lu useless as an s-process chronometer.

Many mechanisms have been suggested to be responsible for the production of ^{180}Ta though none have been firmly established.[25,26] Recently an s-process origin for ^{180}Ta has been suggested[27,28] and the necessary reactions demonstrated.[29] The rarity of ^{180}Ta^m was concluded to be a consequence of the fact that this nucleus lies aside the main path of cosmic nucleosynthesis.[30] Fig. 8 clearly shows again that equilibrium will occur at the canonical s-process temperature of 3.5×10^8 °K unless the gateway lies above 1.5 MeV. The discovery of a gateway laying below 1.5 MeV would then imply that ^{180}Ta could not be employed as an s-process chronometer. This could only be avoided if the s-process can proceed at temperatures below 1.5×10^8 °K.

These interesting results point to the importance of locating the participating gateways more precisely. This could be accomplished if a variable endpoint linac were available that was capable of delivering sufficient dosage. Indeed, should multiple gateways be found below 6 MeV the results of this analysis may be drastically altered. Also of importance is the more manageable problem of determining the linac spectrum for smaller bin sizes. Each curve in Figs. 6 and 8 must represent a range in possible gateway locations rather than simply one gateway energy. Smaller bin sizes would enable more exact examination of the temperatures at which equilibration becomes important for given gateway locations.

References

1. A. G. W. Cameron, <u>Essays in Nuclear Astrophysics</u>, edited by C. A. Barnes, D. D. Clayton, and D. N. Schramm (Cambridge Univ. Press, Cambridge, 1982), p. 23.

2. E. B. Norman, T. Bertram, S. E. Kellogg, S. Gil, and P. Wong, Ap. J. 291, 834 (1985).

3. E. B. Norman, S. E. Kellogg, T. Bertram, S. Gil, and P. Wong, Ap. J. 281, 360 (1984).

4. A. Ljubicic, K. Pisk, and B. A. Logan, Phys. Rev. C 23, 2238 (1982).

5. M. Krcmar, A. Ljubicic, K. Pisk, B. Logan, and M. Vrtar, Phys. Rev C 25, 2097 (1981).

6. K. Yoshihara, Zs. Nemeth, L. Lakosi, I. Pavlicsek, and A. Veres, Phys. Rev. C 33, 728 (1986).

7. I. Bikit, J. Slivka, I. V. Anicin, L. Marinkov, A. Rudic, and W. D. Hamilton, Phys. Rev. C 35, 1943 (1987).

8. C. B. Collins, J. A. Anderson, Y. Paiss, C. D. Eberhard, R. J. Peterson, and W. L. Hodge, Phys. Rev. C 38, 1852 (1988).

9. J. A. Anderson, M. J. Byrd, and C. B. Collins, Phys. Rev. C 38, 2838 (1988).

10. J. A. Anderson, K. N. Taylor, J. J. Carroll, M. J. Byrd, C. B. Collins, E. C. Scarbrough, and P. P. Antich, Center for Quantum Electronics Report #GRL/8803, University of Texas at Dallas, 1988 (unpublished).

11. C. B. Collins, C. D. Eberhard, J. W. Glesener, and J. A. Anderson, Phys. Rev. C 37, 2267 (1988)

12. R. Mohan, C. Chui and L. Lidofsky, Med. Phys. 12, 595 (1985).

13. N. C. Ikoro, D. A. Johnson, and P. P. Antich, Med. Phys. 14, 93 (1987).

14. R. A. Dewberry, R. K. Sheline, R. G. Lanier, L. G. Mann, and G. L. Struble, Phys. Rev. C 24, 1628 (1981).

15. O. A. Wasson and R. E. Chrien, Phys. Rev. C 2, 675 (1970).

16. E. Warde, R. Seltz, C. J. Costa, D. Magnac, and C. Gerardin, Phys. Rev. C 27, 98 (1983).

17. K. Takahashi and K. Yokoi, At. Data and Nuc. Data Tables 36, 375 (1987).

18. B. Stromgren, Zeits. fur Ap. 4, 118 (1932).

19. J. Audouze, W. A. Fowler, and D. N. Schramm, Nature 238, 8 (1972).

20. M. Arnould, Astr. Ap. 22, 311 (1973).

21. B. J. Allen, G. C. Lowenthal, and J. R. de Laeter, J. Phys. G 7, 1271 (1981).

22. H. Beer, F. Kappeler, K. Wisshak, and R. A. Ward, Ap. J. Suppl. 46, 295 (1981).

23. An Introduction to Nuclear Astrophysics, J. Audouze and S. Vauclair (D. Reidel Publishing Company, Boston, 1979).

24. Astrophysics, W. K. Rose (Holt, Rinehart, and Winston, Inc., New York 1973).

25. J. Audouze, Ast. Ap. 8, 436 (1970).

26. K. L. Hainebach, D. N. Schramm, and J. B. Blake, Ap. J. 205, 920 (1976).

27. H. Beer and R. A. Ward, Nature 291, 308 (1981).

28. K. Yokoi and K. Takahashi, Nature 305, 198 (1983).

29. S. E. Kellogg and E. B. Norman, Phys. Rev. C 31, 1505 (1985).

30. E. Runte, W. D. Schmidt-Ott, W. Eschner, I Rosner, R. Kirchner, O. Klepper, and K. Rykaczewski, Z. Phys. A 328, 119 (1987).

SPECTRAL CHARACTERIZATION OF INTENSE, SHORT DURATION BREMSSTRAHLUNG PULSES WITH NUCLEAR PHOTOACTIVATION TECHNIQUES

by J. A. Anderson, C. D. Eberhard, K. N. Taylor, J. M. Carroll,
J. J. Carroll, M. J. Byrd, and C. B. Collins
Center for Quantum Electronics, University of Texas at Dallas

Introduction

Pulsed power machines that generate high intensity x-ray pulses are often used to assess the radiation hardness of electronic components and systems but have also recently found application in research programs studying ultrashort wavelength (gamma-ray or x-ray) laser mechanisms. For this research, an accurate understanding of the bremsstrahlung spectrum emitted by the machine is necessary. This information can also be of interest to the nuclear simulation community if radiation hardness tests are required to mimic the average photon energy as well as the total dose and dose rate for the simulated operating environment. Unfortunately, the x-ray spectrum of such a device is difficult to determine and in practice is often estimated using Monte Carlo transport calculations in lieu of being experimentally measured. This paper discusses the use of resonant photonuclear activation as a simple experimental technique that can be used on a shot-by-shot basis to characterize these spectra.

A pulsed power bremsstrahlung generator can readily deliver doses of several tens of kRads in an x-ray pulse lasting less than 100 ns. Endpoint energies for the bremsstrahlung can range from near 1 MeV up to about 10 MeV. Because of the magnitude of energy expended in each pulse, practical devices built to deliver these doses can only fire a few times each day. This combination of high flux, high photon energy, and very low duty cycle presents a problem for conventional measurement techniques.[1] Energy dispersive methods using scintillators or solid state detectors are statistically limited by the small number of events that can be pulse height analyzed during an x-ray burst that lasts less than 100 ns and which can be repeated only after several hours. Standard techniques for wavelength dispersive x-ray spectroscopy with crystal spectrometers are practical only in the region below about 150

keV due to the range of available lattice spacings. Thus, neither of the two most commonly used tools for x-ray spectroscopy is well suited for characterizing these radiation pulses.

The sensitivity of absorption spectrometers,[2] which obtain a spectrum by deconvolving the responses of arrays of differently filtered dosimeters, is limited to the range where mass attenuation coefficients vary strongly with energy. This is well below 1 MeV. A second technique, that of photoneutron spectroscopy, suffers from the converse problem of being insensitive at low energies. At photon energies high enough to induce (γ, n) reactions, the resulting photoneutrons can be detected with activation foils, and this information can be used to deconvolve the incident x-ray flux. Unfortunately, there are only two materials with photoneutron thresholds E_n below 3 MeV, these being ^2H (E_n = 2.22 MeV) and ^9Be (E_n = 1.67 MeV); even if the energy range is extended to 6 MeV, only 8 isotopes are suitable for this application.[3] The photoneutron technique requires high photon fluxes and may also suffer from interferences in mixed radiation fields.

Another approach to characterizing bremsstrahlung pulses is to analyze the momentum of Compton scattered electrons emitted from a material illuminated by the x-ray pulse and from this information to deduce the spectrum of the incident radiation.[4] This approach is theoretically capable of dealing with a wide energy range, but it is complex and costly to implement.

The limitations of the techniques outlined above are graphically summarized in Fig. 1. Resonant nuclear photoactivation is a method which complements these techniques and which requires little in the way of specialized equipment. It may be the only practical approach in some applications.

82

Limitations {

Technique

Scintillation or Solid State Spectrometers

Crystal Spectrometer

Absorption Spectrometer

Photoneutron Detectors

Compton Electron Spectrometer

Photoactivation Detectors
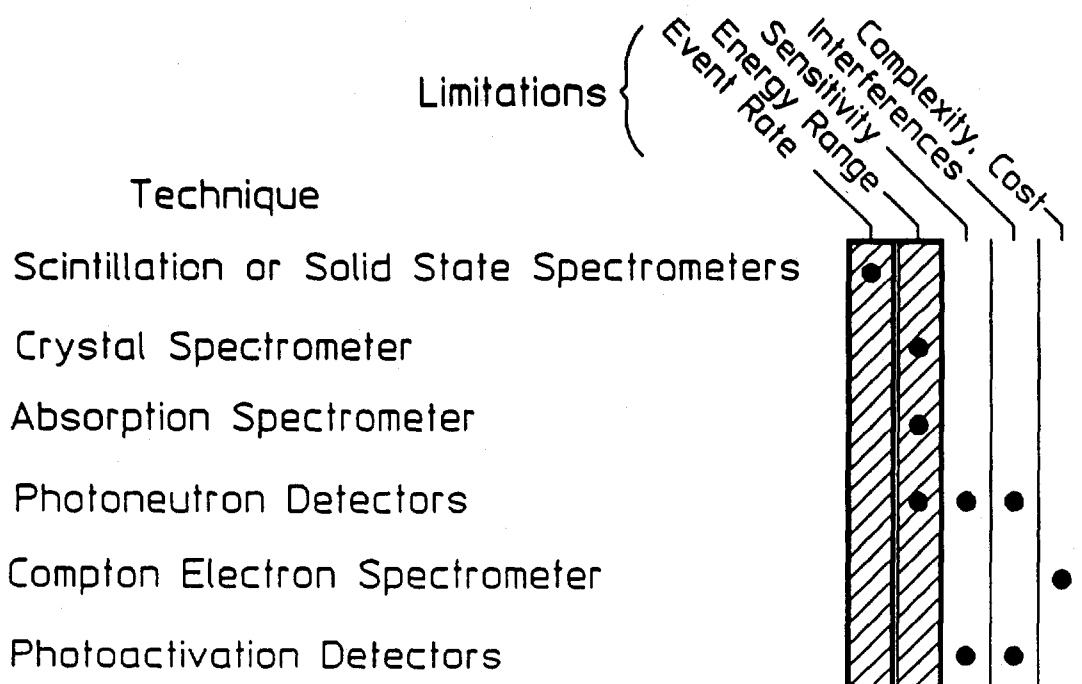
Figure 1: *Limitations of different measurement techniques for measuring short (< 100 ns), non-repetitive x-ray bursts. The shaded area includes major limitations that may exclude, in general, the use of a given method.*

Resonant Nuclear Photoactivation Detectors

Determining photon fluxes with resonant nuclear photoactivation of nuclear isomers is analogous to monitoring fast neutron fields with neutron activation foils, with one important difference: neutron activation foils are threshold detectors, but photoactivation monitors determine the photon flux in a narrow window at the resonance energy. The process is illustrated in Fig. 2. Incident photons excite the ground state to a short-lived intermediate, or gateway, state that promptly decays to form an isomer. The exposed sample can then be transported to a conventional counting system and the population of the isomeric state can be quantified. From this information and the value of the transfer cross section, the photon flux at the gateway energy can be obtained. If several materials with different gateway energies are available, the spectrum of the incident radiation can be deduced as shown in Fig. 3.
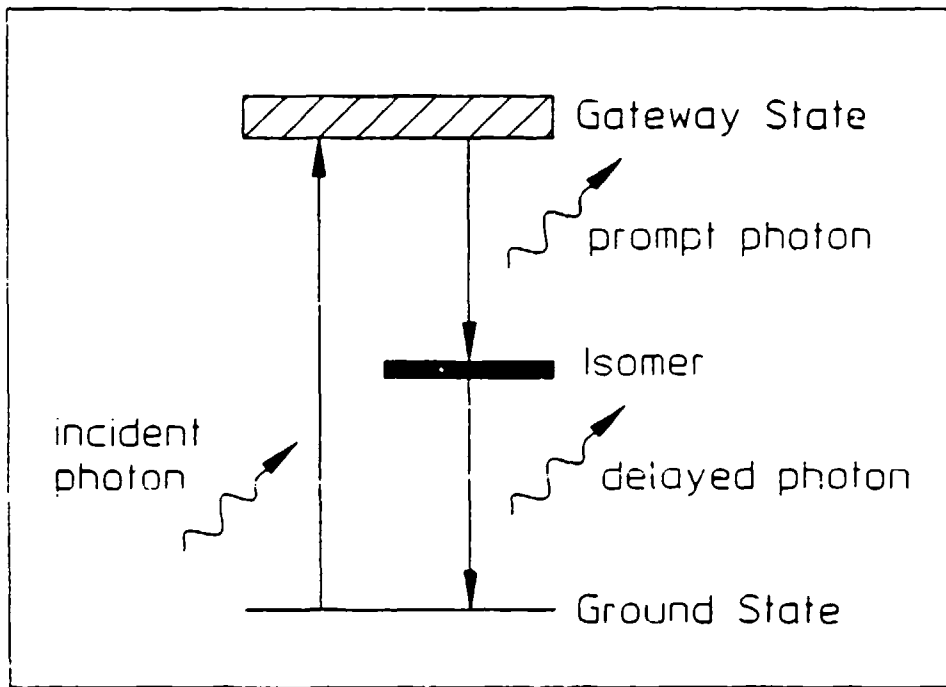
Figure 2: Mechanism of resonant photo-activation of nuclear isomeric states. Given the transfer cross section through the gate-way state, the number of delayed photons emitted can be used to determine the incident photon flux.
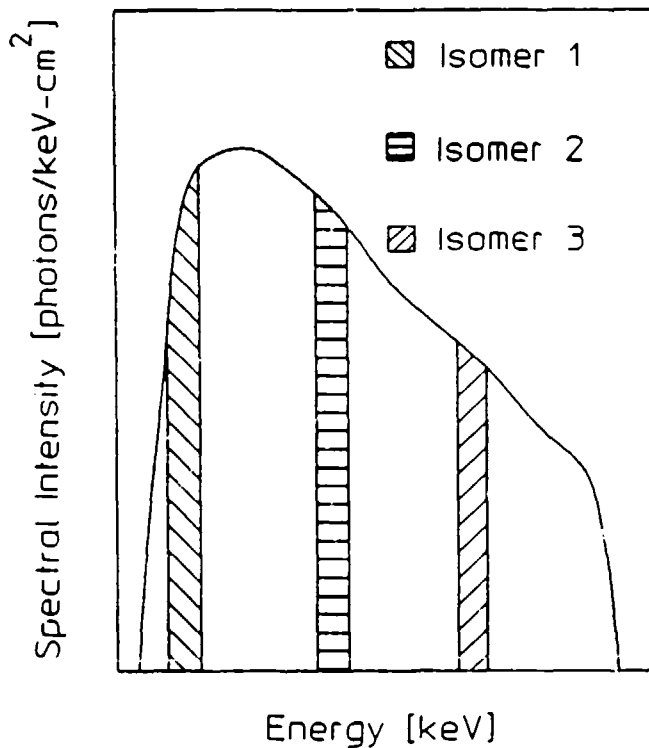
Figure 3: The technique for determining an x-ray spectrum using nuclear photoactivation. Isomers having different gateway states provide measurements of the spectral intensity in specific energy windows.

One complication of this scheme is that isomeric materials in general will possess more than one gateway, thus necessitating a more complicated deconvolution than the idealized case given above. If the irradiation pulse is short compared to the half-lives of the isomeric states involved, the isomeric population can be written as

$$N_{excited} = N_o \sum_i [\pi b_a b_o \sigma_o \Gamma/2]_i \; \phi(E_i) \qquad , \qquad (1)$$

where N_o is the number of target nuclei in the sample, the quantity in brackets is the effective integrated cross section for transfer through the ith gateway state, $\phi(E_i)$ is the incident photon flux at the energy E_i of the ith gateway, and the summation is taken over all accessible gateways. The terms appearing in the integrated cross section are the Breit-Wigner cross section, σ_o, the width of the resonance, Γ, and the branching ratios from the gateway state to the ground and excited

85

states, b_a and b_o. The units of the integrated transfer cross section are cm^2-keV; the units for the photon flux are photons/cm^2-keV.

One of the major difficulties in implementing resonant photoactivation detectors is obtaining good values for the energy and cross section parameters of the gateway states. A summary of parameters appropriate for measurements in the range below 1.5 MeV is given in Table I.[5,6,7]

Table I: Resonant photoactivation parameters for measurements below 1.5 MeV. The integrated cross section corresponds to the term appearing in brackets in Eq. (1). Branching ratios for the decay are not given but may be found in the literature.[8]

Isomer	Isomeric Energy [keV]	Gateway Energy [keV]	Cross Section [10-29 cm^2-keV]	Observed Decay Energy [keV]	Half-life	
$^{79}Br^m$	207	761	6.2	207	4.86	s
$^{77}Se^m$	162	250	0.2	162	17.4	s
		480*		0.87		
		818		0.7		
		1005		30.		
$^{115}In^m$	336	1078	18.7	336	4.486	h
$^{111}Cd^m$	396	1190	5.8	245	48.6	m

*This represents the weighted average of two levels at 440· and 521·keV.

The experimental arrangement for this type of work is illustrated in Fig. 4. Samples may be mounted either in a stationary fixture or inside a pneumatic transfer system. After the exposure, they are transported to a conventional spectroscopy system in a remote area for counting. The equipment can be made readily portable and requires only limited space in the test cell. In normal operation, the x-ray device will automatically trigger the transfer system and a transit timer. Arrival of the sample at the detector stops this timer and starts the spectrometer acquisition cycle. The resulting spectra are analyzed for photopeak areas, from which the total number of excited states produced by the irradiation can be calculated.
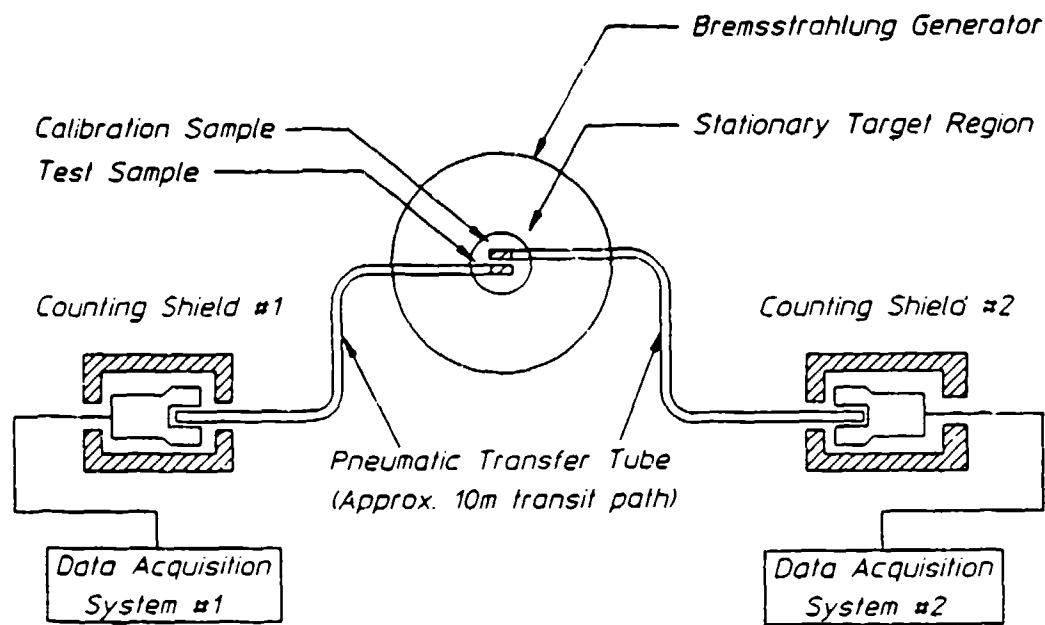
Figure 4:   Apparatus for the implementation of nuclear photoactivation measurements.

Example: Bremmstrahlung Endpoint < 1.5 MeV

The cross sections shown in Table I were obtained in a series of experiments[5,6,7] conducted with the DNA/PITHON flash x-ray device, operated by Physics International in San Leandro, CA.   In this work, the endpoint of the machine was varied from about 1.0 to 1.5 MeV, and the dose delivered to the samples ranged up to approximately 20 kRad.   An example of the type of data obtained with a single shot of PITHON is shown in Fig. 5. By using TIGER[9] code calculations for the variation of the spectral intensity as a function of endpoint energy, it was possible to standardize all of the gateway parameters listed in Table I against the values for ^{79}Br, which were considered to be the best information from the literature.   A comparison of the experimental results for a particular shot and the TIGER code calculation for the same shot, adjusted for the estimated source-sample separation, is shown in Fig. 6.
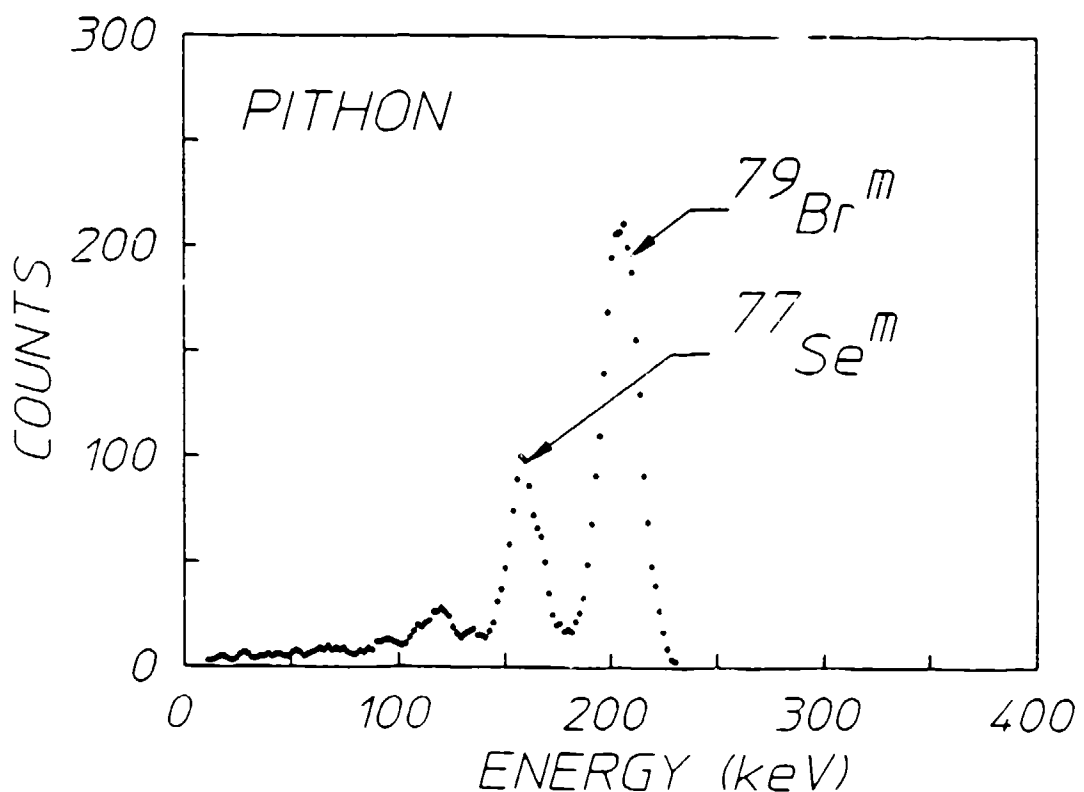
Figure 5: NaI(Tl) spectrum obtained following a single irradiation at the PITHON x-ray facility. The sample was a mixture of 1.25 g of LiBr and 1.20 g of Se powder. Acquisition time was 80 s.
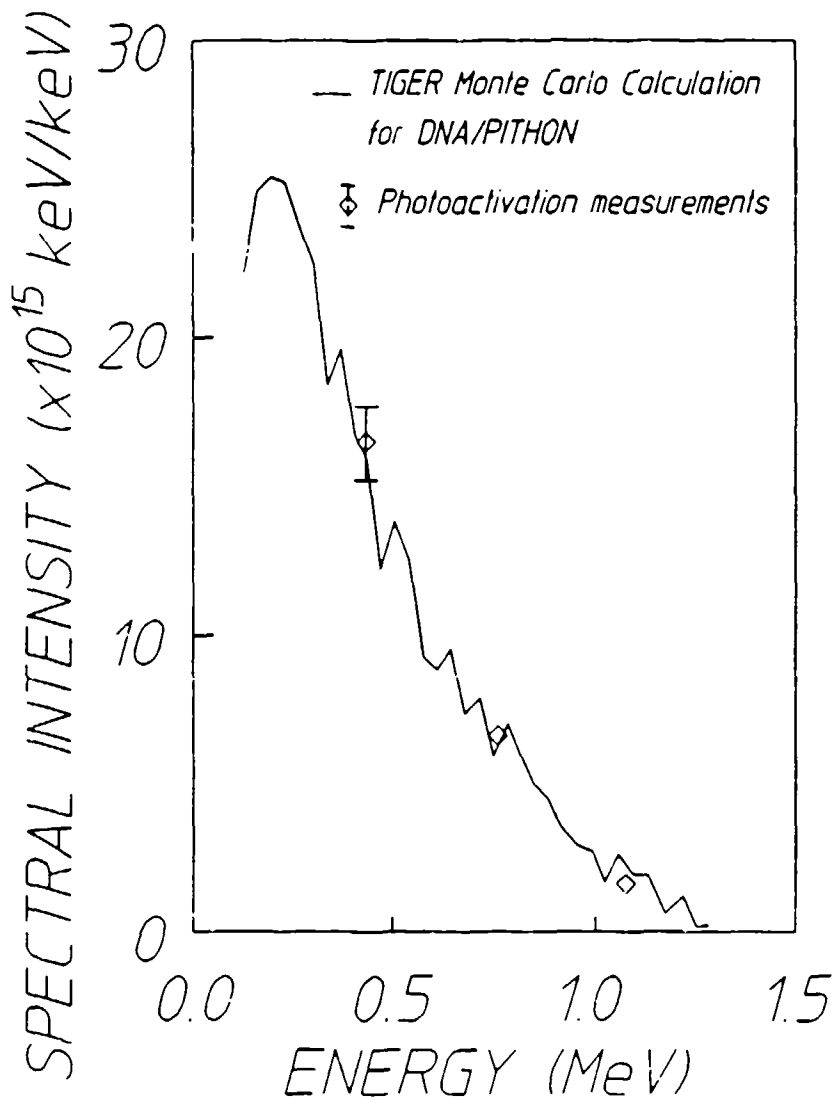
Figure 6: Comparison of calculated (solid line) and measured (diamonds) spectral intensity for PITHON shot 4379.

Example: Bremmstrahlung Endpoint > 1.5 MeV

As the endpoint energy of the x-ray spectrum is increased, more reaction channels open. This complicates the situation by allowing interfering reactions to compete with the selected photoactivation process. These competing channels may be (γ,n) reactions, (n,γ) reactions with the neutrons produced in the environment by high energy source photons, and additional (γ,γ') reactions with high gateway energies.

In experiments conducted at the U.S. Army's Harry Diamond Laboratory in Adelphi, MD, bremsstrahlung from the Aurora machine with a nominal endpoint of 10 MeV was used to further study the use of photoactivation as a spectral characterization tool. This device, which develops 14 TW of electrical power, is the world's largest flash x-ray machine. In one mode of operation, the direct output of the machine is softened by Compton backscattering in a large block of plastic in an arrangement similar to that described in Ref. 2. In this case, the test volume is in a massive high Z shield that prevents the unscattered radiation from illuminating the devices or samples under study. Because the Compton scattering is occurring at close to 180°, the peak in the softened spectrum is expected to lie near 100 keV. Measurements with an absorption spectrometer confirm this.[10]

A set of photoactivation measurements were made in this softened environment and were analyzed in the manner described above. However, significant differences were encountered in this data. An example of the data obtained in this work is shown in Fig. 7. It was not possible to observe photoactivation in the indium sample in this case because of strong interference from the ^{115}In$(n,\gamma)^{116}$In^m reaction, which has large cross sections in the thermal and resonance regimes. High energy source photons interacting in the plastic block through ^{2}H$(\gamma,n)^1$H reactions created the slow neutrons responsible for the interference. By counting both bare and cadmium covered foils, it was possible to quantify ϕ_{th}' and ϕ_{epi}', the thermal and epithermal neutron fluxes in the sample region, normalized to the delivered dose. The values $\phi_{th}' = (4.2 \pm 0.3) \times 10^6$ n/(cm^2-kRad) and $\phi_{epi} = (9.5 \pm 0.6) \times 10^4$ n/(cm^2-kRad) were obtained using conventional analysis techniques.[11,12] From these values, it was possible to calculate the degree of neutron contamination in the ^{77}Se and ^{111}Cd measurements. The ^{77}Se observation shown in Fig. 7 was found to be dominated by neutron capture interferences, but only about 15% of the ^{111}Cd^m activation was due to this mechanism. Lack of the precursor ^{78}Br as a stable isotope insured that the ^{79}Br^m measurement was free of slow neutron contamination. Application of the cross sections of Table I and use of Eq. (1) yielded values of $\phi(761$ keV$) = (3.9 \pm 0.3) \times 10^{10}$ photons/(cm^2-keV-kRad) and $\phi(1190$ keV$) = (3.4 \pm 0.9) \times 10^{10}$ photons/(cm^2-keV-kRad) for the photon flux normalized to the total delivered dose at the sample location. These values have been converted to units of MeV/(MeV-cm^2) for a particular shot so that they may be plotted in Fig.

8(a) with both the theoretical expectations for the backscattering geometry and a spectrum obtained with an absorption spectrometer.
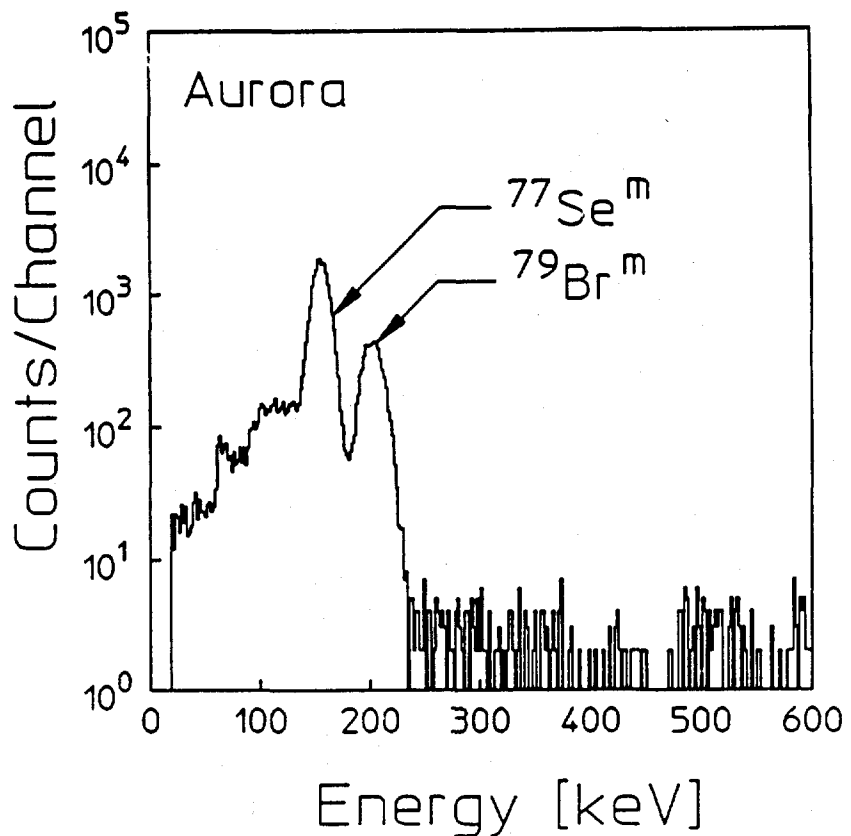
Figure 7: NaI(Tl) spectrum obtained following a single irradiation (shot 6221) at the Aurora facility in backscattered mode. Sample size is identical with that in Fig. 5. Note the difference in scale between the two figures.

As can be seen, the photoactivation measurements lie about two orders of magnitude higher than the expected values. The reason for this discrepancy lies in the high energy tail detected by the absorption spectrometer. It should be noted that although the presence of this tail is indicated by the absorption technique, the lack of sensitivity above 1 MeV in the absorption method does not permit determining the real shape of the spectrum in this region. The solid curves in Fig. 8 above about 1 MeV reflect the initial guess used in the iterative deconvolution process used for the absorption spectrometer rather than a true measurement. Separate investigations[13] of photoactivation processes in the range 1.5-6 MeV using a fixed endpoint linac designed for cancer therapy have revealed that cross sections in this interval may be

91

two to three orders of magnitude larger than those prevailing in the
range below 1.5 MeV. Because the spectrum from the linac used in this
work was fixed, it has not been possible to identify the gateway
energies uniquely; thus the results have been presented in terms of
possible cross section values for a single gateway state at various
energies. Plots showing these single gateway cross sections versus
energy are given in Fig. 9 for the four materials listed in Table I. If
a gateway energy of 2.1, 3.1, 4.1, or 5.1 was assumed for either of the
two materials ^{79}Br or ^{111}Cd, then the flux measurements would lie as
shown in Fig 8(b). Thus, both the photoactivation measurements and the
absorption spectrometer indicate the presence of a high energy tail
extending above the expected backscattered spectrum. This is probably
due to leakage either through the walls of the shield enclosure or
around its entrance aperture.
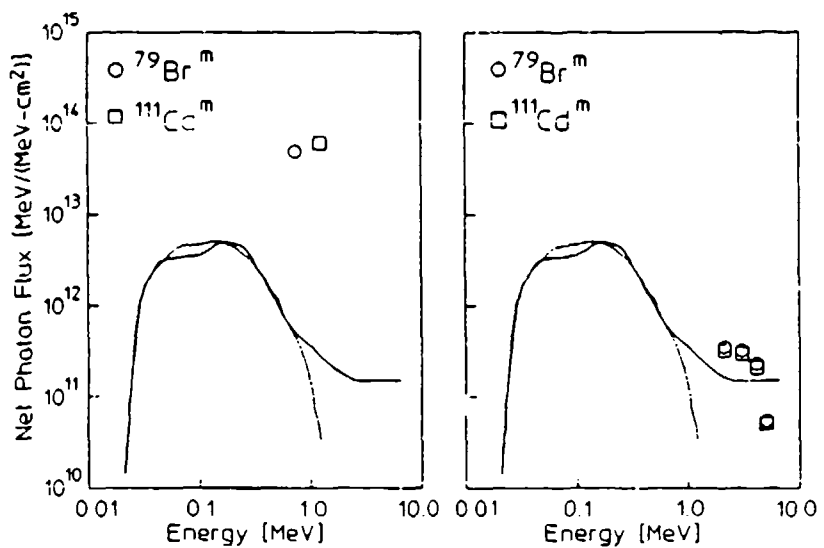
Figure 8: Comparison of photoactivation measurements in which (a) only
low energy gateway states are included and (b) higher energy gateways
are included. In (b) the 4 sets of points represent assumed single
gateways at 2.1-, 3.1-, 4.1-, and 5.1-MeV. The dashed line is the
calculated spectrum for this geometry and the solid line reflects an
absorption spectrometer measurement.
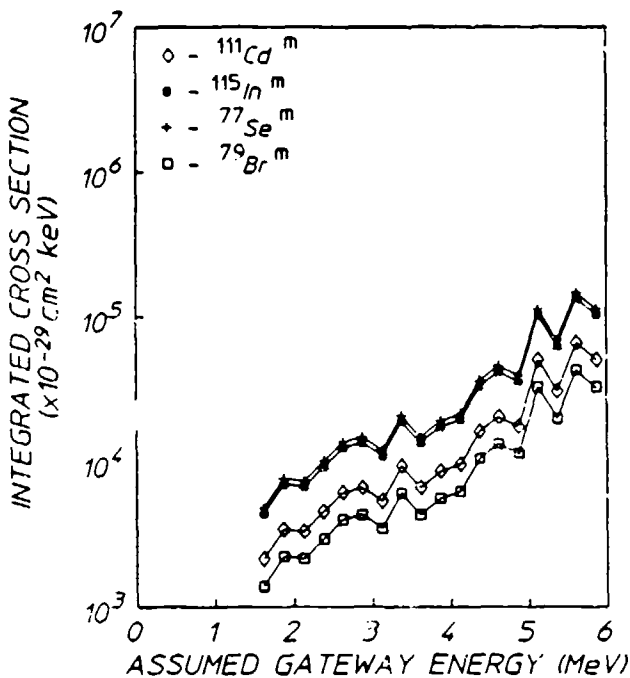
Figure 9: *Possible single-gateway cross sections deduced from fixed-endpoint linac measurements.*

Conclusions

Resonant nuclear photoactivation is a valuable tool that complements both more complex electronic systems and alternative activation or dosimetric methods for determining the spectrum of single-shot, intense bremsstrahlung pulses having widths of less than a microsecond. Either alone or in combination with these other methods, a properly designed photoactivation monitor package can provide the user with specific spectral intensity information on a shot-by-shot basis. Although it appears that the cross sections listed in this paper are adequate for characterizing x-ray spectra with endpoints below 1.5 MeV, additional cross section determinations for high-lying gateway states are required to extend the power of the method to higher energies.

References

1. Y. Paiss, C. D. Eberhard, and C. B. Collins, "Photonuclear Excitation for the Calibration of Pulsed Bremsstrahlung Spectra," Proof of the Feasibility of Coherent and Incoherent Schemes for Pumping a Gamma-Ray Laser, University of Texas at Dallas, Report #GRL/8702, Innovative Science and Technology Directorate of Strategic Defense Initiative Organization, September 1987, pp. 71-89.

2. D. A. Whittaker, K. G. Kerris, M. Litz, S. G. Gorbics, and N. R. Pereira, "Softening of Hard Bremsstrahlung by Compton Backscattering," J. Appl. Phys. 58, 1034-1036 (1985).

3. M. D. Goldberg and J. A. Harvey, "Neutrons," in American Institute of Physics Handbook, edited by D. E. Gray (New York: McGray Hill, 1972).

4. G. T. Baldwin and J. R. Lee, "Time Projection Compton Spectrometer (TPCS)," IEEE Trans. Nucl. Sci., NS-33, 1298-1304 (1986).

5. J. A. Anderson and C. B. Collins, "Calibration of Pulsed X-ray Spectra," Rev. Sci. Instrum. 59, 414-419 (1988), and references cited therein.

6. C. B. Collins, J. A. Anderson, Y. Paiss, C. D. Eberhard, R. J. Peterson, and W. L. Hodge, "Activation of 115In^m by Single Pulses of Intense Bremsstrahlung," Phys. Rev. C 38, 1852-1856 (1988).

7. J. A. Anderson, M. J. Byrd, and C. B. Collins, "Activation of 111Cd^m by Single Pulses of Intense Bremsstrahlung," Phys. Rev. C (to be published Nov. 1988).

8. E. Browne and R. B. Firestone, Table of Radioactive Isotopes, edited by V. S. Shirley, (New York: J. Wiley, 1986).

9. J. A. Halbleib and T. W. L. Sanford, "Predicted Flash X-ray Environments Using Standard Converter Configurations," Sandia Report SAND83-2572, 1983.

10. J. A. Anderson, J. M. Carroll, K. N. Taylor, J. J. Carroll, M. J. Byrd, T. W. Sinor, C. B. Collins, F. J. Agee, D. Davis, G. A. Hutclin, K. G. Kerris, M. S. Litz, D. A. Whittaker, N. R. Pereira, and S. G. Gorbics, "Nuclear Activation Techniques for Measuring Direct and Backscattered Components of Intense Bremsstrahlung Pulses," Nucl. Instrum. and Meth. (submitted).

11. "ASTM Standard Method for Determining Neutron Flux, Fluence, and Spectra by Radioactivation Techniques," Publication E 261-77, Philadelphia: American Society for Testing and Materials, 1987.

12. "ASTM Standard Method for Determining Thermal Neutron Reaction and Fluence Rates by Radioactivation Techniques," Publication E 262-86, Philadelphia: American Society for Testing and Materials, 1987.

13. J. A. Anderson, C. D. Eberhard, M. J. Byrd, J. J. Carroll, C. B. Collins, E. C. Scarbrough, and P. P. Antich, "Nuclear Photoactivation Cross Sections for Short-lived Isomeric States Excited with a 6 MeV LINAC," Nucl. Instrum. and Meth. (submitted).

THE USE OF A COMPTON SPECTROGRAPH/MONOCHROMATOR FOR THE PHOTOACTIVATION OF NUCLEI INTO METASTABLE STATES

by Y. Paiss, C. D. Eberhard, and C. B. Collins
Center for Quantum Electronics, University of Texas at Dallas

Introduction

Photoactivation of nuclei by gamma rays was reported as early as 1939.[1,2] Since then, a few tens of papers have appeared describing the $X(\gamma,\gamma')X^m$ reactions of about 20 nuclei.[3] It is assumed that one or more broad nuclear levels above the metastable level serve as gateways for the excitation, and that the contribution to the activation due to direct excitation is neglected since the width of the metastable level is extremely narrow.

In recent years, there appeared claims that part of the photoexcitation is due to a non-resonant process mediated by the K electrons around the nuclei.[4] Some papers, on the other hand, have refuted this claim by indirect measurements.[3,5]

In analogy with techniques used in atomic excitation studies, the only unequivocal investigation of the mechanism for production of metastable nuclei by gamma irradiation can be conducted through the use of a scanning monochromator. For example, ^{197}Au is easily excited by the bremsstrahlung of 3 MeV electrons into the metastable $^{197}Au^m$. Although gold has 20 known levels between the metastable level at 409 keV and 1242 keV, nothing is known of the excitation mechanism or which levels are involved, if any, within this energy range.[6]

It is the aim of this paper to describe a Compton spectrograph/monochromator (CSM) with "fast optics" to down-convert single energy gammas from a radioactive source and to use them to study the nuclear excitation function for the $X(\gamma,\gamma')X^m$ production of the metastable state. Single energy radioactive nuclei are rare. Here, this term is used for cases in which the spectrum contains only a few discrete gammas and no ambiguity occurs, e.g., ^{60}Co with two distinct energies, or ^{140}La with one dominant energy.

General Considerations

The CSM is basically a source, a scatterer, and an absorber. The source emits single energy photons of initial energy E_0 which are scattered by an electron in the scatterer through a given angle, θ, and lose a portion of their energy. The new energy E, a function of the original energy, E_0, and the scattering angle θ, is given by

$$E = \frac{E_0}{1 + (E_0/mc^2)(1 - \cos \theta)} \quad , \quad (1)$$

where mc^2 is the rest mass energy of the electron. The absorber is fabricated from the material under investigation. Upon striking it, the scattered photon is absorbed by the electrons in the sample unless the energy of the scattered photon is equal to that of a nuclear resonance transition. If this nuclear resonance transition corresponds to a gateway state connected by one or more electromagnetic transitions to the metastable state, the nuclear isomer can be formed. If the absorber is in the shape of a large foil, areas on the foil will become radioactive when they correspond to the scattering angle θ which degrades the photon energy from E_0 to the resonance energy E_r. The angle θ can be measured and E_r can be estimated.

Assuming a basic configuration which is determined by the energy resolution needed with a free parameter scale length l, then:

1. For a given source, the number of photons striking the scatterer is independent of l because it depends only on the solid angle which the scatterer is presenting to the source, which is limited by the energy resolution required. (The area of the scatterer varies as l^2 and the flux density on the scatterer is proportional to the solid angle subtended by the absorber, that is as l^{-2}.)

2. For a source of a given specific activity, the source strength is proportional to the source volume, that is, varies as l^3, when self absorption effects are neglected. Thus, the total flux density on the scatterer goes as $l^3 \cdot l^{-2} = l$ and the flux density on the absorber as $l^3 l^{-2} l^3 l^{-2} = l^2$. The total number of absorbed resonance photons is proportional to the product of the flux density and the absorber area (not volume, since the

absorption depth is very shallow and is independent of l), or l^2 (flux density) $\times$ l^2 (area) $= l^4$. This means that the number of absorbed photons varies with the fourth power of the scale parameter. The limit on the size is governed by the absorption in the source and scatterer and by double Compton scattering.

Three forms of CSM are described with increasing complexity and efficiency.

A Single Massive Scatterer

This configuration is the basic one used by Compton himself.[7] It consists of a source, scatterer and an absorber foil as shown in Fig. 1. The part of the foil illuminated by photons scattered through angle θ which brings E to E_f will become radioactive.
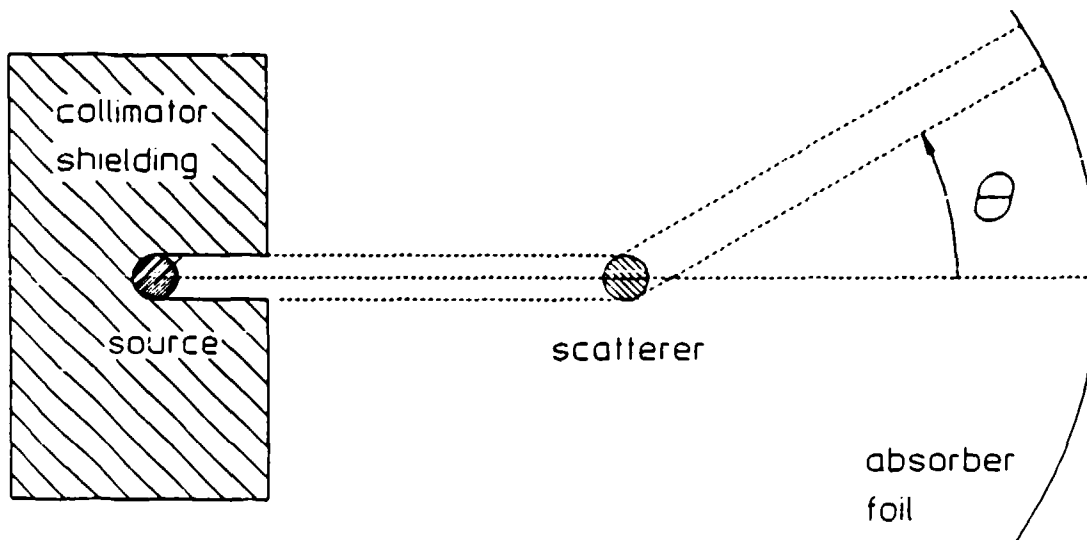
Figure 1: Geometry of the basic Compton spectrometer showing the source, single massive scatterer and a curved absorber foil.

Strip Circular Compton Spectrograph

The gamma source, the scatterer and the absorber are parts of the same circle of radius R as shown in Fig. 2. The scatterer and the absorber can be the same curved strip. All gammas scattered through the angle θ in the plane of the curve so that they strike the strip again, will arrive at the same place regardless of their scattering points on the strip (classical geometry). Therefore, they will have the same energy provided that the source is monoenergetic, such as ^{60}Co (only two lines) or ^{24}Na or ^{140}La or ^{124}Sb etc. and the photons are scattered only once.
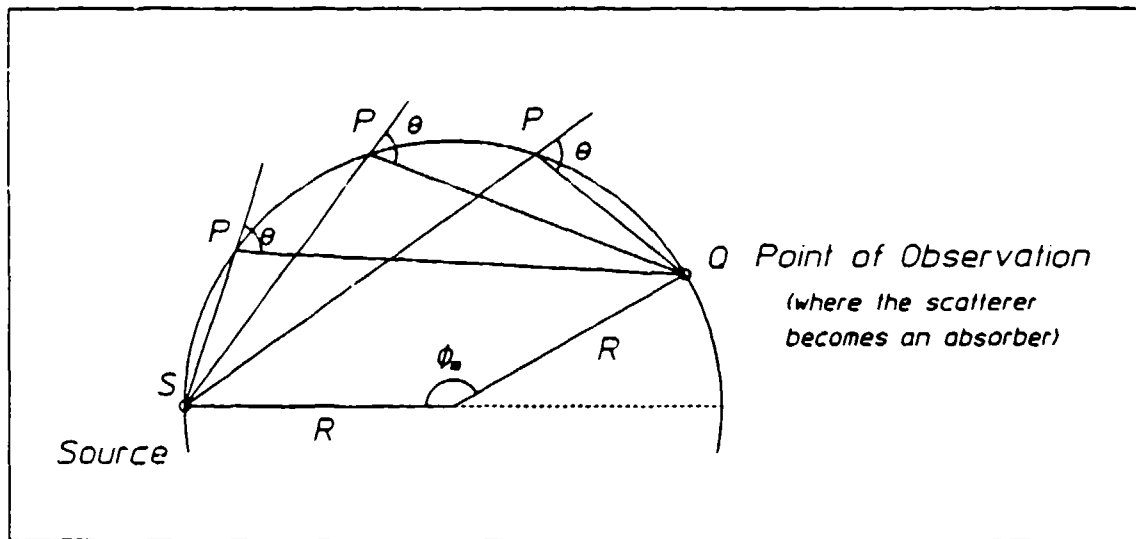
Figure 2: Compton spectrograph with curved scatterer/absorber. The curved scatterer/absorber is a section of a right-circular cylinder of radius R and height W. If the source may be considered a point source, then the angle θ is the same for all single scattering paths ending on the point Q and does not depend on the coordinates of the scattering point P. The angle θ depends only on the relative coordinates of the source S and the point of observation Q and is given by $\theta = u_m/2$.

If the energy of the photons, after being scattered through an angle θ, changes from E_o to E_r, which is the resonance energy for a nuclear absorption transition resulting in the production of an isomeric state, then after the irradiation, the strip can be auto-radiographed. If the isomer formed has a sufficiently long half-life, the area on the strip corresponding to scattering through the angle θ will be radioac-

100

tive.   The remainder of the strip, although irradiated by direct gamma
from the source, will stay "cold" with a general background activation
caused by Compton scattering inside the source, construction material,
shielding and air, or by double scattering in the strip.

Fig. 3 indicates the angles inherent in the geometry in the circu-
lar strip scatterer. The source is located at S which corresponds to ϕ
= 0, the scattering point P at ϕ = ϕ (arbitrary on the curve), and the
absorbing point Q at ϕ = ϕ_m. The scattering point P is characterized by
the angle ϕ, the P-Q distance $R'(\phi)$, and the S-P distance $R''(\phi)$. The
S-Q distance is L. The scattering angle is given by θ = $\phi_m/2$ for all
scattering points on the arc of the circle of radius R. The width and
thickness of the foil are given by W and D, respectively. The electron
density in the foil is η. It is assumed that the mean free path of the
photon of energy E_0 is greater than $D/\sin(\phi/2)$ which is the maximum
slant range of a photon inside the foil.
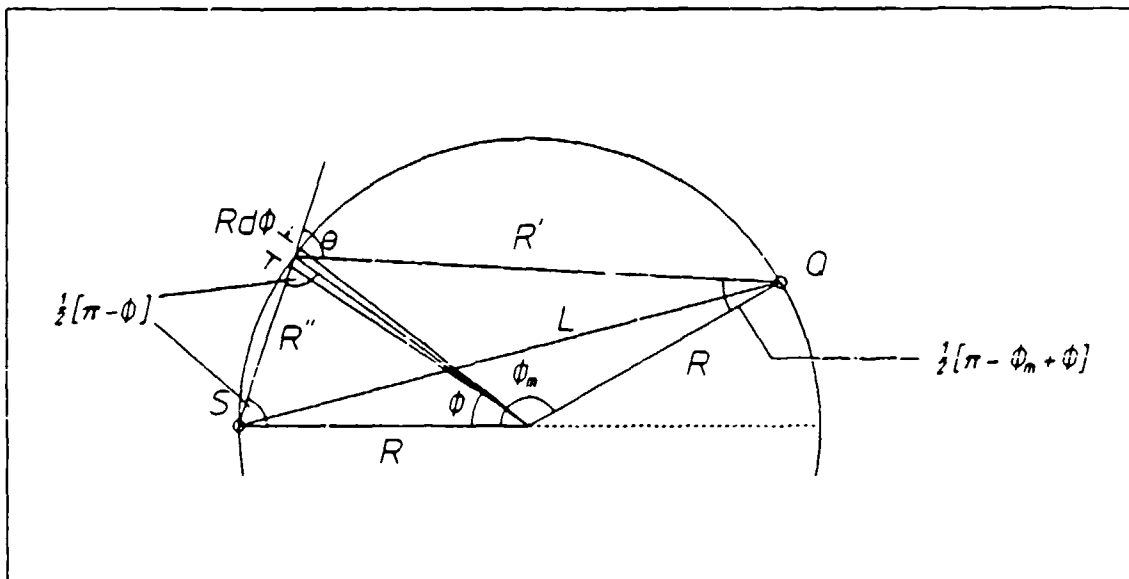
Figure 3:   Compton spectrograph with curved scatterer/absorber showing
the geometrical details employed in the calculations. From this, the
following definitions are easily seen:
   R' = 2 R sin $[(\phi_m-\phi)/2]$
   R'' = 2 R sin $(\phi/2)$
   L = 2 R sin $(\phi_m/2)$ = 2 R sin θ

There is a one-to-one correspondence between the scattering angle θ and the energy of the scattered photon E when a monoenergetic source is used. The scattering efficiency of an electron is determined by the Kline-Nishina cross section σ_C. By integrating it over the azimuthal scattering angle and substituting dependence on E for the dependence on θ, the following expression[8] can be used to determine the cross section for the scattering of a photon of initial energy E_o into the energy interval $E_r \pm \Gamma/2$ of the nuclear resonant absorption transition at E_r:

$$\sigma(E_r, E_o) = \int_{E_r-\Gamma/2}^{E_r+\Gamma/2} \sigma(E, E_o)\ dE \approx \sigma_C(E_r, E_o)\ \Gamma \qquad (2)$$

$$= \pi r_o^2\ \frac{mc^2\Gamma}{E_o^2}\left[\frac{E_o}{E_r} + \frac{E_r}{E_o} + \left(\frac{mc^2}{E_r} - \frac{mc^2}{E_o}\right)^2 - 2mc^2\left(\frac{1}{E_r} - \frac{1}{E_o}\right)\right]\ .$$

where $r_o = e^2/mc^2$ is the classical radius of the electron and E_r may range from a minimum of $E_o/(1 + 2E_o/mc^2)$ for $\theta = \pi$ (backscattering) to E_o for $\theta = 0$ (no scattering).

The total number of scattering events in the differential volume dV at P which produce photons of energies in the interval $E_r \pm \Gamma/2$ is given by

$$dn(E_r) = \eta\ \sigma(E_r, E_o)\ \Phi(P)\ dV \qquad (3)$$

$$= \eta\ \sigma(E_r, E_o)\ \frac{1}{4\pi(2R \sin \phi/2)^2}\ W\ D\ R\ d\phi\ ,$$

where $\sigma(E_r, E_o)$ is the cross section as defined above, η is the electron density, and $\Phi(P)$ is the flux of monoenergetic photons produced by the radioactive source S (which is assumed to be isotropic and normalized to one disintegration/sec).

102

The differential increment of the spectral density at Q, dψ, is defined as follows: the number of photons per unit area per unit time at Q with energies in the interval $E_r \pm \Gamma/2$ produced by Compton scattering in the volume dV at P per unit energy interval per Bq. This differential increment is given by

$$d\psi = [dn(E_r)/\Gamma] \cdot \sin \frac{\phi_m - \phi}{2} \cdot [1/2\pi R' \sin \theta] \cdot [1/g] \quad . (4)$$

The first multiplicative factor corrects for the oblique incidence of the scattered photons on the absorber at Q. The second factor represents the percentage of the total scattered flux intercepted by the absorber (σ_c has already been integrated azimuthally in Heitler's expression) and finally g is the width of the active line formed on the absorber. It is larger than the width dictated by the level width of the absorber, and we assume it to be the image of the source on the absorber. In our geometry, the magnification is unity.

Integration over the angle ϕ from the minimum ϕ_0 to ϕ_m yields the total Compton scattered flux with energy in the interval $E_r \pm \Gamma/2$ at the point of activation Q,

$$\psi = \int_{\phi_0}^{\phi_m} \frac{\eta WDRd\phi \sigma_c(E_r, E_o)}{16\pi R^2 \sin^2 (\phi/2)} \cdot \frac{\sin \dfrac{\phi_m - \phi}{2} \; \dfrac{1}{g}}{2\pi \; 2R \sin \dfrac{\phi_m - \phi}{2} \sin \theta} \quad (5)$$

$$= K \int_{\phi_0}^{\phi_m} \frac{d\phi}{\sin^2 (\phi/2)} = 2 K [\cot(\phi_0/2) - \cot (\phi_m/2)] \quad ,$$

where $K = [\eta WD\sigma_c/(8\pi R)^2 \sin \theta \; g]$ and ϕ_0 is the minimum ϕ corresponding to the closest edge of the scattered/absorber outside the source volume.

Equation (5) may be rewritten as

$$\psi = 2 K \frac{\sin \dfrac{\phi_m - \phi_0}{2}}{\sin (\phi_m/2) \sin (\phi_0/2)} \quad (6)$$

This expression becomes infinite as ϕ_0 approaches zero, so that we must look more closely to discover the limitation of our geometry and the restraints on ϕ_0.

The original diverging term arises from the description of the source as a point source,

$$\Phi = \frac{1}{4\pi r^2} = \frac{1}{4\pi \ [2R \sin \phi/2]^2} \qquad , \qquad (7)$$

where ϕ describes the point of observation on the arc. As one approaches the point source, $\phi \to 0$, $r \to 0$ and $\Phi \to \infty$. In reality, the source has a finite size and the flux is integrated over a sphere outside the source. If the minimum size of this sphere is $r = 2R \sin (\phi_0/2)$, then the minimum ϕ could be found from this.

A second concern is that in the usual planar scattering geometry, the effective thickness $(D/\sin [\phi/2])$ as expressed in our geometry becomes infinite as $\phi \to 0$ which corresponds to the beam becoming parallel to the surface. For a spherical shell or a narrow circular strip, the maximum effective thickness is given by $[D(2R+D)]^{1/2}$. So one must impose the condition on ϕ_0 that

$$\frac{D}{\sin \phi_0/2} << [D(2R+D)]^{1/2} \qquad , \qquad (8)$$

which should be fulfilled also to prevent double Compton scattering. This is equivalent to moving the edge of the scatterer far enough away that the spherical shell can be approximated by the planar sheet.

As shown in Fig. 3, the dependence of the flux on ϕ_0 may also be expressed as

$$\psi(\phi_0) = \frac{\eta \ WD \ \sigma_C}{8\pi^2 \ g} \ \frac{R'(\phi_0)}{L^2 \ R''(\phi_0)} \qquad (9)$$

$$\simeq \frac{\eta \ WD \ \sigma_C}{8\pi^2 \ g} \ \frac{1}{R''(\phi_0) \ L} \qquad ,$$

when $R'(\phi_0) \simeq L$, which implies that ϕ_0 is very small.

Let us assume that the same parameters (n, D , W, etc.) describe both the massive scatterer and the extended scatterer (strip). Now as shown in Fig. 4, let us consider the massive scatterer to be the beginning segment of the extensive one (strip).
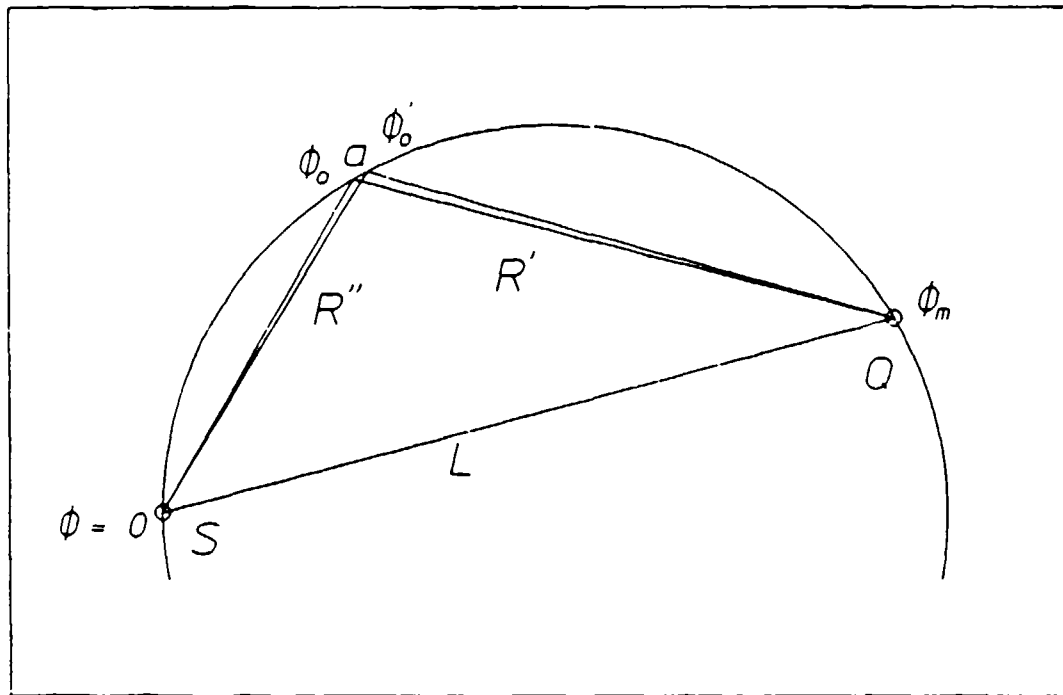
Figure 4: Compton spectrograph with curved scatterer/absorber with geometrical details for the comparison of the extended strip scatterer with the single massive scatterer.

Its contribution is the difference between that of an extensive scatterer from ϕ_o to ϕ_m to that from ϕ_o' to ϕ_m.

$$\psi_{massive} = \psi(\phi_o) - \psi(\phi_o') \qquad (10)$$

$$= \frac{\eta \; WD \; \sigma_c \; [\cot(\phi_o/2) - \cot(\phi_o'/2)]}{32\pi^2 R^2 \sin\theta \; g}$$

$$= \frac{\eta WD\sigma_c}{32\pi^2 R^2 \sin\theta \; g} \frac{\sin([\phi_o'-\phi_o]/2)}{\sin(\phi_o'/2)\sin(\phi_o/2)}$$

Thus the ratio is given by

$$\frac{\psi_{massive}}{\psi_{strip}} = \frac{\sin([\phi_o'-\phi_o]/2) \; \sin(\phi_m/2)}{\sin(\phi_o'/2) \; \sin([\phi_m-\phi_o]/2)} \qquad (11)$$

$$\simeq \frac{aL}{R''(\phi_o')R'(\phi_o)}$$

As shown in Eq. (9), $\psi(\phi_o)$ is greater when $R''(\phi_o) < R'(\phi_o)$. Therefore, in an optimal strip, $R'(\phi_o) \simeq L$ and Eq. (11) can be written

$$\frac{\psi_{massive}}{\psi(\phi)} \simeq \frac{a}{R''(\phi_o)} \qquad (12)$$

To estimate the maximum value of the parameter a which characterizes the size of the scatterer, let us consider the massive scatterer to be a ball with the diameter a, situated such that $R'(\phi_o) = R''(\phi_o)$. Figure 5 shows this arrangement.
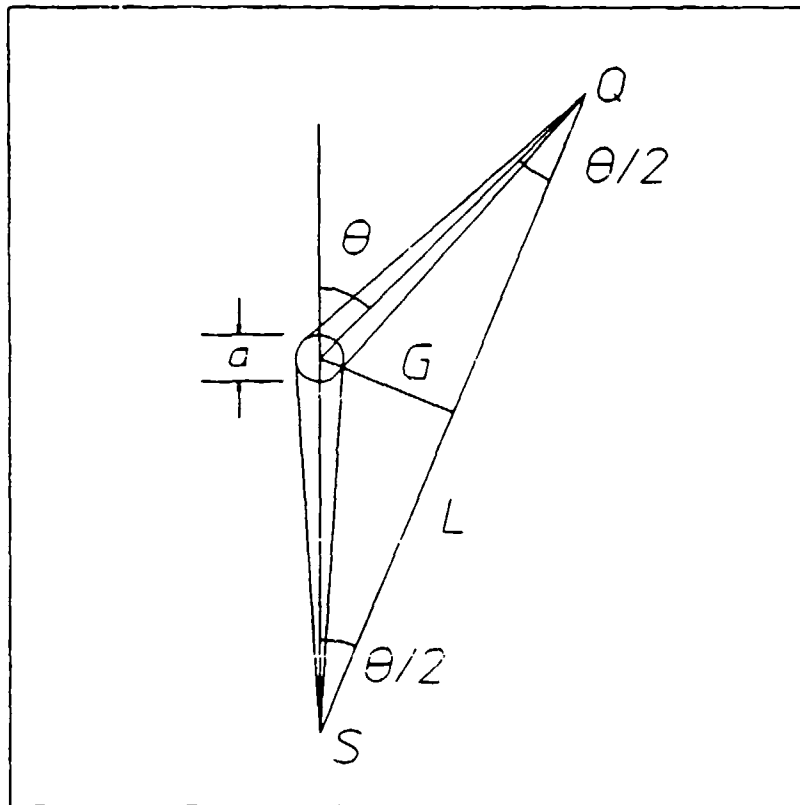
Figure 5: Geometrical details for the estimate of maximum size of a single massive spherical scatterer for a given energy spread.

By simple trigonometry,

$$G = \frac{L}{2} \tan (\theta/2) = \frac{L}{2} \frac{1 - \cos \theta}{\sin \theta} \quad , \quad (13)$$

and the energy E of the Compton scattered photon may be rewritten as

$$E = \frac{mc^2}{1 - \cos \theta + (mc^2/E_0)} \quad . \quad (14)$$

A change of the scattering point along G will change the energy of the scattered photon E as

$$\frac{dE}{dG} = \frac{dE}{d\theta} \frac{d\theta}{dG} = \frac{-mc^2 \sin \theta}{[1 - \cos \theta + (mc^2/E_0)]^2} \frac{2}{L} \frac{\sin^2\theta}{(1 - \cos \theta)} \quad . \quad (15)$$

or

$$-\frac{dE}{dG} = \frac{E^2}{mc^2}\frac{\sin^2\theta}{G} \qquad , \qquad (16)$$

by the substitution of (13) and (14) in (15). Now assuming $(a/2) \ll G$, the change in energy of the scattered photon from the most remote part of the ball along G, $\Delta G = a/2$. is given by

$$\Delta E = \frac{dE}{dG}\Delta G = \frac{E^2}{mc^2}\frac{a}{2C}\sin^2\theta \qquad . \qquad (17)$$

For example, to reduce the 1.33 MeV gamma from ^{60}Co to 1 MeV, the scattering angle θ is about 29°, so that

$$\Delta E \simeq \frac{(1.0)^2}{(0.51)}\frac{a}{2G}\sin^2 29° = \frac{(0.461)(a/2)}{G} \qquad . \qquad (18)$$

If a 5% maximum spread in energy E is desired, then Eq. (17) is

$$\frac{\Delta E}{E} = \frac{E}{mc^2}\frac{(a/2)}{G}\sin^2\theta \qquad (19)$$

$$= \frac{(1.0)}{(0.51)}\frac{(a/2)}{G}(0.235) = 0.05 \qquad .$$

Solving for the radius of the ball, $(a/2)$, we have

$$(a/2) = (0.05)(2.17)\ G = 0.11\ G \qquad . \qquad (20)$$

Typically, experimental parameters would be $R'' \simeq R' \simeq 30$ cm, $G = R''\sin(\theta/2) \simeq 7.5$ cm and $(a/2) \simeq 0.8$ cm. Substituting this into Eq. (11), we get

$$\frac{\psi_{massive}}{\psi_{strip}} = \frac{(1.6)(58)}{(30)(30)} = 0.11 \qquad . \qquad (21)$$

The strip then is about an order of magnitude more efficient than the massive scatterer.

108

The Football Geometry Compton Spectrograph

By rotating the strip around L as an axis, one obtains a football shaped scattering surface for $\theta < \pi/2$. For $\theta - \pi/2$, the shape is a sphere and for $\theta > \pi/2$, it is a donut with a clogged hole. Here we shall limit our discussion only to the football shape because $\theta \geq \pi/2$ will seldom be used.

The source is located at one apex of the football and the absorber at the other apex of the scatterer as shown in Fig. 6.
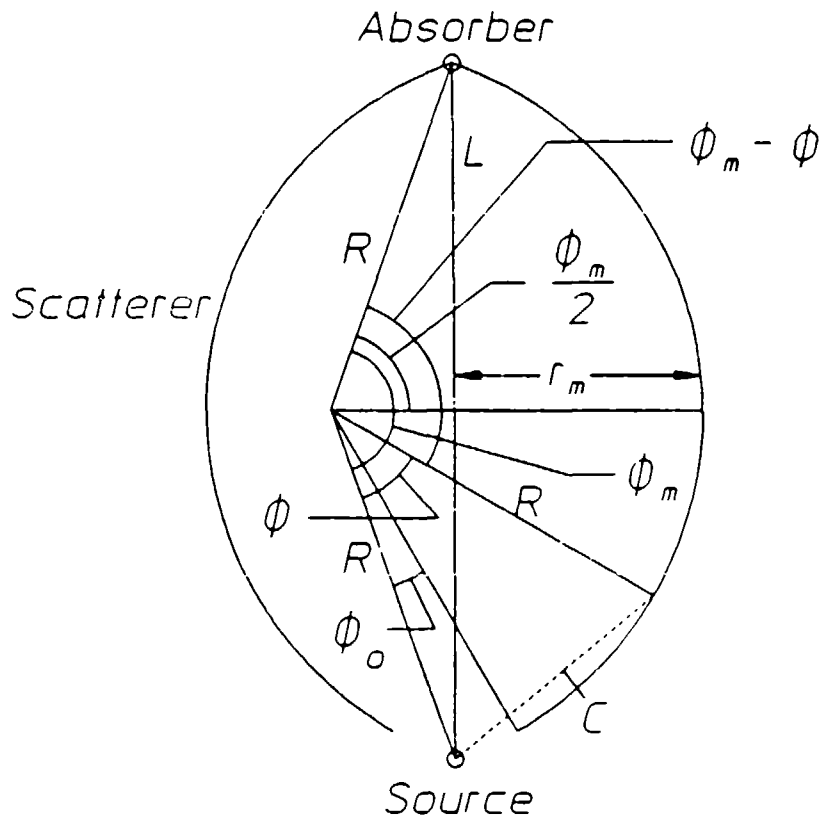

Figure 6: "Football-shaped" spectrometer utilizing the curved scatterer/absorber concept. From this, the following definitions used in the calculation may be seen:

$\sin (\phi_m/2) = L/2R;\ 1 - \cos (\phi_m/2) = r_m/R$
$\sin (\phi_i/2) = \phi_i/2;\ 1 - \cos (\phi_i/2) = \phi_i^2/4$
$c = 2R \sin (\phi/2)$
$r = c \sin [(\phi_m-\phi)/2] = 2R \sin (\phi/2) \sin [(\phi_m-\phi)/2]$

To calculate the flux density on the absorber, we can use an equation similar to Eq. (5), replacing the strip width W by the length of the circumference at latitude ϕ on the ball,

$$W = 2\pi r = 4\pi R \sin(\phi/2) \sin([\phi_m - \phi]/2) \qquad . \qquad (22)$$

Another change from Eq. (5) is the omission of the $\sin([\phi_m - \phi]/2)$ in the numerator. This arises because the absorber is no longer a part of the scatterer, but a plug at the top of the ball. The gammas strike the absorber practically normal to the surface and no correction for the slant angle is needed. With these modifications, Eq. (5) becomes

$$\psi = \int_{\phi_0}^{\phi_m} \frac{\eta D[4\pi R \sin(\phi/2) \sin((\phi_m - \phi)/2)] R \, \sigma_c \, d\phi}{16\pi R^2 \sin^2(\phi/2) \, 4\pi R \sin((\phi_m - \phi)/2) \sin\theta \, g} \qquad (23)$$

$$= \frac{\eta \sigma_c D}{8\pi R g \sin\theta} \log \left[\frac{(1 - \cos(\phi_m/2))}{\sin(\phi_m/2)} \frac{\sin(\phi_0/2)}{(1 - \cos(\phi_0/2))} \right] \quad .$$

Referring to Fig. 6, we may rewrite this for small values of ϕ_0 as

$$\psi = \frac{\eta \sigma_c D}{8\pi R g \sin\theta} \log \frac{2 r_m / L}{\phi_0 / 4} \qquad , \qquad (24)$$

where r_m is the distance $R[1 - \cos(\phi_m/2)]$.

By dividing Eq. (24) by Eq. (9), we get the relative efficiency of the football to the strip configuration,

$$\frac{\psi_{football}}{\psi_{strip}} = \frac{2\pi R''(\phi_0) L \log[(2 r_m / L)/(\phi_0/4)]}{W R'(\phi_0)} \qquad (25)$$

$$\approx \frac{2\pi R''(\phi_0) \log[(2 r_m / L)/(\phi_0/4)]}{W} \qquad ,$$

since $R'(\phi_0) \approx L$. The quantity $\log[(2 r_m / L)/(\phi_0/4)]$ is on the order of 2 to 5 in our geometry. The quantity $R'(\phi_0)/W$ is of the order of 5. The relative efficiency is therefore on the order of 60 to 160, or, about two orders of magnitude more than that of a simple solid scatterer.

Let us consider an example case in which the scatterer and absorber have the following parameters:

σ_c = 1.7×10^{-28} cm^2 (Klein-Nishina cross section[8] for scattering a 1.3 MeV photon to 1 MeV) ,

R = 100 cm ,

θ = 29° ,

g = the source radius = 1 cm ,

D = 0.3 cm ,

$\log [(2r_m/L)/(\phi_0/4)]$ = 4 , and

$\eta \approx 1.9 \times 10^{24}$ cm^{-3} (typical value for In) .

The normal component of the flux at the absorber calculated from Eq. (24) is

$$\psi = 9.7 \times 10^{-7} \text{ photons/cm}^2 \text{ sec keV Bq} \qquad . \qquad (26)$$

Therefore, a 6 kilocurie ^{60}Co source will deliver a 1 MeV photon flux of 2.2×10^8 photons/cm^2 sec keV to the absorber. These are the 1.33 MeV photons scattered through an angle of 29°.

Discussion

We see that the "football-shaped" scatterer can serve as a monochromator for the production of gamma rays with an energy range between the maximum energy of the available gamma sources and those energies obtained by the crystal diffraction methods. Although the football has relatively "slow optics," it is the best tunable gamma source available. One drawback is that by contrast to the strip CSM, the football lacks continuous tunability. For each source-absorber combination, a different arc of the scatterer must be used for each value of energy. We should investigate the potential for continuous tuning by inflating a uniform, expandable ball or by constructing the scatterer from elastic ribs which can be adjusted at the poles. Care must be taken to insure a circular configuration, perhaps by varying the thickness of the substrate material holding the scatterer.

111

A fast shuttle between the ball's apex and a shielded detector would enable the determination of gateway levels of isomers with half-lives down to a second. With high specific activity sources (e.g., ^{140}La) and optimization (no attempt to optimize was done in the example given) of the CSM by ray tracing and Monte Carlo calculations, we hope to increase the flux by at least an order of magnitude.

References

1. B. Pontecorvo and A. Lazard, C. R. Acad. Sci. 208, 99 (1939).

2. G. B. Collins, B. Waldman, E. M. Stubblefield, and M. Goldhaber, Phys. Rev. 55, 507 (1939).

3. K. Yoshihara, Zs. Nemeth, L. Lakosi, I. Pavlicsik, and A. Veres, Phys. Rev. C33, 728 (1986) contains a thorough review.

4. A. Ljubicic, K. Pisk, and B. A. Logan, Phys. Rev. C23, 2238 (1981).

5. C. B. Collins, J. A. Anderson, Y. Paiss, C. D. Eberhard, R. J. Peterson, and W. L. Hoddge, Report GRL/8702, 45 (1987).

6. B. Harmatz, Mucl. Data Sheets 34, 101 (1981).

7. A. H. Compton and S. K. Allison, X-rays in Theory and Experiment, (D. Van Nostrand Co., Inc., New York, 1935).

8. W. Heitler, The Quantum Theory of Radiation, (Oxford University Press, London 1944).

PHOTOACTIVATION OF NUCLEAR ISOMERS BY (γ,γ') REACTIONS THROUGH RELATIVELY UNHINDERED TRANSITIONS ACCESSED WITH BREMSSTRAHLUNG FROM MEDICAL LINEAR ACCELERATORS

by J. J. Carroll, J. A. Anderson, M. J. Byrd, K. N. Taylor,
D. G. Richmond, T. W. Sinor, W. L. Hodge, Y. Paiss,
C. D. Eberhard and C. B. Collins

Center for Quantum Electronics, University of Texas at Dallas

and E. C. Scarbrough and P. P. Antich

University of Texas Southwestern Medical Center

Introduction

The photoexcitation of isomeric nuclei through (γ,γ') reactions has been investigated for more than fifty years.[1,2] Surprisingly there is very little convergence among the few tens of experimental results that have been published in this time.[3] The extreme variance between measurements is surprising when compared with the precision routinely achieved in the examination of all types of particle reactions. Moreover, the analogous optical double resonance technique is among the most powerful methods of investigation at the molecular level. Nevertheless, (γ,γ') studies have provided widely differing results as exemplified by investigations of the reactions $^{111}Cd(\gamma,\gamma')^{111}Cd^m$ and $^{115}In(\gamma,\gamma')^{115}In^m$.

The stable nuclide ^{111}Cd would seem to be nearly ideal for nuclear fluorescence studies due to the readily observable lines at 150.6 and 245.5 keV radiated from its 396 keV isomer and the moderate isomeric half-life of 48.6 min.[4,5] Only slightly less convenient is the isomer $^{115}In^m$, having a half-life of 269 min and a fluorescence line at 336 keV, the isomeric energy. A variety of irradiations using either radioactive ^{60}Co or ^{137}Cs sources or bremsstrahlung from accelerators have been performed to activate samples containing these nuclei at energies up to about 1.5 MeV. Each of these sources was intense enough to excite sufficient numbers of nuclei to insure reasonable counting statistics and good signal-to-noise ratios. However, in several carefully conducted experiments[6,7,8] values of the integrated cross-section for the photoexcitation of $^{111}Cd^m$ were found to range from 5.8 ± 0.8 to 35 ± 4 in

the usual units of 10^{-29} cm^2-keV. Likewise, values for ^{115}In^m were found[9,10] to range from 5.38 $\pm$ 0.64 to 23 $\pm$ 4 in the same units.

It has been generally thought that (γ,γ') reactions occur through resonant processes. However, in attempting to explain the seemingly excess activations observed in some experiments, several investigators[7,9] have postulated that the photoexcitation proceeded instead through a non-resonant channel. Theory has never been able to supply a mechanism of sufficient magnitude to account for this behavior at energies below 1.5 MeV but the idea remained a controversial[3] alternative to resonant excitation for some time.

Recently the technology has become available[11,12] to measure directly the spectrum of a variable energy source of pulsed bremsstrahlung in the 0.5 to 1.5 MeV range. With such a device, the DNA/PITHON nuclear simulator at Physics International, it was found[13,14] that both ^{115}In^m and ^{111}Cd^m were excited by predominantly resonant absorption through intermediate states, called gateway states, near 1 MeV which were broadened by their relatively short lifetimes. The sharp onset of the (γ,γ') reactions with increasing energy relegated to less than 3% any contributions from non-resonant processes and indicated that the gateway states were reasonably well connected by radiative transitions to both the ground states and the isomers. It appears that the principle cause for the large discrepancy between previous measurements was the difficulty in adequately characterizing the spectra of the irradiating sources. This is particularly true for radioactive line sources since all spectral contributions off the resonance line are due to Compton continua generated by environmentally-sensitive radiation transport processes.

The identification of relatively narrow gateway states below 1.5 MeV for the photoexcitation of isomers and the measurement of their cross-sections has reopened the question of the existence of similar gateways in the region from 1.5 to 6 MeV. In this energy range very early data[15,16] indicated that yields from (γ,γ') reactions increased as mediating states were accessed at higher energies. Evidence was accumulated in the form of increases in the slopes of curves showing isomeric yields as functions of the endpoint energies of the bremsstrahlung used to pump the reactions, but the changes were not dramatic. The largest value found[16] was 580 $\cdot$ 10^{-29} cm^2-keV for the photoexcitation of ^{87}Sr^m through a gateway at 2.66 MeV.

A renaissance in the study of (γ, γ') reactions has been launched by the availability of medical linear accelerators which can serve as intense and stable bremsstrahlung sources. The total doses which these devices can deposit in reasonable working periods have made possible the examination of reactions involving even rare nuclides for which target masses are limited to milligrams. In this way, the first (γ, γ') reaction leading to the deexcitation of an isomeric sample, $^{180}Ta^m(\gamma, \gamma')^{180}Ta$, was studied[17] with unexpected results.

The isomer $^{180}Ta^m$ is nature's rarest naturally occurring isotope.[18] Requiring an unlikely change of $\Delta J = 8$, the isomer was dumped to the ground state by bremsstrahlung having an endpoint of about 6 MeV. The partial width for this reaction was found[17] to be at least 0.5 eV, an enormous value exceeding any previous reports for (γ, γ') reactions by two to three orders of magnitude. The amount of deexcitation of the isomer observed was astonishing, corresponding to a total integrated cross-section in excess of $4 \cdot 10^{·25}$ cm^2-keV. Even more recently, this strength of the dumping reaction $^{180}Ta^m(\gamma, \gamma')^{180}Ta$ was qualitatively confirmed[19] with bremsstrahlung from the injector to the Darmstadt superconducting electron machine operated at 4.6 MeV. In this work the extension of these results to endpoint energies as low as 4.0 MeV will be described.

In general the endpoint energies of medical linacs cannot be continuously tuned and this presents a severe impediment to the duplication of the kind of detailed successes achieved[10·14] below 1.5 MeV. Nevertheless, experimental results obtained from samples irradiated with this type of device form a foundation for further investigations which might provide better resolution. Reported here are the results of two experimental series in which a variety of isomeric nuclei were excited by irradiating targets with 4 and 6 MeV fixed endpoint linacs.

Analytical Method

The photoexcitation rate for the production of an isomer through a
(γ,γ') reaction is given by

$$\frac{dN_{excited}}{dt} = N_T \int_{-\infty}^{\infty} \sigma(E) \, \Phi(E) \, dE, \qquad (1)$$

where $\sigma(E)$ is the cross-section in cm^2, $\Phi(E)$ is the spectral intensity
of the pump source in photons/cm^2-keV-sec and N_T is the number of target
nuclei. The spectral intensity can be expressed as the product of the
total photon flux Φ_0 and a relative spectral intensity function $F(E)$.
The combination $d/dt(N_{excited}/N_T)$ is commonly referred to as the activa-
tion rate. Assuming that the (γ,γ') reactions proceed through resonant
mediating states which are narrow relative to any structure of the
irradiating source spectrum, as is the case below 1.5 MeV, Eq. 1 becomes

$$\frac{dN_{excited}}{dt} = N_T \sum_i (\sigma\Gamma)_i \, \Phi(E_i). \qquad (2)$$

Here $\Phi(E_i)$ is the photon intensity at the gateway energy E_i and Γ_i is the
natural width in keV of the ith mediating state. From the uncertainty
principle, $\Gamma_i \geq \hbar/\tau_i$, where τ_i is the lifetime of the state. The
quantity $(\sigma\Gamma)_i$ is the integrated cross-section in cm^2-keV and is defined
by

$$(\sigma\Gamma)_i = \int_{i^{th} \text{ resonance}} \sigma(E) \, dE. \qquad (3)$$

The integrated cross-section is usually expressed as $\pi b_a b_0 \sigma_0 \Gamma/2$ where b_a
and b_0 are the branching ratios for decay from the gateway level to the
ground and isomeric states. The product $b_a b_0 \Gamma$ is called the partial
width for the transition. The quantity σ_0 is the amplitude of the
Breit-Wigner cross-section for the absorption transition,

$$\sigma_0 = \frac{\lambda^2}{2\pi} \frac{I_e + 1}{I_g + 1} \frac{1}{\alpha_p + 1}. \qquad (4)$$

where λ is the wavelength in cm of the γ-ray at the resonant energy, I_e and I_g are the nuclear spins of the excited and ground states, and α_p is the internal conversion coefficient of the absorption transition.

An exact evaluation of the integrated cross-sections in Eq. 2 requires the energy region in question to be scanned by a variable endpoint photon source with a well known spectrum. This was not possible in the current experiments because of the availability of only fixed endpoint medical linacs as pump sources, and thus the results are most accurately quoted in the form of activations normalized to the total photon flux of the irradiating device. However, it was instructive to assume that only one gateway was accessed and to compute its effective integrated cross-section. The integrated cross-section for such a hypothetical state located at energy E is then given by

$$(\sigma\Gamma) = \frac{1}{N_T \, \Phi(E)} \, \frac{dN_{excited}}{dt}. \qquad (5)$$

The cross-sections of these assumed single gateways was found by experimentally measuring the number of isomers excited during exposure to a source for which $\Phi(E)$ is well known.

Experimental Methods and Results

The irradiation of sample materials was accomplished with the aid of 4 and 6 MeV medical linacs at the Department of Radiology of the University of Texas Southwestern Medical Center at Dallas. Bremsstrahlung having a nominal endpoint of 6 MeV was obtained with a Varian Clinac 1800 linac operating in the 6 MeV mode. This device produced a dose rate of 4 Gy(H_2O)/min at a distance of 101.5 cm from the photon source. The 4 MeV irradiations were performed with a Varian 4/100 linac which provided a dose rate of 2 Gy(H_2O)/min at a distance of 101.2 cm from the photon source. The spectra of these machines have been well characterized[20,21] by use of the established EGS4 code[22] with a resolution of 0.25 MeV. The relative spectral intensity functions F(E) of each linac are shown in Fig 1. For convenience, these numbers are given explicitly in Table I. The absolute spectral intensity was found from the delivered dose by standard techniques.[23] The total flux of the 6 MeV Clinac 1800 beam was $5.35 \cdot 10^{15}$ photons/r^2-min while that of the 4/100 was found to be $3.23 \cdot 10^{15}$ photons/r^2-min. The inclusion of the variable r, the

119

distance in cm from the target location to the bremsstrahlung source, allowed these values to be adjusted to various sample positions.
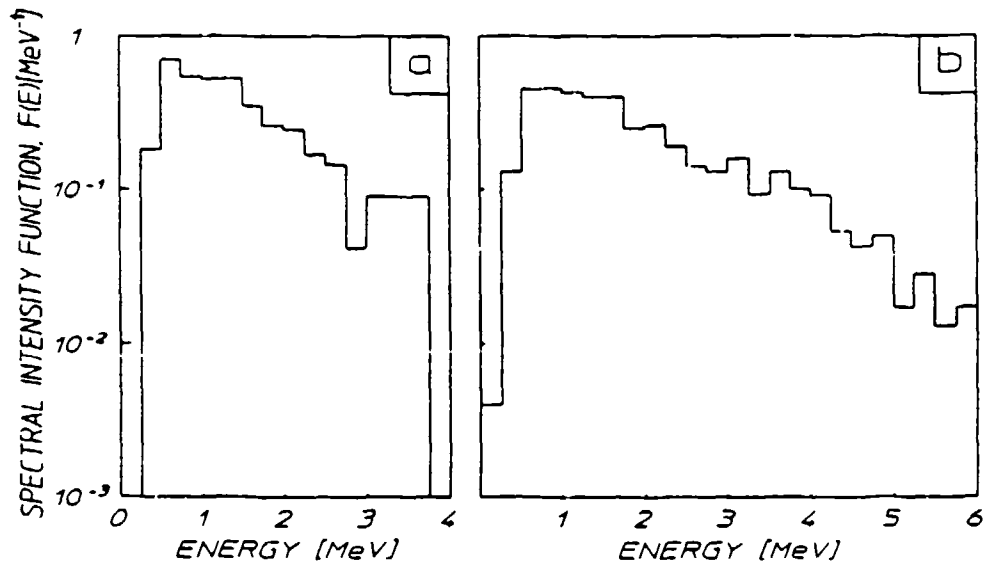
Figure 1: Relative spectral intensity functions F(E) of the bremsstrahlung produced by the medical linear accelerators used to irradiate samples in these experiments. The plots are normalized so that the integral under the curves is unity. The devices employed were:
a) Varian 4/100, with nominal endpoint energy of 4 MeV.
b) Varian Clinac 1800, operated in the nominal 6 MeV endpoint energy mode.

120

Table I

Relative spectral intensity function F(E) for the two medical linacs used in these experiments.

Energy [MeV]	4 MeV Linac F(E) [MeV^{-1}]	6 MeV Linac F(E) [MeV^{-1}]
0.125	0.001	0.004
0.375	0.180	0.130
0.625	0.711	0.450
0.875	0.549	0.460
1.125	0.524	0.430
1.375	0.529	0.400
1.625	0.350	0.400
1.875	0.258	0.250
2.125	0.246	0.260
2.375	0.168	0.190
2.625	0.145	0.140
2.875	0.041	0.130
3.125	0.089	0.160
3.375	0.089	0.092
3.625	0.089	0.130
3.875	0.001	0.100
4.125		0.090
4.375		0.053
4.625		0.042
4.875		0.049
5.125		0.017
5.375		0.028
5.625		0.013
5.875		0.017

The isotopes studied in these experiments are listed in Table II along with some relevant physical parameters. For each nuclide, the excitation rate was calculated from the number of isomeric decays observed in the samples following irradiation. This was reflected by the total counts in the full energy peaks of the isomeric fluorescence lines. These observations were corrected for detector efficiency, fluorescence intensity and the finite periods of exposure and counting. The latter factors used literature values for the half-lives of the isomers.[24] The samples were essentially transparent at the pump energies, but at the fluorescence energies some self-absorption was possible. A further correction which accommodated non-unity transparencies was calculated by Monte-Carlo methods for each sample. These calculations were tested by comparing the cross-sections obtained from samples containing identical materials, but in different geometries. The experimental methods employed to measure the activity present in each sample fall into three categories due to the physical properties of the nuclei. In the interest of brevity, these measurements will be illustrated in detail by an example of each technique.

The first nine nuclides listed in Table II have half-lives of less than about 153 sec. These samples therefore consisted of either powders or metallic foils enclosed in cylindrical polyethylene vials, termed rabbits, which could be pneumatically transported to a NaI(Tl) detector after individual exposures. The low energy resolution of the NaI(Tl) detector necessitated some care in the identification of the prominent features in the pulse height spectra obtained. Confirmation that these features were indeed the fluorescence signatures of the isomers present was made by determining the half-lives of these lines and comparing them with literature values. Data was simultaneously acquired through two Ortec 918A ADCAM multichannel buffers controlled by a personal computer. Thus, while one ADCAM served to produce a pulse height spectrum, the other collected a record of the total counts received in a preset dwell interval as a function of time.

Table II

Summary of isomeric nuclei studied. Nuclei marked * were present in isotopically enriched samples. In the sample column, R refers to samples contained in rabbits, P to flat planchettes, F to metallic foils, and B to scintillation bottles. The [180]Ta sample consisted of a dusting of oxide on a thin aluminum plate, referred to by D. In the case of the [176]Lu sample, β^- particles were observed instead of fluorescence photons; the NA in the transparency column indicates that this factor was not applicable for [176]Lu.

Nuclide	Abundance [%]	Sample Form	$T_{1/2}$	Principle Fluorescence [keV]	Transparency
[167]Er	91.54 *	Er_2O_3 (R)	2.28 sec	207.79 (41.70%)	57.90
[79]Br	50.69	LiBr (R)	4.86 sec	207.20 (75.80%)	84.90
[191]Ir	37.30	Ir (R)	4.94 sec	129.43 (25.70%)	10.50
[197]Au	100.00	Au (R)	7.80 sec	279.11 (73.00%)	92.70
[89]Y	100.00	YF_3 (R)	16.06 sec	909.15 (99.14%)	94.70
[77]Se	94.38	Se (R)	17.45 sec	161.92 (52.40%)	72.28
[179]Hf	13.63	HfO_2 (R)	18.68 sec	214.31 (94.20%)	52.40
[199]Hg	16.90	Hg_2Cl_2 (R)	43.20 sec	158.40 (53.00%)	43.96
[137]Ba	11.74	BaF_2 (R)	153.12 sec	661.66 (90.10%)	95.50
[111]Cd	12.80	Cd (F)	48.6 min	245.49 (94.00%)	76.35
[113]In	4.30	In (F)	1.66 hr	391.69 (64.20%)	98.30
[87]Sr	7.00	SrF_2 (P)	2.81 hr	388.40 (82.30%)	95.78
[176]Lu	2.59	$LuCl_2$ (B)	3.63 hr	beta	NA
[115]In	95.70	In (F)	4.49 hr	336.26 (45.80%)	98.00
[180]Ta	4.00 *	TaO_2 (D)	8.15 hr	55.79 (36.00%)	100.00
[135]Ba	6.60	BaF_2 (P)	1.20 d	268.27 (15.60%)	94.33
[195]Pt	33.80	Pt (Coin)	4.02 d	98.88 (11.40%)	4.76
[117]Sn	7.70	Sn (F)	13.6 d	158.56 (86.40%)	92.89
[123]Te	0.908	Te (P)	119.7 d	158.99 (84.00%)	62.68

A typical example of the data obtained in this way is given in Figs. 2 and 3, showing the pulse height and time spectra measured for the isomer $^{167}Er^m$. The total number of counts in the full energy peak at 207.8 keV was determined with a commercially available data reduction package. The information was then used to evaluate the integrated cross-section as a function of assumed gateway energy for both 4 and 6 MeV irradiations as shown in Fig. 4. The values shown in this graph have been corrected for the very small amounts of slow neutron contamination as discussed below.

207.8 keV - $^{167}Er^m$ a

207.8 keV - $^{167}Er^m$ b

Counts

10^4 10^3 10^2 10^1 10^0

0 100 200 300 400 Energy [keV]

0 100 200 300 400 Energy [keV]
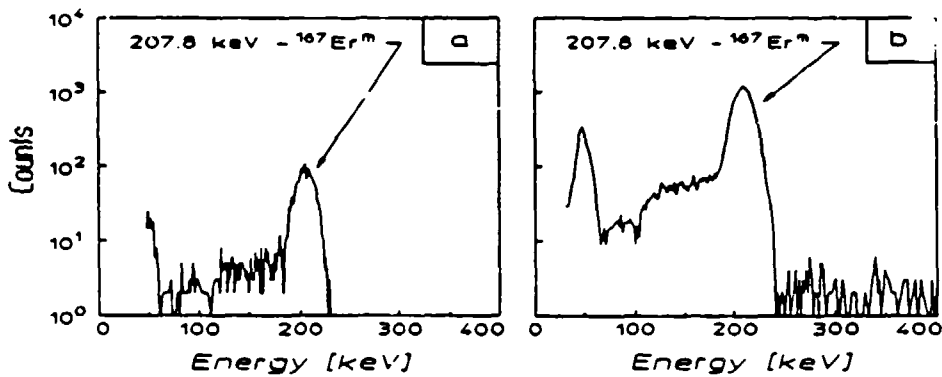
Figure 2: Pulse height spectra showing the 207.8 keV fluorescence line from the decay of $^{167}Er^m$. These spectra were obtained with a 7.6 cm × 7.6 cm diameter NaI(Tl) detector having a 5.1 cm × 2.5 cm diameter well. The samples were irradiated for 25 sec and the counting periods were 5 sec in duration. The endpoint energies of the bremsstrahlung used to activate the samples and the delay times from the end of irradiation to the start of counting were:
a)   4 MeV exposure, delay of 1.583 sec.
b)   6 MeV exposure, delay of 2.060 sec.

$T_{1/2} = 2.28$ s   a

$T_{1/2} = 2.28$ s   b

Counts/Channel

10^3 10^2 10^1 10^0

0 5 10 15 20 Time [sec]

0 5 10 15 20 Time [sec]
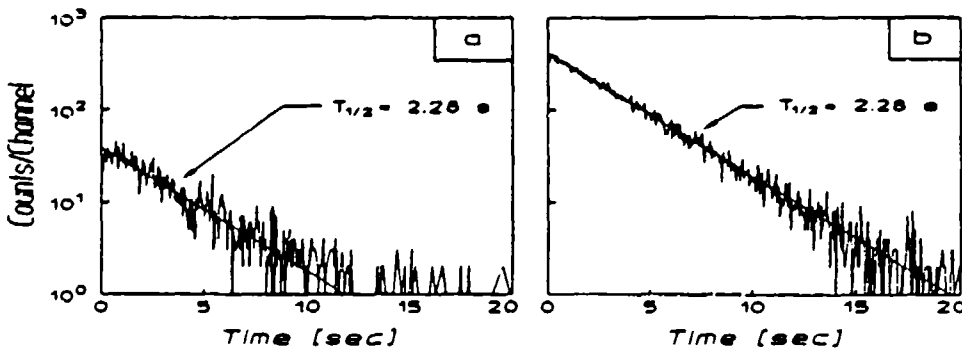
Figure 3: Time decay spectra of the total counting rate as a function of the time elapsed from the start of counting for $^{167}Er^m$. The solid lines indicate the decay expected from the literature value of the half-life, 2.28 sec. The spectra were obtained by recording the number of counts observed in successive dwell intervals of 0.05 sec with a multichannel scalar. The counting device was a 7.6 cm × 7.6 cm diameter NaI(Tl) detector having a 5.1 cm × 2.5 cm diameter well. All events above a chosen lower level discriminator were measured for samples after the following exposures:
a)   4 MeV exposure, delay of 1.583 sec.
b)   6 MeV exposure, delay of 2.060 sec.
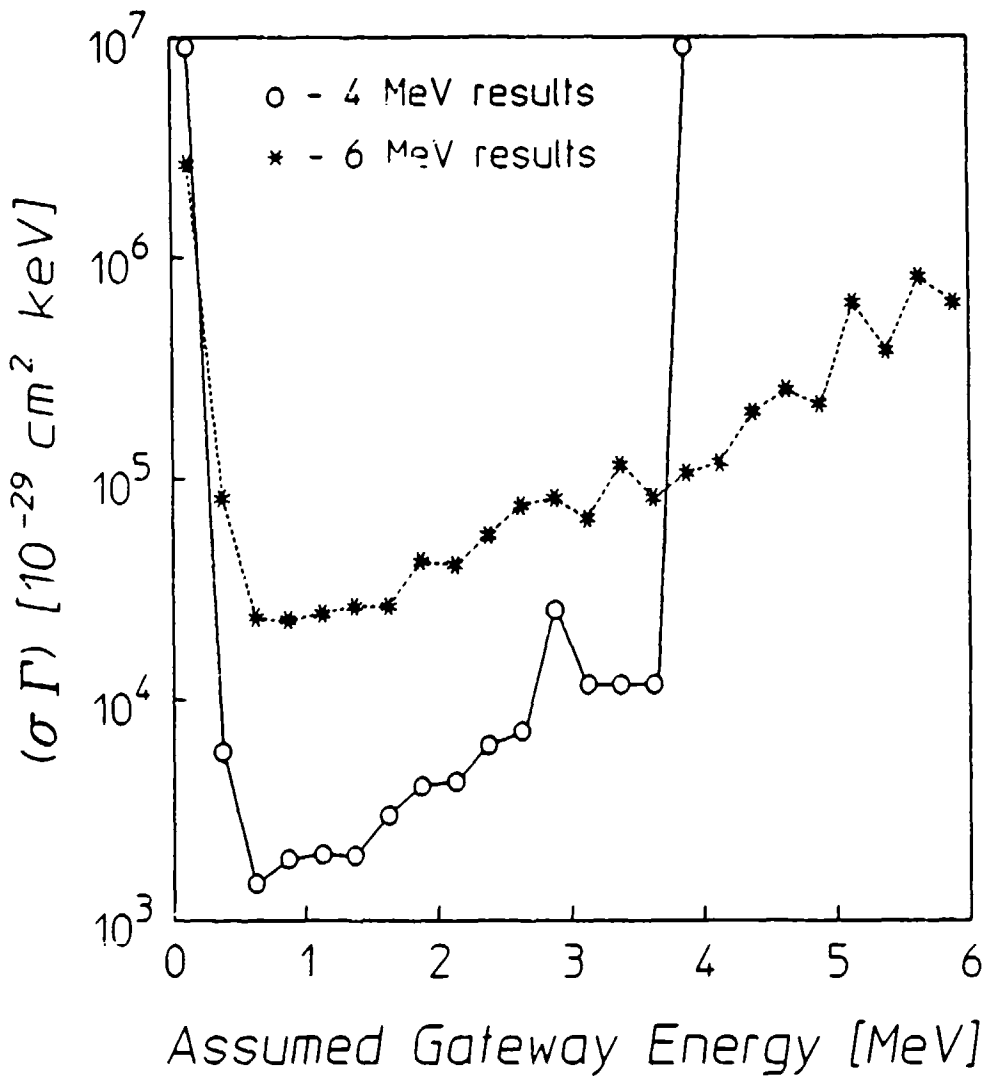
Figure 4: Integrated cross-sections for the reaction $^{167}Er(\gamma,\gamma')^{167}Er^m$ through single, unknown gateway states as functions of the energies at which these states could be assumed to lie. The circles indicate the results of measurements using the 4 MeV linac while the asterisks show those from the 6 MeV experiments.

A second experimental method was used to investigate the remaining nuclides in Table II, with the exception of ^{176}Lu. All of these have half-lives longer than 48.6 min, which allowed the samples to be irradiated in complex packages placed perpendicular to the photon beam. The packages were exposed for periods of up to four hours, removed by hand from the linac chambers at the end of the irradiations, and transported to the Center for Quantum Electronics at the University of Texas at Dallas for counting.

The measurements of the observed activities were made with a 10% relative efficiency, n-type germanium detector. Because of the higher energy resolution of this type of detector it was not necessary to monitor the time decay in detail for these samples although in some cases energy spectra were acquired after several different elapsed times. This second type of measurement is typified by the examination of the isomer ^{123}Te^{m}, which has a half-life of 119.7 days. Pulse height spectra following 4 and 6 MeV exposures are shown in Fig. 5. The fluorescence line at 159 keV was well defined in spectra excited with both 4 and 6 MeV linacs, and good counting statistics were observed. This was rewarding since there was some concern that the activation of such a long-lived isomer might be hidden by the natural background of the counting chamber. Nevertheless, since this is the longest-lived isomer ever reported to be excited by a (γ,γ') reaction, the time decay was experimentally determined from a sequence of energy spectra taken following a 6 MeV exposure. The count rate was observed in the fluorescence peak as a function of time as shown in Fig. 6 and the literature value of the half-life of ^{123}Te^{m} was in good agreement with this data. The resulting integrated cross-sections are displayed in Fig. 7, again corrected for very small amounts of neutron contamination.
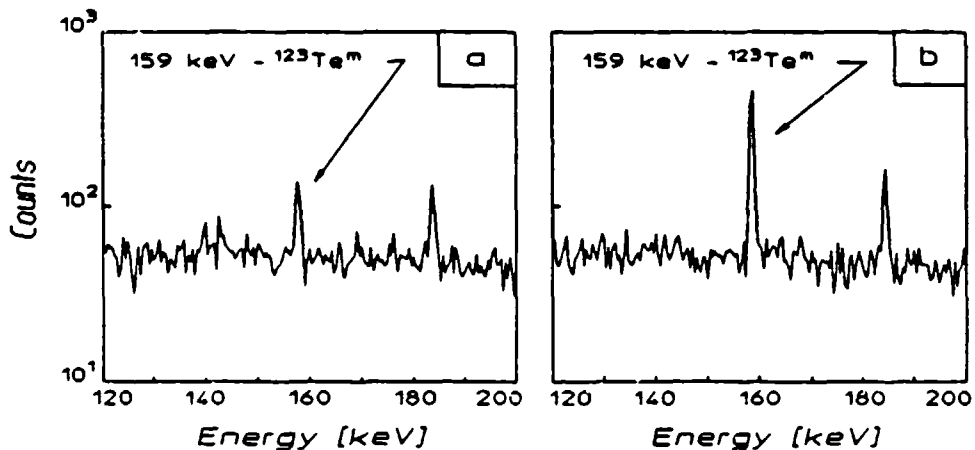
Figure 5: Pulse height spectra showing the 159 keV fluorescence line from the decay of $^{123}Te^m$. The spectra were obtained with an n-type high purity germanium detector. The samples were irradiated for 2 hours and the counting periods were 10 hours in duration. The endpoint energies of the bremsstrahlung used to activate the samples and the delay times from the end of irradiation ot the start of counting were:
a) 4 MeV exposure, delay of 43.91 hours.
b) 6 MeV exposure, delay of 22.98 hours.
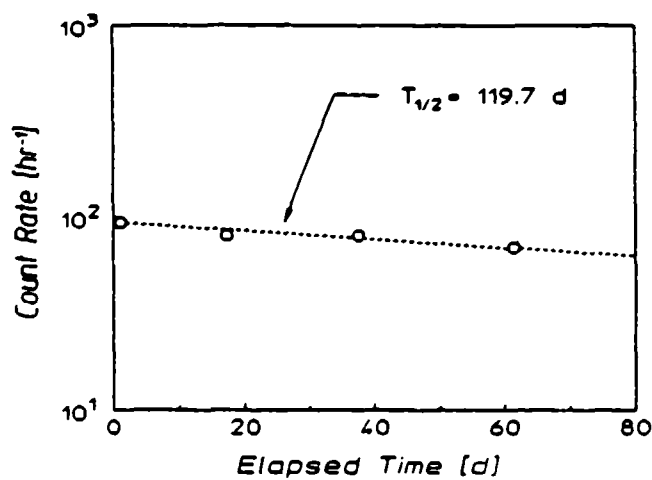
Figure 6: Plot of the time decay of the 159 keV fluorescence line from the decay of $^{123}Te^m$ following exposure to bremsstrahlung from the 6 MeV linac. The points represent the counting rate observed in several pulse height spectra obtained at different elapsed times. The size of the symbols is comparable to one standard deviation and the counting periods were of 10 hour duration. The dashed line indicates the expected decay half-life of 119.7 days, taken from the literature, and is in good agreement with the measurements.

128
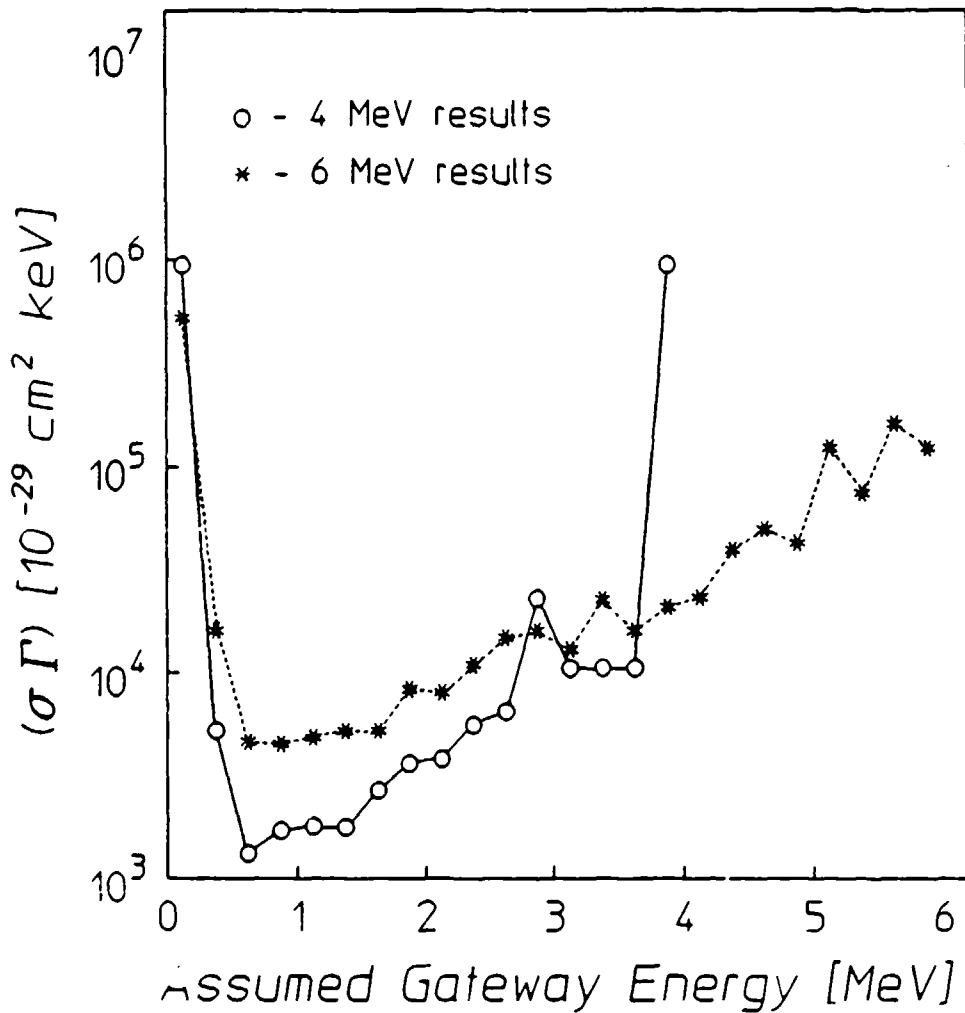
Figure 7: Integrated cross-sections for the reaction $^{123}Te(\gamma,\gamma')^{123}Te^m$ through single, unknown gateway states as functions of the energies at which these states could be assumed to lie. The circles indicate the results of measurements using the 4 MeV linac while the asterisks show those from the 6 MeV experiments.

The remaining nuclide, ^{176}Lu, was examined with a third detection scheme. The ground state of this isotope β^- decays with an endpoint energy of 565 keV and the isomer β^- decays with endpoint energies of 1313 keV (39.6%) and 1225 keV (60.4%). Since the isomer does not return to the ground state by a radiative transition, the number of excited nuclei must be measured by the detection of either the β^- particles or the signature photons from the daughter nucleus. This type of deexcitation process is similar to that of ^{180}Ta, which decays by both electron capture and β^- modes.

In the case of ^{176}Lu, the decay energies allowed the use of a Cerenkov detector. Samples consisting of 5 g of LuCl$_3$, dissolved in distilled water to make about 20 ml of solution, were contained in polyethylene scintillation bottles. The Cerenkov threshold in water is about 250 keV; β^- particles emitted in the decay of the isomeric states were nearly 10 times more efficient in producing Cerenkov events than those emitted from ground state nuclei. These events were measured by a system consisting of two RCA 8850 photomultiplier tubes in EG & G bases. The tubes were used in a coincidence mode by connecting their time synchronized outputs through a 150 MHz Phillips 755 logic unit, thereby recognizing only coincident signals from the Cerenkov photons produced by single β^- particles. These were recorded as a function of elapsed time in multichannel scalar spectra where each channel represented a dwell time of 40 sec. The detector was calibrated with ^{40}K decays from a KCl solution of known activity. The β^- particles resulting from ^{40}K decay have roughly the same endpoint energy as from ^{176}Lu^m. In these measurements, the individual count rates were monitored to avoid contributions from accidental coincidences triggered by separate β^- events or by thermoluminescence from the bottle. A fit to the experimental data shown in the typical spectrum of Fig. 8 produced a value for the half-life of ^{176}Lu^m, 3.58 $\pm$ 0.05 hours, which was in good agreement with the literature value of 3.63 hours. The integrated cross-section as a function of gateway energy was calculated from the activation present immediately after irradiation and is shown in Fig. 9.
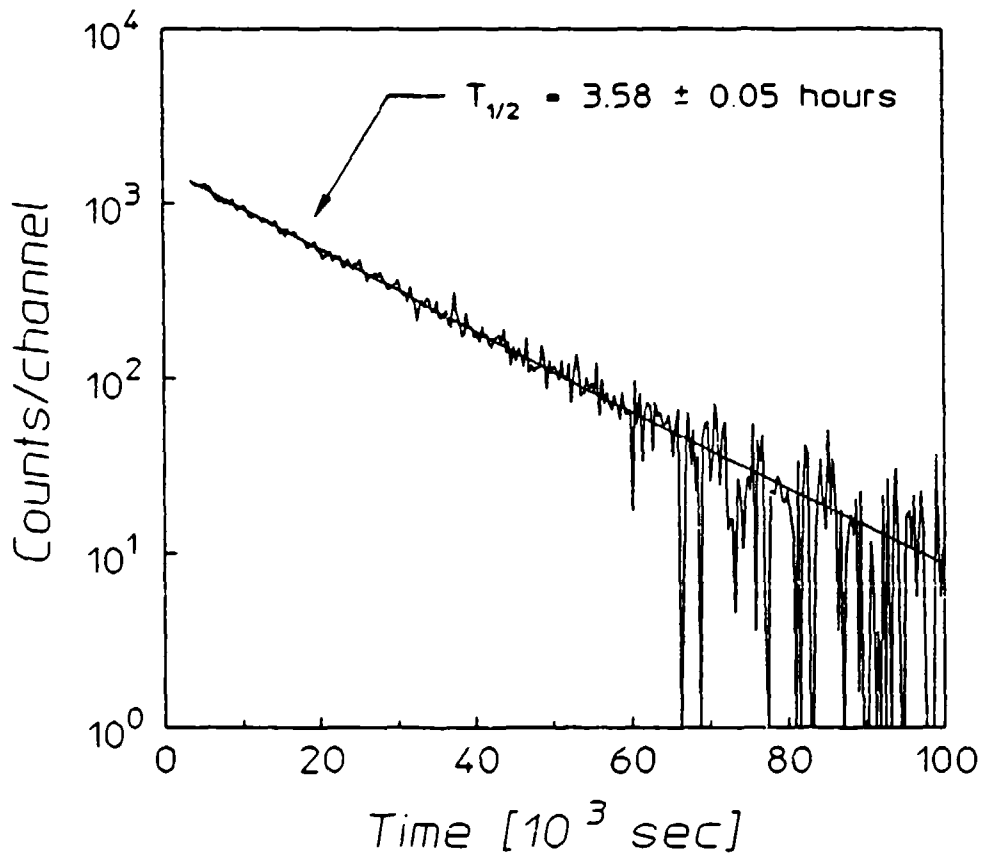
Figure 8:   Time decay spectrum of the total counting rate as a function of the time elapsed from the start of counting for ¹⁷⁶Lu^m following a 6 MeV exposure.   This was obtained by recording the number of counts observed in successive dwell intervals of 320 sec with a multichannel scalar.   The device used to make these measurements consisted of two RCA 8850 photomultiplier tubes operated in a coincidence mode.   Samples were composed of LuCl₃ dissolved in distilled water in plastic bottles.   The observed decay signatures were β⁻ particles which were detected from the Cerenkov radiation produced in the water.   The sample was irradiated for 40 minutes and the delay time was 53 minutes.   A fit to the data is shown by the solid line and gives a half-life of 3.58 ± 0.05 hours, in good agreement with the literature value of 3.63 hours.

131
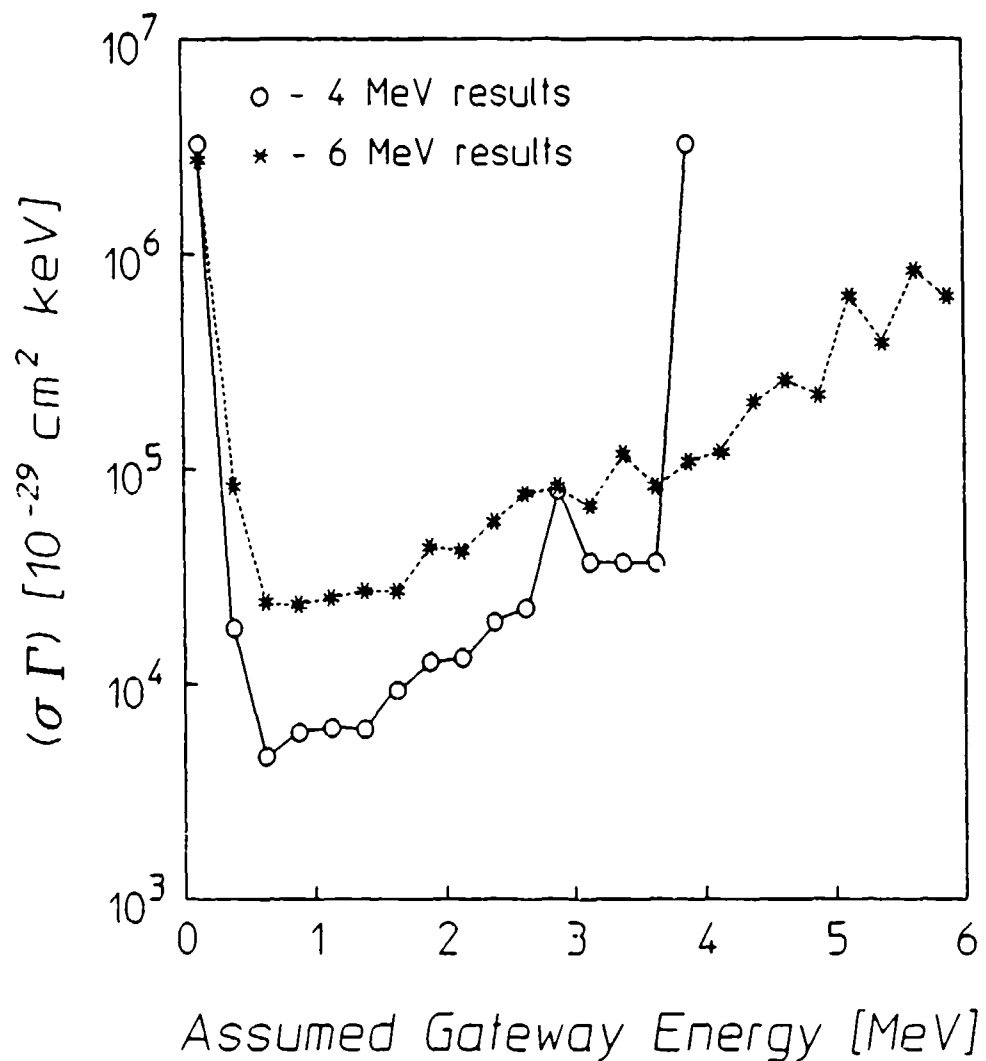
Figure 9: Integrated cross-sections for the reaction $^{176}Lu(\gamma,\gamma')^{176}Lu^m$ through single, unknown gateway states as functions of the energies at which these states could be assumed to lie. The circles indicate the results of measurements using the 4 MeV linac while the asterisks show those from the 6 MeV experiments.

Since the high energy photons used in these experiments were capable of evaporating neutrons from some materials, the possibility of neutron excitation of the isomeric populations had to be carefully considered. The principal objective of this study was to characterize (γ,γ') reactions in the energy range from 1.5 to 6 MeV. Thus any contributions to the yield from processes indirectly mediated by neutrons would have appeared as unwanted contaminations of the photoexcitation cross-sections finally obtained. In principle, two types of neutron reactions could have occurred: inelastic (n,n') reactions which would have required hot neutrons and neutron capture (n,γ) processes driven by any fluxes of thermal or epithermal neutrons which might have been present. Both would have required a primary source of neutrons to have been active during the bremsstrahlung irradiation.

Only eight isotopes have thresholds for (γ,n) reactions below 6 MeV. Four of these are rare and can be reasonably excluded from consideration. The materials used in the irradiation device and facility were documented. In these materials only ^{2}H, ^{9}Be, ^{13}C and ^{17}O can be expected to have served as sources of neutrons in the irradiation environment actually used in these experiments.

As the photon intensity was monitored throughout the course of these experiments, the flux of primary photoneutrons can be calculated with reasonable accuracy from the following potential sources:

1) a 0.025 cm thick Be window located below the bremsstrahlung converter target in the 6 MeV linac.

2) the ^{2}H in the cooling water in the bremsstrahlung converter target.

3) the ^{2}H in the humidity in the chamber and the ^{13}C and ^{17}O in the volume of atmosphere incidentally irradiated.

4) the ^{2}N, ^{13}C and ^{17}O in the concrete used in construction.

Of these, the first dominated by orders-of-magnitude, giving an expected flux of 10^{3} neutrons/cm^{2} sec at the position of the experimental samples.

The potential activation produced by such a flux is difficult to estimate because the cross-sections for (n,n') reactions are poorly known. However, if it is assumed that all of the flux carries at least

threshold energy, the cross-section $\sigma_{n,100\%}$ necessary to produce all of the measured activation from all sources of neutrons can be calculated. These resulting values are summarized in Table III in units of barns and values can be seen to range from tens to thousands. This is to be compared with the few hundreds of millibarns that describe (n,n') reactions in those few cases where measurements have been reported in the literature.

Total neutron cross-sections, which certainly must be greater than the inelastic component, are available for all of the materials stud-ied.[25] They are summarized in Table III, together with any other cross-sections which might bound more closely the value ected for the relevant (n,n') reaction producing the observed isomer.[26-33] Finally, in Table III is tabulated the ratio, Ω, which compares the most restrictive upper limit to $\sigma_{n,100\%}$, the cross-section for inelastic neutron excitation which would be necessary to explain all of the observed yield.

In effect Ω is the maximum fractional contamination through the fast neutron channel of the photoexcitation yield. As can be seen, values are generally smaller than 1% and exceptions occur only in cases for which restrictive estimates of (n,n') cross-sections are unavail-able.

The fast neutron flux expected in these experiments, 10^3 neu-trons/cm^2-sec was too small to confirm by direct measurement in such a high ambient level of photon irradiation. However, in order to com-pletely exclude the remote possibility of an undocumented emplacement of some strong photoneutron source such as ^{235}U in the irradiation environ-ment, a measurement was attempted using standard procedures.[34,35] The (n,p) reactions of ^{46}Ti, ^{47}Ti and ^{58}Ni are well-documented and provide clear signature photons for convenient periods of decay. These nuclei are not affected by the photon beam in this energy range but they are sensitive to fast neutrons, producing the daughters ^{46}Sc, ^{47}Sc and ^{58}Co, respectively.

134

Table III

Summary of fast neutron contamination limits. The fast neutron cross-section, $\sigma_{n,100\%}$ is that required to produce 100% of the observed activations. Maximum values for the true total neutron cross-section of the element of interest,[25] σ_{tot}, are shown for the energy range 0.1 to 6 MeV. When available, the non-elastic cross-section for the element has been shown in parentheses following the elastic cross-section. The most restrictive additional cross-section, σ_{lim}, for the particular isotope or element is given with its type and E_{max}, the energy up to which it was determined. Cross-section types are as follows: ie - inelastic in element; i - inelastic in isotope; n - non-elastic in isotope; fi - inelastic in isotope, average for fission spectrum. The factor Ω is the ratio of the most specific observed cross-section to the cross-section required for a 100% contamination effect, and thus represents an upper limit for contamination of the neutron effects.

Nuclide	$\sigma_{n,100\%}$ [b]	σ_{tot} [b]	σ_{lim} [b]		Type	E_{max} [MeV]	Ω [%]
^{167}Er	2700	9	-		-	-	0.33
^{79}Br	140	7.5	-		-	-	5.4
^{191}Ir	2590	10.3	-		-	-	0.40
^{197}Au	95	10	1.3	[32]	i	5.3	1.4
^{89}Y	20	11.5	0.2	[27]	i	4.0	1.0
^{77}Se	490	8.3(2.4)	0.73	[26]	fi	-	0.15
^{179}Hf	1940	20	0.4	[31]	i	1.6	0.02
^{199}Hg	120	10(2.6)	0.14	[33]	i	2.1	0.12
^{137}Ba	130	7.3(2)	0.66	[30]	i	3	0.51
^{111}Cd	210	8	0.23	[26]	fi	-	0.11
^{113}In	320	6.3	0.047	[28]	i	1.0	0.01
^{87}Sr	60	10	0.11	[26]	fi	-	0.18
^{176}Lu	2638	7	-		-	-	0.27
^{115}In	430	6.3	0.38	[29]	i	5.3	0.09
^{180}Ta	3016	8.5(2.9)	1.8	[32]	ie	1.8	0.06
^{135}Ba	420	7.3(2)	-		-	-	0.48
^{195}Pt	1350	10	0.68	[32]	ie	1.8	0.05
^{117}Sn	70	6.8(2)	-		-	-	2.9
^{123}Te	530	6	-		-	-	1.1

135

In this measurement, the foils were irradiated, removed to the HPGe detector system and counted to obtain pulse height spectra. In these spectra no signature photon peaks from the daughters were evidenced at any levels above the background of the counting chamber. It was therefore possible to obtain only an upper bound on the fast neutron flux at the sample position, that of $7 \cdot 10^4$ neutrons/cm^2 sec.

As can be seen, the limit established by measurement is not particularly restrictive, being 70 times larger than the calculated values of fast neutron flux. Nevertheless, even if the limits of contamination in Table III are raised by this factor of 70, at least half of the samples would still be affected by of errors less than 10%. Only in the case of unknown inelestic cross-sections for a (n,n') reaction closely approaching the total values shown in Table III could an undocumented sample of rare material have produced a level of fast neutron flux sufficient to contaminate the results of the (γ,γ') reactions being studied. Such occurrances would have required the coincidence of very improbable circumstances and merit no further consideration. That so little fast neutron contamination occurred due to the 6 MeV linac precluded any possibility of significant effects of fast neutrons in the 4 MeV experiments.

The thermal and epithermal neutron fluxes due to the 6 MeV linac, Φ_{th} and Φ_{ep}, could be measured in this environment by irradiating two thin indium foils, one of which was shielded from thermal neutrons by a cadmium cover. In accordance with standard techniques,[36] energy spectra obtained from these foils were examined after exposure for signature photons from the isomer ^{116}In^m, which is produced by a branch of the reaction ^{115}In(n,γ)^{116}In^{m,g}. The magnitudes of the fluorescence lines observed in both the bare and the shielded samples allowed the determination of the neutron fluxes Φ_{th} = 12 neutrons/cm^2-sec and Φ_{ep} = 6 neutrons/cm^2-sec from literature values of the thermal and epithermal neutron cross-sections.[37] The neutron fluxes from the 4 MeV linac were bounded in a similar way. A bare indium foil was exposed, but later showed no photopeaks from ^{116}In^m observable above the background. Upper bounds for the neutron fluxes were found by assuming for the 4 MeV environment the same 2.1 ratio of thermal to epithermal neutrons found at 6 MeV. The activation was taken to be just below the level of noise, which gave $\Phi_{th} \leq 6$ neutrons/cm^2-min and $\Phi_{ep} \leq 3$ neutrons/cm^2-min during operation of the 4 MeV linac. The small amount of activation of each of

136

the isomers due to these neutrons was subtracted from the total activation observed. In no case did the contribution from thermal and epithermal neutrons in the 4 McV environment exceed 0.05%. The thermal and epithermal neutron fluxes in the 6 MeV chamber produced contributions below 1.51% for all isomers except for $^{179}Hf^m$ (6.41%) and $^{199}Hg^m$ (5.40%). Even in these materials, it is apparent that photoexcitation is the dominant mechanism for the observed activation.

Limits on the fractional contamination of the (γ,γ') activation of the isomers studied in these experiments are summarized as Ω in Table III for processes initiated by fast neutrons and as A_n/A_{Tot} in Table IV for processes involving slow neutrons. In all cases, the values exceeding 1% are primarily the consequence of poorly bounded neutron cross-sections for the intermediate steps. In those cases the only available values were those describing total processes which certainly bound the (n,n') reactions, but generously so. There is no reason to suspect that the unmeasured reactions are uniformly larger and that only the smallest appear in the literature. The best resolved limits are those bounding neutron contributions to a few tenths of a percent. It seems reasonable to conclude that in all cases examined in this work the (γ,γ') channels dominated by orders-of-magnitude.

The final results for the integrated cross-sections of the nuclides examined here are shown in Table IV, from which the normalized activations may be obtained with the information of Table I. The integrated cross-sections are given at the reference energy of 2.125 MeV but values at other energies may be obtained from the numbers in Table I. The limiting fraction of neutron activation present in the total activation is also displayed for isomers which could be produced by neutron capture in stable isotopes.

In addition to the materials listed, several other nuclei were irradiated. A sample was exposed which contained natural abundances of the nuclides, ^{107}Ag, whose isomer has a half-life of 44.2 sec and a fluorescence line at 93.2 keV, and ^{109}Ag, whose isomer has a 39.6 sec half-life and a photopeak at 88.0 keV. This sample was activated, but the resolution available with the NaI detector was not sufficient to separate the two contributions. The isomer $^{183}W^m$ was also successfully activated, but uncertainties in the transparency factor due to the nature of the sample prevented quantitative analysis in this case. Six

other isomeric nuclei, ^{207}Pb, ^{90}Zr, ^{177}Hf, ^{178}Hf, ^{176}Yb and ^{190}Os were irradiated but exhibited no measurable activation.

Table IV

Summary of experimental results. The quantity ΔJ is the change in spin between ground state and isomer. For both 4 and 6 MeV irradiations, the integrated cross-sections of a single gateway state at the reference energy of 2.125 MeV are given as $(\sigma\Gamma)$ and have been corrected for thermal and epithermal neutron contaminations. The term "units" is used for the sake of brevity to represent units of 10^{-29} cm^2-keV. Also given is the fraction of neutron contamination in the total activation, A_n/A_{Tot}, and the ratio of 6 MeV activation to 4 MeV activation, κ. The comment NA is used when no naturally abundant parent is available for (n,γ) reactions.

Nuclide	ΔJ	4 MeV $(\sigma\Gamma)$ [units]	A_n/A_{Tot} [%]	6 MeV $(\sigma\Gamma)$ [units]	A_n/A_{Tot} [%]	κ
^{167}Er	3	4225 ± 9	0.01	40611 ± 426	0.32	9.61
^{79}Br	3	607 ± 16	NA	2199 ± 27	NA	3.62
^{191}Ir	4	6995 ± 558	NA	42352 ± 1133	NA	6.05
^{197}Au	4	2383 ± 37	NA	15628 ± 75	NA	6.56
^{89}Y	4	8 ± 5	NA	307 ± 10	NA	38.38
^{77}Se	3	303 ± 4	0.03	7734 ± 38	0.76	25.52
^{179}Hf	4	8655 ± 112	0.04	29007 ± 128	6.41	3.35
^{137}Ba	4	304 ± 21	<0.01	2296 ± 27	0.07	7.55
^{199}Hg	6	234 ± 9	0.05	1686 ± 50	5.40	7.21
^{111}Cd	5	846 ± 11	<0.01	2992 ± 52	0.07	3.54
^{113}In	4	1182 ± 54	NA	5501 ± 208	NA	4.65
^{87}Sr	4	362 ± 12	<0.01	1027 ± 21	0.89	2.84
^{176}Lu	6	13212 ± 87	0.01	41502 ± 2680	1.51	3.14
^{115}In	4	1643 ± 15	NA	7936 ± 16	NA	4.83
^{180}Ta	8	16481 ± 6021	NA	41603 ± 772	NA	2.52
^{135}Ba	4	1152 ± 57	<0.01	7121 ± 134	0.39	6.18
^{195}Pt	4	2723 ± 150	<0.01	16521 ± 263	0.03	6.06
^{117}Sn	5	292 ± 43	<0.01	1040 ± 31	0.07	3.56
^{123}Te	5	3829 ± 672	<0.01	8038 ± 373	1.45	2.10

Conclusions

The values of the integrated cross-section shown in Table IV are unexpectedly large, in many cases two to three orders of magnitude larger than any previous results. The Breit-Wigner model indicates that these cross-sections correspond to remarkably large partial widths. Although these numbers are surprising, there are several considerations which inspire confidence in the results, not the least of which is the reproducibility of the findings under different experimental conditions. Perhaps the most compelling argument is seen in the result for the reaction $^{87}Sr(\gamma,\gamma')^{87}Sr^m$. As was previously mentioned, an early value was measured of $580 \cdot 10^{-29}$ cm^2-keV for the integrated cross-section at 2.66 MeV. The current derived value for a hypothetical single gateway at 2.66 MeV taken from the 4 MeV irradiations is $(613 \pm 21) \cdot 10^{-29}$ cm^2-keV. These two measurements are in good agreement when the amount of variability in early experiments is considered. The fact that the cross-section at the reference energy of 2.125 MeV obtained from the 6 MeV linac is 2.87 times larger than that from the 4 MeV exposures indicates that at least one other gateway has been accessed by photons with energies above about 3 MeV.

The example of ^{87}Sr demonstrates the utility of the single gateway assumption in discussing the results. Another important case is that of $^{123}Te^m$. Examination of Fig. 6 shows that the cross-section curves from the 4 and 6 MeV experiments become equal in the vicinity of 3 - 3.5 MeV. This would strongly imply that the reaction $^{123}Te(\gamma,\gamma')^{123}Te^m$ proceeds through a single mediating level located in this range, having an integrated cross-section of about $16500 \cdot 10^{-29}$ cm^2 keV. If this is indeed true, $^{123}Te^m$ may form the cornerstone of the extension of the spectral calibration technique used in Refs. 11 and 12 to energies up to 6 MeV. The isomer $^{79}Br^m$ was instrumental in implementating this technique, as below 1.5 MeV it is photoactivated through only a single gateway at 761 keV with integrated cross-section of $6.2 \cdot 10^{-29}$ cm^2-keV. It should be noted that no other nuclide in this study other than ^{123}Te exhibited such strong evidence for an actual single gateway state in the range of 1.5 - 6.0 MeV.

As stated earlier, the current values for the integrated cross-sections are orders of magnitude larger than those obtained in earlier experiments. It has been suggested that this is caused by non-resonant channels which open near the threshold for (γ,n) reactions. The state density is particularly high near this threshold and the earlier work,[15,16] conducted with sources having endpoint energies below 3 MeV, may not have accessed this process. However, this suggestion would not seem to be supported by the data. The ratios of activation with 6 MeV bremsstrahlung to that from 4 MeV bremsstrahlung, given in Table IV as κ, vary from 2.10 to 9.61 for all but two isomers. These ratios would not appear large enough to signify that a non-resonant process near the (γ,n) threshold was accessed by the few photons in the high energy tail of the bremsstrahlung spectrum. The exceptions to this behavior are ^{89}Y, with $\kappa = 38.38$, and ^{77}Se, having a ratio of 25.52. The magnitude of the cross-section determined for $^{89}Y^m$ from the 6 MeV irradiations, $(307 \pm 10) \cdot 10^{-29}$ cm^2-keV, would seem too small to be evidence for a non-resonant process which is directly related to the large state density above 4 MeV. However, for $^{77}Se^m$ it is possible that the larger cross-section, $(7734 \pm 38) \cdot 10^{-29}$ cm^2 keV, from the 6 MeV exposures does indeed point to this type of excitation mechanism. It is important to note that if this is the case, such a process is the exception rather than the rule in this energy range.

The pervasiveness found for the unexpectedly large values for the integrated cross-sections in this energy range suggests some type of core property varying slowly with increasing nuclear size. In such a case, however, there would seem to be the need for a mixing of several single particle states. The decay of the gateway level could then occur by several different cascades with comparable probabilities. The partial widths corresponding to these cross-sections are characteristic of relatively unhindered E1 transitions. Systematic studies[38] have shown that collective octupole oscillations of the nuclear core can unhinder E1 transitions, making very short lived states available for (γ,γ') reactions excited from ground states at energies between 1 and 2 MeV. The literature,[39] however, suggests that the branching for such a collective state would almost entirely favor the initial transition so that the product $b_a b_0$ would be severely diminished. This would largely offset the increased width Γ in expressions for the integrated cross-section. This expectation is supported by the early data of Refs. 15 and 16.

Since the density of states is elevated at energies of 1 to 2 MeV above the ground state, an alternate speculation is attractive. A strong collective oscillation of the core might serve to mix enough single particle states so that radiative branches to several different lower levels become comparable. In this case a very large integrated cross-section for photoexcitation of isomers through (γ,γ') reactions might be found to be only slightly dependent upon the detailed single particle assignments of neighboring nuclei. This would seem to be the case since the results of these experiments do not show a strong correlation with quantities such as ΔJ or its projection, ΔK.

The study of photoexcitation of isomeric nuclei through (γ,γ') reactions is obviously far from complete and detailed investigations which allow a final determination of the presence of resonant gateways are underway. These experiments employ several methods to modify the energy spectra of fixed endpoint sources and show great promise. Nevertheless, the lack of availability of a true variable endpoint source capable of producing sufficient photon fluences is still the largest single barrier to the measurement of the physical processes underlying these reactions.

References

1. B. Pontecorvo and A. Lazard, C. R. Acad. Sci. 208, 99 (1939).

2. G. B. Collins, B. Waldman, E. M. Stubblefield and M. Goldhaber, Phys. Rev. 55, 507 (1939).

3. K. Yoshihara, Zs. Nemeth, L. Lakosi, I. Pavlicsek and A. Veres, Phys. Rev. C 33, 728 (1986).

4. B. Harmatz, Nucl. Data Sheets 27, 453 (1979).

5. *Evaluated Nuclear Structure Data File* (Brookhaven National Laboratory, Upton, New York, 1986).

6. Y. Watanabe and T. Mukoyama, Bull. Inst. Chem. Res. 57, 72 (1979).

7. M. Krcmar, A. Ljubicic, K. Pisk, B. Logan and M. Vrtar, Phys. Rev. C 35, 1943 (1987).

8. I. Bikit, J. Slivka, I. V. Anicin, L. Marinkov, A. Rudic and W. D. Hamilton, Phys. Rev. C 35, 1943 (1987).

9. A. Ljubicic, K. Pisk and B. A. Logan, Phys. Rev. C 23, 2238 (1981).

10. N. Ikeda and K. Yoshihara, Radioisotopes 7, 11 (1958).

11. J. A. Anderson and C. B. Collins, Rev. Sci. Instrum. 58, 2157 (1987).

12. J. A. Anderson and C. B. Collins, Rev. Sci. Instrum. 59, 414 (1988).

13. C. B. Collins, J. A. Anderson, Y. Paiss, C. D. Eberhard, R. J. Peterson and W. L. Hodge, Phys. Rev. C 38, 1852 (1988).

14. J. A. Anderson, M. J. Byrd and C. B. Collins, Phys. Rev. C 38, 2838 (1988).

15. M. L. Wiedenbeck, Phys. Rev. 67, 92 (1945).

16. E. C. Booth and J. Brownson, Nucl. Phys. A98, 529 (1967).

143

17. C. B. Collins, C. D. Eberhard, J. W. Glesener and J. A. Anderson, Phys. Rev. C 37, 2267 (1988).

18. A. G. W. Cameron, in *Essays in Nuclear Astrophysics*, edited by C. A. Barnes, D. D. Clayton and D. N. Schramm (Cambridge Univ. Press, Cambridge, 1982), p. 23.

19. A. Richter and W. Ziegler, Private communication.

20. R. Mohan, C. Chui and L. Lidofsky, Med. Phys. 12, 595 (1985).

21. N. C. Ikoro, D. A. Johnson and P. P. Antich, Med. Phys. 14, 93 (1987).

22. *The EGS4 Code System*, Walter R. Nelson, Hideo Hirayama and David W. O. Rogers, SLAC Report 265 (Stanford Linear Accelerator Center, Stanford, Calif. 1985).

23. H. E. Johns and J. R. Cunningham, *Physics of Radiology*, Fourth Edition, (Charles C. Thomas, Springfield, Illinois, 1983), pp. 217 - 224, Appendix A - 3.B.

24. E. Browne and R. B. Firestone, *Table of Radioactive Isotopes*, edited by V. S. Shirley (Wiley, New York, 1986).

25. *Neutron Cross Sections: Volume II, Curves*, Third Edition, D. I. Garber and R. R. Kinsey, BNL 325 (National Neutron Cross Section Center, Brookhaven National Laboratory, Upton, New York, 1976).

26 A. Calamand, "Cross Sections for Fission Neutron Spectrum Induced Reactions" in *Handbook of Nuclear Activation Cross Sections*, International Atomic Energy Agency Technical Report Series No. 156 (IAEA, Vienna, 1974), pp. 273 - 324.

27. E. Ramstrom, Nucl. Phys. A315, 143 (1979).

28. H. A. Grench and H. O. Menlove, Phys. Rev. 165, 165 (1968).

29. H. C. Martin, B. C. Diven and R. F. Taschek, Phys. Rev. 93, 199 (1954).

30. C. P. Swann and F. R. Metzger, Phys. Rev. 100, 1329 (1955).

31. G. L. Sherwood, A. B. Smith and J. F. Whalen, Nucl. Sci. & Eng. 39, 67 (1970).

32. J. B. Guernsey and A. Wattenberg, Phys. Rev. 101, 1516 (1956).

33. K. Sakurai and I. Kondo, Nucl. Inst. and Meth. 187, 649 (1981).

34. *ASTM Standard Method for Determining Neutron Flux, Fluence and Spectra by Radioactivation Techniques*, Publication E 261-77 (American Society for Testing and Materials, Phyladelphia, 1987), and references cited there.

35. K. H. Beckurts and K. Wirtz, *Neutron Physics*, Trans. by L. Dresner (Springer-Verlag, New York, 1964).

36. *ASTM Standard Method for Determining Thermal Neutron Reaction and Fluence Rates by Radioactivation Techniques*, Publication E 262-86 (American Society for Testing and Materials, Philadelphia, 1987) and references cited there.

37. F. W. Walker, D. G. Miller and F. Feiner, Eds., *Chart of the Nuclides*, Thirteenth Edition (General Electric Company, San Jose, Calif. 1983).

38. A. de Schalit and H. Feshback, *Theoretical Nuclear Physics Vol. 1: Nuclear Structure* (Wiley, New York 1974).

39. C. F. Perdrisat, Rev. Mod. Phys. 38, 41 (1966).

LIMITS ON NEUTRON ACTIVATION INTERFERENCES IN PHOTOACTIVATION CROSS-SECTION MEASUREMENTS IN THE 1.5-6 MeV RANGE

by J. A. Anderson, C. D. Eberhard, J. J. Carroll, M. J. Byrd,
and C. B. Collins
Center for Quantum Electronics, University of Texas at Dallas
and E. Scarbrough and P. P. Antich
University of Texas Southwestern Medical Center

Introduction

Recent measurements[1-4] have indicated that (γ,γ') cross sections at energies between 1.5 and 6 MeV may be three orders of magnitude or more greater than corresponding cross sections at lower energies. Since the high-energy photons used in these experiments can also produce neutrons through (γ,n) reactions, it is necessary to rule out contamination of the (γ,γ') cross section results by this incidental neutron field. This study establishes limits on the contributions of neutron reactions in previous experiments. Two basic approaches can be made toward this end: quantifying contributions from known neutron sources and making independent measurements of the neutron flux. Both approaches have been taken in this work and have been compared for mutual agreement. On the basis of this study, neutron-induced interferences are at least two to three orders of magnitude less than the observed isomeric activity due to photoexcitation.

Neutron Interference in Photoactivation Measurements

Two types of interfering neutron reactions can affect nuclear photoactivation studies on isomeric nuclei. The first is excitation of the isomer through (n,n') processes that populate the isomer either directly or through cascades from higher lying states. This, of course, requires neutrons with energies greater than the energy separation between the ground and isomeric states. All isomers can be excited

through the (n,n') process, which typically has a cross section on the order of several hundreds of millibarns. A summary of the isomers studied in references 1-4 is given in Table I. Note that $^{77}Se^m$, the lowest lying isomer which was excited from the ground state, requires a minimum neutron energy of 162 keV to initiate an (n,n') reaction. Measured integrated cross sections for isomeric photoactivation have been included in Table I. These values have been updated from previous reports to include additional trials and improved instrumental parameters. Because the earlier technique does not permit identification of a unique photoactivation gateway, a hypothetical single gateway at 2.125 MeV has been used to calculate the cross section values listed here. These values can be adjusted to other assumed gateway energies by using the spectrum of the bremsstrahlung source employed in these experiments[5,6] which is shown in Fig. 1. If the relative intensity of the source at 2.125 MeV is $\phi(2.125)$ and if the intensity at the desired energy E is $\phi(E)$, then the adjusted value for the cross section is given by

$$\sigma(E) = \sigma(2.125 \text{ MeV}) \times [\phi(2.125)/\phi(E)] \qquad . \qquad (1)$$

Values for the ratio $\phi(2.125)/\phi(E)$ are tabulated in Table II.

Isomeric states can also be populated by neutron capture in the isotope having one less neutron than the isomer. This can occur through capture in either the resonance or thermal regions. For example, when neutron capture occurs in the 1.46 eV resonance of ^{115}In, there is an 79.5% probability of populating the 127 keV ($T_{1/2} = 54.1$ min) isomer in ^{116}In. The remainder of the capture products populate[8] the ground state ($T_{1/2} = 14.1$ s) of ^{116}In. In contrast, thermal neutron capture in ^{115}In can produce not only the $T_{1/2} = 54.1$ min and $T_{1/2} = 14.1$ s activities, but also $T_{1/2} = 2.16$ s activity[9] from the 290 keV isomer in ^{116}In. This second, short-lived isomer decays to the 127 keV isomeric level through emission of a 162 keV photon.

Table I

Isomers studied in current investigations. Values for the nuclear parameters are taken from reference 7. Values for $\sigma\Gamma(2.125)$, the integrated cross section for an assumed gateway state at 2.125 MeV, are taken from the work of references 1-4. In some cases, the cross sections have been updated from the previous values to reflect new data. When multiple trials or sample counts were available, the standard deviation of the mean has been given for the $\sigma\Gamma$ value.

| Isomer	Ground State Abundance (%)	Energy (MeV)	Isomeric Halflife		J_g	J_i	$\sigma\Gamma(2.125)$ $(10^{-29}$ cm^2·keV)
^{77}Se^m	7.6	0.162	17.45	s	1/2-	7/2+	7734 ± 38
^{79}Br^m	50.69	0.207	4.864	s	3/2-	9/2+	2200 ± 27
^{87}Sr^m	7.0	0.388	2.81	h	9/2+	1/2-	1037 ± 21
^{89}Y^m	100.0	0.909	16.06	s	1/2-	9/2+	306 ± 10
^{111}Cd^m	12.8	0.396	48.6	m	1/2+	11/2-	2994 ± 52
^{113}In^m	4.3	0.392	1.658	h	9/2+	1/2-	5501 ± 208
^{115}In^m	95.7	0.336	4.486	h	9/2+	1/2-	7938 ± 17
^{117}Sn^m	7.68	0.315	13.61	d	1/2+	11/2-	1040 ± 31
^{123}Te^m	0.91	0.247	119.7	d	1/2+	11/2-	8157 ± 372
^{135}Ba^m	6.59	0.268	28.7	h	3/2+	11/2-	7149 ± 134
^{137}Ba^m	11.74	0.662	2.5513	m	3/2+	11/2-	2297 ± 27
^{167}Er^m	22.95	0.208	2.28	s	7/2+	1/2-	40731 ± 426
^{179}Hf^m	13.63	0.375	18.68	s	9/2+	1/2-	30842 ± 117
^{180}Ta^m	0.00	0.032	1.2×10^{15}	y	1+	9-	41604 ± 772
^{183}W^m	14.3	0.309	5.15	s	1/2-	11/2+	3745 ± 1378
^{191}Ir^m	37.3	0.171	4.94	s	3/2+	11/2-	42354 ± 1133
^{195}Pt^m	33.8	0.259	4.02	d	1/2-	13/2+	16529 ± 264
^{197}Au^m	100.0	0.409	7.8	s	3/2+	11/2-	14503 ± 62
^{199}Hg^m	16.84	0.532	42.6	m	1/2-	13.3+	1783 ± 50
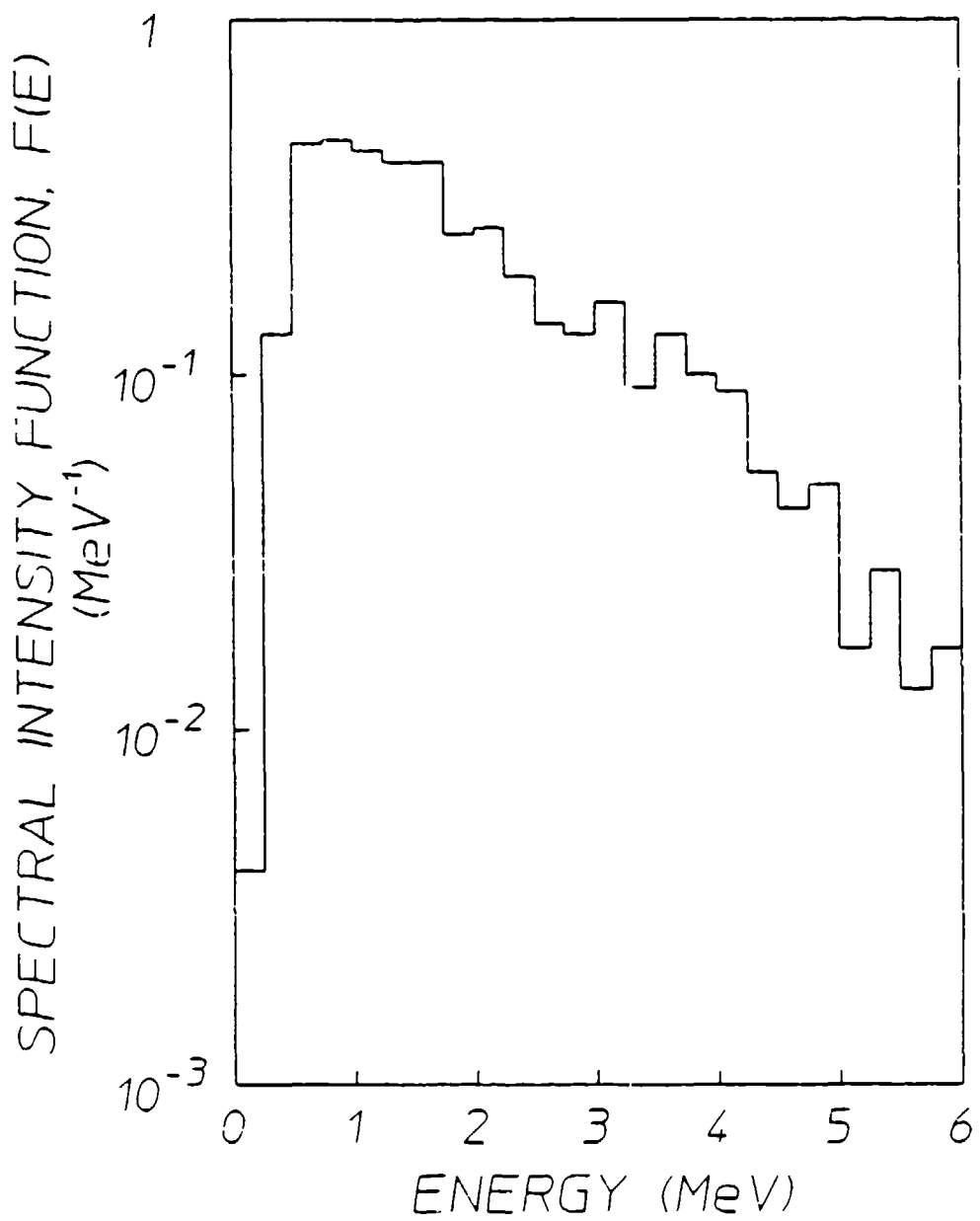
Figure 1:   Relative   spectral   intensity   for   the
bremsstrahlung used in the experiments of references 1-4.
The values have been normalized so that the integral under
the curve is unity.

Table II

Ratios of the photon intensities at energies E to that at 2.125 MeV for the spectrum shown in Fig. 1.

Energy	$\phi(2.125)/\phi(E)$ [MeV]
0.125	0.015
0.375	0.500
0.625	1.731
0.875	1.769
1.125	1.654
1.375	1.538
1.625	1.538
1.875	0.962
2.125	1.000
2.375	0.731
2.625	0.538
2.875	0.500
3.125	0.615
3.375	0.354
3.625	0.500
3.875	0.385
4.125	0.346
4.375	0.204
4.625	0.162
4.875	0.188
5.125	0.065
5.375	0.108
5.625	0.050
5.875	0.065

Capture cross sections are quite small at high energy, but can be thousands of barns in the resonance and thermal energy regimes. However, in the experiments described in references 1-4, interference from this process requires that both the isotope undergoing capture and the ground state of the isomer be naturally occurring nuclides. A list of isomers from Table I satisfying this criterion and their appropriate capture cross sections is given in Table III.

Table III

Isomers susceptible to (n,γ) interferences and the isotopes which would produce them through neutron capture. The natural abundances of the capturing species are shown. Cross sections for total thermal capture (σ_T), thermal capture to the isomer $(\sigma_{T,I})$, total resonance capture (σ_R), and resonance capture to the isomer $(\sigma_{R,I})$ are listed.[9]

Isomer	Isotope	Natural Abundance[7] (%)	σ_T (b)	$\sigma_{T,I}$ (b)	σ_R (b)	$\sigma_{R,I}$ (b)
$^{77}Se^m$	^{76}Se	9.00	85	21.00	42	17
$^{87}Sr^m$	^{86}Sr	9.86	0.84	0.84	5	5
$^{111}Cd^m$	^{110}Cd	12.49	11.1	0.10	42	2
$^{117}Sn^m$	^{116}Sn	14.53	0.11	0.01	11.5	0.5
$^{123}Te^m$	^{122}Te	2.60	3		80	
$^{135}Ba^m$	^{134}Ba	2.42	2.16	0.16	20	
$^{137}Ba^m$	^{136}Ba	7.85	0.41	0.01	1.6	
$^{167}Er^m$	^{166}Er	33 60	20	15.00	100	
$^{179}Hf^m$	^{178}Hf	2".30	80	50.00	1900	
$^{183}W^m$	^{182}W	26.30	21		600	
$^{195}Pt^m$	^{194}Pt	32.90	1 2	0.10	4	
$^{199}Hg^m$	^{198}Hg	10.02	1.92	0.02	70	

Photoneutron Sources

The approximate threshold energy E_t for a (γ,n) reaction can be calculated from

$$E_t = \delta n + \delta(A-1,Z) - \delta(A,Z) \quad , \quad (2)$$

where $\delta(A,Z)$ is the mass excess for the nuclide characterized by atomic number Z and mass number A, and δn is the mass excess for the neutron. The value calculated in this way does not include the correction necessitated by the recoil of the absorbing nucleus, but this is insignificant (<<1%) in practice.

For monochromatic incident photons, neutrons produced by a (γ,n) reaction will also be nearly monochromatic because the momentum of the incident photon is very much less than that of the target nucleus. Part of the decay energy of the compound nucleus will be carried away by the recoil nucleus, resulting in the neutron energy, $E_n(\theta)$, being given[10] approximately by

$$E_n \approx \frac{M(E_\gamma - E_t)}{m + M} + \frac{E_\gamma[(2mM)(m + M)(E_\gamma - E_t)]^{1/2}}{(m + M)^2} \cos\theta \quad , \quad (3)$$

where

θ = angle between the momentum vectors of the incident photon and emitted neutron,

E_γ = incident photon energy,

M = rest mass of recoil nucleus in energy units, and

m = rest mass of neutron in energy units = 938 MeV.

The second term, which contains the angular dependence of Eq. 3, is no more than 10% of the first term for the cases considered here and will be neglected in the following analysis.

Fast Neutron Contributions from Known Sources

The approximate neutron source spectrum and integrated neutron production rate for a given (γ,n) reaction can be calculated from the

incident photon spectrum using Eq. 3. Assuming that the target material is optically thin, the number N_n of neutrons produced in the range E_n to $E_n + \delta E_n$ from a sample of N_T target nuclei will be given by

$$N_n(E_n) = N_T \sigma(E_\gamma) \phi(E_\gamma) T \, \delta E_\gamma \qquad (4)$$

where $\sigma(E_\gamma)$ is the (γ,n) cross section, $\phi(E_\gamma)$ is the spectral intensity in units of photons/cm^2-keV, T is the irradiation time, and $\delta E_n = \delta E_\gamma \times [M/(M + m)]$. The integrated production rate for all neutrons above a given energy E_n' is then simply

$$R_n(E_n') = N_n(E_n')/T = N_T \times \int_{E_{\gamma 0}}^{E_{max}} \sigma(E_\gamma) \phi(E_\gamma) dE_\gamma \qquad (5)$$

where $E_{\gamma 0} = E_t + (1 + m/M) E_n'$.

High energy photons for the previous photoactivation studies were obtained from the bremsstrahlung output of a Varian CLINAC 1800 linac normally used for medical therapy. This source has been well character-ized,[5,6] and its spectrum is shown in Fig. 1. The intensity reaches a maximum near 1 MeV and then drops by a factor of about thirty as it approaches its cut-off at 6 MeV. Therefore, the only neutron production mechanisms that are relevant are (γ,n) reactions with thresholds less than 6 MeV. A list of naturally occurring materials meeting this criterion is given in Table IV. Only these materials could serve as neutron sources in the experiments considered here. Several of them are rare and are not present in the linac construction or in its environ-ment. The exceptions are ^2H, ^9Be, ^{13}C, and ^{17}O. Deuterium occurs as coolant water in the machine and as bound water in the concrete shield-ing of the irradiation cell. Beryllium is present in the beam exit window in the linac head. The other two possible contributors, ^{13}C and ^{17}O, occur in the atmosphere and in the shield walls of the linac cell. The cross sections[11] for ^2H and ^9Be are on the order of a few millibarns in the range between their reaction thresholds, near 2 MeV, and the maximum photon energy at 6 MeV. The thresholds for ^{13}C and ^{17}O are both above 4 MeV. The cross sections for these two nuclides are poorly known at such low energies, but may safely be assumed to be considerably less than a millibarn.[12,13]

Table IV

Naturally occurring materials with (γ,n) thresholds less than 6 MeV. The neutron energies, $E_{n,max}$, for neutrons ejected by 6 MeV photons were calculated neglecting the angular term in Eq. (3). The neutron binding energy, B_n, has been taken from reference 14.

Material	Natural Abundance (%)	B_n (keV)	$E_{n,max}$ (keV)
^{2}H	0.015	2224.6	1886.764
^{6}Li	7.5	5662	281.3626
^{9}Be	100	1665.1	3849.664
^{13}C	1.1	4946.5	971.7887
^{17}O	0.038	4142.5	1747.277
^{145}Nd	8.3	5760.4	237.9317
^{149}Sm	13.8	5846.2	152.7579
^{235}U	0.72	5307	690.0251

In the linac head itself, Be in the 0.025 cm thick beam window will be the dominant contributor to the neutron field. This is true because Be occurs monoisotopically as ^{9}Be, and has both a lower threshold energy (1.665 MeV vs 2.224 MeV) and a larger (γ,n) cross section averaged over the bremsstrahlung spectrum than ^{2}H. The beam window is lccated approximately 6 cm from the converter target and is illuminated over a diameter of about 3 cm. It comprises about 2.4×10^{22} ^{9}Be nuclei. Under equivalent irradiation conditions, almost 3 liters of normal water would be required to produce the same number of neutrons from the ^{2}H(γ,n)H reaction. This is far in excess of the several milliliters of water actually in the target cooling loop at any one time. Thus, for neutrons originating in the linac head, only those from the Be window are significant.

Under the assumptions that the photoneutrons are emitted isotropi-
cally from the Be foil[15] and that the foil dimensions are small compared
to r, the source-sample distance, one obtains

$$\phi_n(E_n') = R_n(E_n')/(4\pi r^2) \qquad (6)$$

for $\phi_n(E_n')$, the intensity at the sample position of neutrons with $E_n \geq$
E_n'. The results for a sample located at the position normally used for
the work in references 1-4 are shown in Fig. 2. Note that the neutron
intensity at the sample location due to this source is only 1000
n/(cm²-s), about 7 orders of magnitude less than the corresponding
integrated photon flux.
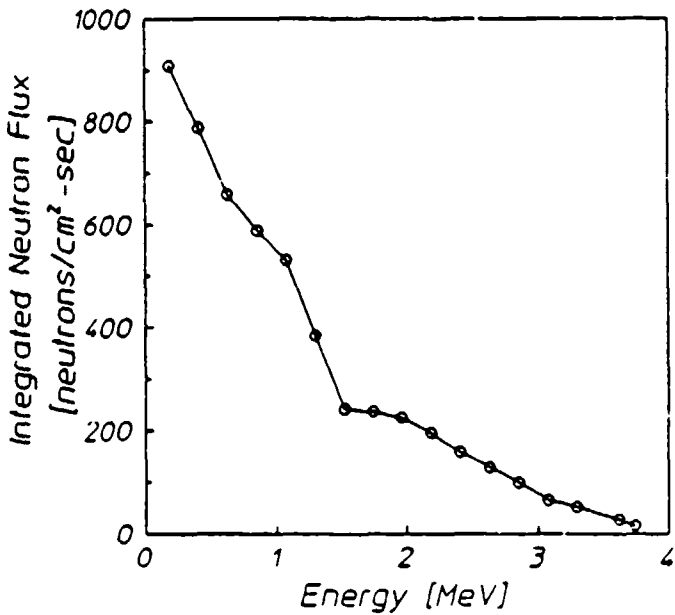
Figure 2:   Calculated net neutron flux
above the neutron energy E_n' at a distance
of 65 cm from the bremsstrahlung source
used for the work of references 1-4.

Neutron production due to (γ,n) reactions with ^2H, ^{13}C, and ^{17}O in
the air is limited by the low density of the target nuclei, and, in the
case of the last two materials, by small (γ,n) cross sections. If the
x-ray output is assumed to pass through a conical volume with semi-angle
$\vartheta_c = 8.75°$ --corresponding to the typical conditions of a field width of
20 cm at a sample distance of 65 cm -- then the volume of irradiated air

between the converter target and the floor is about 2.99×10^5 cm^3. The standard atmosphere[16] comprises 20.95% oxygen and 0.0314% carbon dioxide by volume. Using natural abundances of 0.038% and 1.1%, one obtains about 1.3×10^{21} atoms of ^{17}O and 2.8×10^{19} atoms of ^{13}C in the irradiated volume. A similar calculation for deuterium in the case of 100% relative humidity (T = 300 K) yields a result of 7.71×10^{19} ^{2}H atoms in the volume. Therefore, there are at least ten times more (γ,n) targets in the Be exit window on the linac than there are in the entire irradiated volume in the atmosphere. Moreover, most of the atmospheric targets occupy the bottom half of the cone, where the $1/r^2$ decrease in the photon beam intensity will have reduced the irradiation level by more than two orders of magnitude. As a result of these two conditions and the small cross sections for ^{17}O and ^{13}C, the atmospheric contribution to neutron production through the (γ,n) process is negligible compared to neutron production in the linac head itself.

The final possible source of neutrons in the linac environment is the concrete floor of the irradiation cell. Because an exact analysis of the concrete in place was not available, the typical composition[17,18] of concretes used in standard construction practice in this area was used to estimate the neutron production from this source. For a bulk density of 2.62 g/cm^3, atomic concentrations for the materials of interest were found to be as follows:

$$N(^2H) = 1.59 \times 10^{18} \text{ cm}^{-3} \quad ,$$

$$N(^{13}C) = 8.16 \times 10^{19} \text{ cm}^{-3} \quad , \text{ and}$$

$$N(^{17}O) = 1.91 \times 10^{19} \text{ cm}^{-3} \quad .$$

Since the mass attenuation coefficient for a 6 MeV photon in concrete is about[19] 0.027 cm^2/g, the relaxation length for photons entering the floor slab is 14 cm. The neutrons created in the concrete obviously must escape the floor before being captured if they are to participate in (n,n') or (n,γ) processes in the sample, and therefore it is required that that contributing targets must lie within about 1 neutron migration length from the surface of the floor.[20] The neutron migration length is the sum, in quadrature, of the neutron slowing down length and the thermal diffusion length, and it can be considered to be the average straight line distance traveled between emission and thermalization of the neutron. For the composition model being used, the migration length for a 2 MeV neutron is 14 cm.[21] Thus, it is reasonable for the purposes of estimating the neutron flux from interac-

tions in the floor to assume that the neutrons originate in a cylindri-
cal slab which is 15 cm thick and has the same diameter (d = 50.6 cm) as
the beam envelope at floor level. Using Eq. 6, the estimated neutron
flux at the sample position can be calculated for each of the species in
the slab. The (γ,n) cross sections for ^{13}C and ^{17}O were assumed to have
a constant value of 1 mb above the threshold energies; this represents a
substantial overestimation. Measured cross sections[13] for ^2H were used.
The results for the neutron fluxes produced by the different target
nuclides are as follows:

$$\phi_n(^2H) = 0.08 \text{ n/cm}^2\text{-sec} \quad ,$$

$$\phi_n(^{13}C) = 0.8 \text{ n/cm}^2\text{-sec} \quad , \text{ and}$$

$$\phi_n(^{17}O) = 0.5 \text{ n/cm}^2\text{-sec} \quad .$$

As in the case of the atmospheric contributions, the contributions
from the irradiation cell floor are insignificant compared to those from
the Be beam window. Only the neutron flux produced by the Be window
will be considered in the following analysis of contamination limits.

Contamination limits for the integrated cross sections listed in
Table I could be directly determined from the integrated neutron flux
shown in Fig. 2 and the appropriate cross sections for the (n,n')
processes. Unfortunately, not all of the cross sections are known. To
present the results of this study in a usable form even when the cross
section data is not available, an alternate approach was chosen. For
each of the materials in Table I, the (n,n') cross section that would be
required to produce an arbitrary fraction f of the observed activation
was calculated. A value of 100% was used for f in this work. The
resulting cross sections have been compared with known (n,n') cross
sections or other limiting cross sections, such as the total neutron
cross section, when possible.

The (n,n') cross section necessary to produce the observed isomeric
activation, $\sigma_{n,100\%}$, was obtained using the expression

$$\sigma_{n,100\%} = \frac{N_m}{N_T \phi_n(E_n') T} \quad , \quad (7)$$

which follows from the assumption of negligible self-absorption effects.
In this equation, N_m is the total number of isomers activated in the
course of the irradiation, T is the time of the irradiation, and N_T is
the number of ground state nuclei of the material of interest. A value

of E_n' — 0 was employed to evaluate Eq. 7, thus insuring that the minimum cross section value required would be obtained. Note that since the photoactivation cross section is obtained[1-4] from

$$(\sigma\Gamma)_\gamma = \frac{N_m}{N_T \phi_\gamma(E_\gamma) T} \qquad , \qquad (8)$$

the hypothetical neutron cross section required to produce the observed activation is related to the reported photon cross section by

$$\sigma_{n,100\%} = \frac{(\sigma\Gamma)_\gamma \phi_\gamma(E_\gamma)}{\phi_n(E_n')} \qquad . \qquad (9)$$

The (n,n') reaction cross sections which would have been necessary to produce the observed activations were calculated using Eq. (7) and have been tabulated as $\sigma_{n,100\%}$ in Table V. The actual total neutron cross sections and, where available, the non-elastic cross sections are also listed in Table V for the elements studied in references 1-4. Literature values for the true (n,n') cross sections for the selected isotopes are listed for those cases in which they are available. The actual (n,n') cross sections are on the order of several hundreds of millibarns or less. Some of the (n,n') cross sections listed in Table V are averages weighted against a fission spectrum. Although the fission spectrum is peaked at lower energies than the Be photoneutron spectrum whose integrated intensity is shown in Fig. 2, it still has significant intensity ($\approx 1/3\ I_{max}$) near 1 MeV, the point below which about half of the Be photoneutron intensity lies. Comparison of the (n,n') cross sections which would have been required account for the observed amounts of activation with the sizes of cross sections actually prevailing indicates that in all cases the neutron contamination is substantially less than 10%. The parameter Ω shown in Table V is the ratio of the best observed limiting cross section to $\sigma_{n,100\%}$. If the (n,n') cross section was available, then Ω was calculated using it; if not, then the non-elastic or total cross section was used. Thus, Ω always either equals or overestimates the ratio of the amount of true (n,n') induced activity to 100% of the observed activity in the photoactivation experiments, and thus it represents the fraction of fast neutron contamination expected in the photoactivation results. As can be seen from the table, Ω ranges from 0.0002 to about 0.06, corresponding to contamination limits for the photoexcitation results of between 0.02% and 6%. The maximum value of 6% occurs in the case of ^{79}Br, for which

only the total neutron cross section, rather than the smaller (n,n') cross section, was available. For the materials for which realistic values of the (n,n') cross section were available, the maximum fast neutron contribution to the observed isomeric activation is much less than 1%, based on an examination of all potential sources of fast neutrons in the experimental environment. This indicates that activation via the (n,n') reaction is not a significant process in the photoactivation studies being considered here.

Fast Neutron Flux Measurements

Measurement of such low neutron fluxes as the analysis above yielded at the sample position is difficult in the presence of an intense photon field. Although neutron counters based on the $^{10}B(n,\alpha)$ reaction or on the $^{3}He(n,p)$ reaction have some gamma-ray rejection capabilities, they are inadequate for the experimental situation encountered in this work. Boron counters are more robust than ^{3}He proportional tubes and can operate in gamma fields up to about 1000 R/hr, but the gamma field at the sample position in these experiments is about 60 times higher than this. Moreover, these counters are principally sensitive to thermal neutrons, and a moderator must be used to thermalize incident fast neutrons. Since the two most common and effective moderators are H and C, both potential sources of photoneutrons, there is also the possibility of creating a considerable perturbation in the neutron flux by introducing the detector.

160

Table V

Neutron cross sections required to produce 100% of the observed activation in previous photoexcitation studies[1-4]. Maximum values for the true total neutron cross section of the element of interest, $\sigma_{e\ell}$, are shown for the energy range 0.1-6 MeV. When available, the non-elastic cross section for the element has been shown in parentheses following the total cross section. The most restrictive additional cross section, $\sigma_{\ell im}$, for the particular isotope or element is given with its type and E_{max}, the energy up to which it was determined. Cross section types are as follows: ie — inelastic in element; i — inelastic in isotope; n — non-elastic in isotope; fi — inelastic in isotope, average for fission spectrum. The factor Ω is the ratio of the most specific observed cross section to the cross section required for a 100% contamination effect, and thus represents an upper limit for contamination of the reported photoactivation cross section by neutron effects.

Isomer	$\sigma_{n,100\%}$ (b)	$\sigma_{e\ell}$ (b)	$\sigma_{\ell im}$ (b)		Type	E_{max} (MeV)	Ω (%)
^{77}Se	490	8.3(2.4)	0.73	24	fi	-	0.15
^{79}Br	140	7.5					5.4
^{87}Sr	60	10	0.11	24	fi	-	0.18
^{89}Y	20	11.5	0.2	25	i	4.0	1.0
^{111}Cd	210	8	0.23	24	fi	-	0.11
^{113}In	320	6.3	0.047	26	i	1.0	2.0
^{115}In	430	6.3	0.38	27	i	5.3	0.088
^{117}Sn	70	6.8(2)					2.8
^{123}Te	530	6					1.1
^{135}Ba	420	7.3(2)					0.48
^{137}Ba	130	7.3(2)	0.66	28	i	3	0.51
^{167}Er	2700	9					0.33
^{179}Hf	1940	20	0.4	29	i	1.6	0.02
^{180}Ta	3016	8.5(2.9)	1.8	30	ie	1.8	0.06
^{183}W	140	9.3(2.4)	0.93	30	ie	1.7	0.66
^{191}Ir	2590	10.3					0.40
^{195}Pt	1350	10	0.68	30	ie	1.8	0.05
^{197}Au	95	10	1.3	30	i	5.3	0.14
^{199}Hg	120	10(2.6)	0.14	31	i	2.1	0.12

Another common approach to making fast neutron measurements is the use of neutron activation foils. Unfortunately, some of the most sensitive threshold reactions[33,34], are either (n,n') inelastic scattering reactions or (n,f) fission reactions, which can suffer from (γ,γ') or (γ,f) reaction interferences. However, other foils can be selected that have lower sensitivities but which are relatively free of photon induced interferences. A foil activation experiment was conducted to corroborate the results in the previous section and to verify that no significant neutron sources had been omitted from that analysis. Although the sensitivity of the experiment was inadequate to detect neutrons at the very low levels expected, it demonstrated that there were no unexpected neutron sources of significance in the environment.

Threshold detectors, commonly in the form of activation foils, have long been employed in the determination of neutron spectra. The techniques necessary for such measurements are well documented.[35] The practice is to expose a set of thin foils to the neutron flux in question. The materials of these foils are chosen to be sensitive to neutrons through a variety of reactions, such as (n,n'), (n,p), (n,2n) and (n,np). When the products of these reactions are sufficiently long-lived the activation due to each reaction can be easily measured. The number of activated nuclei produced, N_e, is given by

$$N_e = NT \int_0^\infty \sigma(E)\phi_n(E)dE \quad , \tag{10}$$

where N is the number of target nuclei, T is the irradiation time, $\sigma(E)$ is the reaction cross section, and $\phi_n(E)$ is the neutron spectral density at energy E. For a given material, each reaction occurs only when incident neutrons possess a kinetic energy greater than a particular threshold value. Thus each reaction can be thought of as sampling only the part of the total neutron spectrum which lies above the reaction's threshold, E_t. For this reason, Eq. 10 is often written as

$$N_e = NT\sigma_{eff} \int_{E_t}^\infty \phi_n(E)dE \quad , \tag{11}$$

162

where σ_{eff} is the effective reaction cross section[35] and E_t is the threshold for the reaction. To determine a complete neutron spectrum, it is necessary to use a number of materials with different thresholds and to deconvolve the effects on all of these materials of neutrons in successively lower energy groups. The numerical procedure which used to accomplish this is called an unfolding.[36]

The experiment performed to determine the neutron flux present in the vicinity of the CLINAC 1800 operating in the 6 MeV photon mode employed Ti and Ni as foil materials. These were chosen for a variety of reasons. First, no naturally occurring isotopes of these elements possess isomeric states, so no (γ,γ') activation could occur. Next, (γ,n) and $(n,2n)$ reactions were not accessible since the threshold energy required for each exceeded that available from the linac. For those processes which were energetically possible, many had long lifetimes, important in our experiment. Finally, the thresholds of these reactions occurred at energies well suited for examining the energy range of interest. A summary of relevant properties of the reactions considered is given in Table VI.

Table VI

Accessible reaction properties for naturally abundant isotopes present in the chosen materials.[37]

Reaction	Daughter Halflife (d)	Signature Photon Energy (keV)
$^{46}Ti(n,p)^{46}Sc$	83.83	889.25
		1120.51
$^{47}Ti(n,p)^{47}Sc$	3.34	159.38
$^{58}Ni(n,p)^{58}Co$	70.92	810.79

The Ti and Ni foils were in the form of disks having radii of 2.54 cm and 0.65 cm and thicknesses of 0.005 cm and 0.025 cm. Two disks of each element were employed, with one disk of each encased in a Cd cover

to suppress activation due to thermal neutrons. All four disks were irradiated simultaneously at a distance of 65 cm from the bremsstrahlung converter and were oriented with their axes parallel to the direction of the beam. At the conclusion of a one hour irradiation, the samples were counted individually with a high purity germanium spectrometer system to determine the activation of the foils.

In general, for any peaks evident in the measured gamma-ray spectra which correspond to signature photons of reaction products, it is possible to determine the number of excited nuclei in each foil according to

$$N_e = \frac{C}{\eta f D A} \qquad (12)$$

Here, C is the total number of counts observed within a peak, and η, f, D and A are the corrections for detector efficiency at the energy of interest, gamma ray intensity, finite duration of both irradiation and counting intervals, and self-absorption. This information can then be used in the unfolding process described above to make a determination of the neutron spectrum.

However, in the spectra obtained in this experiment no peaks were detectable above the level of the background, and a direct deconvolution could not be made. Instead, an upper bound for the neutron flux was determined by calculating the maximum number of counts in the signature photon peak which could have been hidden by the statistical variation of the background. The maximum number of excited nuclei was then found from Eq. 12. An upper bound for the neutron flux was then found with Eq. 11 for each reaction. These results are shown in Table VII, together with values of σ_0 and E_t.

Table VII indicates that the (n,p) reaction on ^{58}Ni in the Cd covered foil provides the least upper bound for the neutron flux above 2.8 MeV, 8.72×10^3 n/cm^2-sec. Consideration of the spectrum of Fig. 2 implies the total neutron flux can be estimated from that above 2.8 MeV by increasing the value by a factor of 8. The neutron flux at the sample position must then be less than or equal to the maximum level of undetected neutrons in this experiment, 6.98×10^4 n/cm^2-sec. This is about two orders of magnitude greater than the limits obtained in the previous section; thus the experiment has inadequate sensitivity to

closely verify the preceding neutron source analysis, but does rule out
the presence of significantly large sources which had not been included
in that analysis. It should be noted that even the worst case neutron
flux derived from this experiment would have only a small effect on the
production of isomeric states through (n,n') reactions. For the case of
$^{115}In^m$, a value for $(\sigma\Gamma)_\gamma$ at 2.125 MeV of 6700×10^{-29} cm^2-keV can be
taken from Table I. With a photon flux incident on a sample at a
distance of 65 cm of 5.7×10^6 photons/cm^2-keV-sec at 2.125 MeV and the
maximum neutron flux taken from above, Eq. 9 indicates that an inelastic
neutron scattering cross section of 5470 mb would be required to produce
the observed amount of activation. Since the literature value from
Table V is 380 mb, in this worst case scenario less than 10% of the
observed isomeric activation could have been due to inelastic neutron
processes.

Table VII

Calculated upper bounds for the neutron flux incident on the activation
foils both with and without Cd covers. The values employed for σ_0 and
E_t^{23} are also given.

Foil	Reaction Daughter	σ_0 (mb)	E_t (MeV)	ϕ_n (10^3 n/cm^2-sec) wo/Cd	w/Cd
Ti	^{46}Sc	275	3.0	34.18	287.27
	^{47}Sc	21.4	2.2	29.91	107.48
Ni	^{58}Co	109	2.8	13.76	8.72

Thermal Neutron Measurements

Thermal and epithermal components of the neutron flux can be
measured by a similar activation method. Samples in the form of foils
are exposed to the unknown neutron flux, and the resulting activation

present in each foil is determined by standard counting techniques. Sample materials are chosen to be sensitive to (n,γ) neutron capture reactions in the thermal and resonance regions, rather than the (n,n') and (n,p) reactions considered previously. The foils are irradiated in pairs, one foil being fully exposed to the neutron flux, the other being enclosed in a cadmium cover. Because cadmium possesses a large thermal neutron capture cross section, a cover of about 0.076 cm thickness serves to remove almost all thermal neutrons from the flux seen by the shielded foil. Thus, the two foils will exhibit different activities, making it possible to calculate the separate thermal and epithermal neutron fluxes. This requires more than taking the simple difference of the foil activities, however, since a number of correction factors relating to neutron interactions in both the foils and the cadmium covers must be included. The approach used in this work is outlined in ASTM Standard E 262-86, "Standard Method for Determining Thermal Neutron Reaction and Fluence Rates by Radioactivation Techniques",[38] which includes numerous references to the literature. In this formalism, the thermal neutron flux, ϕ_{th}, is related to the saturated activities of the bare foil, A_s, and the cadmium covered foil, $A_{s,Cd}$, by

$$\phi_{th} = \frac{A_s}{g\sigma_o G_{th}} - \frac{A_{s,Cd}F_{Cd}}{g\sigma_o G_{th}} \left(1 + \frac{g\sigma_o}{G_{res}I_o} f_1 + \frac{\sigma_o w'}{G_{res}I_o} \right) \quad , \quad (13)$$

where the σ_o is the cross section for thermal neutron capture and I_o is the resonance integral. The two saturation activities A_x for the bare and cadmium covered foils are obtained directly from experiment as

$$A_x = \frac{N}{N_T T} \quad , \quad (14)$$

where N is the total number of excited nuclei produced, N_T is the number of target nuclei, and T is the irradiation period. Finally, the epithermal flux, ϕ_e, can be determined from

$$\phi_e = \frac{A_{s,Cd}F_{Cd}}{I_o} \quad . \quad (15)$$

The factors g, w', f_1, G_{res}, G_{th}, and F_{Cd} occurring in Eq. 13 represent corrections[38] required by neutron interactions in both foils and in

the cadmium covers used with the epithermal neutron detector. Determination of thermal and epithermal neutron fluxes in the general case would require a detailed knowledge of the spectral distribution of the neutrons, which is typically not available. The problem is simplified if the detector material exhibits a cross section that varies inversely with its velocity, since then the reaction rates are proportional to the neutron density and are insensitive to the shape of the spectrum. In practice, the problem is formulated assuming that the detector material has a $1/v$ cross section behavior and the factor g appearing in Eq. 13 is introduced to correct for deviations from this ideal behavior. The correction factors f_1 and w' are required to account for epithermal activation of the detector material that occurs between the lower bound of the epithermal range (about 0.13 eV at room temperature) and the cutoff energy of the cadmium filter (about 0.5 eV). Again, a $1/v$ cross section is assumed for the purpose of calculating the principal correction f_1; deviations from $1/v$ behavior are corrected with factor w'. For both thermal and resonance reactions, if the foil is thick compared to the mean free path of a neutron, then corrections G_{th} and G_{res} for self-absorption of the neutrons must be made. Finally, in the case of indium the additional correction factor F_{Cd} is required.[39] The principal resonance in indium occurs at an energy of 1.44 eV, and the low energy wing of this resonance is affected by the presence of the cadmium cutoff filter. As a consequence, the observed number of counts from the epithermal detector must be increased by the factor F_{Cd} to account for the resulting reduction in activation.

An experiment was performed to investigate the thermal and epithermal flux produced in the environment of the CLINAC 1800 operating in the 6 MeV mode. Because more than one experimental objective was being pursued in this work, the linac was not operated in the vertical orientation used for the photoactivation measurements, but was operated horizontally. The principal difference resulting from this change in configuration was that the beam was stopped by the cell wall at a distance of about 4 m from the bremsstrahlung converter instead of the floor at a corresponding distance of 2.29 m. Two 0.0254 cm thick indium disks with diameters of 5.08 cm were simultaneously irradiated for 40 minutes at a distance of 100 cm from the photon source, with the axes of the disks parallel to the beam axis. The 0.076 cm thick cadmium cover used with the epithermal detector was formed of two 6.35 cm diameter disks stamped to create a recess for the indium sample to occupy. This

167

recess was slightly larger than that of the indium foil to insure its complete enclosure. After irradiation, the 54.15 minute half-life activity of the neutron capture product, $^{116}In^m$, was counted with a NaI(Tl) spectrometer system. Standard corrections for detection efficiency, finite transit and counting times, gamma ray intensity, and photon self-absorption were made.

The saturation activities for each foil were calculated from the ratio $N/N_T T$ and were found to be $A_s = (27.58 \pm .16) \times 10^{-20}$ min^{-1}, and $A_{s,Cd} = (11.82 \pm .13) \times 10^{-20}$ min^{-1}. Under the assumptions that the cadmium cutoff energy was 0.5 eV and that the neutrons were thermalized to room temperature (293.4 °K), f_1 was found to be 0.445 using the methods of ASTM E 262. Values of σ_o, I_o, g, w', G_{th}, and G_{res} may also be found in that reference. Indium of the thickness used in this work presents an areal density of 177 mg/cm^2 to the neutron flux. Because relatively large cross sections are involved ($\sigma_o = 161$ b, $I_o = 2593$ b), these foils cannot be considered to be thin in comparison to the mean free path of a neutron, and the values of G_{th} and G_{res} differ substantially from 1. The cross section σ_o given above is for the activation of the 127 keV, 51.15 minute isomer $^{116}In^{m1}$ either directly or through the intermediate 290 keV, 2.18 s isomer $^{116}In^{m2}$. For the thickness of cadmium used in this experiment, the value of F_{Cd} was estimated[39] to be 1.15. The thermal and epithermal fluxes were then calculated to be

$$\phi_{th} = 12 \text{ n/cm}^2 \cdot \text{sec} \quad ,$$

and

$$\phi_e = 6 \text{ n/cm}^2 \cdot \text{sec} \quad .$$

It is possible to use these fluxes to estimate the interference effects that thermal and epithermal neutron activation might have on the photonuclear cross sections listed in Table I. The maximum activities that could be produced by the thermal flux, $A_{n,th}$, and by the epithermal flux, $A_{n,R}$, can be calculated with the cross sections listed in Table III by using

$$A_{n,T} = \sigma_{T,I} \phi_{th} \quad . \tag{16}$$

and

$$A_{n,R} = \sigma_{R,I} \phi_e \quad . \tag{17}$$

The activities A_p corresponding to the photoactivation cross sections in Table I can be obtained in a similar fashion for any arbitrary sample position from

$$A_p = \sigma(2.125)\phi(2.125) \quad , \tag{18}$$

where $\sigma(2.125)$ is the single state cross section for a hypothetical state at 2.125 MeV and $\phi(2.125)$ is the spectral intensity at that energy in the sample position. Most of the photoactivation data previously obtained in this effort has been acquired with a sample distance of 65 cm ($\phi(2.125) = 5.7 \times 10^6$ photons/cm^2-sec).

Because the linac was used in a different geometrical configuration for the thermal and epithermal activation measurements than for the photoactivation studies, an estimated correction factor must be employed to obtain values for the neutron flux at the sample position in the correct geometry. This estimate was obtained from the consideration that the thermal neutrons must originate either in the cell floor or the linac head. Of these two possible sources, the cell floor is much more probable because of its substantial hydrogen content. Since the low energy neutrons are formed by what is effectively a secondary emission process, the functional dependence of the neutron flux on the position of the secondary source is analogous to the classic radar signal problem. If the sample and the photon source were at the same position, then the thermal neutron flux would depend on the inverse fourth power of the distance to the cell floor. Because the sample and the photon source are separated in this case, the flux should instead vary as the product of the inverse squares of the source-wall distance and the wall-sample distance. Using this approximation, the ratio of expected low energy neutron fluxes for the vertical and horizontal configurations described above was found to be about 10. It should be noted that for the less likely case in which the low energy neutrons originate in the linac head, the variation of the flux with sample position will depend only on the inverse square of the separation between the neutron source and the sample. Thus for the geometry existing in the experiments described here, the chosen correction factor will also form a comfortable upper bound in this second, less likely, case.

For the purpose of estimating potential neutron activation interferences with Eqs. 15 and 17, the neutron fluxes obtained by the foil activation experiment were multiplied by the geometrical factor lis-

cussed above. The expected isomeric activities due to neutron capture were then calculated for all materials from Table III for which the neutron activation cross sections for the isomeric states were available. These values and the experimentally observed activations calculated from Eq. 18 are tubulated in Table VII, which also lists Ω, the fraction of the observed activation that could be ascribed to neutron capture processes.

For those cases for which the neutron activation cross sections for populating isomeric states are not available, the upper bound for neutron contamination can be estimated by assuming that 100% of the neutron captures that occur lead to the isomeric state. The values for these upper limits were obtained by using the appropriate total neutron capture cross sections from Table III and are listed within parentheses in Table VIII. Note that even these cases, the degree of contamination of the photoactivation results is less than 6 percent except in the instance of $^{183}W^m$. For this nuclide, use of the total neutron capture cross section to estimate the interference with the (γ,γ') reaction indicates that the upper limit for contamination is about 30%. This may, of course, greatly overestimate the true amount of neutron interference since it represents only the limiting value

In conclusion, for all cases in which the neutron cross sections are available, the neutron activation resulting from the measured thermal and epithermal neutron fluxes is less than 1% of the observed activation and thus represents a minimal contamination of the photoactivation measurement. Where the appropriate cross sections are not available and the total neutron capture cross section must be used to estimate the degree of neutron capture interference, only the case of $^{183}W^m$ presents the possiblity of significant contamination. Further resolution of the interference issue for this isotope will require additional information on the neutron activation cross section for ^{182}W associated with the production of the isomer $^{183}W^m$.

Table VIII

Interfering activities due to neutron capture processes calculated from measured thermal and epithermal neutron fluxes. Capture cross sections have been taken from Table III. The observed activites A_p attributed to photoactivation, the calculated thermal neutron activation $A_{n,T}$, and the calculated resonance neutron activation $A_{n,R}$ have been tabulated. The parameters Ω_T and Ω_R are the contamination limits, in percent, of the observed activation by neutron capture processes.

Isomer	A_p (sec^{-1})	$A_{n,T}$ (sec^{-1})	Ω_T (%)	$A_{n,R}$ (sec^{-1})	Ω_R (%)
^{77}Se^m	4.37×10^{-19}	2.5×10^{-21}	0.6	1.0×10^{-21}	0.2
^{87}Sr^m	5.62×10^{-20}	1.0×10^{-22}	0.2	3.0×10^{-22}	0.5
^{111}Cd^m	1.85×10^{-19}	1.2×10^{-23}	0.006	1.2×10^{-22}	0.06
^{117}Sn^m	5.88×10^{-20}	1.2×10^{-24}	0.002	3.0×10^{-23}	0.05
^{123}Te^m	4.54×10^{-19}	(3.6×10^{-22})	(0.08)	(4.8×10^{-21})	(1.0)
^{135}Ba^m	3.65×10^{-19}	1.9×10^{-23}	0.005	(1.2×10^{-21})	(0.3)
^{137}Ba^m	1.19×10^{-19}	1.2×10^{-24}	0.001	(9.6×10^{-23})	(0.08)
^{167}Er^m	2.42×10^{-18}	1.8×10^{-21}	0.07	(6.0×10^{-21})	(0.2)
^{179}Hf^m	1.74×10^{-18}	6.0×10^{-21}	0.3	(1.1×10^{-19})	(6.0)
^{183}W^m	1.24×10^{-19}	(2.5×10^{-21})	(2.0)	(3.6×10^{-20})	(29)
^{195}Pt^m	1.17×10^{-18}	1.2×10^{-23}	0.001	(2.4×10^{-22})	(0.02)
^{199}Hg^m	1.04×10^{-19}	2.4×10^{-24}	0.002	(4.2×10^{-21})	(4.0)

Conclusions

On the basis of this work, the previously reported results for photoactivation cross sections are substantially free of any contamination by neutron capture or neutron scattering processes. The upper limit for contamination by neutron induced activation of the observed isomeric states is less than 6% in all cases for which the appropriate neutron cross sections are available and significantly less than 1% in many instances. These conclusions are based on a consideration of both fast and slow neutron sources and the corresponding (n,n') and (n,γ) interference reactions. The major source of fast neutrons in the experimental environment when the CLINAC 1800 is operated in the 6 MeV bremsstrahlung mode is the beryllium beam window in the linac head. The total neutron flux at the sample position due to this source is about 1000 n/cm^2-sec. Direct measurement of the thermal and epithermal fluxes indicates that at the sample position there are about 120 n/cm^2-sec in the thermal range and 60 n/cm^2-sec in the epithermal region. Using these values for the incident neutron flux and appropriate literature values for the neutron cross sections for isomeric activation leads to the conclusion that neutron activation effects are about two orders of magnitude less than the observed photoactivation effects.

References

1. C. B. Collins, C. D. Eberhard, J. W. Glesener, and J. A. Anderson, Rapid Communications, Phys. Rev. C, 37, 2267 (1988).

2. C. B. Collins, J. M. Carroll, and J. A. Anderson, Center for Quantum Electronics Report #GRL/8702, University of Texas at Dallas, 1987 (unpublished), pp. 13-44.

3. C. B. Collins, J. A. Anderson, C. D. Eberhard, J. F. McCoy, J. J. Carroll, E. C. Scarbrough, and P. P. Antich, Center for Quantum Electronics Report #GRL/8703, University of Texas at Dallas, 1988 (unpublished), pp. 37-56.

4. J. A. Anderson, C. D. Eberhard, J. F. McCoy, K. N. Taylor, J. J. Carroll, M. J. Byrd, C. B. Collins, E. C. Scarbrough, and P. P. Antich, Center for Quantum Electronics Report #GRL/8704, University of Texas at Dallas, 1988 (unpublished), pp. 11-35.

5. R. Mohan, C. Chui, and L. Lidofsky, Med. Phys. 12, 595 (1985).

6. N. C. Ikoro, D. A. Johnson, and P. P. Antich, Med. Phys. 14, 93 (1987).

7. J. K. Tuli, Nuclear Wallet Cards (National Nuclear Data Center, Brookhaven National Laboratory, 1985).

8. K. H. Beckurts and K. Wirtz, Neutron Physics, Trans. by L. Dresner (Springer-Verlag, New York, 1964), p. 266.

9. F. W. Walker, D. G. Miller, and F. Feiner, Eds., Chart of the Nuclides, Thirteenth Edition (General Electric Company, San Jose, Calif. 1983).

10. G. F. Knoll, Radiation Detection and Measurement (John Wiley & Sons, New York, 1979) p. 34.

11. B. Bulow and B. Forkman, "Photonuclear Cross Sections," in Handbook on Nuclear Activation cross sections, International Atomic Energy Agency Technical Report Series No. 156 (IAEA, Vienna, 1974) pp 475-558.

12. K. Fukuda, Nucl. Phys. A156, 10 (1970).

13. J. W. Jury, B. L. Berman, D. D. Faul, P. Meyer, and J. G. Woodworth, Phys. Rev. C 21, 503 (1980).

14. J. A. Harvey and D. J. Hughes, "Neutrons,", in American Institute of Physics Handbook, Ed. D. E. Gray, (McGraw-Hill, New York, 1963).

15. T. Lauritsen and F. Ajzenberg-Selove, Nucl. Phys. 78, 1 (1966).

16. M. F. Harris, "Meteorological Information," in American Institute of Physics Handbook, ed. D. E. Gray (McGraw-Hill, New York, 1972).

17. Southwestern Laboratories of Dallas, TX, kindly provided us with information relating to typical concrete mixtures.

18. G. S. Brady, Materials Handbook, 9th Edition (McGraw-Hill, New York, 1963).

19. Radiological Health Handbook, U.S. Department of Health, Education, and Welfare (U.S. Government Printing Office, Washington, D.C., 1970).

20. S. Glasstone and A. Sesonske, Nuclear Reactor Engineering, Third Edition (Van Nostrand, New York, 1981), p. 180.

21. G. D. Myers, private communication. Calculated using SNUPAR V2A Schlumberger Nuclear Parameters Code written by D. C. McKeon and H. D. Scott, 1988.

22. S. Glasstone and A. Sesonske, Nuclear Reactor Engineering, Third Edition, (Van Nostrand, New York, 1981), p. 13.

23. D. I. Garber and R. R. Kinsey, Eds., Neutron Cross Sections, Volume II, Curves, National Neutron Cross Section Center, Brookhaven National Laboratory publication BNL 325, 1976.

24. A. Calamand, "Cross Sections for Fission Neutron Spectrum Induced Reactions" in Handbook on Nuclear Activation cross sections, International Atomic Energy Agency Technical Report Series No. 156 (IAEA, Vienna, 1974) pp 273-324.

25. E. Ramstrm, Nucl. Phys. A315, 143 (1979).

26. H. A. Grench and h. O. Menlove, Phys. Rev. 165, 165 (1968).

27. H. C. Martin, B. C. Diven, and R. F. Taschek, Phys. Rev. 93, 199 (1954).

28. C. P. Swann and F. R. Metzger, Phys., Rev. 100, 1329 (1955).

29. G. L. Sherwood, A. B. Smith, and J. F. Whalen, Nucl. Sci. & Eng. 39, 67 (1970).

30. J. B Guernsey and A. Wattenberg, Phys. Rev. 101, 1516 (1956).

31. K. Sakurai and I. Kondo, Nucl. Inst. and Meth. 187, 649 (1981).

32. G. F. Knoll, Radiation Detection and Measurement (John Wiley & Sons, New York, 1979), p. 529.

33. Activation Foil Manual, distributed by Reactor Experiments Inc., 1965, and the references cited there.

34. ASTM Standard Method for Determining Neutron Flux, Fluence, and Spectra by Radioactivation Techniques, Publication E 261-77, (American Society for Testing and Materials, Philadelphia, 1987) and references cited there.

35. K. H. Beckurts and K. Wirtz, Neutron Physics, Trans. by L. Dresner (Springer-Verlag, New York, 1964), p. 286.

36. Foil Activation Data Unfolding Code (FATDUD), from the RSIC Computer Code Collection, Radiation Shielding Information Center, Oak Ridge National Laboratory.

37. E. Browne & R. B. Firestone, Table of Radioactive Isotopes, Ed. by V. S. Shirley (John Wiley & Sons, New York, 1986).

38. ASTM Standard Method for Determining Thermal Neutron Reaction and Fluence Rates by Radioactivation Techniques, Publication E 262-86, (American Society for Testing and Materials, Philadelphia, 1987) and references cited there.

39. C. W. Tittle, Nucleonics 8, 6 (1951).

APPENDIX I

Reprints of articles published during this year

"Depopulation of the Isomeric State $^{180}Ta^m$ by the Reaction $^{180}Ta^m(\gamma,\gamma')^{180}Ta$," by C. B. Collins, C. D. Eberhard, J. W. Glesener, and J. A. Anderson, Phys. Rev. C 37, 2267-2269 (1988).

"Diamond-like Carbon Films Prepared with a Laser Ion Source," by S. S. Wagal, E. M. Juengerman, and C. B. Collins, Appl. Phys. Lett. 53, 187-188 (1988).

"Activation of $^{115}In^m$ by Single Pulses of Intense Bremsstrahlung," by C. B. Collins, J. A. Anderson, Y. Paiss, C. D. Eberhard, R. J. Peterson, and W. L. Hodge, Phys. Rev. C 38, 1852-1856 (1988).

"A Flash X-Ray Source Excited by Stacked Blumlein Generators," by F. Davanloo, J. J. Coogan, T. S. Bowen, R. K. Krause, and C. B. Collins, Rev. Sci. Instrum. 59, 2260-2264 (1988).

"Activation of $^{111}Cd^m$ by Single Pulses of Intense Bremsstrahlung," by J. A. Anderson, M. J. Byrd, and C. B. Collins, Phys. Rev. C 38, 2838-2842 (1988).

"Comment on 'Mössbauer Sidebands from a Single Parent Line'," by C. B. Collins, P. W. Reittinger, and T. W. Sinor, Phys. Rev. B 39, 9655-9659 (1989).

"Large Scale Effects of the Magnetic Phase Modulation of Recoilless Gamma Transitions," T. W. Sinor, P. W. Reittinger, and C. B. Collins, Phys. Rev. Lett. 62, 2547-2551 (1989).

"A Laser Plasma Source of Amorphic Diamond," C. B. Collins, F. Davanloo, E. M. Juengerman, W. R. Osborn, and D. R. Jander, Appl. Phys. Lett. 54, 216-218 (1989).

RAPID COMMUNICATIONS

Rapid Communications

The Rapid Communications section is intended for the accelerated publication of important new results. Manuscripts submitted to this section are given priority in handling in the editorial office and in production. A Rapid Communication may be no longer than 3½ printed pages and must be accompanied by an abstract. Page proofs are sent to authors, but, because of the rapid publication schedule, publication is not delayed for receipt of corrections unless requested by the author.

Depopulation of the isomeric state $^{180}Ta^m$ by the reaction $^{180}Ta^m(\gamma,\gamma')^{180}Ta$.

C. B. Collins, C. D. Eberhard, J. W. Glesener, and J. A. Anderson

Center for Quantum Electronics, The University of Texas at Dallas, Richardson, Texas 75083

(Received 27 October 1987)

The irradiation of an enriched sample of $^{180}Ta^m$ with bremsstrahlung from a linear accelerator having an end-point energy of 6 MeV has excited a strong channel for the reaction $^{180}Ta^m(\gamma,\gamma')^{180}Ta$, which requires a total spin change of $8\hbar$. An integrated cross section of 4.8×10^{-25} cm^{2}keV has been found. This is a large value exceeding by two orders of magnitude known cross sections for (γ,γ') reactions producing isomers of other species.

The isotope $^{180}Ta^m$ carries a dual distinction. It is the rarest stable isotope occurring in nature[1] and it is the only naturally occurring isomer.[2] The actual ground state of ^{180}Ta is 1^+ with a half-life of 8.1 h, while the tantalum nucleus of mass 180 occurring with 0.012% abundance is the 9^- isomer $^{180}Ta^m$. It has an adopted excitation energy of 75.3 keV and half-life in excess of 1.2×10^{15} yr.[2]

The stellar s process[3,4] for nucleosynthesis has steadily gained favor for the production of $^{180}Ta^m$ and the role of the most critical intermediary $^{180}Hf^m$ has been well established.[2,5] However, the viability of this cosmic mechanism rests upon the absence of any reactive channel $^{180}Ta^m(\gamma,\gamma')^{180}Ta$ which could destroy the isomeric population in the photon bath present in the stellar interior at the time of creation. Prior experiments[6,7] have failed to show such a channel having any gateway for excitation below 1332 keV, but the rarity of the target material limited the sensitivity of those measurements. Reported here is the measurement of a very large cross section for the photonuclear deexcitation of $^{180}Ta^m$ through a gateway level at an energy $E \geq 1.4$ MeV. This definitive observation of such a strong radiative coupling between isomeric and ground states of ^{180}Ta may affect explanations for the natural occurrence of $^{180}Ta^m$.

The energy-level diagram of ^{180}Ta and its daughters is shown in Fig. 1, together with a schematic representation of the individual steps in the excitation and detection of the $^{180}Ta^m(\gamma,\gamma')^{180}Ta$ reaction. As can be seen in Fig. 1, the principal means for the detection of the ^{180}Ta ground state lies in observing the $K\alpha$ lines of its daughter ^{180}Hf, following the decay by electron capture of the parent ^{180}Ta. The efficiency for the emission of $K\alpha$ photons relative to the number of ^{180}Ta decays is about 57%.[8]

Two targets were used in these experiments. One con-
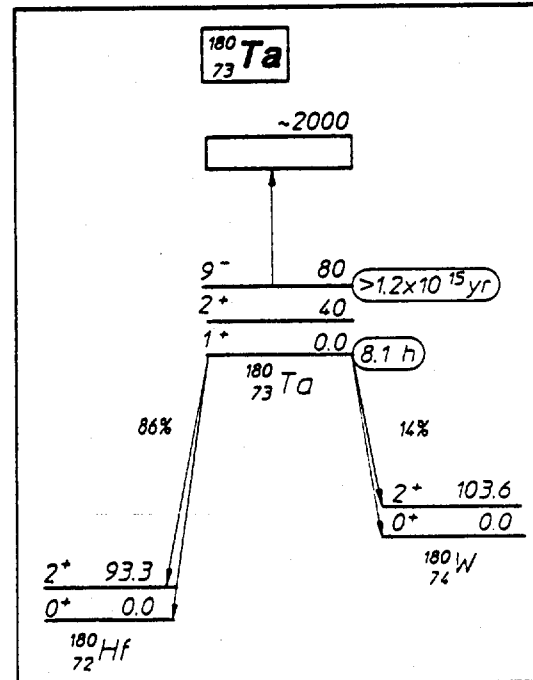
FIG. 1. Schematic energy-level diagram of ^{180}Ta and its daughters. Half-lives are shown in ovals to the right of the ground and isomeric levels. Energies are in keV. The initial transition of the (γ,γ') reaction is shown by the arrow pointing upward to the broad state represented by the rectangle. Cascade through the levels of ^{180}Ta is not known, but leads finally to the ground state. Electron capture to the left and beta decay to the right are indicated by the diagonal downward arrows. The final debris from pumping down the isomer is found principally in the $K\alpha$ fluorescence from the ^{180}Hf characterized by the 8.1 h lifetime of its ^{180}Ta parent.

sisted of a disk 5 cm in diameter of tantalum in natural isotopic abundance. It contained about 0.5 mg of $^{180}Ta^m$ in the surface layer of thickness equal to the mean distance for escape of a 55 keV x-ray photon. The second target was enriched to contain 1.3 mg of $^{180}Ta^m$ in 24.7 mg of ^{181}Ta. Deposited as a dusting of oxide near the center of the surface of a 5 cm disk of Al and overcoated with a 0.25 mm layer of Kapton, this second sample was believed[9] to be free from self-absorption of the x-rays from the daughter Hf.

The samples were exposed to bremsstrahlung radiation from a Varian Clinac 1800 linear accelerator (LINAC) operated with an end-point energy of 6 MeV. This device has been well characterized,[10,11] and its output dose rate has been calibrated with an accuracy of ±3%. After irradiation, the samples were counted with an N-type, HPGe spectrometer having a beryllium entrance window. Conventional techniques were used to calibrate the counting system with isotopic standards.

Figure 2 shows the spectra of the enriched target before and after 4 h irradiation. The spectrum from the other target was entirely similar with the Hf signal reduced by the ratio of the masses of the $^{180}Ta^m$ and the background increased by the appearance of K lines of Ta excited in the large mass of diluent ^{181}Ta by the decay of natural activity in the counting shield.

Figure 3 shows the dependence upon time of the counting rate observed in the Hf($K\alpha$) peaks after irradiation. Data points are plotted at the particular times at which the instantaneous counting rate equals the average counting rate measured over the finite time interval shown. The figure shows the close agreement of the measured rates to the decay expected for a half-life assumed to be 8.1 h.

FIG. 3. Plot of the counting rates measured for the Hf ($K\alpha$) fluorescence from the target fabricated from natural tantalum as functions of the time elapsed from the end of the irradiation. The vertical dimensions of the data points are consistent with 1σ deviations of the measured number of counts accumulated during the finite counting intervals shown at the top of the graph. The dotted line shows the rate expected for a half-life of 8.1 h.

The spectrum of the bremsstrahlung pumping the fluorescence seen in Fig. 2 was taken from the literature[10] and was normalized to the total dose measured in this experiment. In this way, the time-integrated spectral intensity producing the fluorescence was found to be constant[12] to within a factor of 2 over the range 1–5 MeV at a value of 2×10^{14} keV/(keV cm^2). The number of counts observed in the Hf $K\alpha$ lines were corrected for finite irradiation and counting times, the absolute counting efficiency of the spectrometer, and the 57% emission intensity from the parent ^{180}Ta to obtain the total number of nuclei pumped to the ground state. Assuming self-absorption in the enriched target to be negligible, the integrated cross section for the deexcitation of the isomer can be readily calculated if the reaction is assumed to occur through a gateway state narrow in comparison to the range of energies spanned by the irradiation. A value of $\sigma\Gamma = 4.8 \times 10^{-25}$ cm^2 keV is obtained for the integrated cross section if the gateway energy is arbitrarily assumed to be near the lowest value consistent with prior[7] negative results, 2.0 MeV. Even larger cross sections would result from the assumption that the gateway lies at higher energies where the pumping flux is decreased or from the inclusion of an exact self-absorption correction. Once the gateway energy is fixed, experimental error in the integrated cross section is bounded on the lower side by a total uncertainty of 15% contributed by the calibrations of source and detector and on the upper side by a factor of 2 arising from the possible loss of signal because of self-absorption of the Hf x-rays.

FIG. 2. Dotted and solid curves show, respectively, the spectra obtained before and after dumping some of the isomeric $^{180}Ta^m$ contained in a target sample enriched to 5%. An HPGe detector was used to obtain the dotted spectrum before irradiation. The feature at 63 keV is from traces of natural activity in the counting shield. The solid curve shows activity resulting from the transmutation of the pumped ^{180}Ta measured in the same sample and counting system after irradiation. The prominent additions are the $K\alpha$ and $K\beta$ hafnium x-ray lines resulting from electron capture in the ^{180}Ta.

The results of this work show a radiative connection between the isomer ^{180}Ta^m and the ^{180}Ta ground state of remarkable strength. Comparative values for the deexcitation of other isomers are not available as it appears this is the first such measurement. However, the inverse process for the excitation of isomers by (γ, γ') reactions typically proceeds[13-15] with integrated cross sections at least two orders of magnitude smaller. The value reported here for the reaction ^{180}Ta$^m(\gamma, \gamma')$^{180}Ta is inexplicably large and may have several consequences. If the gateway level through which it proceeds is not sufficiently above the thermal energies expected to characterize the s process of nucleosynthesis, current models of the stellar production of ^{180}Ta^m will be severely affected.

[1] A. G. W. Cameron, in *Essays in Nuclear Astrophysics*, edited by C. A. Barnes, D. D. Clayton, and D. N. Schramm (Cambridge Univ. Press, Cambridge, 1982), p. 23.

[2] E. Browne, Nucl. Data Sheets **52**, 127 (1987).

[3] K. Yokoi and K. Takahashi, Nature **305**, 198 (1983).

[4] H. Beer and R. A. Ward, Nature **291**, 308 (1981).

[5] E. Runte, W. D. Schmidt-Ott, W. Eschner, I. Rosner, R. Kirchner, O. Klepper, and K. Rykaczewski, Z. Phys. A **328**, 119 (1987).

[6] J. Law and F. A. Iddings, J. Radioanalytical Chem. **3**, 53 (1969).

[7] E. B. Norman, S. E. Kellogg, T. Bertram, S. Gil, and P. Wong, Astrophys. J. **281**, 360 (1984).

[8] E. Browne and R. B. Firestone, in *Table of Radioactive Isotopes*, edited by V. S. Shirley (Wiley, New York, 1986), pp. 180–182.

[9] Although the grain size of the Ta$_2$O$_5$ was small compared to escape lengths for the 55 keV x-ray, close examination of the target subsequent to the experiment indicated that some clumping of the material had occurred. As discussed in the text, this could cause our result to become a lower limit for the integrated cross section.

[10] R. Mohan, C. Chui, and L. Lidofsky, Med. Phys. **12**, 595 (1985).

[11] N. C. Ikoro, D. A. Johnson, and P. P. Antich, Med. Phys. **14**, 93 (1987).

[12] Since the spectral intensity is roughly constant, the flux decreases as E^{-1} toward the end point with a final more rapid drop between 5 and 6 MeV.

[13] E. C. Booth and J. Brownson, Nucl. Phys. **A98**, 529 (1967).

[14] M. Boivin, Y. Cauchois, and Y. Heno, Nucl. Phys. **A137**, 520 (1969).

[15] M. Boivin, Y. Cauchois, and Y. Heno, Nucl. Phys. **A176**, 626 (1971).

Diamond-like carbon films prepared with a laser ion source

S. S. Wagal, E. M. Juengerman, and C. B. Collins

Center for Quantum Electronics, University of Texas at Dallas, P.O. Box 830688, Richardson, Texas 75083–0688

Diamond-like carbon films have been deposited onto clean, unseeded substrates using a hybrid ion beam technique. In this method the ion fluences available for acceleration were particularly enhanced by the use of laser ablation plumes ejected from highly purified graphite targets. The combination of levels of purity characteristic of ultrahigh vacuum environments, large ratios of ion to neutral concentrations, and high fluences showed considerable merit for the growth of large-area (10 cm^2) films of optical quality and uniformity at deposition rates approaching 20 μm/h.

Interest in diamond-like carbon (DLC) films is motivated by their unique combinations of physical hardness, electrical strength, high thermal conductivity, and optical transparency. Studies have been recently accelerated by prospects of commercial application for optics and semiconductors, but no single technique has yet produced films with uniform properties at practical rates of growth.

Four methods remain at the focus of current interests: ion beam deposition,[1-4] chemical vapor deposition (CVD),[5-7] plasma-enhanced CVD (PECVD),[8-11] and sputtered deposition.[12-15] Contamination is minimized in the first because only the ions of carbon are accelerated to selected energies and deposited on a substrate in a high vacuum environment. In such systems differential pumping and mass separation further reduce the level of the inclusion of impurities into the films. Layers of high quality can be obtained, but at the cost of very slow rates of growth.

In CVD and PECVD both ions and neutral atoms of carbon are produced by the dissociation of organic vapors, such as CH_3OH, C_2H_2, and CH_3OHCH_3, and deposited on substrates. The unwanted collateral products of dissociation provide ready sources of contamination. While growth rates reach practical levels, no one has yet reported the preparation in this way of DLC films of optical quality. The sputtering technique requires two ion sources, one for sputtering carbon from a graphite source with enough velocity to reach the substrate and another for breaking the unwanted graphite bonds which may otherwise remain in the growing film. The two ion sources make the system cumbersome and the higher pressures (10^{-5}–10^{-4} Torr) needed to support the sputtering process introduce problems of contamination that degrade the films to a level comparable to those encountered in CVD and PECVD. In two cases[16,17] lasers have been used in a variant of the sputtering process, but with similar results and problems.

Here we report a hybrid method in which the modest rate of growth that characterizes the cleaner ion beam method is enhanced by the high fluence of carbon ions that can be separated from a discharge plume excited by a laser beam focused upon a cold graphite source. The free expansion of the carbon plume into a UHV chamber rapidly attenuates the flux of neutrals impinging upon a substrate positioned at some distance, while the ions are accelerated directly to the surface of the growing film. Since the laser is pulsed for 10 ns periods the peak growth rates are very high. The duty cycle is low but average growth rates can still reach 20 μm/h. Films of DLC produced in this way show a mirror-smooth surface finish and a uniformity of optical quality. Most surprising is that the growth of these films does not require any seeding of the substrate with debris from abrasive treatment with either diamond or any other particles. Areas of 10 cm^2 have been coated with uniform optical quality on a variety of substrates with only routine cleaning.

Our technique is shown schematically in Fig. 1. As seen there, the output from a Nd-glass laser was focused on a graphite target placed in a UHV environment. The effect of the laser beam was to eject a plume of carbon vapor and then to ionize that portion of it still being illuminated. The neutral cloud expanded isotropically, as evidenced by the pervasive coating of soot which developed in the UHV chamber. The ions were drawn out of the plume and accelerated by the static fields between the graphite target which was grounded and the negatively charged grid structure shown in Fig. 1. The use of highly purified graphite (99.999%) ensured that only the ions of carbon were collected without any necessity for the mass separation techniques often required when using molecular sources of C$^+$. The substrate was contained in a Faraday cage connected to the accelerating grid. A drift space was incorporated in the cage making the path from the laser plume to the substrate total 15 cm.

In operation the laser could be used in either a triggered mode giving 10 J of energy in a 10 μs pulse or a Q-switched mode producing a nominal 1 J of output in a 10 ns pulse. Accelerating potentials typically ranged from 300 to 2000 V. The substrates used in most of the studies reported here were
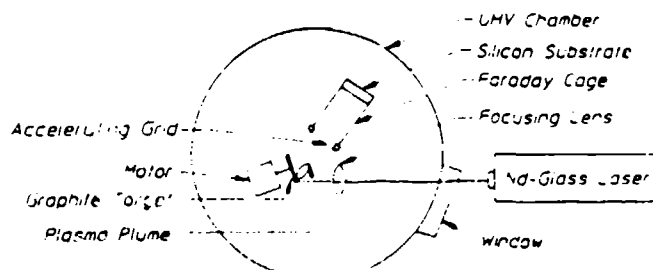

FIG. 1. Schematic representation of the experimental apparatus.

cut from Si(111) disks, 7.5 cm in diameter, but DLC films of comparable quality could be grown on a variety of materials including Ge and quartz. Without any seeding or abrasion of the surfaces, films grown in this way were mirror smooth and uniform, producing no perceptible distortion in reflected images and test patterns. The coloration of a particular sample depended upon the combination of source proximity and accelerating voltage used to prepare it. A brownish cast appeared under conditions which would have increased the proportions of neutral carbon atoms and clusters in the plasma being transported to the growing film.

The predominance of DLC in the films was indicated by Raman spectra such as shown in Fig. 2. The particular signature of the DLC[14] is the broad triangular structure peaking at 1560 cm^{-1} with a base stretching from 1000 to 1600 cm^{-1}. The thickness of this film was only about 200 Å and the DLC spectrum is well developed for such a thin film, probably because of the optical quality. The same spectrum was obtained at different locations sampled on the film. The prominent lines in Fig. 2 were contributed by the Si and were found to be much stronger than were produced by an uncoated substrate. This enhancement has been reported previously[15] and is attributed to the matching of the indices of refraction by the DLC coating.

Ellipsometry measurements showed the index of refraction to be uniform across a single film, but to be dependent upon the accelerating voltage that had been used to deposit the DLC. Several films were grown with different accelerating voltages, each chosen to produce a DLC with a different index of refraction lying within the range 1.5 – 2.15. The ellipsometry mesurements also confirmed that the thickness of the films corresponded to a nominal deposition rate of 1 Å/pulse of the laser for a substrate placed 15 cm from the plasma plume. The particular sample characterized in Fig. 2 was found to have a thickness of 180 Å with a surface roughness of only ± 1 Å.

Tests of chemical and physical parameters showed the films to be completely intact after immersion in boiling water for 1 h and 10% HCl solution for 1/2 h. The resistance measured on the surface was found to vary from a value for freshly prepared films larger than could be measured with available methods, > 40 MΩ/cm to less than 500 Ω/cm in films annealed at 600 °C. This agrees with previous observations[4] of the graphitization of DLC films.
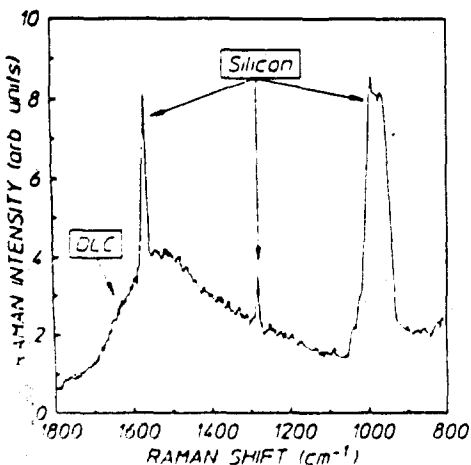
Similar levels of improvement in the optical qualities of the diamond-like films were obtained by cratering the graphite target and by Q switching the laser. Either adjustment should have increased the ratio of ions to neutrals in the ablated plasma, emphasizing again the predominant importance of the carbon ions to the growth mechanism. Rotating the graphite target ensured that each triggered discharge fell on a clean planar surface and under such conditions films were formed which were mostly soot. The contrasting approach of triggering successive discharges into the same crater ensured that the plume reached higher temperatures because of confinement and that a larger proportion of the vapor remained in the illumination to be subsequently ionized. Optical quality films were obtained in this way that matched the best produced with the much greater power densities available from the Q-switched operation.

Our tentative conclusions are that the high proportions of ions to neutrals in the plasmas[2] formed by laser ablation are responsible for the uniform optical quality of the DLC films grown by the hybrid technique we are reporting. In this way the advantages of the ion beam method for the deposition of DLC are enhanced by the greater fluences available from laser plasma sources. At deposition rates currently realized of 1 Å/pulse over tens of cm^2 a growth rate of DLC approaching 20 μm/h could be realized with commercially available lasers.

[1] S. Aisenberg and R. Chabot, J. Appl. Phys. 42, 2953 (1971).
[2] E. G. Spencer, P. H. Schmidt, D. C. Joy, and F. J. Sansalone, Appl. Phys. Lett. 29, 118 (July 1976).
[3] T. Mori and Y. Namba, J. Vac. Sci. Technol. A1, 23 (1983).
[4] S. Kashi, H. Kang, and J. Wayne Rabalias, Phys. Rev. Lett. 59, 75 (1987).
[5] B. V. Spitsyn, L. L. Bouilov, and B. V. Derjaguin, J. Cryst. Growth 52, 219 (1981).
[6] S. Matsumato, Y. Sato, M. Kamo, and M. Sakata, Jpn. J. Appl. Phys. 21, (1982) L183.
[7] A. Sawabe and T. Inuzuka, Appl. Phys. Lett. 46, 2 (1985).
[8] L. Holland and S. M. Ojha, Thin Solid Films 58, 107 (1979).
[9] J. Vora and T. J. Moravec, J. Appl. Phys. 52, 6151 (1981).
[10] S. Matsumoto, M. Hino, and T. Kobayashi, Appl. Phys. Lett. 51, 737 (1987).
[11] K. Kurihara, K. Sasaki, V Motonobu, and N. Koshino, Appl. Phys. Lett. 52, 437 (1988).
[12] C. Weissmantel, K. Bewilogua, D. Dietrich, H. J. Erler, H. J. Hinnerberg, S. Klose, W. Nowich, and G. Reisse, Thin Solid Films 72, 19 (1980).
[13] T. Miyasato, Y. Kawakami, T. Kawano, and A. Miraki, Jpn. J. Appl. Phys. 23, L234 (1984).
[14] M. Kitabatake and K. Wasa, J. Appl. Phys. 58, 1693 (1985).
[15] M. Mirtich, Dan Nir, D. Swec, and B. Bank (unpublished).
[16] K. Kitahama, K. Hirata, H. Nakamatsu, and S. Kawi, Appl. Phys. Lett. 49, 643 (1986).
[17] T. Sato, S. Furuno, S. Iguchi, and M. Hanabusa, Jpn. J. Appl. Phys. 26, L1487 (1987).

FIG. 2. Spectrum of the Raman scattering of the 514.5 nm output of an argon ion laser from a 180-Å-thick film of DLC grown on a Si(111) substrate from carbon ions from the laser ion source.

Activation of ^{115}In^m by single pulses of intense bremsstrahlung

C. B. Collins, J. A. Anderson, Y. Paiss, and C. D. Eberhard

University of Texas at Dallas, Center for Quantum Electronics, Richardson, Texas 75083

R. J. Peterson

University of Colorado, Nuclear Physics Laboratory, Boulder, Colorado 80309

W. L. Hodge

High Energy Laser Associates, 6114 LaSalle Avenue, Ste. 426, Oakland, California 94611

(Received 13 October 1987)

A new technique has been recently described for the absolute calibration of intense sources of pulsed radiation in the 0.2–1.5 MeV range of photon energies. An activation technique, it depended upon the storage of samples of the irradiating spectrum in the form of populations of nuclei excited to isomeric states with lifetimes of seconds to hours. Described here is the use of such a calibrated source to resolve severe conflicts in previous studies of the reaction ^{115}In$(\gamma,\gamma')^{115}$In^m through the 1078 keV $J^\pi = \frac{1}{2}^+$ level; this mode has traditionally served as the archetype for (γ,γ') reactions. We report an integrated cross section of $(18.7\pm2.7)\times10^{-29}$ cm^2 keV with no evidence of any importance of nonresonant channels of excitation.

I. INTRODUCTION

For the study of (γ,γ') reactions that produce isomeric products, ^{115}In has a particularly favorable combination of characteristic properties. Having only a few channels for reaction at energies below 1.4 MeV, it nevertheless displays a large integrated cross section for excitation of the 269 min isomer at 336 keV. For these pragmatic reasons ^{115}In has served as the archetype material for the study of this type of reaction and a number of efforts have been reported[1-13] in the past 48 years.

The relevant part of the energy level diagram[14] of ^{115}In is shown in Fig. 1, indicating only three levels through which a (γ,γ') reaction of multipolarity $E1$, $M1$, or $E2$ could proceed to populate the isomeric state for photons below 1.4 MeV. The importance of the lowest gateway level at 941 keV is negligible because it has a particularly small integrated cross section[15] for excitation in comparison to that of the nearby 1078 keV level, and the 934 keV $\frac{1}{2}^+$ level has a yet smaller cross section because of its longer lifetime.

In practical cases in which ^{115}In samples are excited either with gamma rays from a source or by bremsstrahlung from an accelerator operating below 1.4 MeV, the absorption spectrum for (γ,γ') reactions producing isomers is thus essentially monochromatic at 1078 keV. Nevertheless, measurements by different investigators have shown considerable variance. Table I presents a summary of values reported in the literature together with the results of this measurement in terms of the integrated cross section as usually reported,[16] $\pi b_J b_0 \Gamma \sigma_\gamma/2$, where Γ is the natural width in keV of the pump band, where the branching ratios b_J and b_γ give the probabilities for the decay of the gateway level back into the initial and isomeric level, respectively, and σ_γ is the Breit-Wigner cross section for the absorption transition,

$$\sigma_0 = \frac{\lambda^2}{2\pi} \frac{2I_e+1}{2I_g+1} \frac{1}{\alpha_p+1} , \tag{1}$$

where λ is the wavelength in cm of the gamma ray at the resonant energy, E_r, I_e, and I_g are the nuclear spins of the excited and ground states, respectively, and α_p is the total internal conversion coefficient for the absorption transition. The α's can reasonably be expected to be less than 0.01 for the transitions discussed here.

It has been recently argued[16] that the principal cause of such a large degree of variance among previous measurements of the ^{115}In excitation has been the generally inadequate level of characterization of the spectrum of the pump source. It is particularly awkward to specify the spectrum from a line source. In a previous paper[13] we showed that the spectrum from a pulsed source of intense bremsstrahlung could be determined to a level of accuracy sufficient for the quantitative description of the reactions ^{77}Se$(\gamma,\gamma')^{77}$Se^m and ^{79}Br$(\gamma,\gamma')^{79}$Br^m. This agreement now provides a reliable scheme to normalize other results to the pumping spectrum.

It is the purpose of this paper to report the reexamination of the reaction ^{115}In$(\gamma,\gamma')^{115}$In^m with the same pulsed bremsstrahlung source used for the reconciliation of the absorption cross sections to ^{79}Br^m and ^{77}Se^m. The quantitative value for the integrated cross section we report is in good agreement with the value reported most recently as the result of excitation with a radioactive source.[12]

II. METHODS AND APPARATUS

In this method based on the results of Refs. 13 and 16, the uncertainty in the absolute value of the geometric coefficient coupling the source of pump radiation to the absorbing target is eliminated by normalizing both the
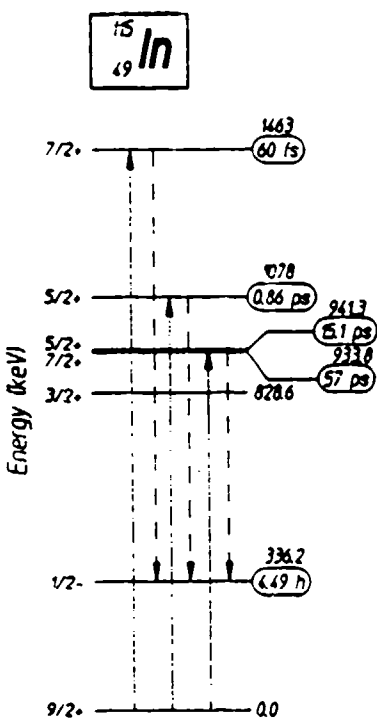
FIG. 1. Energy level diagram of the excited states of ^{115}In important in the production of populations of the isomer (Ref. 14). Half-lives of the states are shown to the right of each and sequences of (γ, γ') reactions leading to the isomer are shown by the arrows. Dashed γ' transitions occur by cascading through levels not shown.

pump fluence and the fluorescence counts to some standard material having a monochromatic excitation spectrum. The reaction ^{79}Br$(\gamma, \gamma)^{79}$Br^m is that standard, having an integrated cross section of 6.2×10^{-29} cm^2 keV and a convenient radioactivity in the isomer. Following the formalism reported earlier,[13] the number of ^{115}In^m nuclei, $S($In$)$, which could be excited by a flash of intense bremsstrahlung can be expressed as a ratio,

$$\frac{S(\text{In})}{S(\text{Br})} = \frac{N(\text{In})}{N(\text{Br})} \frac{\xi_{1078}(\text{In})}{\xi_{761}(\text{Br})} \zeta(1078) , \qquad (2)$$

where $S(x)$ and $N(x)$ are the number of nuclei produced and the number of target nuclei of material x, respectively, $\zeta(1078)$ is the ratio of pumping intensity in units of (keV/keV) at 1078 keV to the intensity in (keV/keV) at 761 keV, and the $\xi_E(x)$ are the combinations of nuclear parameters involved in the excitation of the gateway level at energy E,

$$\xi_E(x) = \frac{(\pi b_a b_0 \Gamma \sigma_0 / 2)_E}{E} . \qquad (3)$$

The collection of terms in parentheses in Eq. (3) comprises the integrated cross section for excitation as usually reported and the calibration value[13] for ^{79}Br is $\xi_{761}($Br$) = 8.2 \times 10^{-32}$ cm^2.

The source of excitation in these experiments[13] was the bremsstrahlung produced by the DNA PITHON nuclear simulator at Physics International. For these particular experiments the nominal firing parameters were deliberately perturbed so that successive irradiations could be obtained with end point energies verying from 0.9 to 1.5 MeV.

Intensities at the target were determined by measuring the nuclear activation of the ^{79}Br component of a sample of LiBr containing isotopes in natural abundance. This calibrating target was run in a pneumatic transfer system which enabled the population of ^{79}Br^m produced by a single irradiation to be subsequently counted with a NaI(Ti) detector of known efficiency at a quiet location 30 m removed from the source. Activation lost during the 1.0 s transit time could be readily corrected during analysis.

The ^{115}In sample under study was in the form of a thin foil taped to a fiduciary mark near the pneumatic system. Since the ^{115}In^m had a substantially longer half-life, it could be manually detached after exposure and transferred to the spectrometer which consisted of a $3'' \times 3''$ NaI(Tl) detector with associated electronics. In typical cases a counting time of 1 h gave better than 2%

TABLE I. Summary of integrated cross sections reported for the reaction ^{115}In$(\gamma, \gamma')^{115}$In^m through the 1078 keV $J^\pi = \frac{3}{2}^+$ level.

Cross Section $\pi b_a b_0 \Gamma \sigma_0 / 2$ (10^{-29} cm^2 keV)	Method[a]	Reference
23±4	S	Ikeda and Yoshihara (Ref. 4)
20±4	S	Veres (Ref. 5)
7.1±2.3	A	Chertok and Booth (Ref. 6)
11.5±4.0	A	Booth and Brownson (Ref. 7)
30(+40, −20)	A	Boivin, Cauchois, and Heno (Ref. 8)
10.5±2.7	S	Lakosi, Csuros, and Veres (Ref. 9)
19±1	S	Watanabe and Mukoyama (Ref. 10)
5.39±0.64	S	Ljubici, Pisk, and Logan (Ref. 11)
18.1±1.5	S	Yoshihara et al. (Ref. 12)
14±1		Calculated from lifetimes and branching ratios (Ref. 14)
18.7±2.7	A	This work

[a] A is bremsstrahlung from an accelerator; S is radiation from ^{60}Co source.
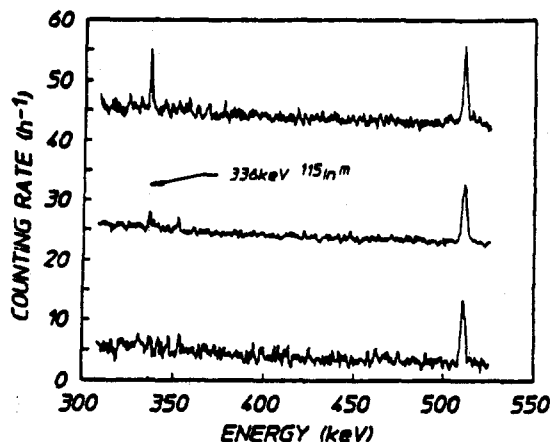
FIG. 2. Three sequential spectra from an intrinsic Ge detector begun at times 6.5, 9.2, and 19.0 h after the irradiation with a flash of bremsstrahlung with an 1.3 MeV end point. Data have been offset by 40, 20, and 0 counts/h, respectively. The 336.2 keV peak is seen to decay with the appropriate half-life of 4.49 h for ^{115}In^m. The other structure is the annihilation peak at 511 keV, present in the background at a constant rate.

typical cases a counting time of 1 h gave better than 2% statistical accuracy in the ^{115}In^m peak after removal of background. In the course of this experimental series 12 shots were obtained for sufficiently high end point energies to yield fluorescent isomeric activity for ^{115}In.

To confirm that the fluorescence being detected resulted only from decay of the ^{115}In^m activity, additional foils were irradiated and then examined with an intrinsic Ge spectrometer, carefully shielded. In Fig. 2 we show spectra from an In foil irradiated by bremsstrahlung with an endpoint of 1.3 MeV. The fluorescence peak is at 336.2 keV, with a half-life seen to be consistent with a tabulated value of 4.49 h.

The relative bremsstrahlung intensity emitted at 1078 keV was a strong function of end-point energy of the accelerator as shown in Fig. 3. These data were obtained
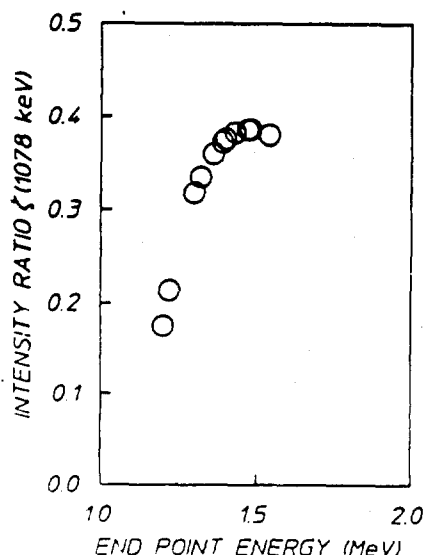
FIG. 3. Plot of the ratio of intensities of the bremsstrahlung spectrum at 1078 keV to that at 761 keV as a function of the end point energy of the electron beam producing the photons. Uncertainties are smaller than the data points.

by numerically fitting theoretical computations of bremsstrahlung spectra. A sample computed spectrum and the verification points from ^{79}Br and ^{77}Se are shown in Ref. 13. For each shot of the PITHON simulator the voltage and current were integrated in a bremsstrahlung modeling code to normalize the activity induced. As described previously,[13] confidence in the present method was established by examining quantitatively the number of fluorescent nuclei produced by successive irradiations of samples of ^{79}Br and ^{77}Se at a variety of end-point energies. The monotonic results in Fig. 3 indicate that the end point determination is reliable to within ±50 keV from shot to shot.

III. RESULTS

Because of a physical displacement between the ^{115}In sample and the mixed ^{79}Br/^{77}Se calibrator, the observed activities required correction for the different x-ray intensity obtained at these two points. This was done by mounting thermoluminescent dosimeters (TLD's) at both positions and comparing delivered doses for each shot. Using the assumption that the relative spectral distribution was constant even though the intensity was varying with position, the ^{115}In activity was scaled by the ratio of the calibrator dose to that of the indium sample. This correction ranged from 1.40 to 0.69 for the shots used in this work. The relative reversals of the positions of calibrator and sample with respect to the center of the irradiation source gave the same results, thus supporting the validity of the method of correction.

The indium sample was optically thin (0.183 g/cm^2) at the 336 keV energy of the fluorescence from the ^{115}In^m thus obviating corrections for self-absorption. Data were corrected for fluorescence and detector efficiencies. The resulting values of S(In)/S(Br) are obtained from Fig. 4 by multiplying the ratios of fluorescent counts shown there by 0.75, the ratio of correction factors for these effects.

The linear form of the dependence of the relative yield of fluorescence from the indium isomers seen in Fig. 4 between 1.0 and 1.45 MeV is a strong indication of the dominance of a single channel of excitation through a gateway level lying at an energy given by the value of intercept. From the data of Fig. 4 it is seen that the intercept lies between 1000 and 1200 keV in agreement with the known $\frac{1}{2}^+$ state at 1078 keV. Also indicated in Fig. 4 is the energy of the next higher gateway state, $\frac{3}{2}^+$ at 1463 keV. It is interesting to observe that for end-point energies above this value there may be a tendency of the data to depart from the simple linear fit because of the availability of this additional gateway. A greater number of measurements at successively higher end-point energies would be needed to confirm this indication.

Once the data below 1.4 MeV are established as being consistent with the model of excitation through a single level at 1078 keV, Eq. (2) provides a means of determining the absolute cross section for the excitation. In Fig. 5 data for the measured values on the left side of Eq. (2) are plotted as functions of the relative intensities, ς(1078), appearing on the right.[17] The scatter in the counting ra-
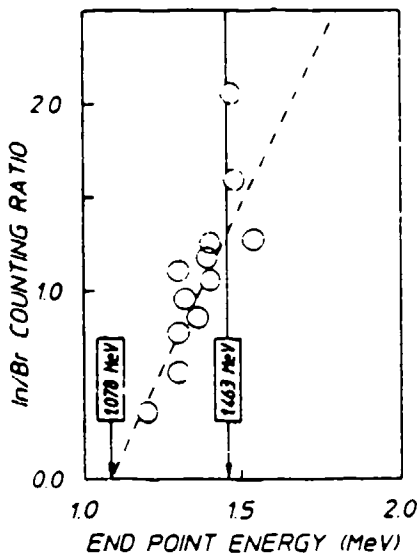
FIG. 4. Ratios of fluorescent photons from ^{115}In^m to those from ^{79}Br^m, produced by single discharges from PITHON, as corrected for the finite duration of the counting interval and plotted as a function of the end-point energies of the electrons producing the bremsstrahlung. The dashed line shows a linear fit to the data intercepting the x axis at a single gateway energy of 1.078 MeV. The excitation energy of the next higher gateway is also shown at 1.463 MeV. Statistical uncertainities are smaller than the data points.

FIG. 5. Plot of the ratios of ^{115}In^m to ^{79}Br^m fluorescence observed as a function of the relative intensity of irradiation at 1078 keV normalized to the intensity at 761 kev. The heavy line shows the least-squares fit including the origin and the lighter lines indicate the uncertainty in such a fit introduced by varying the characterization of the intensities of Fig. 3 over the uncertainties in the characterization of the source. Slopes must be multiplied by 0.75, the product of the ratio of corrections for detector and fluorescence efficiencies and for self-absorptions in the targets before used in expressions such as Eq. (2).

tio is not due to the 2% counting statistics, but to the scatter in the modeled normalized fluxes, for which consistency provides the best estimate of the uncertainty. Note that it is the shape, not the absolute intensity of the pumping spectrum that enters as $\zeta(1078)$. As can be seen from Eq. (2), the best slope around which the data of Fig. 5 scatter would represent our experimental determination of the product of the first two terms on the right of Eq. (2).

From the linear fit to the data of Fig. 5 shown as the heavy line, Eqs. (2) and (3), and the value of integrated cross section for ^{79}Br mentioned earlier, we obtain $\xi_{1078}(In) = (17.3 \pm 2.5) \times 10^{-32}$ cm^2. The uncertainty was obtained from application of the same analyses to the lighter lines in Fig. 5 bounding the scatter from the least-squares fit to the data. The lines shown were obtained by determining the extent to which the fit to the data points of Fig. 5 would be displaced horizontally if the corresponding abscissae were varied by the maximum extent of the uncertainty in the value of $\zeta(1078)$ arising from the nature of the calibration and the interpolations being employed,[13] that is, by the uncertainty in the slope of the pumping spectrum. The scatter of the data is within the bounds established by this uncertainty in intensity. Not explicitly shown in $\xi_{1078}(In)$ is the $\pm 16\%$ uncertainty in the reference value of $\xi_{761}(Br)$ taken from the literature.[14]

Finally, substituting the result for $\xi_{1078}(In)$ into Eq. (3) and solving for the integrated cross section gives for the 1078 keV transition in ^{115}In, $\pi b_J b_0 \Gamma \sigma_0/2 = (18.7 \pm 2.7) \times 10^{-29}$ cm^{2}keV. This is the value we report in Table I.

IV. CONCLUSIONS

The detailed characterization of the spectrum emitted by the intense source of pulsed bremsstrahlung described earlier[13] has been found to be sufficient to determine the yield of the reaction ^{115}In$(\gamma,\gamma')^{115}$In^m. Table I shows this value to agree with some of the prior measurements. In this work there was no need to invoke any nonresonant reaction channels of the type sometimes used[11] in the description of this reaction.

In addition to providing further evidence against the occurrence of nonresonant reactions in ^{115}In, the results of this work have important implications for the calibration of intense sources of pulsed continua. By providing a means for storing a sample of the illuminating intensity at a single well-defined energy of 1078 keV for subsequent measurement at a later, quieter time, a sample of ^{115}In can readily complement the information supplied[15,16] by ^{79}Br about the intensity at 761 keV. Moreover, both together can be used to identify the component of excitation contributed by the higher energy lines of ^{77}Se so that the remainder can be used to characterize the intensities at lower energies.[13]

Finally, it seems this technique of using single pulses of intense continua to measure integrated cross sections for the production of measurable populations of isomers can provide data of use in astrophysical modeling. Cross section at photon energies as low as 1 MeV are quite large for such elements as Se, Br, and In and might provide viable photonuclear channels for the production of enough isomeric population to be important in cosmic nucleosynthesis. It seems that the experiments reported here give evidence that it is possible to advance the precision for the characterization of (γ,γ') reactions toward that enjoyed by other types of particle reactions at comparable energies.

[1] B. Pontecorvo and A. Lazard, C. R. Acad. Sci. 208, 99 (1939).

[2] G. B. Collins, B. Waldman, E. M. Stubblefield, and M. Goldhaber, Phys. Rev. 55, 507 (1939).

[3] G. Harbottle, Nucleonics 12, 64 (1954).

[4] N. Ikeda and K. Yoshihara, Radioisotopes 7, 11 (1958).

[5] A. Veres, Int. J. Appl. Radiat. Isot. 14, 123 (1963).

[6] B. T. Chertok and E. C. Booth, Nucl. Phys. 66, 230 (1965).

[7] E. C. Booth and J. Brownson, Nucl. Phys. A98, 529 (1967).

[8] M. Boivin, Y. Cauchois, and Y. Heno, Nucl. Phys. A137, 520 (1969).

[9] L. Lakosi, M. Csuros, and A. Veres, Nucl. Instrum. Methods 114, 13 (1974).

[10] Y. Watanabe and T. Mukoyama, Bull. Inst. Chem. Res. 57, 72 (1979).

[11] A. Ljubicic, K. Pisk, and B. A. Logan, Phys. Rev. C 23, 2238 (1981).

[12] K. Yoshihara, Zs. Nemeth, L. Lakosi, I. Pavlicsek, and A. Veres, Phys. Rev. C 33, 728 (1986).

[13] J. A. Anderson and C. B. Collins, Rev. Sci. Instrum. 59, 414 (1988).

[14] *Evaluated Nuclear Structure Data File* (Brookhaven National Laboratory, Upton, New York, 1986).

[15] In the units usually employed the integrated cross section $\pi b_3 b_0 \Gamma \sigma_0 / 2$ for the 941 keV level is computed from Ref. 14 to be 0.72×10^{-29} cm^2 keV.

[16] J. A. Anderson and C. B. Collins, Rev. Sci. Instrum. 58, 2157 (1987).

Flash x-ray source excited by stacked Blumlein generators

F. Davanloo, J. J. Coogan, T. S. Bowen, R. K. Krause, and C. B. Collins

University of Texas at Dallas, Center for Quantum Electronics, P.O. Box 830688, Richardson, Texas 75083-0688

Eight triaxial Blumleins have been stacked in series at one end while being synchronously commuted at the other end with a single hydrogen thyratron. Significant voltage gain has been maintained in the stack for periods of the order of 20 ns. Having no other switching elements, operation has been possible at repetition rates to 100 Hz. An x-ray diode has been matched to this pulse power source, making possible the emission of an average bremsstrahlung dose of 5.8 R/s from a sequence of 20-ns pulses. In less than 4 min of operation at 100 Hz, a dose of 1 kR could have been delivered to a target sample. When operated at 50-kV charging voltage, spectral measurements show the output to be a true continuum, peaking at intensities in excess of 2×10^8 keV/keV/shot and containing useful intensities of photons having energies of 150 keV.

INTRODUCTION

Recently we described[1-3] a flash x-ray source producing intense nanosecond pulses at high repetition rates. The principal innovation lay in the development of an x-ray diode of such low geometric profile that it could be matched to Blumlein pulsers having impedances as low as 1 Ω. Output pulses were found to have durations comparable to the transit times of the lines and the combination of pulse duration and line impedance represented entry into a new region of parameter space.[4]

Despite the successes of these x-ray sources, one aspect differed little from devices we had developed earlier for short pulse nitrogen ion[5] and XeF lasers.[6] Each was driven by a Blumlein charged by a resonantly pulse charged power supply, and each line was tightly coupled to a diode load adapted to the application.[2] Commutation was effected by a fast, low inductance thyratron; ringing periods of the order of 100 ns could be realized in the switching cycle. Operating parameters were most strongly constrained by the limitations on peak currents and the voltage tolerances of existing commercial thyratrons. At present the limits are 20 kA and 150 kV, respectively.

Reported is a next step in scaling such impulsive devices to potentials greatly exceeding 100 kV, while retaining the capabilities for operation at high repetition rates. The example we describe is a pulsed x-ray generator, driven by stacked Blumleins that could be charged in parallel at the opposite end and commuted with a single thyratron. The output diode was matched to the series stack so that the endpoint energy of the bremsstrahlung approached the sum of the voltages launched on each individual line. No output switches were needed and x-ray pulse durations were comparable to the transit time of the lines. The only breakdown device was the single thyratron providing the primary commutation. In these aspects, the device we report offers some synthesis of individual advantages optimized in prior efforts.

Pulse-forming lines have long been used in the production of high power electron beams in accelerators and e-beam discharges.[ ] Their specific function is to provide impedance transformation between a power source and a diode load. To do this they must generally be isolated, with fast-closing switches at one or both ends. These lines commonly consist of coaxial or triaxial Blumleins, with dielectrics composed of water, oil, mylar, or a combination of these. In the archetype pulse power system, they are generally not required to provide voltage multiplication as well.

If very high voltages are required, Marx generators with several spark gaps are often used to charge the pulse-forming lines. Examples are found in accelerators and large e-beam machines. It has been reported that the number of spark gaps can be reduced somewhat by using a high-voltage transformer pulsed from a capacitor bank.[7] In either case, inputs to the lines typically consist of voltage pulses of the order of several megavolts from impedances high enough to require durations of 0.1–1.0 μs for charging.

In attempts to combine the functions of voltage multiplication and impedance transformation, Blumlein pulse-forming networks constructed from capacitors and inductors have been used; in this case the lines themselves have successfully multiplied the charging voltages. Ivers *et al.*[ ] designed a pulse generator that utilized seven artificial Blumlein pulse-forming networks which were charged in parallel by a 30- to 50-kV power supply and discharged in a series configuration, avoiding conventional high-voltage Marx generators as a power source. However, the use of this type of artificial Blumlein led to triggering problems. Short commutation time between the load and trigger circuit prevented operation with a single switch. As a consequence Marx triggering columns had to be used, which inevitably limited repetition rates by reintroducing the Marx concepts.

In this work, an array of eight triaxial Blumleins were successfully stacked to add voltage pulses for tens of nanoseconds in a configuration that could be switched with a single hydrogen thyratron without impedance transformation. Operation of a prototype device produced discharge voltages to 200 kV in an x-ray diode at peak currents of 0.5 kA for a 60-kV charging voltage. At 100 Hz an average x-ray dose of 5.8 R/s was obtained from x-ray pulses of 20-ns duration each. Developed here to excite nuclear fluorescence for the study of (γ, γ') reactions, the ultimate signal-to-noise ratio will depend only upon the total radiation that can be deliv-

ered to an extended absorber in a working period. This laboratory-scaled alternative to either synchrotron radiation or ir bremsstrahlung from large e-beam machines may be useful in a more general class of experiments that require access to an extended source of radiation with wavelengths below 0.1 A.

I. DEVICE DESIGN AND CONSTRUCTION

Here we describe a prototype device consisting of three basic sections that comprised a pulse-forming system, which was then matched to a diode load. The essential sections of the pulse-forming system were (i) the commutation assembly, (ii) the transmission lines, and (iii) the pulse stacking module. When integrated, the system with load extended over a nominal length of 4 m. This basic organization is shown schematically in Fig. 1. It was immersed in a closely fitting pan filled with transformer oil. The outer surface of the diode load was sealed with a gasket into the wall of the pan so that the output could emerge without passage through the insulating oil.

The commutation assembly is shown in Fig. 2. As usual, the thyratron provided the impulsive connection of two massive copper plates constructed from 3.2-mm stock with rounded edges. Their purpose was to distribute the switching current to each of the Blumleins in a manner designed to avoid both transit time inequalities and path constrictions, which could bias the distribution. As shown in F 4. 2, the plates were separated by layered Kapton dielectrics and were connected to the Blumleins with a closely lapped joint.

Both plates and dielectric were pierced to permit insertion of a thyratron. Edges of the lower plate were insulated by fingerlike extensions of the Kapton dielectric layer. Connection from the lower plate to the anode well of the thyratron was accomplished with one of several low inductance cans. each designed for a different one of three possible thyratrons.

Details of the construction of the Blumleins are seen in Fig. 2. The eight individual Blumleins consisted of top and bottom (switching and storage) copper plates 3.8 cm in width. The center high-voltage plates were similar, but only 2.5-cm wide to reduce field stresses at the edges and to increase dielectric lifetimes. All lines were made of 3.2-mm-thick copper and were 3.1-m long with rounded edges.

A laminated Kapton (polyimide) dielectric consisting of thirteen 0.127-mm-thick layers separated the plates. These insulators were manufactured using an in-house la-
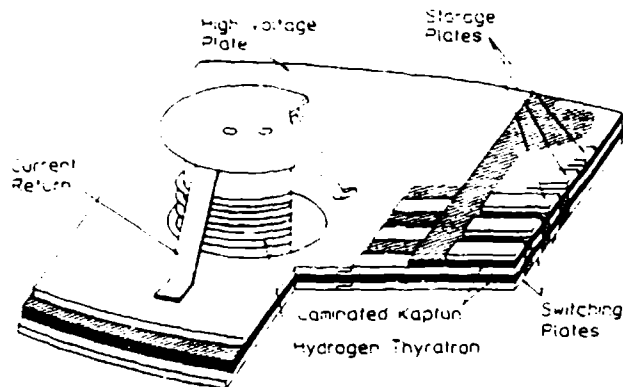
FIG. 2. Layered configuration of the thyratron assembly is presented in a cutaway scheme. The lap joints of the lines to the thyratron plates are shown. The shaded portion of the figure consists of laminated Kapton film.

mination process. Alternate layers of Kapton and high dielectric epoxy were pulled through a press consisting of heavy steel rollers. The finished sheet had an average thickness of 2.3 mm, giving a line impedance of 26 Ω.

The plates and the Kapton were lapped to "plug in" at both the thyratron and series ends, as seen in Fig. 3. These plates were completely sheathed in dielectric. In addition to the layer between the plates, 3.2-mm-thick Lexan (polycarbonate) sheets enclosed the copper on the sides; the Kapton walls were placed between each line to prevent interline flashover.

The Blumleins were switched from parallel to series with the rather complex structure shown in Fig. 4. The conductive lines were lapped to lengths of copper foil cut into curves in the plane of the foil so that the conductors from successive lines could be displaced toward the center. where they would lie one above the other. Dielectric sheets were curved along the same lines to isolate the foils and to try to maintain a reasonably constant transmission line impedance of each Blumlein section being stacked. The resulting series section at the head of the lines was then cast to minimize corona. Figure 4 depicts this in a cutaway view.

Also incorporated into the pulse stacking module were a current transformer and an anode cooling system. Accommodations were made for a water-resistor voltage divider, as well. The top and bottom foils leading to the electrodes were conveyed through high-temperature ceramic directly set into the cast material that formed the base wall of the diode load specific to the particular application.
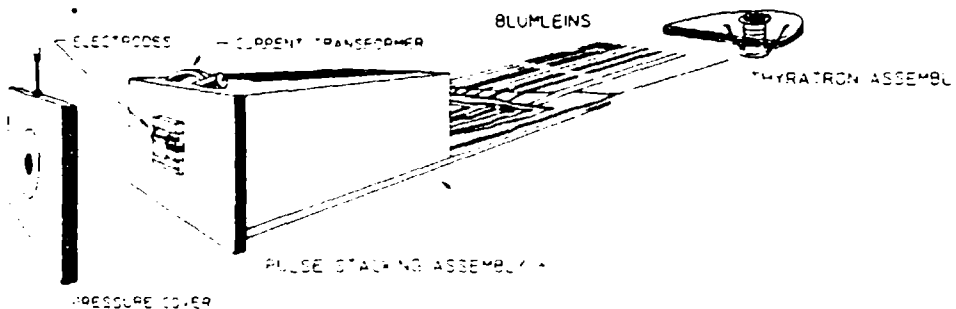

FIG. 1 Schematic drawing of the flash x-ray device
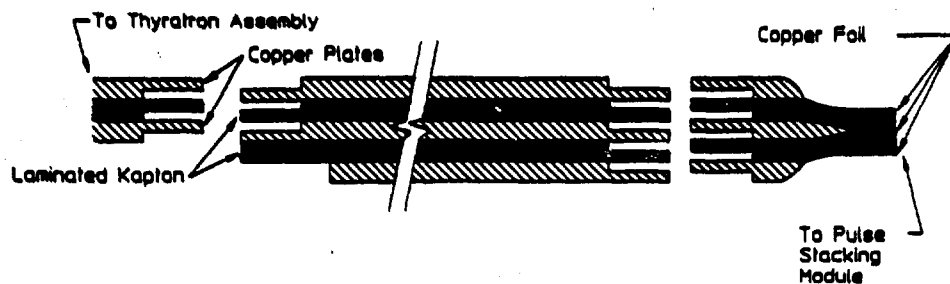
FIG. 3. Side view of each transmission line connecting the commutation assembly and the pulse stacking module.

It is well known that the line and continuous x-ray emission intensities are angularly distributed with respect to incident electron direction. The bremsstrahlung becomes more peaked in forward directions as the incident electron energy increases.[10] Thus in the high-voltage pulsing of x-ray diodes, the most energetic photons of the continuum of x rays are observed in the direction of the discharge electrons.

In this work, the load matched to the voltage-multiplying lines was an x-ray diode configured with two different electrode assemblies, as shown in Fig. 5. In the high-voltage configuration, electrodes were connected to the foils emerging from the base wall from the series part of the lines. A 2.5-cm-wide graphite blade of 0.38-mm thickness was connected to the cathode foil, while the anode foil emerged from the ceramic inset in the wall to connect to an assembly for interchanging anodes. The useful part of the x-rays emerged from the output window in the direction of the incident electron beams colliding with the anode foil. The spacing between the anode and cathode was adjusted by varying the ceramic shim under the anode. An alternative electrode assembly similar to the one described in earlier works[1-3] is shown in Fig. 5. This configuration was used in the low-voltage operation of the device and useful x rays were observed from an output window perpendicular to the direction of the discharge electrons.

A vacuum cover was sealed to the particular head being used by an O-ring. The pressure cover was machined out of Delrin plastic and the completed diode could be routinely evacuated to pressures below 5μ. An output window made of layered Kapton and graphite was placed directly in front of discharge area, as seen in Fig. 1. In operation, all components except for the pressure cover with an output window were immersed in transformer oil.

II. OPERATION AND PERFORMANCE

In operation, the Blumleins were resonantly pulse charged with a source capable of bringing the 16-nF total capacitance of the system to a selected voltage in the range of 3–75 kV in 100μs.[11] The middle conductors were charged to a positive high voltage. For the performances described here, commutation was effected by a three-stage EG&G 5353 hydrogen thyratron mounted in a grounded cathode configuration.

Both the voltages launched on individual lines and the voltage pulse appearing across the series stack at the head were measured with tapped water resistors, as shown in Fig. 5. They were connected to a Tektronix 7912AD transient digitizer. A comparison of pulses launched and received at the stack for both open and loaded circuits is shown in Fig. 6. As can be seen, the output voltage into a matched load approached four times the charging voltage of each line.

The temporal evolution of the x-ray output from the diode is shown in Fig. 7, together with the time dependence
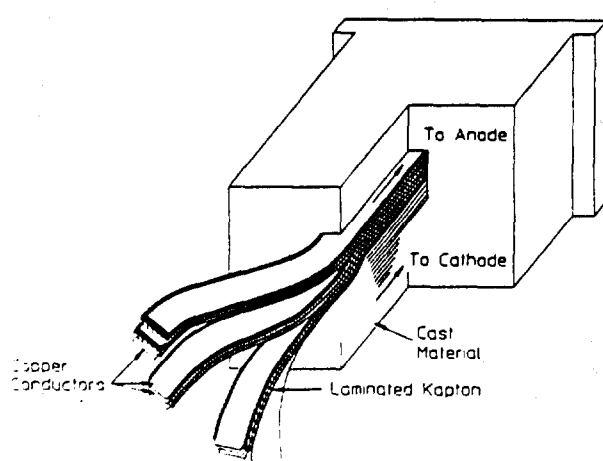

FIG. 4. Three full sets out of a total of eight Blumleins are shown as they are stacked in series when entering the casting material at the base of the x-ray diode. The top set shows the layering of the conductor and dielectric components. The laminated Kapton layers have been shaded for clarity.


Side View of Head Assembly
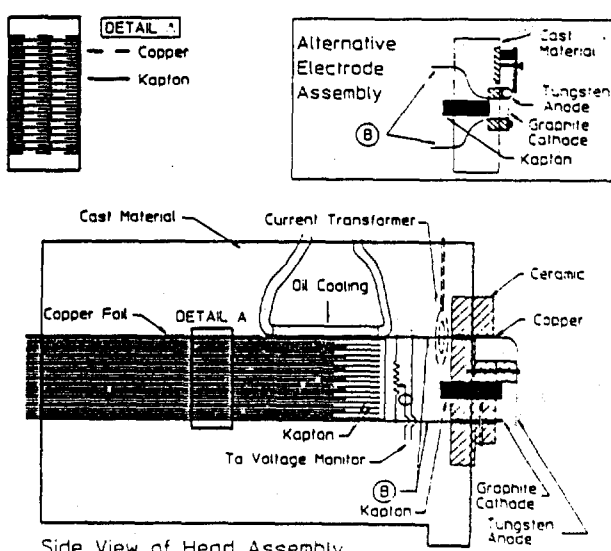
FIG. 5. Schematic drawing of a cross section of the pulse stacking module. An alternative electrode assembly for low-voltage pulsing is shown.
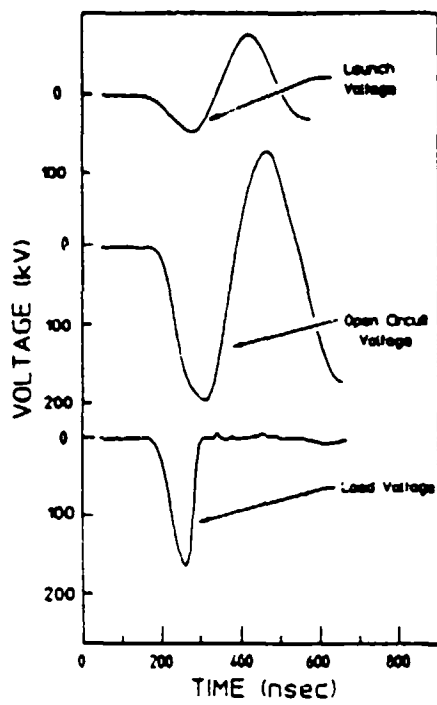
FIG. 6. Voltages measured across the individual lines and across the series stack with and without load as a function of time. The top pulse is typical of the voltage launched down each line by commuting the thyratron. These particular data correspond to a charging voltage of 50 kV.

of the voltage and current at the diode. For this measurement, the x rays were detected with a PIN diode directly coupled to the Tektronix 7912AD. Electrical performance was recorded with the integral diagnostics described above.
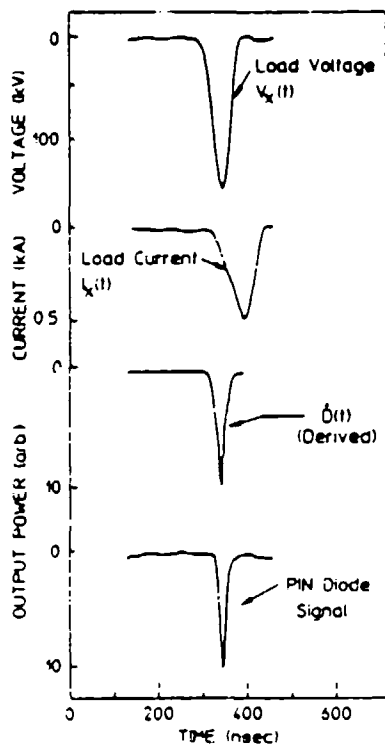

FIG. 7. Typical relationship between the load voltage, load current, and x-ray output emitted from the tungsten anode. These particular data correspond to a charging voltage of 60 kV. The derived x-ray output was obtained from the data as described in the text.

Synchronization was readily maintained between records of voltages and PIN diode signals, but the current monitor required a different grounding arrangement, which disturbed the triggering. The relative phase of the current pulse on the time scale of Fig. 6 had to be determined from the relationship[2] between instantaneous power and the corresponding time derivative of the x-ray dose, $\dot{D}$:

$$\dot{D}(t) = K_c I(t) V^2(t) + K_L I(t) [V(t) - V_K]^{1.7}, \quad (1)$$

where $I(t)$ and $V(t)$ denote the instantaneous values of current and voltage at the x-ray diode, respectively, and V_K is the potential of the K edge for the material of the anode. The first term of Eq. (1) describes the energy emitted as bremsstrahlung continuum, while the second describes emission of the characteristic lines of the anode. The constants K_c and K_L denote the relative efficiencies for the emission of continuum and line radiation, respectively.

For the purposes of synchronizing $I(t)$ with $V(t)$ it was assumed that

$$K_c = 2.1 K_L, \quad (2)$$

in general agreement with previous results. Then Eq. (1) was evaluated for values of load voltage $V(t)$ input from Fig 7 and for $I(t + \tau)$, where $I(t)$ was taken from the raw data and τ was an adjustable phase shift. Shown in Fig. 7 is the $\dot{D}(t)$ computed for the particular value of τ, giving the current waveform plotted for comparison; this $\dot{D}(t)$ represented the best agreement that could be obtained by this procedure. It seems to be reasonably phased with the voltage waveform since appreciable amounts of current are seen to start at the time $V(t)$ begins to break from the form of the open circuit ringing.

The x-ray spectra emitted by this device were sampled with an imaging system formed with a pinhole. The output window was heavily masked with lead collimators and the detector was similarly masked to admit only the image of the open aperture at the source. In this way the contribution from spurious Compton scattering was minimized. A test for the magnitude of the remaining Compton intensity not originating in the source itself was conducted by blocking only the open aperture at the source. No counts were detected on the scale used for the presentation of the spectra.

The detector used to observe the image of the source aperture was a NaI(Tl) crystal mounted to a photomultiplier whose output was connected to an ORTEC preamplifier/amplifier combination servicing a multichannel analyzer. By adjusting the size of the imaging pinhole, the intensity at the scintillator was reduced to the point at which one photoelectron was counted by the electronics on the average of every three discharges. In this way pulse pileup was avoided. These data comprised a pulse-height spectrum that reasonably approximated the desired spectrum of intensity as a function of photon energy. Radioactive sources emitting lines at convenient energies were used to calibrate the relationship between photon energy and detected pulse height. Since the deviation from simple proportionality was less than 4% over the range of energies of interest, a linear relationship was used in the final analysis of the spectral data.
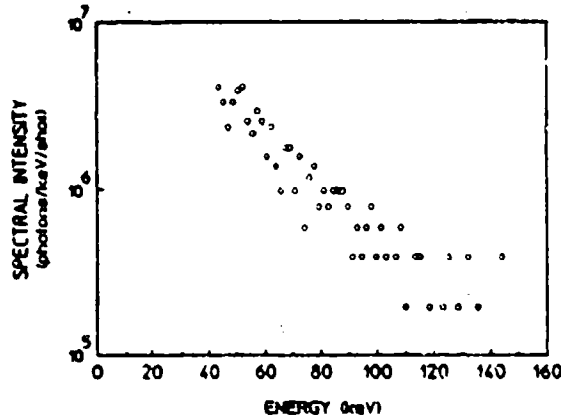
FIG. 8. Typical spectral distribution of flux emitted from the tungsten anode at a charging voltage of 50 kV.


FIG. 9. Average dose outputs emitted as x rays near 1 A as a function of the pulse repetition rates for a charge voltage of 50 kV.

The spectrum of the counting rate detected at each photon energy was multiplied by the ratio of $2\pi/\Omega$, where Ω was the measured solid angle of the pinhole. The resulting spectrum is shown in Fig. 8. Data at lower energies than those shown were rendered uncertain by levels of Compton scattering in the detector and thus were not plotted. Errors in the intensities accrued primarily from statistical uncertainties in the numbers of photons n collected in each of the discrete windows in photon energies. A reasonable expectation is that the statistical error in intensity is $\sqrt{n}$. This can be estimated in Fig. 8 from the identification of the lowest intensity, with the accumulation of a single photon in the corresponding window in energy. Experimentally, this uncertainty is seen in the scatter of the data in Fig. 8.

With this first prototype device, x-ray pulse energies were found to remain largely constant as the pulse repetition rate was varied over the range of 1–100 Hz. Figure 9 shows this to be reflected in the measured values of average dose output in the x-ray pulses of 20-ns duration emitted from a tungsten anode.

Average x-ray powers at 100 Hz resulting from the operation of this device with a charging voltage of 50 kV showed that in less than 4 min, a dose of 1 kR could be delivered to a target sample. This would exceed the dose available in the bremsstrahlung from a shot of a large laser plasma or small e-beam machine.

ACKNOWLEDGMENTS

[1]C. B. Collins, F. Davanloo, and T. S. Bowen, Rev. Sci. Instrum. 57, 863 (1986).

[2]F. Davanloo, T. S. Bowen, and C. B. Collins, Rev. Sci. Instrum. 58, 2103 (1987).

[3]F. Davanloo, T. S. Bowen, and C. B. Collins, in Advances in Laser Science-I, edited by W. C. Stwalley and M. Lapp (AIP Conference Proceedings No. 146, New York, 1986), pp. 60–61.

[4]P. Krehl, SPIE Rev. 689, 26 (1986).

[5]C. B. Collins, IEEE J. Quantum Electron. QE-20, 47 (1984).

[6]R. Sadighi-Bonabi, F. W. Lee, and C. B. Collins, J. Appl. Phys. 53, 65 (1982).

[7]J. R. Smith, R. F. Schneider, M. J. Rhee, H. S. Uhm, and W. Namkung, J. Appl. Phys. 60, 4119 (1986).

[8]M. T. Buttrom and G. J. Rohwein, IEEE Trans. Electron Devices ED-26, 1503 (1979).

[9]J. D. Ivers and J. A. Nation, Rev. Sci. Instrum. 54, 1509 (1983).

[10]E. C. Booth and J. Brownson, Nucl. Phys. A98, 529 (1967).

[11]F. Davanloo, T. S. Bowen, J. J. Coogan, and C. B. Collins, in Center for Quantum Electronics Report No. GRL/8602, University of Texas at Dallas, Dallas, 1987, pp. 47–70.

Activation of ^{111}Cd^m by single pulses of intense bremsstrahlung

J. A. Anderson, M. J. Byrd, and C. B. Collins

University of Texas at Dallas, Center for Quantum Electronics, Richardson, Texas 75083

(Received 9 August 1988)

Described here is the use of a calibrated bremsstrahlung source to resolve conflicts in previous studies of the reaction ^{111}Cd$(\gamma,\gamma')^{111}$Cd^m through a level located near 1200 keV. We report an integrated cross section of $(9.8\pm2.5)\times10^{-29}$ cm^2 keV with no evidence of any importance of nonresonant channels of excitation.

I. INTRODUCTION

Fifty years ago it was first reported[1] that (γ,γ') reactions could produce isomeric nuclei. It is interesting to note that even after such an advance of technology as has occurred over the intervening time, attempts at quantitative measurements still do not converge. For example, the most recent three measurements of the integrated cross sections for the reaction ^{111}Cd$(\gamma,\gamma')^{111}$Cd^m were conducted in 1979, 1982, and 1987 with results of 35, 5.8, and 14, as reported in Refs. 2–4, respectively, in the usual units of 10^{-29} cm^2 keV. Probable errors were quoted as varying only from 7 to 14% and, yet, no two of the measurements were even within a factor of 2 of each other.

The ^{111}Cd^m isomer at 396 keV has a 48.6 min half-life and is readily detected by observing the 150.6 and 245.4 keV gammas radiated in the cascade from the isomer.[5,6] Experimentally this is an almost ideal vehicle for the study of (γ,γ') reactions since the lifetime of the isomer is long enough to collect a substantial dose from any one of a variety of excitation sources during the activation cycle and short enough to count with reasonable signal-to-background ratio afterward.[7,8] Experiments appear to have been carefully executed[2–4] and the drastic disagreement in the results has been attributed[3] to the controversial[4] proposal that some mechanism of nonresonant nuclear absorption dominates the excitation step. However, the data that support this intriguing proposal[3] and the data that seem to refute[4] it agree only in indicating that the (γ,γ') reaction producing ^{111}Cd^m is not well understood.[2–4,5–12]

The relevant part of the energy level diagram[5] of ^{111}Cd is shown in Fig. 1. All of the adopted levels[5] between 1000 and 1500 keV are shown together with the gamma transitions that have been observed[6] in reactions other than (γ,γ'). Additional transitions to the 1190 and 1330 keV levels have been inferred[3,9] from (γ,γ') studies, but those reports depend upon the validity of arguments which do not support all of the data. Moreover, even the existence of the 1330 keV level might reasonably be questioned, since it is based upon a single report[13] of a reaction not dependent upon the interpretations of (γ,γ') data.

For levels in Fig. 1 which might be excited by photons with energies in the range 1000 to 1500 keV, there are a number of possible cascades to the $\frac{11}{2}^-$ isomer through levels below 1000 keV which are not shown. However, no particular path has been proposed.

It has been recently argued[7] that the principal cause of such a large degree of variance among previous measurements of isomeric excitation has been the generally inadequate level of characterization of the spectrum of the pump source. In a previous paper[8] we showed that the spectrum from a pulsed source of intense bremsstrahlung could be determined to a level of accuracy sufficient for quantitative description by the reactions ^{77}Se$(\gamma,\gamma')^{77}$Se^m and ^{79}Br$(\gamma,\gamma')^{79}$Br^m.

Subsequently we reexamined[14] the reaction ^{115}In$(\gamma,\gamma')^{115}$In^m with the same pulsed bremsstrahlung source used for the reconciliation of the absorption cross sections to ^{79}Br^m and ^{77}Se^m. For ^{115}In, the quantitative value for the integrated cross section we found was in good agreement with the other value reported most recently as the result of excitation with a radioactive source.[15] Reported here is an extension of this technique to the reaction ^{111}Cd$(\gamma,\gamma')^{111}$Cd^m. We find an integrated cross section of $(9.8\pm2.5)\times10^{-29}$ cm^2 keV for reaction through a gateway level near 1200 keV.

II. METHODS AND APPARATUS

As usually reported[7] the integrated cross section for a (γ,γ') reaction yielding an isomeric product state is $\pi b_a b_0 \Gamma \sigma_0/2$, where Γ is the natural width in keV of the pump band, where the branching ratios b_j and b_0 give the probabilities for the decay of the gateway level back into the initial and isomeric level, respectively, and σ_0 is the maximum of the Breit-Wigner cross section for the absorption transition.[14] Unlike our previous study[14] of ^{115}In from which this present work has been extended, none of the elementary nuclear properties entering into the computation of the integrated cross section were known for ^{111}Cd. Although it is uniformly assumed[2–4,9–12] that the dominant gateway level lies at 1330 keV, this is not strongly supported by prior data. Early experiments[2,10,12,17] using bremsstrahlung from accelerators with variable end point energies indicated that the reaction turns on between 1200 and 1400 keV. However, the apparent sharpness seen in some early data at 1330 keV is strongly affected by the logarithmic presentation of a linear threshold and the sensitivity of the in-

strumentation to low levels of activation. In more recent experiments using ^{60}Co sources, the high level of activation produced and the proximity of the 1330 keV level of ^{111}Cd to the strong 1332 keV line of ^{60}Co made it attractive to identify the (γ,γ') reaction as occurring through the 1330 keV level of undetermined symmetry. Since the experiments reported here were conducted with an accelerator producing a known[3] bremsstrahlung spectrum it was decided to try to determine experimentally the energy of the gateway needed, as well as the integrated cross section.

In a previous report[7,8] it was shown that the uncertainty in the absolute value of the geometric coefficient coupling the source of pump radiation to the absorbing target could be eliminated by normalizing both the pump
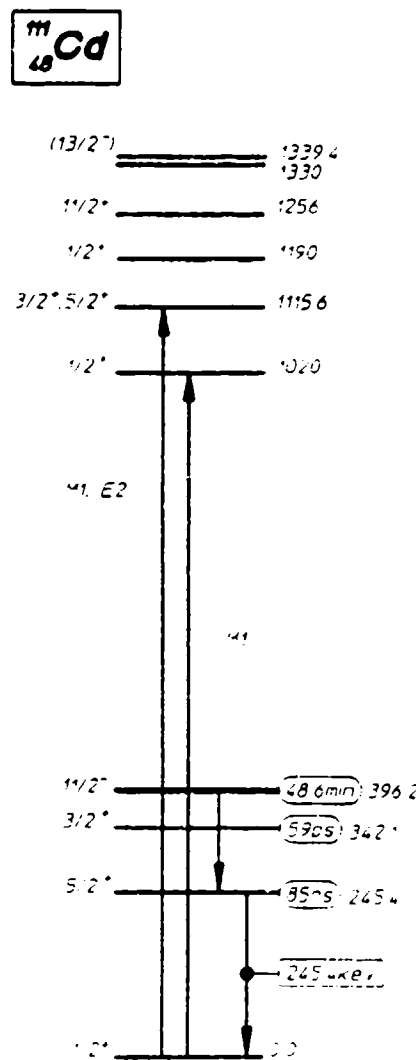
FIG. 1. Energy level diagram of the excited states of ^{111}Cd between 1000 and 1500 keV which may be important in the production of the 48.6 m isomer as reported in Ref. 5. Also shown are all excited states below 400 keV. Half-lives of the states are shown to the right of each state and known (Ref. 6) gamma transitions are shown by the arrows. Populations of the 48.6 m isomer are most conveniently detected by the 245.4 keV fluorescent transition as indicated.

fluence and the fluorescence counts to some standard material having a monochromatic excitation spectrum. The reaction ^{79}Br$(\gamma,\gamma')^{79}$Br^m was found to be an ideal standard, having a single pump level at 761 keV, an integrated cross section of 6.2×10^{-29} cm^2 keV, and a convenient radioactivity in the isomer.

Following the formalism reported earlier,[8] the number of ^{111}Cd^m nuclei, $S(\mathrm{Cd})$, which could be excited through a single gateway state at an energy E by a flash of intense bremsstrahlung can be conveniently expressed as a ratio,

$$\frac{S(\mathrm{Cd})}{S(\mathrm{Br})} = \frac{N(\mathrm{Cd})}{N(\mathrm{Br})} \frac{\xi_E(\mathrm{Cd})}{\xi_{761}(\mathrm{Br})} \zeta(E) , \qquad (1)$$

where $S(x)$ and $N(x)$ are the number of nuclei produced and the number of target nuclei of material x, respectively; $\zeta(E)$ is the ratio of pumping intensity at the gateway energy E in keV to the intensity at 761 keV and the $\xi_E(x)$ are the combinations of nuclear parameters involved in the excitation,

$$\xi_E(x) = \frac{(\pi b_a b_0 \Gamma \sigma_0/2)_E}{E} . \qquad (2)$$

The collection of terms in parentheses in Eq. (2) comprises the integrated cross section for excitation as usually reported, and the calibration value for ^{79}Br is $\xi_{761}(\mathrm{Br}) = 8.2 \times 10^{-32}$ cm^2. Still more convenient for analysis is the weighted activation ratio, R, obtained by multiplying Eq. (1) by the ratio of the number of target nuclei,

$$R = \frac{N(\mathrm{Br})S(\mathrm{Cd})}{N(\mathrm{Cd})S(\mathrm{Br})} = \frac{\xi_E(\mathrm{Cd})}{\xi_{761}(\mathrm{Br})} \zeta(E) . \qquad (3)$$

The source of excitation in these experiments' was the bremsstrahlung produced by the DNA/PITHON nuclear simulator at Physics International. The deliberate perturbation of the firing parameters provided for a sequence of irradiations with end point energies varying from 1.3 to 1.54 MeV.

Intensities at the target were determined by measuring the nuclear activation of the ^{79}Br component of a sample of LiBr containing isotopes in natural abundance. The ^{111}Cd sample under study occurred in natural isotopic abundance in a thin Cd foil taped to a fiduciary mark near the pneumatic system used to convey the LiBr calibrator to a counting system. Since the ^{111}Cd^m had a substantially longer half-life than the calibrating Br, it could be manually detached after exposure and transferred to the spectrometer which consisted of an intrinsic germanium detector with associated electronics. In typical cases a counting time of 1 h gave better than 5% statistical accuracy in the area of the ^{111}Cd^m peak. In the course of this experimental series, six shots were obtained for sufficiently high end-point energies to yield statistically significant numbers of fluorescent isomeric activity.

To confirm that the fluorescence being detected resulted only from decay of the ^{111}Cd^m activity, the spectra from irradiated foils were first examined for traces of interference from the 238 keV line from ^{212}Pb contaminating the counting environment. The clear separation of the 238 keV line from the 245 keV line obtained from
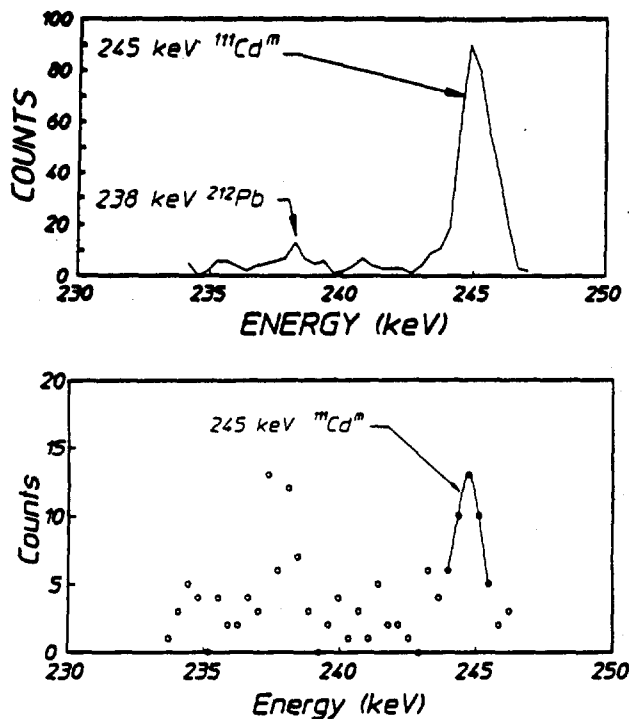
FIG. 2. Spectra showing the 245 keV line from the decay of $^{111}Cd^m$. The spectra were obtained from an 8.02 gm, natural Cd foil sample. The small peak near 238 keV is due to the decay of naturally occurring ^{212}Pb in the counting environment. (a) Fluorescence from $^{111}Cd^m$ following irradiation with a single bremsstrahlung pulse having an end point energy of 1.4 MeV. Counting time was 3600 sec. (b) Fluorescence following excitation with an end point of 1.3 MeV; counting time was 2700 sec.

$^{111}Cd^m$ following irradiation with a 1.4 MeV end point bremsstrahlung pulse is shown in Fig. 2(a). At an end point energy of 1.3 MeV, where the spectral intensity at the 1330 level in $^{111}Cd^m$ should have been negligible, the 245 keV line is weak but clearly observable, as shown in Fig. 2(b).

In order to determine an experimental value of the $\xi_E(Cd)$ by fitting Eq. (3) to measurements of the fluorescence yields from the sample and from the LiBr calibrator, the relative bremsstrahlung intensity, $\zeta(E)$, emitted
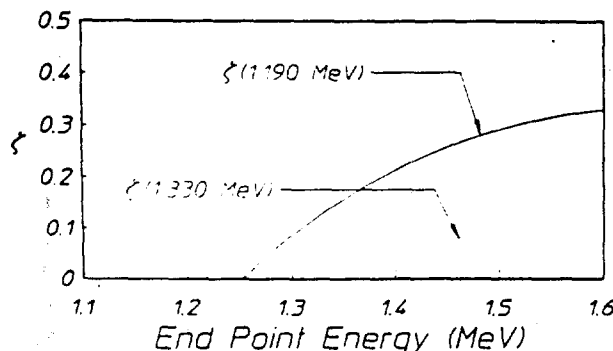
FIG. 3. Plots showing the ratio of the spectral density at energy E normalized to the spectral density at the 761 keV gateway of ^{79}Br for varying end-point energies. The solid and dotted lines show the ratio for energies $E = 1.190$ and 1.330 MeV.

at E must be known. For these experiments, these data were obtained by numerically fitting theoretical computations of bremsstrahlung spectra. As reported previously,[8] confidence was established by examining quantitatively the number of fluorescent nuclei produced by successive irradiations of samples of ^{79}Br and ^{77}Se at a variety of end-point energies. The relative bremsstrahlung intensity emitted at a particular energy was found to be a strong function of the end-point energy of the accelerator; two examples are shown in Fig. 3.

III. RESULTS

Because of a small physical displacement of the ^{111}Cd sample from the mixed $^{79}Br/^{77}Se$ target providing calibration, the observed number of fluorescent photons counted had to be corrected for the different source intensities. This was done by mounting thermoluminescent dosimeters (TLD's) at both positions and then comparing the total dose recorded at the different points for each shot.[14] The number of photons from $^{111}Cd^m$ was scaled by the value of relative dose received at the ^{111}Cd and at the calibrating positions.

The cadmium sample was optically thin (0.5–0.7 gm/cm^2) at both the 150 and 245 keV fluorescence energies, requiring relatively small factors of 1.645 and 1.222 for the self-absorption correction. Data were corrected for fluorescence and detector efficiencies, as well as for variations in measurement time. Fluorescent counts from each line were used to calculate the total number of nuclei pumped for each exposure. Good agreement was
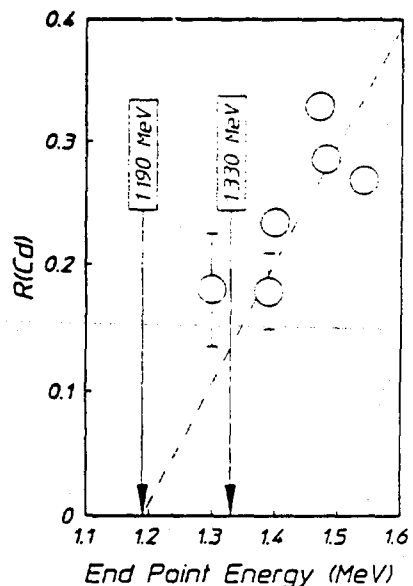

FIG. 4. Ratios of isomeric fractions produced in $^{111}Cd^m$ to those in $^{79}Br^m$, as corrected for the finite duration of the counting interval and plotted as a function of the end-point energy of the bremsstrahlung. Error bars show the counting statistical uncertainty. The dashed line shows a linear fit to the data intercepting the x axis at a gateway energy of 1.19 MeV. Excitation energy of the next higher gateway is shown at 1.33 MeV. In this figure and in Fig. 5, the error bars for the two least precise points have been shown. The statistical errors for the other points are commensurate with the plotting symbols in the figures.

found and the weighted average was taken to reduce statistical error. The resulting values of weighted activation ratio, R, from Eq. (3) are shown in Fig. 4.

The linear form of the dependence of the relative yield of fluorescence from the cadmium isomers seen in Fig. 4 between 1.1 and 1.6 MeV is a strong indication of the dominance of a single channel of excitation through a gateway level lying at an energy given by the value of the x intercept. While uncertainties in the actual endpoint energy of the electrons could be as great as ± 100 keV, the agreement between the intercept obtained in a similar experiment[14] for the activation of ^{115}In^m and the known energy of the predominant gateway at 1078 keV support the values given for end points in this energy range.

From the data of Fig. 4 it is seen that the intercept lies near 1200 keV, in agreement with the known $\frac{1}{2}^+$ state at 1190 keV. Also shown in Fig. 4 is the energy of the next higher gateway state having an acceptable J^π, the poorly characterized level at 1330 keV. It is interesting to observe that for end-point energies above this value there seems to be no clear tendency of the data to depart from the simple linear fit because of the availability of this additional gateway. A greater number of measurements at successively higher end-point energies would be needed to confirm this indication that the 1330 keV level has no particular role in the excitation of ^{111}Cd^m.

Once most of the data are established as being consistent with the model of excitation through a single level at 1190 keV, Eq. (3) provides a means of determining the absolute cross section for the excitation. In Fig. 5(a) data for the measured values on the left side of Eq. (3) are


TABLE I. Summary of integrated cross sections reported for the reaction ^{111}Cd$(\gamma,\gamma')^{111}$Cd^m through a level near 1200 keV.

Cross section $\pi b_a b_0 \Gamma \sigma_0 / 2$ $(10^{-29}$ cm^2 keV$)$	Reference
8($+4,-0.5$)	Cauchois, Heno, and Boivin (Ref. 9)
6± 2	Boivin, Cauchois, and Heno (Ref. 10)
15± 3	Yoshihara (Ref. 11)
10.2± 2.6	Lakosi, Csuros, and Veres (Ref. 12)
35± 4	Watanabe and Mukoyama (Ref. 2)
5.8± 0.8	Krcmar et al. (Ref. 3)
14± 1	Bikit et al. (Ref. 4)
9.8± 2.5	This work

plotted as functions of the relative intensities, $\zeta(1190)$, appearing on the right. As can be seen from Eq. (3), the best slope around which the data of Fig. 5(a) scatter would represent our experimental determination of the product of the first two terms on the right of Eq. (3). For comparison, the same approach is repeated in Fig. 5(b) to show the difficulty in attempting to force the interpretation that the principal gateway level is the state at 1330 keV. In Fig. 5(b) the weighted activation ratios are plotted as functions of $\zeta(1330)$. It is difficult to consider these data as approximating a linear dependence of R upon ζ, and particularly one which extrapolates to the origin as required by Eq. (3).

From the linear fit to the data of Fig. 5(a) shown as the heavy line, Eqs. (2) and (3), and the value of integrated cross section for ^{79}Br mentioned earlier, we obtain

$$\xi_{1190}(\text{Cd})=(8.2\pm 2.1)\times 10^{-32} \text{ cm}^2 .$$

The uncertainty was obtained from application of the same analyses to the lighter lines in Fig. 5(a) bounding the scatter from the least squares fit to the data. The scatter in the data is within the bounds established by this uncertainty in intensity.

Finally, substituting the value for $\xi_{1190}(\text{Cd})$ into Eq. (2) and solving for the integrated cross section gives for the 1190 keV transition in ^{111}Cd,

$$\pi b_a b_0 \Gamma \sigma_0 / 2 = (9.8\pm 2.5)\times 10^{-29} \text{ cm}^2 \text{ keV} .$$

This is the value we report in Table I.

IV. CONCLUSIONS

The detailed characterization of the spectrum emitted by the intense source of pulsed bremsstrahlung described earlier[8] has been found to be sufficient to determine the quantitative yield of the reaction ^{111}Cd$(\gamma,\gamma')^{111}$Cd^m. Table I shows that value to fall within the interval over which the prior measurements have scattered. In this work there was no need to invoke any theory of nonresonant reaction channels of the type sometimes used[3] in the description of this reaction.

In addition to providing further evidence against the occurrence of nonresonant reactions in ^{111}Cd, in concordance with the conclusions for ^{115}In, the results of this work have important implications for the calibration of intense sources of pulsed continua. By providing a pho-

FIG. 5. Plots of the weighted activation ratio R(Cd) as a function of the spectral intensity at energy E normalized to the intensity at the 761 keV gateway in ^{79}Br^m. (a) Plot for $E = 1190$ keV. The heavy line shows the least squares fit through the origin, and the lighter lines bound the uncertainty in such a fit. (b) Plot for $E = 1330$ keV, showing the absence of a reasonable fit that would include the origin.

toactivation channel with a well-defined gateway at 1190 keV, a sample of ^{111}Cd can readily complement the information supplied[3] by ^{80}Br about the intensity at 761 keV and by ^{115}In at 1078 keV.[14] Moreover, the results of this work may indicate why previous work gave such disparate results, no matter how carefully done. The most recent experiments[3,4] with ^{60}Co sources were strongly model dependent. In those efforts the irradiating intensity and its dependence upon experimental variables were assumed to be a result of Compton scattering from the ^{60}Co line at 1332 keV to the absorption energy at 1330 keV. From Fig. 4 it can be seen that the actual excitation energy is nearer 1200 keV. In the ^{60}Co experiments the intensities at the real gateway must have differed drastically from what had been calculated because of the substantial differences in energies assumed for the gateway.

[1] B. Pontecorvo and A. Lazard, C. R. Acad. Sci. 208, 99 (1939).

[2] Y Watanabe and T. Mukoyama, Bull. Inst. Chem. Res. 57, 72 (1979).

[3] M. Krcmar, A. Ljubicic, K. Pisk, B. Logan, and M. Vrtar, Phys. Rev. C 25, 2097 (1982).

[4] I. Bikit, J. Slivka, I. V. Anicin, L. Marinkov, A. Rudic, and W. D. Hamilton, Phys. Rev. C 35, 1943 (1987).

[5] B. Harmatz, Nucl. Data Sheets 27, 453 (1979).

[6] Evaluated Nuclear Structure Data File (Brookhaven National Laboratory, Upton, New York, 1986).

[7] J. A. Anderson and C. B Collins, Rev. Sci. Instrum. 58, 2157 (1987).

[8] J. A. Anderson and C. B. Collins, Rev. Sci. Instrum. 59, 414 (1988).

[9] Y. Cauchois, Y. Heno, and M. Boivin, C. R. Acad. Sci. Ser. B 262, 503 (1966).

[10] M. Boivin, Y Cauchois, and Y. Heno, Nucl. Phys. A137, 520 (1969).

[11] K. Yoshihara, Isot. Radia. Technol. 3, 464 (1960).

[12] L. Lakosi, M. Csuros, and A. Veres, Nucl. Instrum. Methods 114, 13 (1974).

[13] B. Rosner, Phys. Rev. 136, B664 (1964).

[14] C. B. Collins, J. A. Anderson, Y. Paiss, C. D. Eberhard, R J Peterson, and W. L. Hodge, Phys. Rev. C 38, 1852 (1988).

[15] K. Yoshihara, Zs. Nemeth, L. Lakosi, I. Pavlicsek, and A. Veres, Phys. Rev. C 33, 728 (1986).

[16] M. L. Wiedenbeck, Phys. Rev. 67, 92 (1945).

[17] E. C. Booth and J. Brownson, Nucl. Phys. A98, 529 (1967).

Comment on "Mössbauer sidebands from a single parent line"

C. B. Collins, P. W. Reittinger, and T. W. Sinor

Center for Quantum Electronics, University of Texas at Dallas, P.O. Box 830688, Richardson, Texas 75083-0688
(Received 25 March 1988)

Foils composed of alternating layers of ferromagnetic and nonmagnetic materials immersed in magnetic fields oscillati   radio frequencies display sidebands on Mössbauer transitions from the nuclei contained i.. the nonmagnetic regions. Attributed by Chien and Walker [Phys. Rev. B 13, 1876 (1976)] to the transfer into the nonmagnetic layer of acoustic phonons excited by magnetostriction in the ferromagnetic layers, this accepted cause of such effects is challenged by new data resulting from a reexamination and extension of that classical experiment.

The paper of Chien and Walker[1] was of such critical importance that it warrants comment over a decade later. Generally perceived as reporting an unarguable proof of a certain basic proposition, it has now been found to have rested upon a demonstrably false assumption. A reexamination of the original experiment shows it to have been so flawed that any conclusions drawn from it must now be considered unproven.

The point of inception had been the original proposal of Mitin[2,3] that Mössbauer transitions could be excited as part of a multiphoton process in nuclei immersed in intense radio-frequency (rf) fields. In those cases the Mössbauer spectrum was expected to show additional sum and difference frequency lines displaced from the normal lines by integral multiples of the perturbing frequency. In appearance such multiphoton spectra are expected to resemble the transmission spectra which Ruby and Bolef[4] obtained by imposing periodic Doppler shifts of purely mechanical origin upon the Mössbauer source. This unfortunate similarity in appearance between phenomena arising from such different origins provided the basis for years of critical controversy seemingly resolved by the work of Chien and Walker.[1] The purpose of this comment is to report new data from a repetition and extension of the Chien and Walker experiment that shows their conclusions to be unjustified. Without the force of conviction conveyed by their work, the controversy must be reopened to further investigation.

The earliest experiment in radio-frequency sideband production, reported by Perlow[5] in 1968, focused upon the components of the 14.4-keV transition in ^{57}Fe. Several ^{57}Co sources diffused into ferromagnetic hosts were immersed into intense magnetic fields oscillating at radio frequencies. Those results were attributed[5] to successive jumps in the hyperfine energies of the radiating states that had been caused by rotations of the local direction of the magnetization at the nucleus. Those jumps were assumed

to occur at the random times when domain walls passed, but with an average periodicity which was treated as a fitted parameter. Such a treatment could be termed a magnetodynamic model of sideband development which anticipated the results of the more complex propagation of the rotations of the magnetization in foils and tapes that was subsequently developed.[6,7] It generally conformed to the Mitin hypothesis for multiphoton transitions. Two of the three groups who initially documented this phenomena favored the magnetodynamic explanation which required no mechanical action[5,8,9] while the other group began to develop an alternative based entirely upon magnetostriction.[10,11] Most of the actual experiments had used ferromagnetic hosts to enhance the applied magnetic fields, and such materials are almost invariably magnetostrictive. In the model finally synthesized, periodic Doppler shifts were assumed to be driven by acoustic phonons which were excited by magnetostriction along the greatest dimensions of the material and scattered onto the axis connecting source and absorber. To be effective, this mechanism required the sample to have a large acoustic Q so that displacements of the active nuclei could build to significant values.

Despite the accretion over the years of a large body of phenomenology presumed to described rf sidebands on Mössbauer transitions, the magnetostrictive-acoustic theory never quantitatively predicted the amplitudes of the sidebands as functions of either applied power or frequency. However, the magnetodynamic models of that time fared no better, and attention turned to "proving" a magnetostrictive origin by distressing the alternative explanations.[12] The obvious difficulty with proving a theory by distressing the alternatives is that those other explanations may not have reached comparable levels of maturation. The magnetodynamic models of the late 1960's were relatively easy to destroy.[12] However, the recent successes of ferromagnetodynamics[6,7] show the early models[5] of

sideband formation to have been inspired, but inadequate approximations. Those models simply did not embody the level of sophistication necessary to describe the complex switching behavior of magnetization in ferromagnetic foils subjected to various combinations of static and oscillating fields in those geometries employed.

More recent experiments[13,14] have shown that the applications of such oscillating magnetic fields to Mössbauer nuclei embedded in nonmagnetic hosts do produce radio-frequency sidebands by directly modulating the phases of the nuclear states involved in the transitions. However, amplitudes were rather small in those experiments because the driving forces depended only upon the value of applied field $\mu_0 H$. In 1984, we extended such approaches further by deriving the phase modulation of a nuclear state in a magnetic material.[15] In this case driving forces were proportional to the magnetization $\mu_0 M$ and effects were found to be large.[15-17] It appears that many prior results attributed exclusively to acoustic effects driven by magnetostriction could have also benefited from an unrecognized contribution from direct phase modulations of the nuclear states involved.

From a current perspective it is the experiment reported by Chien and Walker[1] that forms the bulwark of the magnetostrictive-acoustic explanation of Mössbauer sidebands. In that experiment an absorbing foil composed of ferromagnetic and nonmagnetic layers was used to study transport of the causitive agent from the ferromagnetic layer into the nonmagnetic region where the sidebands were produced upon Mössbauer transitions of embedded ^{57}Fe nuclei. Very clear evidence showed that the cause did arise in the ferromagnetic Ni layers, producing sidebands in the nonmagnetic stainless-steel layers. The most ready explanation at that time was a transport of phonons from one layer to the next with a high acoustic Q. Those experiments were repeated in the work reported here, but with extensions which contradict the classic interpretation of Chien and Walker.[1]

Although not unique for all sidebands in a spectrum,[1] the idea of a modulation index m as a measure of the strength of the development of the sidebands offers practical convenience for descriptions. For a magnetostrictive origin,[1]

$$m = x_0/\lambda , \qquad (1)$$

where x_0 is the amplitude of the periodic displacement of the nuclei and $\lambda = 0.137$ Å for the 14.4 keV line of ^{57}Fe. In the corresponding magnetodynamic model,[15]

$$m = bH . \qquad (2)$$

where H is the applied magnetic field and b provides proportionality between M_s, the saturation magnetization of the medium, and H. For relatively small m, the ratio of the magnitude of the first order sidebands to the intensity in the original parent line is proportional to m^2, which in turn is proportional to P, the applied radio-frequency power.

One of the most compelling results presented by Chien and Walker[1] was a demonstration supposed to show the enhancement of m^2 afforded by tighter acoustic coupling of the layers. They found that electroplating Ni upon a stainless-steel foil produced much higher values of m^2 in absorption experiments than could be obtained by gluing a Ni foil to the stainless foil. They attributed the difference to the obviously poorer acoustic properties of the glue. However, as part of this report we observe that their stainless-steel foil was electroplated on *both* sides with Ni while the epoxied bond was used to join a *single* Ni foil to one side of the stainless absorber. While the m defined by Eq. (1) for a single foil could not be additive if produced in different magnetostrictive layers, in principle the H upon which m depends in Eq. (2) could add coherently. Two sources of m arising from distinctly separate sources could give a resulting modulation of $4m^2$ in a magneto-dynamic model. Chien and Walker failed to recognize[1] that even in the magnetostrictive model two sources of m generated in the two electroplated layers should give a modulation index of $2m^2$ in the absorber foil. Instead, they attributed the increased sideband intensity developed by the two plated sources in comparison to the one glued source only to the advantage they assumed for a plated contact over a glued interface. They reported no comparison of the effects of gluing or plating the *same number of ferromagnetic layers to the absorber foil*. Reported here is a repetition of the Chien and Walker experiment which showed that the effect of two foils varied from two to four times that produced by a single foil joined in the same fashion, depending upon the static magnetic bias applied.

In our experiment the absorber was a 2.5 μm paramagnetic stainless-steel (SS) foil with 90.6% enrichment of ^{57}Fe. For the nonabsorbing ferromagnetic drivers, 2.5 μm Ni foils were used, all of which were cut from a single sheet of polycrystalline Ni. The stainless-steel absorber was sandwiched between two Ni foils and held in rigid contact by mounting the foils between glass cover slides of 100 μm thickness. A conventional Mössbauer spectrometer, modified for rf experiments (Fig. 1), utilized a 25-mCi source in a Rh matrix to obtain the ^{57}Fe absorption spectra. The 14.4-keV gamma rays were detected with a Kr gas filled proportional counter biased with 1.8 kV.

A 25 MHz rf magnetic field was applied by mounting the foils in the cylindrical induction coil of an L-C tank circuit. In obtaining data for a direct comparison between the effect of one Ni driver versus two, the product of the applied rf power P and the electrical Q of the circuit containing the rf induction coil was maintained at constant values. Elementary analysis shows that if PQ is constant the rf current in the coil of such a circuit is also constant and hence the two absorber arrangements are subjected to applied fields of the same intensity H. The results of the first experiment verified the linearity of the first-order sideband amplitudes at 25 MHz for SS with two Ni drivers with PQ products of 75, 150, and 300 W as shown in Fig. 2. The spectra are scaled so that the intensity of the central Mössbauer absorption peak of ^{57}Fe in SS is held constant in order to make direct comparisons of the sideband amplitudes.

Having established the linearity of the first-order sidebands in the Ni-SS-Ni sandwich, one of the Ni drivers was removed and the experiment was repeated with the same PQ products as before. Figure 3 shows a comparison of the sideband amplitude for two Ni drivers versus
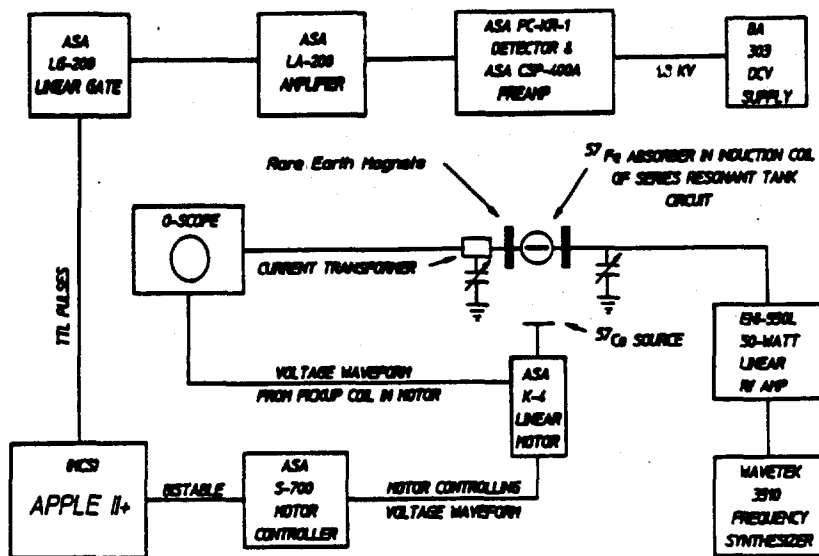
FIG. 1. Schematic drawing of the experimental arrangement used.

one; in this configuration two Ni drivers give twice the effect of one driver foil.

In the next experiments a comparison was made between the effect of one source of excitation with that from two sources when both were biased with a static magnetic field. Rare-earth element magnets were placed about the induction coil such that the static magnetic field was mutually orthogonal to the rf magnetic field and to the direction of gamma-ray propagation.

The linearity of the sideband amplitudes at 25 MHz as a function of PQ was again established as shown in Fig. 4 to insure that the introduction of the static magnetic field did not introduce any nonlinearities into the system. The scale thus established was used to measure the decrease in the sideband amplitude when one of the sources of excitation was removed from this biased sandwich. As is clearly shown in Fig. 5, the sideband amplitudes obtained with two driver foils are four times the amplitudes obtained with one driver foil. Therefore, with the application of a
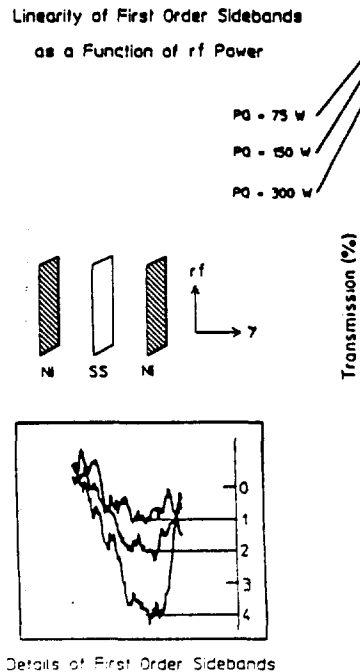

FIG. 2. Experimental verification of the linearity of the first-order sidebands at 25 MHz as a function of the applied rf power. The product of the applied rf power P and the quality factor Q of the circuit are used to insure reproducibility of the rf field strengths.
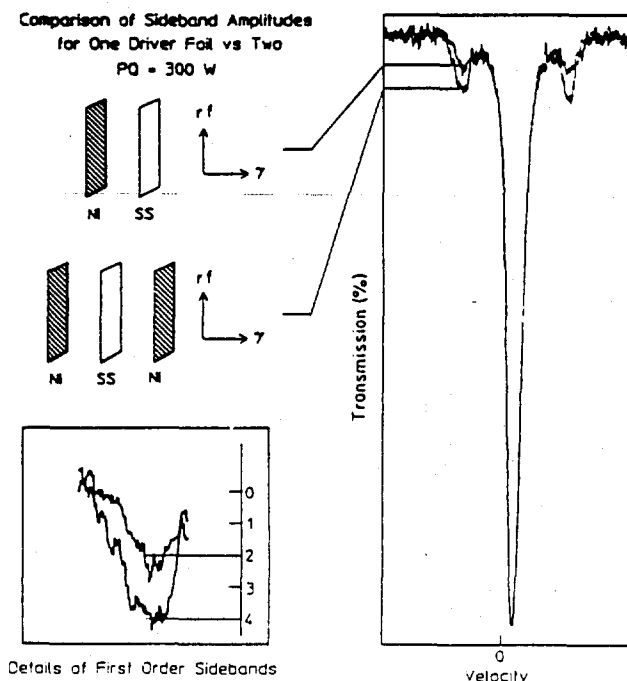

FIG. 3. Comparison of first-order sideband amplitudes for one Ni driver foil vs two at 25 MHz with a PQ product of 300 W.
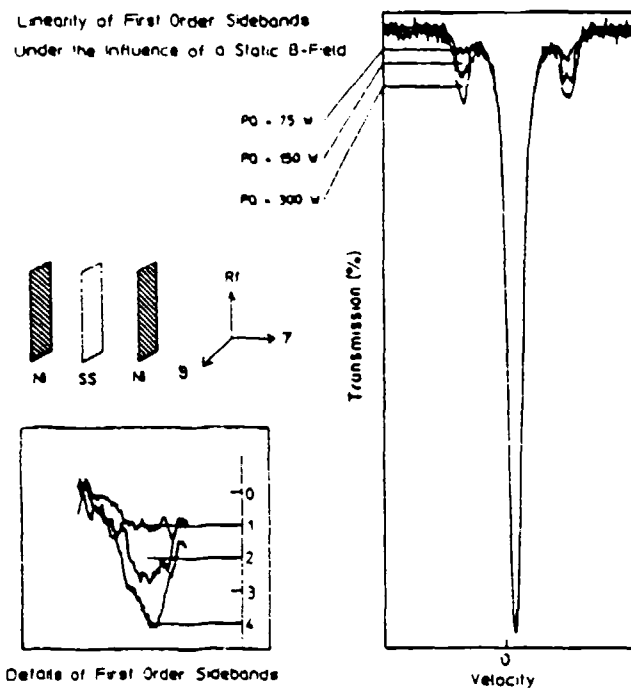
FIG. 4. Establishment of linearity of the first-order sidebands at 25 MHz with $PQ=75$, 150, and 300 W when the foils are biased with a static B field.

FIG. 5. Comparison of sideband amplitudes for one driver foil vs two when both are biased by a static B field with $PQ=300$ W. Here two foils give four times the effect of one thus giving a modulation index of $4m^2$.

static B field, two sources of excitation give four times the effect.

The results of this reexamination of the Chien and Walker experiment support only the first conclusion reached in that original work, namely that the causitive agent of rf sidebands can be produced in a ferromagnetic layer and then transported into a nonmagnetic layer. Their other conclusion is completely refuted by this demonstration because the effects they attributed to the type of coupling between layers most probably resulted from the relative numbers of magnetic and nonmagnetic layers.

These new results go beyond the propositions tested by Chien and Walker[1] and display behaviors completely inconsistent with the traditional magnetostrictive-acoustic origin of Mössbauer sidebands. In experiments such as these, acoustic phonons are the bosons associated with vector fields driven by tensor forces, not vector forces. Without invoking stimulated emission, we can conceive of no way in which tensor sources which are physically separated can produce coherent vector fields in a space between them, even if they are temporally synchronized. As the fields increase the magnetostrictive foils will become stressed along parallel axes which are displaced by the thickness of the stainless layer between them. There is no mechanism to produce a displacement vector in a particular transverse direction as a consequence of the resulting strains in the Ni foils. Only a small scale bulging or buck-

ling of each Ni foil is to be expected and this is usually described as the scattering of phonons at right angles to the source. Without the stimulated emission of such phonons, there is no way to insure that one foil buckles toward the stainless layer at a particular point while the other buckles away.

The stimulated emission of phonons that would be necessary to produce coherent additions of the displacements arising from the different sources would imply the existence of a threshold of power, above which two modulation indices of m would give an effect of $4m^2$ and below which only $2m^2$. No such threshold was suggested by data similar to that of Fig. 5 which was obtained over an adequate range of powers.

In view of the growing number of successes of the model for the direct modulati of the phases of the nuclear states and these new results which question the validity of the conclusions of the Chien and Walker[1] experiment, it would appear that the controversy over the origin of Mössbauer sidebands must be reopened.

[1] C. L. Chien and J. C. Walker, Phys. Rev. B 13, 1876 (1976).

[2] A. V. Mitin, Zh. Eksp. Teor. Fiz. 52, 1596 (1967) [Sov. Phys. JETP 25, 1062 (1967)].

[3] A. V. Mitin, Dok. Akad. Nauk SSSR 194, 59 (1971) [Sov. Phys. Dokl. 15, 827 (1971)].

[4] S. L. Ruby and D. I. Bolef, Phys. Rev. Lett. 5, 5 (1960).

[5] G. L. Perlow, Phys. Rev. 172, 319 (1968).

[6] T. H. O'Dell, *Ferromagnetodynamics* (Wiley, New York, 1981), Chap. I.

[7] C. W. Chen, *Magnetism and Metallurgy of Soft Magnetic Materials* (North-Holland, Amsterdam, 1977).

[8] G. Asti, G. Albanese, and C. Bucci, Nuovo Cimento B 57, 531 (1968).

[9] G. Asti, G. Albanese, and C. Bucci, Phys. Rev. 184, 260 (1969).

[10] N. D. Heiman, L. Pfeiffer, and J. C. Walker, Phys. Rev. Lett. 21, 93 (1968).

[11] N. D. Heiman and J. C. Walker, Phys. Rev. 184, 281 (1969).

[12] L. Pfeiffer, N. D. Heiman, and J. C. Walker, Phys. Rev. B 6, 74 (1972).

[13] P. J. West and E. Matthias, Z. Phys. A 288, 369 (1978).

[14] E. Ikonen, P. Helistö, J. Hietanieni, and T. Katila, Phys. Rev. Lett. 60, 643 (1988).

[15] C. B. Collins and B. D. DePaola, Opt. Lett. 10, 25 (1985).

[16] B. D. DePaola and C. B. Collins, J. Opt. Soc. Am. B 1, 812 (1984).

[17] B. D. DePaola, S. S. Wagal, and C. B. Collins, J. Opt. Soc. Am. B 2, 541 (1985).

Large-Scale Effects of the Magnetic Phase Modulation of Recoilless γ Transitions

T. W. Sinor, P. W. Reittinger, and C. B. Collins

Center for Quantum Electronics, University of Texas at Dallas, P.O. Box 830688,
Richardson, Texas 75083-0688

(Received 6 July 1988)

The excitation of coherent transients in Mössbauer spectra has been previously limited by the high powers required to modulate the nuclear phases. Reported here is an orders-of-magnitude increase in the efficiency through which such phenomena can be produced. Magnetic modulation of the quantum phases of ^{57}Fe nuclei in paramagnetic media has been produced by spin waves of large amplitude transported from ferromagnetic sources.

A recent Letter[1] reported variations in recoilless γ-ray spectra produced by directly modulating the interaction energies arising from the couplings of the nuclear magnetic moments to the hyperfine fields. Described in terms of the phase modulation of the nuclear states involved in the transition, those results represent important realizations of some of the general possibilities for developing nuclear analogs[2,3] of coherent transient effects studied in quantum optics.

An example is found in the frequency domain in the excitation of sidebands on γ-ray transitions, and precursive work[4–6] had treated that problem in a manner equivalent to an application of the phase modulation formalism.[3] For cases in which there is no static magnetic field[5] or in which the modulation is parallel to the static field,[6] the effect of the time-varying component $H_0 f(t)$ upon an eigenstate of the nucleus, $\Psi_{a,m}^{(0)}$, can be written

$$\Psi_{a,m} = e^{-i\phi_a(t)}\Psi_{a,m}^{(0)}, \qquad (1)$$

where $\phi_a(t)$ is the modulation angle of the phase,

$$\phi_a(t) = m\omega_a \int_0^t f(t')dt', \qquad (2)$$

and the Larmor frequency ω_a is

$$\omega_a = \mu_N g_a H_0/\hbar, \qquad (3)$$

where μ_N is the nuclear magneton, g_a is the gyromagnetic ratio for the ath excited or ground state of the nucleus, and m is the magnetic quantum number of the eigenstates.

In principle, the difference in phase modulation between the ground state, g, and an excited state, e, may be observed during an absorption transition because the Fourier components of $\phi_e(t) - \phi_g(t)$ will be manifested as sidebands. However, since the transition will have a width Γ associated with the time-dependent decay of the states, unless,

$$\hbar\omega_a \gtrsim \Gamma, \qquad (4)$$

the sidebands will be buried in the natural wings of the probing transition.

Only the ingeneous use of the ultranarrow, 93-keV line of ^{67}Zn permitted the quantitative study of the coherent phase modulation effects recently described.[1] That benchmark achievement required field amplitudes reaching 13.4 mT for sinusoidal modulation at applied frequencies ω up to 10 kHz and effects were reported[1] to scale as $(H_0/\omega)^2$.

The conceptual key to orders-of-magnitude enhancement of phase modulation effects has been reported[7–9] to lie in the use of smaller powers to manipulate the greater magnetic fields arising from the natural correlations of individual spins in ferromagnetic materials. However, the modulation $\partial M/\partial t$ of the magnetization M of a ferromagnetic material is rarely parallel to either the applied field H_0 or even to M itself.[10] For such cases of nuclei in ferromagnetic media, the modulation angle of Eq. (2) takes a more complex form;[7] and one which causes a mixing of the eigenstates $\Psi_{a,m}^{(0)}$. Nevertheless, the principal parameter is still a Larmor frequency Ω_a which for magnetic environments becomes

$$\Omega_a = \mu_N g_a M/\hbar, \qquad (5)$$

a value much larger than that found in Eq. (3) for non-magnetic samples. Unfortunately, magnetic materials are almost invariably magnetostrictive and the concern has lingered that even the enhanced effects of phase modulation might always be overwhelmed by the periodic Doppler shifts produced by vibration in the lattices excited by magnetostriction.

The propagation of magnetoelastic waves is a complex problem which has been intensively studied since 1958.[11] For many magnetic media the dispersion equation for such waves displays several branches[12,13] which can be individually identified with spin waves, magnetostatic waves, or elastic waves. Mixed waves coupling magnons and phonons occur principally when branches intersect, so that the frequencies and wavelengths for both are nearly equal.[11] Away from those values of parameters magnetic and acoustic waves can be separated. In principle this offers a means to propagate only the former to some remote part of a sample where it is desired to magnetically modulate the phases of the states of the nuclei without carrying acoustic noise along to the same place.

The most convenient of the Mössbauer transitions for modulation experiments is the 14.4-keV transition of

^{57}Fe diluted in a thin metal foil. The propagation of magnetic waves in conductive foils presents a special problem because of eddy-current losses; Kittel has given an approximation[11] which would limit the mean free path for a magnon to a few wavelengths for the frequencies of tens of MHz which would be interesting for use with ^{57}Fe. For this reason the preferred choices for the propagation of magnetization in such thin metallic foils are the magnetostatic waves characterized by long wavelengths and high group velocities[12,14] that are quite removed from intersections with acoustic branches. Wavelengths can readily reach the scale of millimeters, and it has been demonstrated that dispersion properties are little affected by raising the temperature of the foil above the Curie point.[15] Thus, if they can be excited at the boundaries, such spin waves should propagate in paramagnetic foils as well as they do in conductive ferromagnetic foils.

A stainless-steel foil 10 mm×20 mm×2.5 μm was used in these experiments. It was rolled from a nonmagnetic alloy, 310, which was expected[16] to have a susceptibility of about 4000×10^{-6} cgs. When enriched in ^{57}Fe, it displayed a single absorption line at 14.4 keV. Relatively recently, it has been shown[17] how to communicate the large values of magnetization characteristic of ferromagnetic materials into thin foils of paramagnetic media, such as stainless steel at room temperature, by sandwiching it between ferromagnetic layers. Grünberg demonstrated that at small separations ferromagnetic foils switch coherently so that lines of fringing flux emerging from one continue across to the other. Flux refraction insures that this small normal component is compressed in the separating layer by a factor comparable to its ratio of length to thickness, an aspect ratio of about 10^4 in these experiments. In this way a wave of

oscillating magnetization was launched into a stainless-steel tape, enriched in ^{57}Fe so that nuclear phase modulation might be observed at a distance from the source of the disturbance that was greater than the range for the transport of acoustic phonons.

This experiment employed a conventional Mössbauer spectrometer with a 2 mCi ^{57}Co source in a Pd matrix to obtain the ^{57}Fe resonance spectra in a transmission geometry. To detect the 14.4-keV γ rays we used a high-resolution EG&G high-pu ty Ge detector. A Wavetek Model 3000 signal generator and a 50-dB ENI-325LA linear radio-frequency (rf) amplifier provided the oscillating magnetic field.

To calibrate the contributions from ultrasonic and from phase modulation effects two independent techniques of sideband generation were used. As a basis for comparison, ultrasonic sidebands were excited on the unsplit absorption line of ^{57}Fe nuclei in the same stainless-steel foil by sinusoidal vibrations injected with two different 25-MHz piezoelectric transducers. One was X cut and the other AT cut in order to inject the widest possible variety of phonons of vibration for transmission to the point of observation in the geometry of Fig. 1(a).

As shown in the lower panel of Fig. 1(b) an 8×10 mm^2 section of the foil was acoustically bonded to each of the transducers used in this experiment. The remaining length was gently curved, forming a 90° angle with the plane of the transducer. Mechanical support was provided for the remote section of foil by mounting it between glass cover slides which were then fastened to the transducer cell.

In the usual geometry for a transmission experiment arranged to sample excitation at the source, a convenient level of input power of 0.06 W to the X-cut crystal produced the reference level of sideband development seen
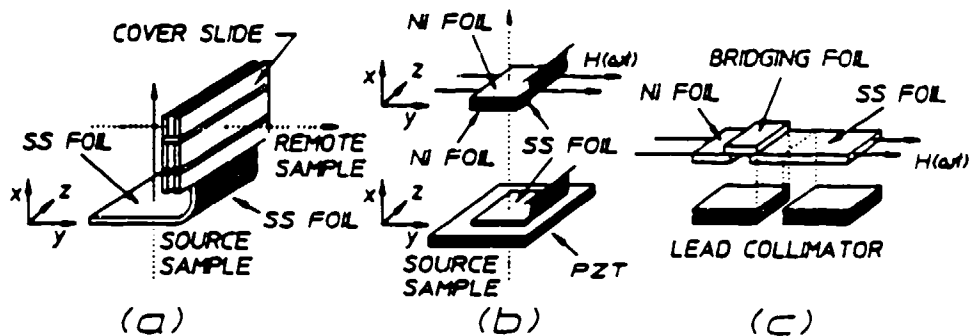

FIG. 1. Schematic representation of the mounting arrangements used in the excitation of sidebands on the Mössbauer absorption line of ^{57}Fe in the 2.5-μm-thick stainless-steel (SS) foil. (a) The optical path from γ source to detector is shown by the dotted arrow for the orthogonal x and y directions arranged to sample sideband development at the source of the phenomenon and at a remote point, respectively, as marked. Excitation is injected into the horizontal face of the SS foil and the vertical face is mechanically stabilized by the 100-μm-thick glass cover slides sandwiching the absorber foil. (b) Upper: spin waves injected by the periodic oscillation of the Ni foils pressed onto the absorber foil by additional cover slides not shown and excited by the magnetic field in an inductor containing the Ni foils. The vertical section protrudes from the coil between windings. Lower: vibrational excitation injected by the X-cut quartz-crystal transducer connected to a radio-frequency oscillator. (c) Geometry used in the experiments designed to bridge a break in the conductive path with 25-μm-thick foils of various materials.

in Fig. 2 in which the fourth order contained 34% of the intensity remaining in the parent transition. Nevertheless, the effect of phonons transported in the foil about 1 cm around a bend of 90° could not be detected even with a tenfold increase in power above the reference level. Nor could they be observed at the remote sampling point when excitation was provided by the AT-cut transducer which required a larger input power of 2.9 W in order to obtain the same reference level of sideband development at the source position. The presence of a high level of phonon excitation *in the stainless-steel foil at the source end* was clearly demonstrated by the strong development of the sidebands seen there, but evidently those phonons could not propagate to the remote point of observation. If there had been any low-loss modes for the transport of purely elastic waves in the stainless-steel foil, the population of phonons already in the foil at the source end should have coupled into them. However, the absence of phonon transport actually observed seems consistent with the difficulties expected in propagating transverse vibrations through a medium which is very thin in comparison to a wavelength and one in which the local acoustic Q is expected to be high.[18]

In the experimental arrangement used to launch spin waves, the piezoelectric transducer was replaced with a pair of 2.5-μm foils of ferromagnetic Ni (8×10 mm^2) which were periodically magnetized as shown in the upper panel of Fig. 1(b). The foils (Ni-SS-Ni) were held in rigid contact by sandwiching them between glass cover slides at the source end. Only the source end of the experiment was changed and the protruding section of the stainless-steel foil was again bent at an angle of 90° and enclosed between glass cover slides in the same way as before. Mechanical rigidity was provided to the absorber assembly by a plastic frame.

An rf magnetic field of 0.07 mT was applied to the absorber via a flattened induction coil of a tuned LC circuit. During observation in the x direction at the source end the rf power level was adjusted to give about the

same reference level of sideband development as had been generated with the piezoelectric transducer. This insured the same ambient level of phonons in the foil at the source end and thus provided for a direct comparison of the phase modulation effects propagated by magnetostatic waves with the null level of acoustic noise that had reached the same point of observation during calibration.

The spectra obtained in the samples of the source and remote points in the geometry of Fig. 1(b) are shown in Fig. 3. At the remote point for this same level of input power, first-order sidebands containing about 22% of the intensity of the parent line developed. This represents a level 10 times the threshold for detection and hence 100 times any component contributed by acoustic phonons as determined from the data of Fig. 2. It seems that these experiments have shown that an oscillating alignment of spins can be propagated through a paramagnetic foil better than mechanical vibrations can be transported under the same conditions.

Moreover, such effects of spin waves were not sensitive to mechanical pressures or spurious damping and the complete disassembly, substitution of foils, and reassembly served to reproduce closely the levels of excitation seen in Fig. 3. Only the thickness and length of the foil, together with the level of input power, were found to be variables that significantly affected the result.

Finally, to confirm the magnetic nature of the transport of the cause of the sidebands, the Ni foil generating the spin waves was separated from the SS foil by a gap which was then bridged as shown in Fig. 1(c) by foils having various magnetic and acoustic properties. To insure reliable and reproducible contact of the foils the layers were pressed between two thin glass plates. As expected, these plates alone were unable to communicate the spin waves from the Ni to the SS and no sidebands could be produced without a bridging foil.

All of the bridging foils were of a uniform size and thickness, being 4 mm by 10 mm by 25 μm, respectively. They differed only in acoustic and magnetic properties.


FIG. 2. Absorption spectra of ^{57}Fe in stainless steel showing sidebands developed by phonons present in the sample foil. (a) Reference spectrum observed in the x direction at the source at a level of excitation of 0.06 W in the piezoelectric crystal. (b) Spectrum observed in the y direction at the remote point shown in Fig. 1(a) for an excitation level of 0.7 W. Only the unsplit parent line is seen.


FIG. 3. Absorption spectra of ^{57}Fe in stainless steel showing sidebands resulting from the modulation of nuclear phases by spin waves present in the sample foil. (a) Reference level of excitation observed at the source in the x direction shown in Fig. 1(b) at a field amplitude of 0.07 mT. (b) Sidebands observed in the y direction at the remote point for the same driving field of 0.07 mT.

TABLE I. Summary of experimental results for the rf bridging experiments.

Bridging material	Susceptibility χ $(10^{-6}$ cgs)	Acoustics impedance $Z = \rho c$ $(10^5$ g/cm^{2}sec)	Effect transported
Aluminum	+16.5	17.33	Yes
Copper	−5.46	44.74	No
Silver	−19.5	37.96	No
310-SS	+4000	45.4	Yes
Tin	−37.0	24.24	No
Titanium	+153	27.32	Yes

FIG. 4. Absorption spectra of ^{57}Fe in stainless steel in the geometry of Fig. 1(c) for a certain constant level of radiofrequency input. (a) Sidebands developed with an Al bridge. (b) Null effect obtained with a Cu bridge.

As shown in Table I, the transport of the spn waves correlated completely with the susceptibility of the bridge and showed no dependence upon the matchings of acoustic impedances.

For example, consider the case for Al which has a magnetic susceptibility of $+16.5 \times 10^{-6}$ cgs but which offers a very poor matching of its acoustic impedance to that of either Ni or SS. With an Al bridge there was a strong transport of the cause of the sidebands as seen in Fig. 4(a). In contrast Cu which is diamagnetic, as indicated by its negative susceptibility, should have been unable to propagate spin waves across the gap, despite its very close match of acoustic properties to both Ni and SS. Figure 4(b) shows that sidebands did not develop with the Cu bridge.

While it is expected that the transport of purely acoustic waves should be quite sensitive to interface contacts and damping effects, the spin waves propagated in these experiments were not found to be affected by the contact pressure or by the mechanical mounting. The area of contact and length of the bridge were important parameters but the pressure of the cover glasses and placement of the supports were not important. The data of Fig. 4(a) were routinely reproduced to within the noise level even after disassembly and rearrangement of the mechanical parts.

In these experiments the driving amplitude H_0 in the Ni was around 0.07 mT while the frequency was 23.74 MHz. Without the excitation of spin waves the effect should have been smaller by at least the ratios of the scaling parameters, $(B_0/\omega)^2$, a factor of 10^{11} for this case. The great enhancement in the effects of coherent modulation which spin waves produce makes possible the examination of many other coherent phenomena predicted at practical ranges of tuning and accessible levels of input powers.

[1]E. Ikonen, P. Helisto, J. Hietaniemi, and T. Katila, Phys. Rev. Lett. 60, 643 (1988).
[2]P. Helisto, E. Ikonen, T. Katila, and K. Riski, Phys. Rev. Lett. 49, 1209 (1982).
[3]E. Ikonen, P. Helisto, T. Katila, and K. Riski, Phys. Rev. A 32, 2298 (1985).
[4]A. V. Mitin, Zh. Eksp. Teor. Fiz. 52, 1596 (1967) [Sov. Phys. JETP. 25, 1062 (1967)].
[5]P. J. West and E. Matthias, Z. Phys. A 228, 369 (1978).
[6]S. Olariu, I. Popescu, and C. B. Collins, Phys. Rev C 23, 1007 (1981).
[7]C. B. Collins and B. D. DePaola, Opt. Lett. 10, 25 (1985).
[8]B. D. DePaola and C. B. Collins, J. Opt. Soc. Am. B 1, 812 (1984).
[9]B. D. DePaola, S. S. Wagal, and C. B. Collins, J. Opt. Soc. Am. B 2, 541 (1985).
[10]T. H. O'Dell, Ferromagnetodynamics (Wiley, New York, 1981), Chap. 2.
[11]C. Kittel, Phys. Rev. 110, 836 (1958).
[12]P. C. Fletcher and C. Kittel, Phys. Rev. 120, 2004 (1960)
[13]E. Schlömann, J. Appl. Phys. 31, 1647 (19 0)
[14]R. W. Damon and J. R. Eshback, J. Appl. Phys. Suppl. 31, 1045 (1960).
[15]H. A. Mook, J. W. Lynn, and R. M. Nicklow, Phys. Rev. Lett. 30, 556 (1973).
[16]T. Lyman, Metals Handbook (American Society for Metals, Metals Park, OH, 1961), 8th ed., Vol. I, p. 793.
[17]P. Grünberg, J. Appl. Phys. 51, 4338 (1980).
[18]L. Pfeiffer, N. D. Heiman, and J. C. Walker, Phys. Rev. B 6, 74 (1972).

Laser plasma source of amorphic diamond

C. B. Collins, F. Davanloo, E. M. Juengerman, W. R. Osborn, and D. R. Jander

Center for Quantum Electronics, The University of Texas at Dallas, P. O. Box 830688, Richardson, Texas 75083-0688

Amorphic diamond films characterized by a high percentage of sp^3 bonds have been prepared in an UHV environment with a laser plasma source of carbon ions. Peak power densities in excess of 10^{11} W/cm^2 were found necessary to produce films at growth rates of 0.5 μm/h over areas of 20 cm^2 having optical quality sufficient to show bright interference colors.

The past few years have witnessed a renaissance in the preparation and study of thin films of carbon having diamond-like properties.[1] However, while natural diamond is a well-defined substance, these diamond-like films are not. In many cases different materials result from the different methods of preparation and this has contributed much complexity to the evaluation of the merits of the different techniques of growth.

From a structural viewpoint, Spencer[2] has identified six allotropes of carbon, two for each of the numbers of dimensions through which the carbon atoms may bond. The ones most important in the formation of thin films of diamond-like carbon (DLC) are the two-dimensional sp^2 bonds which characterize graphite and the three-dimensional sp^3 bonds which give cubic diamond its unique properties.

From the standpoint of mechanical and electrical properties the best results have been obtained with a class of DLC materials denoted as a-C:H, the a suggesting an amorphic structure. They can be grown by a variety of techniques for chemical vapor deposition (CVD) at rates practical for commercial applications. Surprisingly, these materials contain hydrogen in amounts which vary from about 20 to 60%. Within these limits the amount of hydrogen correlates with the proportions of sp^3 to sp^2 bondings and thus, with the prevalence of diamond-like properties. A reduction in the amount of hydrogen in such a film degrades it toward graphite. At 20% there is a discontinuity in stability and only pure carbon films can exist with less than this limiting amount of hydrogen.[1]

Denoted as a-C films, these unhydrogenated DLC films have received relatively little attention, although they have been known for quite some time. As early as 1971, Aisenberg and Chabot[3] reported the quenching of a beam of C$^+$ ions in the presence of Ar and Ar$^+$ on a cold substrate to form an amorphic layer containing no hydrogen, yet having some diamond-like properties. Spencer et al.[2] continued this line of development in 1976, attributing the favorable properties of the deposited layers to the selective destruction of exposed sp^2 bonds by the bombarding ions. However, with these early ion beam methods the growth rates were extremely slow and the material they produced remained only a curiosity until relatively recent times.

With a high fluence ion source Miyazawa et al.[4] brought growth rates up to about 360 A/h on a 1 cm^2 substrate, while Savvides[5,6] achieved 500 A/h on a 20 cm^2 area with a sputtered source of carbon ions and atoms. Even higher growth

rates were demonstrated at the cost of degraded film quality. The resulting availability of samples of a tangible scale together with the potential importance of such films in optical applications seems to have motivated an intensive study of their optical properties. Unlike the a-C:H materials these unhydrogenated DLC films were moderately clear in the visible wavelengths and Miyazawa recorded the observation of colored interference fringes.[4] The resulting indices of refraction reported by Miyazawa and Savvides[6] are collected in Figs. 1(a) and 1(b).

(a)   PHOTON ENERGY (eV)
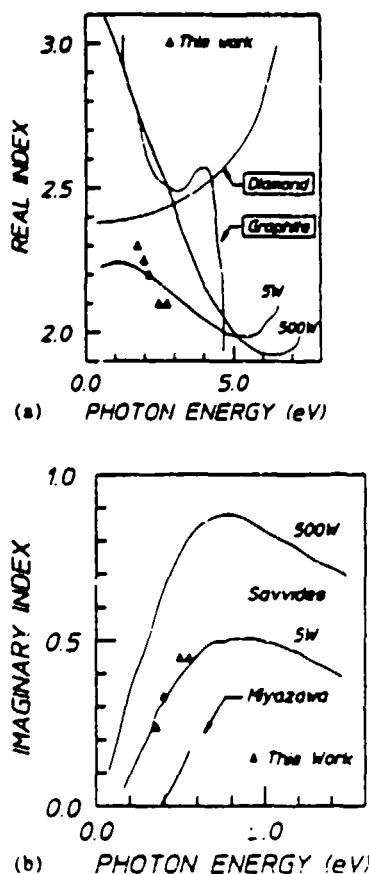

(b)   PHOTON ENERGY (eV)

FIG. 1. Symbols plot the real and imaginary parts of the refractive indices of a-C films produced by the laser plasma source described in this work as functions of photon energy. (a) Real parts plotted together with comparative values for diamond and graphite as indicated. Dotted curves show the results reported in Ref. 6 for films prepared with a sputtered ion source operated at the powers shown. (b) Imaginary components of the refractive indices of a-C films reported by Savvides in Ref. 6 are shown by the dotted lines for the two powers used in his process while results reported by Miyazawa in Ref. 4 are plotted by the solid curve.

While the real parts of the indices in Fig. 1(a) are interesting in their approaches to the value of 2.42 for natural diamond, the greatest diagnostic significance lies in the imaginary parts, shown in Fig. 1(b). Savvides has shown[5,6] how at small values this extinction coefficient is reasonably proportional to the fraction of sp^2 bondings in the film, provided the real part is reasonably constant. Purely diamond-like sp^3 bonding would give no loss at these photon energies. The lower curve, identified by the 5 W of input power to the sputtering source in Savvides' system, provides a calibration that is identified with a 25% content of graphitic, sp^2 bonds. Though not computed previously, it can be seen that Miyazawa's films should have contained only about 10% of the sp^2 bonding. This compares favorably with the best results[1] attained by using hydrogen to minimize to 14% the proportions of sp^2 bonds in a-C:H. Since the latter material is black in the visible because of the hydrogen bonding, the a-C films might be the preferred choice for some applications, if the growth rates were of practical magnitudes. Moreover, if the residual sp^2 bonds could be shown to be an artifact of the production, as opposed to being a necessary ingredient for stability, then the direction would be shown toward the development of truly amorphic diamond containing only sp^3 bonds.

Reported here are the deposition and characterization of several a-C films grown at rates of 0.5 μm/h on 20 cm^2 areas with a laser plasma source. The experimental arrangement is shown in Fig. 2. As can be seen, it represents a substantial evolution from the laser plasma device we described earlier,[7] both in the electronics and in the laser. The laser plasma source of Wagal,[7] together with the earlier sources of Richter[8] and Sato,[9] had been limited to peak intensities at the graphite feedstock of a few $\times$ 10^{10}, 10^8, and 10^9 W/cm^2, respectively. The system shown in Fig. 2 uses a Q-switched Nd-YAG laser to deliver 250 mJ to the focus at a repetition rate of 10 Hz. Because of an improved optical system it produces 5 $\times$ 10^{11} W/cm^2 in a 15 ns pulse at the graphite target. While Sato[9] and Wagal[7] used supplementary electrodes for cleaning the substrate and for steering the ions, respectively, the system in Fig. 2 incorporates an auxiliary discharge to further increase the plasma temperature by Joule heating in the small volume of the ablation plume.
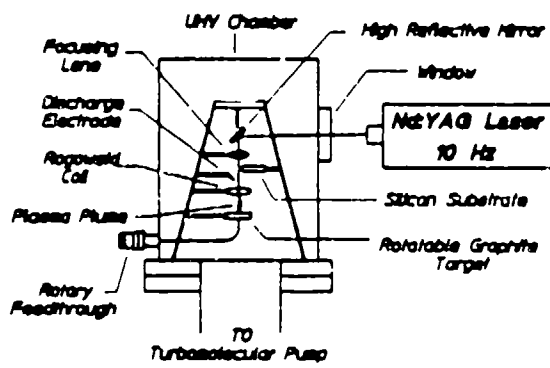
The current which was passed from electrode to the ablation plume was measured with a Rogowski coil, electrically isolated from the deposition system. A typical result is shown in Fig. 3 where it can be seen that currents peak in the 1–10 A range in a pulse are found to have FWHM of the order of 2 μs. From the time dependence of the current it appears that it flows only when the ejected material is filling the space between the point of ablation and the electrode, as would be expected.

The current-voltage (I-V) characteristics seen in Fig. 3 are typical for a gas-filled diode with the "forward" direction for conduction that is shown in the first quadrant being established when the plume is negative, and so able to function as a hot filament. The selection of either positive or negative voltages to give the same absolute values of current generally yielded very similar depositions on Si(100) substrates. Usually a value of 10 A was used. There was no particular sensitivity of the results to the placement of the collecting electrode, but no effect of the discharge current unless it passed through the small volume at the laser focus.

The characterization of such thin lossy films as produced in this work requires particular attention to the fact that ellipsometry, as customarily employed, does not give a unique result, when both real, n_0 and imaginary indices, n, are to be measured together with the thickness z. In our experiments, ellipsometry was used at 632.8 nm and reflectance spectroscopy was employed to obtain uniqueness. Measurements of reflectance spectra at normal incidence were fitted to textbook expressions[10] to give values of ($n_0 z$) and (n/n_0) and with these a unique result could be obtained from the ellipsometry data.

Phenomenology was examined over a wide range of process variables. All experiments were conducted in an UHV environment operated around 10^{-6} Torr, as residual pressures seemed of little actual significance. The only variables of particular importance were the peak laser intensity in the ablation plume and the peak discharge current. Generally, lower current could be compensated by higher laser power. Consistent with this was the observation that cratering the graphite or defocusing the laser gave larger plumes and high-

FIG. 2. Schematic representation of the laser plasma source used in this work to prepare amorphic diamond films.
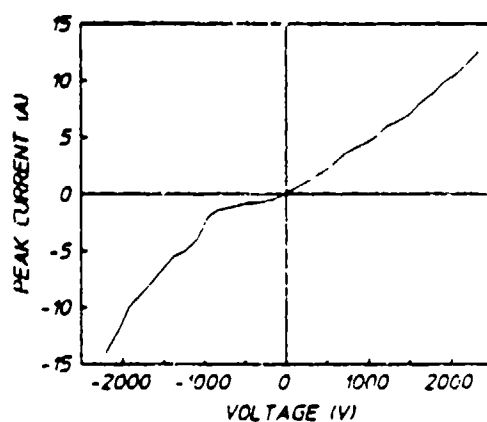

FIG. 3. Plot of the current and voltage characteristics of the diode formed by the graphite target and the electrode containing the conductive plasma ablated from the graphite by the laser.

er growth rates at the substrate but the resulting a-C film had much greater loss. Characteristics of films deposited at the lower power densities of Wagal,[7] Richter,[8] and Sato[9] could not be plotted on the scale of Fig. 1(b).

Optical constants for a typical film prepared at 5×10^{11} W/cm^2 are plotted in Figs. 1(a) and 1(b). In each case the substrate was 5.5 cm from the laser plasma source and radial expansion of the ejected material produced a domed profile of thickness which could be appreciated by the visual appearance of bright Newton's rings of interference. Optical constants were measured to be consistent across the 20 cm^2 over which thickness varied from 0.1 to 0.2 μm.

The laser pulse energies used here were not particularly different from those employed previously,[7] but the power densities developed at the graphite feedstock were much greater in the present work. The fact that a smaller growth rate was observed supports the expectations that a tighter focus gives a higher temperature to a smaller amount of carbon material. This in turn strengthens the perception of Miyazawa[4] that the carbon ions are the critical precursors of sp^3 bonding, but refute his conclusion that the concurrent transport of electrons is detrimental. At these densities the ablated material must be traveling as largely neutral plasma. However, in agreement with Savvides[5] these results suggest that such sputtering techniques depending upon ion beam sources may be intrinsically limited by the inability to reach high-power densities at high enough values of fluence to be practical. Losses indicate that the proportion of sp^2 bonding in our material is comparable to the best of Savvides' samples and can be reduced further with lasers of higher power that are commercially available. It is believed that this material can be reasonably described as amorphic diamond with 25% impurities and that the sp^2 inclusions serve no necessary role.

[1] An excellent review can be found in J. C. Angus and C. C. Hayman, Science 241, 913 (1988).
[2] E. G. Spencer, P. H. Schmidt, D. C. Joy, and F. J. Sansalone, Appl. Phys. Lett. 29, 118 (1976).
[3] S. Aisenberg and R. Chabot, J. Appl. Phys. 53, 2953 (1971).
[4] T. Miyazawa, S. Misawa, S. Yoshida, and S. Gonda, J. Appl. Phys. 55, 188 (1984).
[5] N. Savvides and B. Window, J. Vac. Sci. Technol. A 3, 2386 (1985)
[6] N. Savvides, J. Appl. Phys. 58, 518 (1985); 59, 4133 (1986)
[7] S. S. Wagal, E. M. Juengerman, and C. B. Collins, Appl. Phys. Lett. 53, 187 (1988).
[8] A. Richter, H. J. Scheibe, W. Pompe, K. W. Brzezinka, and I. Muhling, J. Non-Cryst. Solids 88, 131 (1986).
[9] T. Sato, S. Furuno, S. Iguchi, and M. Hanabusa, Jpn. J. Appl. Phys. 26, L1487 (1987).
[10] M. Born and E. Wolf, Principles of Optics, 6th ed. (Pergamon, Oxford, 1980), Sec. 13.4.1.